STATE OF CALIFORNIA DEPARTMENT OF TRANSPORTATION
TECHNICAL REPORT DOCUMENTATION PAGE
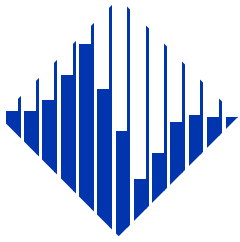TR0003 (REV. 10/98)

1. REPORT NUMBER CA15-2171	2. GOVERNMENT ASSOCIATION NUMBER	3. RECIPIENT'S CATALOG NUMBER
4. TITLE AND SUBTITLE Structural Behavior of Column-Bent Cap Beam-Box Girder Systems in Reinforced Concrete Bridges Subjected to Gravity and Seismic Loads, Part II: Hybrid Simulation and Post-Test Analysis		5. REPORT DATE November 2015
		6. PERFORMING ORGANIZATION CODE UCB
7. AUTHOR(S) Mohamed A. Moustafa, Khalid M. Mosalam		8. PERFORMING ORGANIZATION REPORT NO. UCB/CA15-2171 PEER Report 2015/10
9. PERFORMING ORGANIZATION NAME AND ADDRESS Department of Civil and Environmental Engineering University of California, Berkeley 747 Davis Hall Berkeley, CA 94720-1792		10. WORK UNIT NUMBER
		11. CONTRACT OR GRANT NUMBER 65A0391
12. SPONSORING AGENCY AND ADDRESS California Department of Transportation Engineering Service Center 1801 30th Street, MS 9-2/5i Sacramento, California 95816 California Department of Transportation Division of Research and Innovation, MS-83 1227 O Street Sacramento CA 95814		13. TYPE OF REPORT AND PERIOD COVERED Final Report 6/29/2011 – 6/15/2015
		14. SPONSORING AGENCY CODE 913

15. SUPPLEMENTAL NOTES
Prepared in cooperation with the State of California Department of Transportation.

16. ABSTRACT

This report presents the second half of the mixed experimental-computational study that aimed at investigating the structural and seismic behavior of integral bent caps in reinforced concrete (RC) box-girder bridges. The main objective of the study was to accurately estimate the contributions of the deck and soffit slabs framing into the bent cap in as-built and retrofitted RC bridge systems under the combined effect of vertical and lateral loading. In particular, the study estimated the effective flange width of the bent cap beam due to the box-girder slabs contributions. Computational and experimental methods were utilized to investigate the problem at hand. The finite element (FE) computational part of the study consisted of two phases: pre-test and post-test analyses. The experimental program involved testing two 1/4-scale column-bent cap beam-box-girder sub-assemblies using quasi-static and hybrid simulation (HS) testing methods. This report presents the results of HS tests conducted on the second specimen and post-test analysis, which involved calibration of the FE model and parametric studies at the specimen and full prototype bridge levels. The pre-test analysis phase and the first part of the experimental program are discussed in Part I of the report (PEER 2015/09).
To conduct the HS tests, this study developed a new practical approach that utilized readily available laboratory data acquisition system as a middleware for feasible HS communication. The proper communication among the HS components and verification of the HS system were first performed using tests conducted on standalone hydraulic actuators and the previously tested specimen. A carbon fiber reinforced polymer retrofit scheme was adopted for the second specimen to study the behavior of the bent cap at higher moment demands into its inelastic range of structural response. The retrofitted second specimen was then tested using multi-degree-of-freedom HS under gravity load using several scales of ground motions. The post-test analysis was the final stage of this study. The results from the as-built first-specimen cyclic tests were used to calibrate a detailed three-dimensional FE model. The calibrated model was used to explore the effect of reducing the bent cap reinforcement on the overall system behavior and to investigate the box-girder contribution at higher levels of bent cap seismic demand. The study revised the effective slab width for integral bent caps and concluded that the slab reinforcement within an effective width should be included for accurate bent cap capacity estimation. An illustrative design example to investigate the design implications of the revised effective slab width and bent cap capacity estimation on the optimization of the bent cap design for a prototype bridge is presented. To optimize the box-girder geometry for the most efficient slabs contribution to the bent cap structural behavior, another parametric study was conducted of the entire bridge level to investigate the effect of the box-girder geometry on the slab contributions and the bent cap effective width.

17. KEY WORDS Bent Caps, Effective Slab Width, Seismic Behavior, Box-Girder Bridges, Cyclic Testing, Finite Element Modeling	18. DISTRIBUTION STATEMENT No restrictions. This document is available to the public through the National Technical Information Service, Springfield, VA 22161	
19. SECURITY CLASSIFICATION (of this report) Unclassified	20. NUMBER OF PAGES 218	21. PRICE

Reproduction of completed page authorized

DISCLAIMER STATEMENT

This document is disseminated in the interest of information exchange. The contents of this report reflect the views of the authors who are responsible for the facts and accuracy of the data presented herein. The contents do not necessarily reflect the official views or policies of the state of California or the Federal Highway Administration. This publication does not constitute a standard, specification, or regulation. This report does not constitute an endorsement by the Department of any product described herein.

For individuals with sensory disabilities, this document is available in Braille, large print, audiocassette, or compact disk. To obtain a copy of this document in one of these alternate formats, please contact: the Division of Research and Innovation, MS-83, California Department of Transportation, P.O. Box 942873, Sacramento, CA 94273-0001.

Structural Behavior of Column-Bent Cap Beam-Box Girder Systems in Reinforced Concrete Bridges Subjected to Gravity and Seismic Loads

Part II: Hybrid Simulation and Post-Test Analysis

Mohamed A. Moustafa

Khalid M. Mosalam

Department of Civil and Environmental Engineering
University of California, Berkeley

Structural Behavior of Column-Bent Cap Beam-Box-Girder Systems in Reinforced Concrete Bridges Subjected to Gravity and Seismic Loads

Part II: Hybrid Simulation and Post-Test Analysis

Mohamed A. Moustafa

Khalid M. Mosalam

Department of Civil and Environmental Engineering
University of California, Berkeley

ABSTRACT

This report presents the second half of the discussion of a mixed experimental-computational study that aimed at investigating the structural and seismic behavior of integral bent caps in reinforced concrete (RC) box-girder bridges. The main objective of the study was to accurately estimate the contributions of the deck and soffit slabs framing into the bent cap in as-built and retrofitted RC bridge systems under the combined effect of vertical and lateral loading. In particular, the study estimated the effective flange width of the bent cap beam due to the box-girder slabs contributions for more accurate and effective consideration of the stiffness and capacity of a bent cap. Computational and experimental methods were utilized to investigate the problem at hand. The finite element (FE) computational part of the study consisted of two phases: pre-test and post-test analyses. The experimental program involved testing two 1/4-scale column-bent cap beam-box-girder sub-assemblies using quasi-static and hybrid simulation (HS) testing methods. This report presents the results of HS tests conducted on the second specimen and post-test analysis, which involved calibration of the FE model of the specimen and extended parametric studies at the specimen and full prototype bridge levels. The pre-test analysis phase and the first part of the experimental program that involved cyclic loading testing of the first specimen are discussed in the companion report (Part I of the companion report).

To conduct the HS tests, this study developed a new practical approach that utilized readily available laboratory data acquisition system as a middleware for feasible HS communication. The proper communication among the HS components and verification of the HS system were first performed using tests conducted on standalone hydraulic actuators. A full-specimen HS trial test was conducted using the previously tested repaired specimen to validate the entire HS system. A retrofit scheme was adopted for the second specimen that used a carbon fiber reinforced polymer (CFRP) column jacket before any HS testing was begun to study the behavior of the bent cap at higher moment demands into its inelastic range of structural response. The retrofitted second specimen was then tested using multi-degree-of-freedom HS under constant gravity load using several scales of unidirectional and bi-directional near-fault ground motions. The post-test analysis was the final stage of this study. The results from the as-built first-specimen cyclic tests were used to calibrate the most detailed three-dimensional FE model, which was previously developed as part of the pre-test analysis stage. The calibrated model was used to explore the effect of reducing the bent cap reinforcement on the overall system behavior and to investigate the box-girder contribution at higher levels of bent cap seismic demand. Based on the computational and experimental results obtained at the specimen level, the effective slab width for integral bent caps was revisited. The study concluded that the slab reinforcement within an effective width, especially in tension, should be included for accurate bent cap capacity estimation. An illustrative design example to investigate the design implications of the revised effective slab width and bent cap capacity estimation on the optimization of the bent cap design for a prototype bridge is presented. To optimize the box-girder geometry for the most efficient slabs contribution to the bent cap structural behavior, another parametric study was conducted of the entire bridge level to investigate the effect of the box-girder geometry on the slab contributions and the bent cap effective width.

ACKNOWLEDGMENTS

CONTENTS

LIST OF TABLES

LIST OF FIGURES

xviii

1 Introduction

This companion report complements the pre-test finite element (FE) analysis and the first phase of the experimental program discussed in Part I, and presents the second phase of the experimental program and the post-test FE analysis. The second phase of the experiments involved hybrid simulation (HS) system development, verification, and application of the developed system to conduct the retrofitted Specimen No. 2 HS tests. The post-test FE analysis involved the specimen model calibration against the experimental results and parametric studies at both of the specimen and full prototype bridge levels. A brief summary of the problem statement, and the experimental and computational programs adopted for this study is presented in this introduction, but the reader is referred to Part I of this report for more details. The organization of this report is also presented.

1.1 PROBLEM STATEMENT AND OBJECTIVES

The motivation of this study and the mechanics of the sought framework were inspired by previous research studies that were carried out to quantify the effective width and moment capacity of floor beams that are monolithically integrated with the floor slabs in buildings. The undertaken study attempted to answer the following question: how should accurate estimation of the stiffness and capacity of a bent cap be assessed considering the contributions of the deck and soffit slabs framing into the bent cap in reinforced concrete (RC) box-girder bridge systems under the combined effect of vertical and lateral loading? Alternatively, the problem statement can be stated as: what is the accurate estimate of the effective flange width of the bent cap beam due to the box-girder slabs contributions? Three overall research objectives further clarify the general problem statement. These are: (1) to investigate the behavior of bridge column-superstructure systems in light of the most recent AASHTO [2007] and Caltrans Seismic Design Criteria (SDC) [2013] provisions; (2) to investigate the system, particularly the integral cap beam, in different scenarios of as-built, repaired, and retrofitted bridge columns; and (3) to determine what are the possible design implications and code recommendations, if any, dictated by accurate estimate of cap beam effective flange width and capacity calculation.

1.2 EXPERIMENTAL AND COMPUTATIONAL FRAMEWORKS

A mix of computational and experimental methods was utilized to achieve the defined research objectives. The experimental program at the core of this research study was undertaken to

provide conclusive observations about the contribution of box-girder slabs to the bent cap beam behavior that served as the underlying foundation for the computational model calibration and extended parametric study. The experimental program composed of two identical 1/4-scale sub-assembly specimens were tested using two different lateral loading schemes. Specimen No. 1 was tested under quasi-static cyclic lateral loading in as-built and repaired conditions, as discussed in details in Part I of this report. Specimen No. 2 was retrofitted and tested using HS, which utilized an online computational model subjected to selected earthquake excitation that interacted with the physically tested specimen. A similar test set-up was used for all Specimen No. 1 and Specimen No. 2 tests, which involved testing the 1/4-scale sub-assembly in an inverted position. This set-up was chosen for practical reasons and for its feasibility to easily apply the combined gravity and the lateral loads at the column tip in its inverted position. A practical HS system was developed in this study, and the repaired Specimen No. 1 was utilized to provide a real HS test trial to verify the new HS development. The verified HS system was used afterwards to test the retrofitted Specimen No. 2. Details of the HS development and Specimen No. 2 HS tests are the essence of the experimental program presented in this companion report.

The computational framework adopted in this study complemented the experimental program, resulting in comprehensive design implications and conclusions. This framework comprises two broad phases: the pre-test analysis phase, which is discussed in Part I report, and the post-test analysis phase, which is presented herein. All the computational work was based on the FE analysis method. Several linear and nonlinear one-, two-, and three-dimensional (1D, 2D, and 3D) models were utilized to conduct the pre-test analysis before the experimental test specimens were built or the test set-up was assembled; see the Part I report. The post-test analysis used some of the pre-test analysis models to calibrate them against the experimental results; additional analysis and a parametric study was conducted at the specimen level to complement the experimental work. Moreover, extensions to prototype bridge models and a parametric study at the full-bridge level were conducted to investigate the effect of box-girder geometry on the bent cap behavior.

1.3   ORGANIZATION OF THE REPORT

This companion report consists of six chapters. Chapter 1 presents a brief review of the problem statement, methodology, and main objectives of the undertaken study. Chapter 2 presents the HS background, the developed HS system components, and the verification tests in detail. This chapter presents the HS trial tests that were conducted on the repaired Specimen No. 1 as well. The main test results and discussion of the retrofitted Specimen No. 2 that focused on the bent cap beam behavior and effective slab width are presented in Chapter 3. The second phase of the computational framework, which is the post-test analysis, is discussed in Chapters 4 and 5. Chapter 4 is concerned with the specimen FE model calibration and parametric study. Also included in Chapter 4 are the design implications based on the outcome of this study are investigated through an illustrative design example for a prototype bridge bent cap. Another parametric study that focused on the effect of the box-girder geometry on the bent cap effective width and slab contribution at the full-bridge level was conducted and presented in Chapter 5. A brief summary of the entire study, and the main conclusions and future work based on the full study are presented in Chapter 6. The concluding remarks are comprehensive, including results, analysis, and conclusions from both Parts 1 and 2.

2 Hybrid Simulation: Development and Verification

Hybrid simulation (HS) is a mixed computational/physical testing technique that can replace shaking table tests. The essence of HS is to use an online computational substructure to update the earthquake input signal at each time step based on the force feedback from the physical substructure. A complementary objective of this study was to develop a practical HS system that utilizes readily available laboratory data acquisition systems along with inexpensive TCP/IP-Ethernet connections to establish the communication between the physical and computational substructures. The main development in this study is the Pacific Instruments (PI) interface to communicate with the Open-source Framework for Experimental Set-up and Control (OpenFresco) [Schellenburg et al 2008] from the computational side, through an inexpensive Ethernet connection to replace expensive shared memory communication cards such as SCRAMNet, and the digital signal processor (DSP) card from the experimental side to control the laboratory hardware and receive the physical substructure feedback. Another development is the implementation of a new test set-up component in OpenFresco that is capable of performing geometric transformations between the global degrees-of-freedom (DOFs) in the computational model and the actuators' local DOFs for the command displacements and force feedbacks. A set of verification tests were conducted that used single and double actuators that were not attached to any specimens. To validate the whole system, a complete HS test was conducted using repaired Specimen No. 1. A brief background of HS, the main components and developments of the HS system, and verification tests are presented in this chapter. The successfully validated HS system was utilized for conducting the retrofitted Specimen No. 2 HS tests, as discussed in the Chapter 3.

2.1 BACKGROUND

Hybrid simulation was first mentioned by Takanashi et al. [1975], who referred to the testing method as an "online test." The next decade saw significant development efforts in the U.S. that included the research at the University of California, Berkeley (UCB) [Mahin and Williams 1980; Mahin and Shing 1985; and Mahin et al. 1989], and in Japan [Takahashi and Nakashima 1987; Nakashima et al. 1988]. Previous research on HS investigated different areas included, but were not limited to (1) the development of suitable integration methods; (2) the study of the effect of experimental errors; and (3) real-time HS. The following subsections briefly discuss basic procedures in HS, including numerical integration methods, errors in HS, real-time HS, and

a brief summary of a relevant HS bridge test. Note that targeted HS tests were slow tests, but a very brief discussion of the real-time HS is provided for completeness.

2.1.1 Integration Methods

A wide spectrum of numerical integration methods, such as Newmark's methods [1959], generalized-alpha methods, predictor-corrector methods, and Runge-Kutta methods, exist for solving the governing equations of motion, which are discretized in time domain for different structural dynamics problems. Not all of the numerical integration methods can be used directly for solving the equations of motion in HS testing. Thus, one of the main areas of HS-related research is concerned with adopting and/or modifying the existing integration methods, or developing new specialized integration methods for HS purposes. A brief background on integration methods and some of the relevant previous work is presented. The most common classification of numerical integration methods and algorithms is explicit versus implicit methods. Only an explicit integration scheme was utilized for all the tests in this study, but a brief comparison with the implicit scheme is presented for completeness. Selected previous studies that used explicit methods are Takanashi et al. [1975], Mahin and Williams [1980], Nakashima and Masaoka [1999] and Magonette [2001]. On the other and, implicit schemes were developed and used in HS in several studies [e.g. Dermitzakis and Mahin 1985; Thewalt and Mahin 1987; Nakashima et al. 1990; Shing et al. 1991; Bayer et al. 2005]. The reader is referred to Schellenberg et al. [2009] for a comprehensive review of HS integration methods.

2.1.1.1 Explicit Integration Methods

For an explicit algorithm, the new solution at time step (i+1) can be expressed entirely by known terms such as the current solution state at time step (i) or even previous step (i-1) as in Central Difference Method (CDM); e.g., $u_{i+1} = f\left(u_i, \dot{u}_i, \ddot{u}_i, u_{i-1}, \dot{u}_{i-1}, \ddot{u}_{i-1}\right)$. Explicit integration methods are usually conditionally stable, meaning that the integration time step (Δt) should be smaller than the shortest natural period of a structure (T_n) divided by a factor (α) to yield a stable and accurate solution ($\Delta t \leq T_n/\alpha$). Also the new solution for the next time step can often be determined in a single calculation step without the knowledge of the tangent stiffness matrix. Two well-known examples of explicit integration methods are CDM and the explicit Newmark method. Generally, the explicit Newmark method is used more often in HS than CDM for the following reasons: it does not require any quantities before the start time (i.e., at $t = 0$), the velocities and accelerations are directly obtained as the solution advances (there is no need to be calculated separately as in the CDM), and it has more favorable error-propagation characteristics as shown by Shing and Mahin [1983]. Explicit methods are generally advantageous because they are computationally very efficient, easy to implement, and fast in their execution; that said, a limiting factor for the application of the explicit methods is their stability criteria. Hence, they are not suitable for stiff problems (short periods) and cannot even be used at all for infinitely stiff problems. Although this limitation can be overcome by choosing smaller integration time steps, the integration time step might need to be reduced to an extent that the application of explicit methods to HS becomes impractical. Implicit methods are sought in these cases.

2.1.1.2 Implicit Integration Methods

For an implicit algorithm, the solution at time step (i+1) not only depends on known quantities from the current and previous time steps, but also on the solution itself: $u_{i+1} = f\left(u_{i+1}, \dot{u}_{i+1}, \ddot{u}_{i+1}, u_i, \dot{u}_i, \ddot{u}_i\right)$. Because of this, implicit algorithms contain algebraic formulas that need to be solved iteratively in order to determine the solution at the end of a time step. Many implicit integration methods are generally unconditionally stable, thus they are ideal for stiff and infinitely stiff problems. This also means that only the accuracy of the algorithm needs to be considered when determining the time step size since the method is stable for any step size. Generally, this permits the selection of larger analysis time steps as compared to the explicit methods. Implicit methods are well suited for large problems with many DOFs or for infinitely stiff problems, which occur in the cases with structural DOFs with no mass. However, they are computationally more demanding because they require iterative solution schemes, and they can introduce spurious loading and unloading cycles on the physical parts of the HS. A comparison of the features of explicit and implicit integration methods is shown in Table 2.1.

Table 2.1   Comparison between explicit and implicit integration methods.

Item	Explicit methods	Implicit methods
Required input	$u_{i+1} = f\left(u_i, \dot{u}_i, \ddot{u}_i, u_{i-1}, \dot{u}_{i-1}, \ddot{u}_{i-1}\right)$	$u_{i+1} = f\left(u_{i+1}, \dot{u}_{i+1}, \ddot{u}_{i+1}, u_i, \dot{u}_i, \ddot{u}_i\right)$
Iterations	not required	Required
Tangential stiffness	not required	required at each time step
Stability	conditionally stable: $\Delta t \leq T_n/\alpha$	generally unconditionally stable
Computational cost	easy to implement, and computationally efficient	harder to implement, and computationally expensive due to iterative schemes
Execution time	generally faster	generally slower because of iterations
When to use	• When only physical specimen is tested, and analytical part consists of mass and damping only; • For MDOF systems with non-singular mass matrix (all DOFs have nonzero masses).	• Stiff or infinitely stiff problems with short periods; • For MDOF systems with singular mass matrix (some DOFs have zero masses such as rotational DOFs, without considering the associated mass moment of inertia, in moment resisting frames)

2.1.2 Errors in Hybrid Simulation Testing

Due to the nature of the multi-component of HS system (HSS), there are numerous possibilities for error sources either computationally or experimentally, especially in the controller and boundary conditions. Elimination or at least minimizing these errors is necessary for a valid and reliable HSS. Errors in HS can be categorized into three groups: (1) errors due to structural modeling such as the structural idealization that consists of replacing a continuous system by a

discrete number of DOFs; (2) errors due to the numerical methods; and (3) experimental errors constitute the third group, which can be further classified as random and systematic errors. Although numerical and random errors have been found to be insignificant in contaminating the results and thus typically ignored. Because of the propagation and accumulation of systematic experimental errors, better understanding of the nature of these errors was desired in order to either eliminate or minimize them or correct the results by compensating for such errors to achieve a more reliable system.

A brief survey of HS errors-related previous research is presented. Mosqueda [2003] provided a comprehensive summary of the nature and sources of HS errors and available error compensation techniques. The effect of experimental errors has always been an important area of HS research, especially before the advent of modern digital controllers and closed loop control of hydraulic actuators. In two of the earliest works, the propagation of random and systematic errors was evaluated by Mahin and Williams [1980] and Shing and Mahin [1983]. The cumulative nature of experimental errors introduced by the control and data acquisition systems in HS tests using explicit numerical integration algorithm was studied by Shing and Mahin [1987]. Reliability of the HS method was investigated by Yamazaki et al. [1989], where experimental error behavior was examined based on an elastic test of a six-story steel structure. Thewalt and Roman [1994] presented several parameters for identifying errors and quantifying their magnitude and effect. Mosqueda [2003] simulated the experimental errors, such as the random noise in the load cells and displacement lag errors, using Simulink models and derived linear transfer functions for time delay errors and for the dynamic behavior of experimental set-ups, including the specimen, the transfer system, and the reaction wall.

An example of research aimed at reducing the effect of errors on HS includes Chang et al. [1998], who proposed solving the momentum equation of motion that is obtained by integrating the force equation of motion. This approach filters out the measured forces are by the integration algorithm before being used in the numerical solution. Horiuchi et al. [1999] measured the time lag of the actuator response, i.e., the difference between command and feedback displacements, and predicted the command of the actuator by advancing the current time with the delay time using a polynomial extrapolation procedure. Alternatively, Elkhoraibi and Mosalam [2007] overcame this time lag by developing a feed-forward error compensation scheme based on the modification of the displacement command with an error term which is a function of the actuator velocity. Stoten and Magonette [2001] have investigated the effect of improvement of the hardware components, such as the use of digital controllers and digital transducers, in order to achieve better experimental results. Development of integration methods aimed at damping out the spurious higher mode participations also strive to reduce the effect of errors on HS.

2.1.3 Real-Time Hybrid Simulation

A HS test is said to be conducted in real-time when the experimental substructure (physical specimen) is loaded with the actual calculated velocities and accelerations. Therefore, highly variable loading rates are expected in real-time tests. Conventional HS with slow rates of loading, which is similar to the tests conducted in this study, is sufficient in most of the cases where rate effects are not important, such as in the case of RC components. However, for rate-dependent specimens, such as triple friction pendulum bearings, real-time HS becomes essential.

Another relevant application is the use of real-time HS for testing rate-dependent composite (polymer) insulator posts [Mosalam et al. 2012].

The first progress in real-time HS was achieved by Nakashima et al. [1992], who used dynamic actuators and a digital servo-mechanism. After the development of actuator-delay compensation methods by Horiuchi et al. [1999], research on real-time HS gained momentum. Darby et al. [1999; 2001] developed various real-time partitioned HS utilizing control system approaches. Nakashima and Masaoka [1999] employed a DSP for the first time to separate the actuator signal generation from the target displacement computation. Nowadays, the rapid development of computing technologies and control methods increases the number of real-time HS research activities for different applications. For example, a large amount of work was conducted on electrical switches using real-time HS [Günay and Mosalam 2014].

2.1.4 Previous Hybrid Simulation Testing of Bridges

As detailed above, much of the research in HS have focused on the development side and robustness of the testing method; however, several studies have utilized HS directly in different applications [Yang et al. 2007; Wang et al. 2007; Chang 2008; Kim and Elnashai 2008; Mosqueda et al. 2008; Takahashi et al. 2008; Xin-Jiang and Shi-Zhu 2009; Frankie et al. 2013]. A short summary of one of the recent studies that focused on HS application to bridges and was consulted during the course of this study is presented below for its relevancy.

An investigation by Terzic and Stojadinovic [2010], which was conducted at UCB and used a similar HS test set-up to the present study, focused on the post-earthquake traffic capacity of modern California bridges using HS. Modern highway bridges in California are designed using the Caltrans SDC [2013] and are expected to maintain—at minimum—a gravity load-carrying capacity during both frequent and extreme seismic events. However, no validated, quantitative guidelines for estimating the remaining load-carrying capacity of such bridges after an earthquake event exist. Terzic and Stojadinovic [2010] combined experimental and analytical methods to evaluate the post-earthquake traffic load-carrying capacity of a modern California highway overpass bridge. An experimental study on models of circular RC bridge columns was performed to investigate the relationship between earthquake-induced damage in bridge columns and the capacity of the columns to carry axial load in a damaged condition. The test results were then used to calibrate a FE model of a bridge column. This bridge column model was incorporated into a hybrid model of a typical California overpass bridge and tested using the HS technique. A multi-DOFs HS tests were conducted that used two translational and two rotational experimental DOFs for the test, which required a new experimental set-up element in OpenFresco, similar to what has been developed in the present study. The FE model of the typical California overpass bridge was validated using the data from the HS tests. The validated model of the typical bridge was used to evaluate its post-earthquake truck load capacity in an extensive parametric study that examined the effects of different ground motions and bridge modeling parameters, such as the boundary conditions imposed by the bridge abutments, the location of the truck on the bridge, and the amount of bridge column residual drift. Terzic and Stojadinovic [2010] concluded that a typical modern California highway bridge is safe for traffic use after an earthquake if no columns failed and the abutments are still capable of restraining torsion of the bridge deck about the longitudinal axis. If any of the columns fail, i.e., fractured column reinforcing bars are discovered in an inspection, the bridge should be closed for regular traffic. Emergency traffic with weight, lane, and speed restrictions may be allowed on a bridge

whose columns have failed if it is determined that the abutments can restrain torsion of the bridge deck. These findings pertain to the bridge configuration investigated in the study.

2.2   HYBRID SIMULATION SYSTEM

To perform a HS test, several key components including software and hardware are necessary. Schellenberg et al. [2009] provided a comprehensive overview of the key components of a generic HSS, as shown in Figure 2.1. The components of the specific HSS utilized in this study in addition to the computational and experimental substructures used are discussed in this section. A brief discussion of a P-delta correction scheme that was devised and used in some of the HS tests is presented as well.
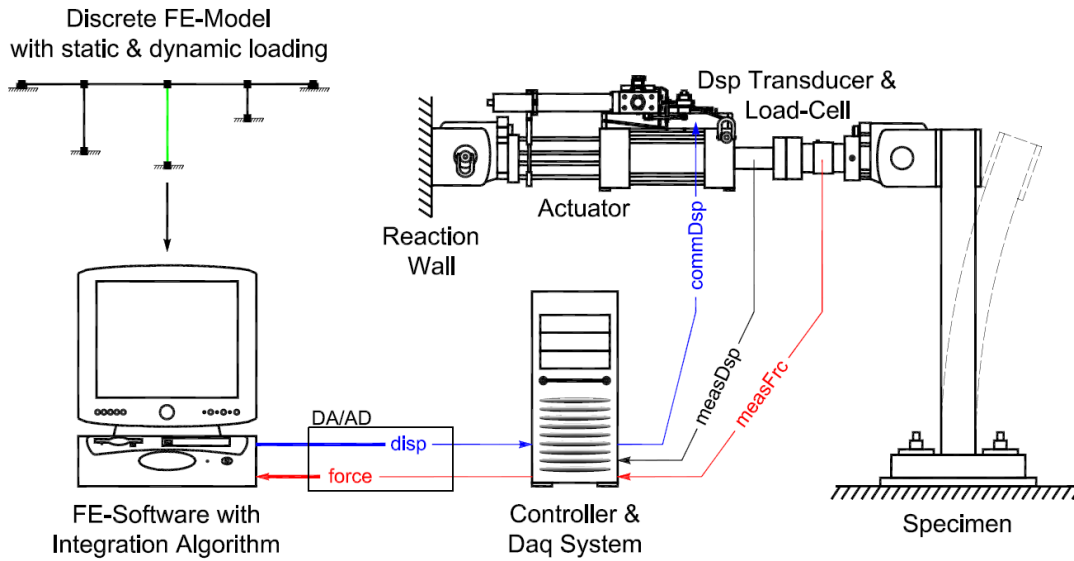
Figure 2.1   Key components of a hybrid simulation system [Schellenberg et al. 2009].

2.2.1 Hybrid Simulation System Components and Connectivity

Four main components comprise a typical HSS. The first component is a discrete model of the structure to be analyzed on a computer, including the static and the dynamic loading. The FE method is used to discretize the problem spatially, and a time-stepping integration algorithm is then used for the solution of the equations of motion with time discretization. The resulting dynamic equations of motion for the finite number of discrete DOFs are a system of second-order ordinary differential equations in time that are initialized and expressed, as shown in Equation (2.1).

$$\mathbf{M}\,\ddot{\mathbf{U}}_{i+1} + \mathbf{C}\,\dot{\mathbf{U}}_{i+1} + \mathbf{P}_r(\mathbf{U}_{i+1}) = \mathbf{P}_{i+1} - \mathbf{P}_{o,i+1}$$

$$\mathbf{U}_{i=0} = \mathbf{U}_0 \qquad\qquad (2.1)$$

$$\dot{\mathbf{U}}_{i=0} = \dot{\mathbf{U}}_0$$

where $\ddot{\mathbf{U}}$, $\dot{\mathbf{U}}$, and $\mathbf{U}$ are the acceleration vector, the velocity vector, and the displacement vector at the structural DOFs, respectively. $\mathbf{M}$ is the mass matrix assembled from the nodal and element mass matrices, $\mathbf{C}$ is the viscous damping matrix, $\mathbf{P}_r$ are the assembled element resisting forces (which depend on the displacements), $\mathbf{P}$ are the externally applied nodal loads, and $\mathbf{P}_o$ are the assembled "equivalent" element loads.

The second required component is a transfer system consisting of a controller and static or dynamic actuators, so that the incremental response (generally the displacements) determined by the time-stepping integration algorithm can be applied to the physical portions of the structure. For slow tests such as the ones conducted in this study, quasi-static testing equipment can be used. Thus, the same controllers and static actuators that were used in the cyclic loading tests of Specimen No. 1 were utilized again in Specimen No. 2 HS tests. The third major component of the HSS is the physical specimen being tested in the laboratory and the support system (e.g., reaction wall or frame) against which the actuators of the transfer system can react. The fourth and last component is a data acquisition system, including displacement transducers and load cells. The data acquisition system is responsible for measuring the response of the test specimen and returning the resisting forces to the time-stepping integration algorithm to advance the solution to the next analysis step.

A vital feature of HS is to connect the above mentioned four components together to achieve vigorous two-way communication for sending the displacement input and receiving the force feedback. The major components and connectivity pieces of the utilized HSS at the Structures Laboratory at UCB are shown in Figure 2.2. The main pieces identified in this figure are as follows: (a) A computational platform where the numerical integration of the governing equations of motion is performed (the Open System for Earthquake Engineering Simulation (OpenSees) [McKenna et al. 2000] was used in this case); (b) OpenFresco [2008] generic middleware that communicates with the computational platform; (c) new interface software developed within the PI data acquisition system (DAQ) that communicates, in turn, with OpenFresco through TCP/IP connection; (d) a DSP card that further complements the communication loop with the laboratory hardware; and (e) digital controllers that command the hydraulic actuators in displacement control. The main development in this study is the PI interface to communicate with OpenFresco from the computational side, and the DSP card from the experimental side. Another development was implementing a new geometric transformation test set-up component in OpenFresco. More details about these developments and their verification are reported later in this chapter. A further discussion of the computational and experimental substructures is presented in the following subsections.
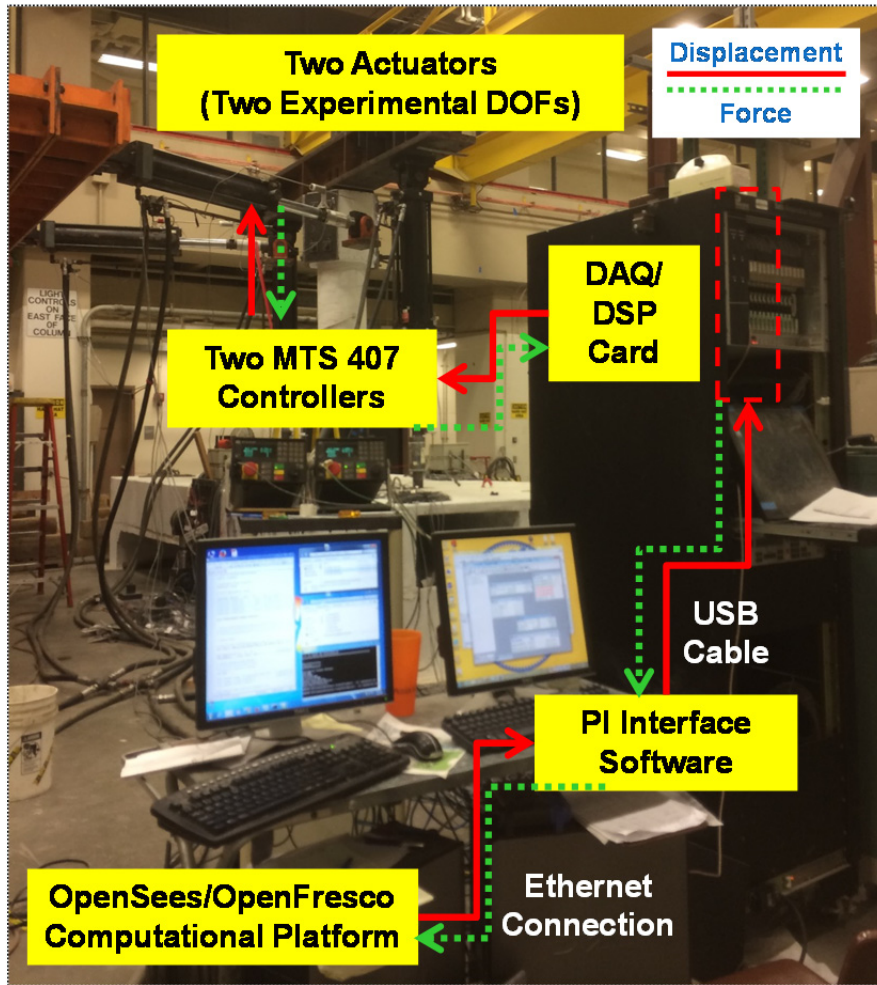
Figure 2.2   Overview of the main components and connectivity of the HSS at the Structures laboratory at UCB.

2.2.2 Computational Model

The computational model consisted of multi-DOFs with mass and damping. The lumped mass used in the computational model was calibrated such that comparable modes of vibration to the prototype bridge (see the companion report) are obtained when the proper similitude relationships were applied. Damping is modeled as Rayleigh damping with damping coefficients determined by using 5% damping ratio for periods corresponding to the transverse and longitudinal modes of vibration. Although a larger computational substructure of the full prototype bridge could have been used in the considered HS tests, the main objective of the HS test was to evaluate the bent cap beam behavior and the contribution from the test specimen box-girder slabs rather than an overall bridge behavior, i.e., a localized behavior of the test specimen and a global behavior of the test sub-assemblage considering the column-bent cap-box-girder interaction rather than the full bridge behavior. Accordingly, the computational model was a multi-DOFs column with lumped mass at the top. OpenSees [McKenna et al. 2000], previously used in the pre-test analysis, was used again in the HS tests as the FE software used to analyze the computational substructure of the test specimen and solve the dynamic equation of motion to solve for the displacement at each time step. Meanwhile, OpenSees was used along with the

middleware, OpenFresco [Schellenberg et al. 2009], to connect the FE model with the control and data acquisition software. OpenFresco was designed in an object-oriented structure that is similar to that of OpenSees; it shares common classes and subroutines for element types and numerical integration methods for instance. Therefore, OpenFresco is most conveniently used with OpenSees as the FE platform even though OpenFresco has the capabilities to communicate with a variety of other FE software programs. Accordingly, a single OpenSees/OpenFresco input file that is prepared using the Tool Command Language (TCL) is used to define the computational model and the communication settings. The specimen is represented in OpenSees using the *GenericElement* type.

The HS tests were conducted using a transverse direction only or bi-directional horizontal components of the ground motion. Again, the vertical component of the ground motion was used only in the tests that incorporated the *P*-delta correction where the total fluctuating axial load, due to both of the gravity load and vertical excitation, was used to correct for the lateral force feedback. As discussed in detail in the companion report, a short list of six ground motions were found to cause the largest demands in the bent cap. Out of the short list of six records identified in Part I of this report, only the Northridge earthquake record at the Rinaldi station was used in Specimen No. 2 HS tests as it was representative of a California earthquake. Figure 2.3 shows the three components of the 100% Rinaldi record.

The above discussion is concerned mainly with the computational model considered for the intended HS tests of Specimen No. 2. However, for the HSS verification tests that used the actuators only—without any attached specimen— a more generic and much larger DOF model was used with a variety of ground-motion records to validate the HSS for larger computational models and different cases. The HSS verification tests used different ground motions with more cycles and harmonic nature, such as the El Centro record, and pulse-like nature, such as the Rinaldi record. Moreover, a multi-story multi-bay frame was used as the computational model where one of the first story columns was replaced by the experimental element. A simulation experimental element, available in OpenFresco and based on input material and geometric properties, was used rather than an actual experimental physical substructure. This was very beneficial where a multiplier (assumed stiffness) of the displacement of the free actuators in the HS verification tests was feedback as a virtual force feedback to the system to check the communication loop against the pure simulation results. More details are presented in the single actuator verification tests; see Section 2.4.2.
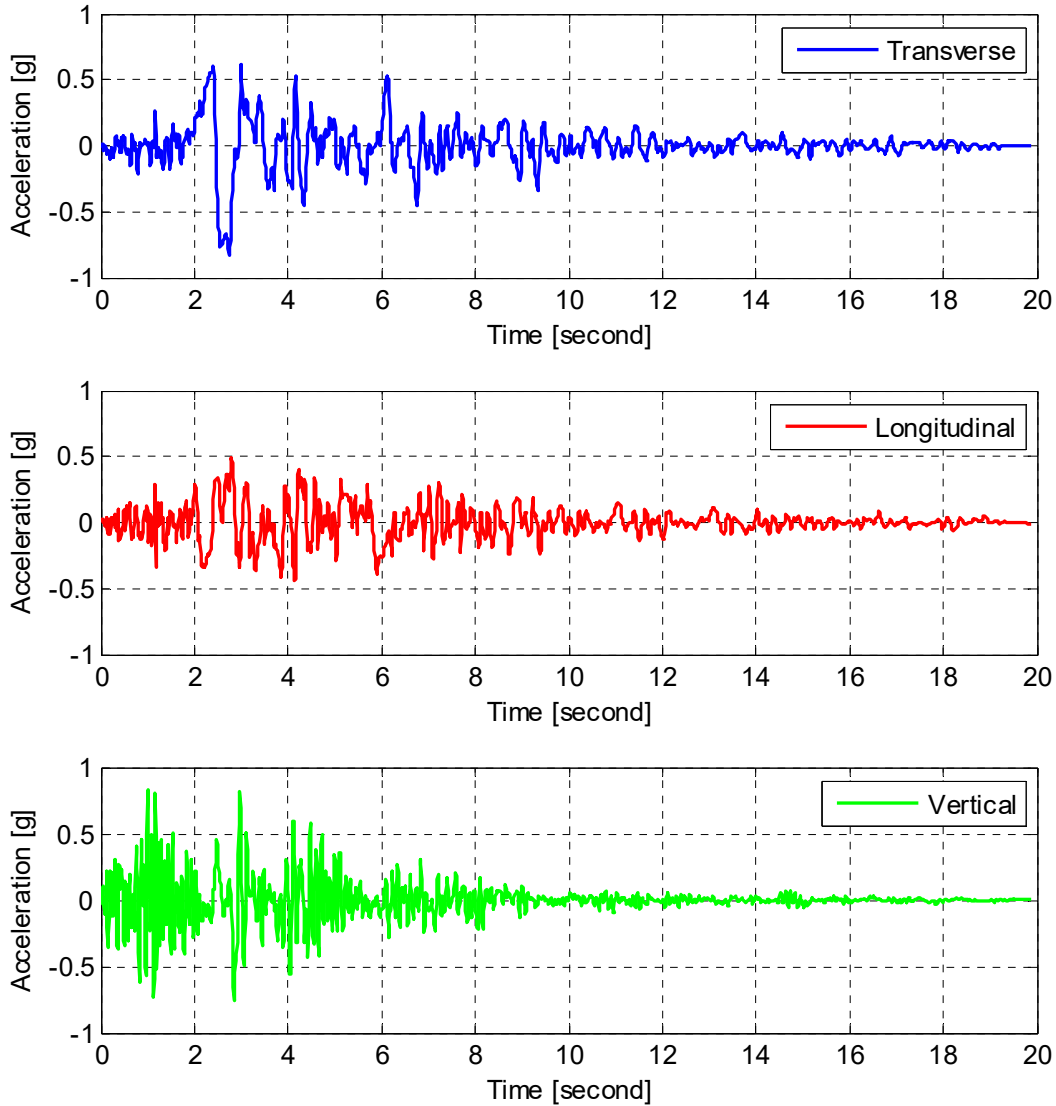
Figure 2.3   Three components of the Northridge earthquake recorded at Rinaldi station.

2.2.3 Physical Substructure

The hybrid nature of the tested model is attributed to the fact that part of the model is a computational analytical model, whereas the rest of the model is a physical experimental substructure. For the HS tests considered in this study, the physical specimen was the column-bent cap-box-girder sub-assemblage, which was similar to the test specimen considered for the quasi-static cyclic loading tests. As previously discussed, the computational model was a column model with lumped mass and damping. The input for the equation of motion was supplemented by the resisting force feedback, which reflected the lateral overall system behavior of the full column-bent cap–box-girder sub-assemblage after the proper geometric transformations were applied. Figure 2.4 shows a view of the retrofitted Specimen No. 2, before setting up the instrumentation and the test loading set-up, which comprised the physical substructure of the HS tests.

Figure 2.4 **Physical experimental substructure (retrofitted Specimen No. 2) used in the HS tests.**

2.2.4 *P*-Delta Correction

In structural analysis, *P*-delta refers to the abrupt changes in a sufficiently tall structural component base shear and bending moment when it is subjected to lateral displacement. The *P*-delta effect can be interpreted as a destabilizing secondary moment that results from a vertical gravity force multiplied by the lateral displacement, as schematically represented in Figure 2.5. Accordingly, in case of progressing lateral displacements, the destabilizing secondary moment increases and can cause instability or complete collapse. The *P*-delta effect is more dramatic in buildings, especially tall buildings, more than bridges because of the elevated gravity load levels at the lower floors columns. Vertical ground excitations can increase axial load levels, which can accelerate the collapse. In bridges the gravity loads are not typically as high as in the case of buildings, yet the *P*-delta effect might be pronounced at large lateral displacements.

This study devised an approximate method for accounting for the *P*-delta effect from both the gravity load and the vertical excitations for HS testing: the lateral force feedback is corrected before it is sent back to the computational model to solve for the next displacement input step. Given the known lateral displacement at a time step, the acting gravity load along with the additional axial load resulting from the solution of the computational model under the vertical excitation were utilized to calculate the *P*-delta secondary moment, and, accordingly, correct the lateral force feedback. Figure 2.5 shows schematically how the corrected force is

13

achieved when the *P*-delta effect is incorporated. The simple arithmetic operation to correct the force feedback was performed using a DSP subroutine. These split computations provided additional flexibility for future development where the conventional DAQ system can be used to accommodate a hybrid computational model, i.e., part of the computations are performed using the FE platform, while another part is performed using a DSP subroutine.

The *P*-delta correction involved the applied gravity load during a HS test as well as the corresponding axial force resulting from the vertical excitation calculated using the model featured in Figure 2.6. Thus, a different *P*-delta correction force was calculated at each time step to accommodate the fluctuating total axial load from the gravity and vertical excitation. The solution in the vertical direction assumed a bi-linear force-deformation of the interacting column-bent cap-box-girder system, as shown in Figure 2.6. This approximation aimed at capping the resulting vertical force at a certain limit that was dictated by the results of the vertical pushover and triaxial time history DIANA [2014] pre-test analysis. The capping value used for the vertical capacity of the system, $P_{capping}$, was ~350 kips; see companion report.

The *P*-delta correction was applied only in the HS tests up to 100% scale. Thus, the larger scale tests at 125%, 150%, 175%, and 200% ground-motion scales, which were conducted only in the transverse direction due to the test set-up limitations, did not include the *P*-delta correction. That was done to avoid the resulting tension from the axial force fluctuation at larger scales of the vertical excitation during some time steps, i.e., the *P*-delta correction was not applied for the runs when $P_g + \min(P_{ve}) < 0$, i.e., tension. The developed tension axial force would reverse the correction component and cause a stiffening effect in the feedback. A future study that focuses more on identifying all the possible consequences of incorporating the *P*-delta effect might be useful. Because the main objective of the HS tests was the bent cap beam response and the box-girder contributions, the *P*-delta effect was not incorporated at the larger scale runs to avoid the influence of any factors that are not fully understood such as the effect of the column subjected to tension due to this effect.
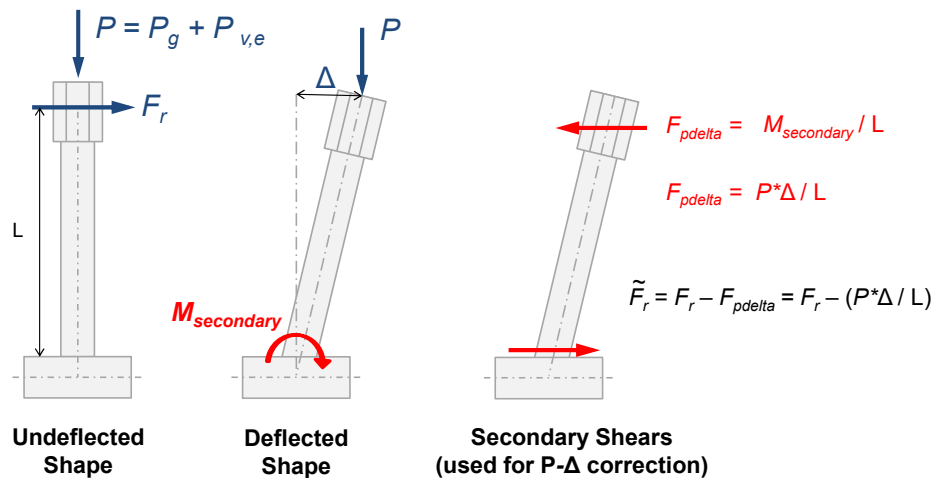
Figure 2.5   **Schematic representation of the P-delta (P-Δ) correction.**
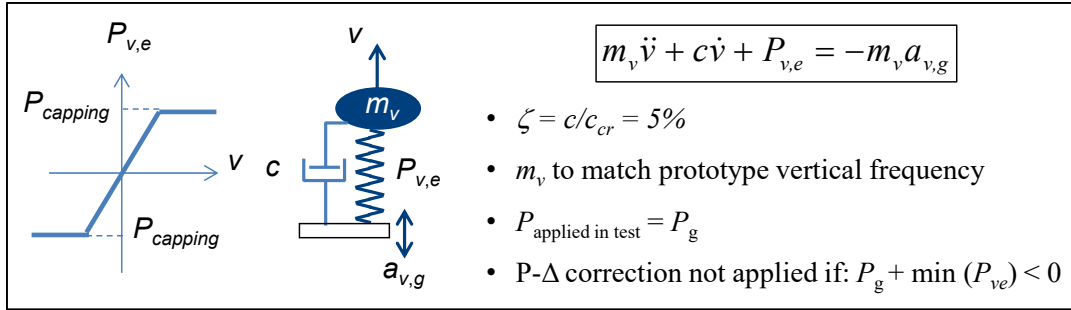
Figure 2.6 Computational model used for including vertical excitation in the *P-Δ* correction.

2.3 HYBRID SIMULATION: NEW DEVELOPMENTS

To properly connect all the HSS components discussed in the previous section, a robust communication loop is indispensable. In a general sense, the readily available OpenFresco software comprised the biggest part of the necessary middleware needed for connecting the FE analysis software and the experimental control and DAQ systems, as illustrated in Figure 2.7. OpenFresco lacked the needed experimental set-up that performs the specific geometric transformations between the global DOF and the local DOF of the lateral actuators per the required set-up in this study. Thus, implementing a new experimental set-up object in OpenFresco was required to achieve the sought HSS. To avoid using expensive shared-memory network cards, such as SCRAMNet, to communicate with the controllers, a practical way of utilizing inexpensive TCP/IP Ethernet connections was another objective. Although a generic TCP control was already available in OpenFresco, a middleware that utilizes such TCP connection to communicate the commands to the controllers was required. To achieve the desired middleware, the PI DAQ software was modified to encompass a new module that could integrate the networking capabilities of the DAQ console along with the programmable DSP card. The new PI interface was the second development achieved in this study. The two developments are shown on the HSS flowchart; see Figure 2.7. More detail about these two developments is presented below.
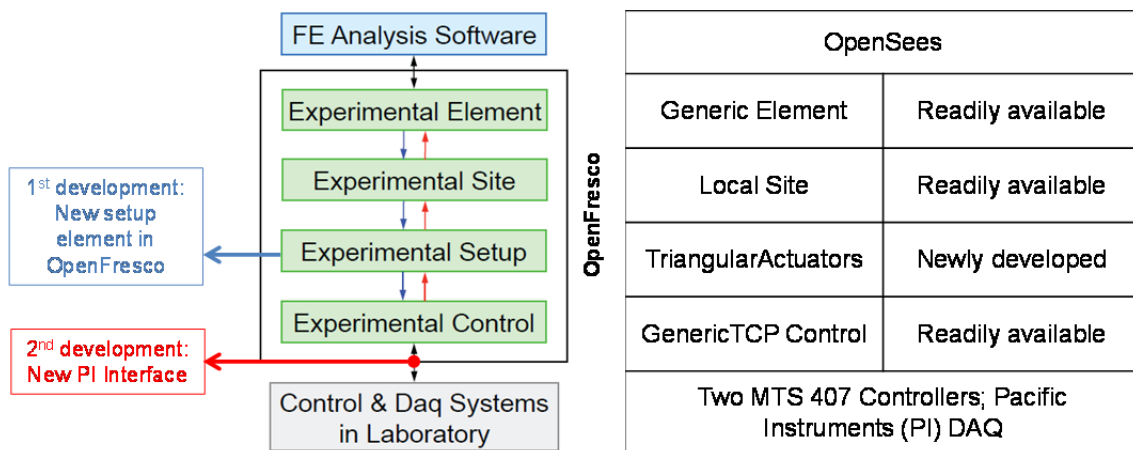
Figure 2.7 Overview of the HSS using OpenFresco and the new HSS developments.

2.3.1 Development I: OpenFresco New Experimental Set-Up

The *ExperimentalSetup* is one of four main classes that compromise OpenFresco. The transformation of the prescribed boundary conditions from the local or basic element DOF of the experimental elements into the actuator DOF of the transfer system is the first core task of the *ExperimentalSetup* class. Similarly, transformation of the work conjugates measured by transducers and load cells back to the experimental element DOF is the second core task of the *ExperimentalSetup* class [Schellenberg et al. 2009]. For the HS tests considered in this study, the two horizontal actuators used for applying the lateral load were arranged in a planer triangular configuration. A new *ExperimentalSetup* object was required in OpenFresco to perform the geometric transformation between the two model (global) DOFs, designated as x and y, and the two actuators (local) DOFs, designated as 1 and 2, as shown in Figure 2.8. The transformation is applied to the computed displacements such that displacement command read in each actuator DOF is delivered to the corresponding controller. Similarly, the received force feedback in each actuator DOF is transformed to the x and y DOFs before passing it to the FE software to proceed with the next step calculations. The *TriangularActautors* object was successfully developed and implemented in an updated version of OpenFresco. The TCL syntax input for the new experimental set-up is as follows:

expSet-up TriangularActuators *$tag* -control *$ExpControltag $A1 $A2 $B1 $B2 $C1 $C2*

where *$ExpControltag* is the defined tag for the used experimental control object, which is the GenericTCP in this case, and *$A1, $A2, $B1, $B2, $C1,* and *$C2* are geometric input parameters that describe the relative locations of the two actuators, as identified in Figure 2.8. The developed set-up element was debugged and implemented in OpenFresco, which was compiled into an updated version that encompassed the new set-up. Further verification of the geometric transformation achieved through the newly implemented experimental set-up element was conducted as discussed in the next section.
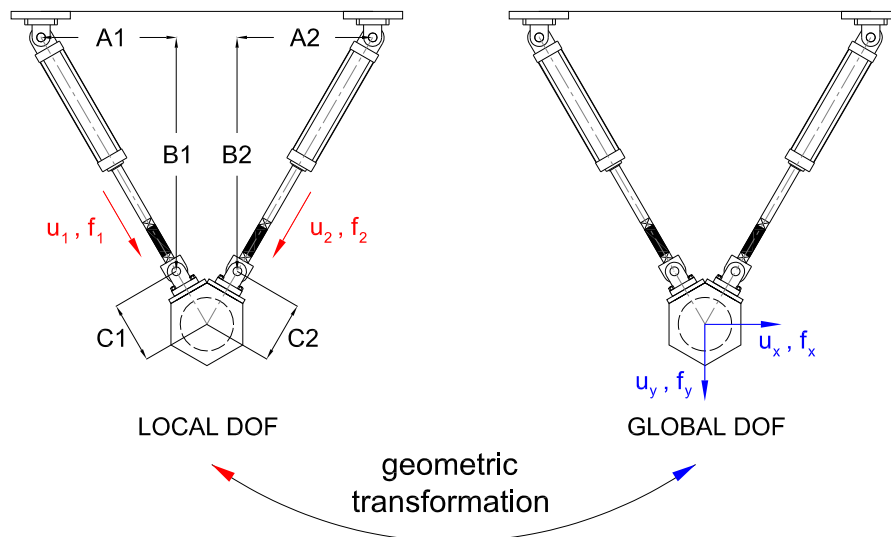
Figure 2.8   **Input displacement and measured force feedback geometric transformation between the model global DOF and the actuators local DOF.**

2.3.2 Development II: New PI Interface

The central development achieved through this part of the study is a practical middleware between OpenFresco and the controllers. This interface is built into the PI DAQ system. The development was achieved through various collaborations with the staff at the Structures Laboratory at UCB. The final product consists of two related parts: (1) Microsoft Windows application customized from the PI DAQ software; and (2) PI test file containing specific PI6042 DSP routines. A more detailed description along with the main purpose of each of the two implemented interface pieces is presented here.

2.3.2.1 Microsoft Windows Custom Application

The Microsoft Windows application, namely PI660C UCB HybridSim interface, is a heavily modified version of the original PI660C DAQ program. The modifications include the addition of a TCP communications interface, an OpenFresco command interpreter, and a raw data format handler and translator. The main purpose of the developed new PI interface is to exchange displacement and force vectors—from 1 to 5 DOF—with OpenFresco over an Ethernet TCP/IP connection. Thus, this application is responsible of receiving the displacement vector from OpenFresco and passing it through the DSP routines to the controllers. In addition, it receives the force feedbacks from allocated memory locations and sends them back to OpenFresco. All the operations performed through this part of the interface utilize data in the actuators' DOF. The geometric transformation to the global DOF for solving the equations of motion under the responsibility of OpenFresco through the new *ExperimentalSet-up* class, as previously discussed.

A screen shot of the PI660C UCB HybridSim Microsoft Windows application is shown in Figure 2.9. The figure shows the implemented module that handles the HS mode and sets its parameters. A set of the parameters that can be pre-assigned are shown in Figure 2.10. All the parameters are considered input for the DSP routines that are called through the PI application. Because the interface can exchange data from up to five DOFs, a span definition is required for each of these five DOFs for control purposes. The rate of loading, defined in terms of the maximum velocity, is one of the parameters input shown in Figure 2.10. A maximum velocity is defined rather than a constant velocity because based on the number of controlled DOFs, one actuator might have to slow its velocity to match other actuators motion; see Section 2.4.3 for more detail. Finally, two additional options that are still under development but were not needed for the tests conducted in this study, are the *superpipelinemode* and *pipelinepredict*. These modes aim at minimizing the communication delays for the prospect of real-time HS application. However, these new options out of the scope of this study and are not discussed further herein.

2.3.2.2 PI6042 DSP routines

The DSP routines are responsible for the low-level, high-priority, and time-sensitive tasks. The main purpose of these routines is the motion interpolation and data generation tasks. Additionally, the DSP routines are responsible for data acquisition hardware handling, such as sending analog outputs or receiving analog inputs for reporting via the USB data link interface to the computer where the new PI interface is running. The DSP program code is uploaded via a USB link from the control computer to the PI6042 DSP cards residing in the PI6000 chassis, shown in Figure 2.11, and executed once per data acquisition scan, which was set at 10 milliseconds intervals in this study.
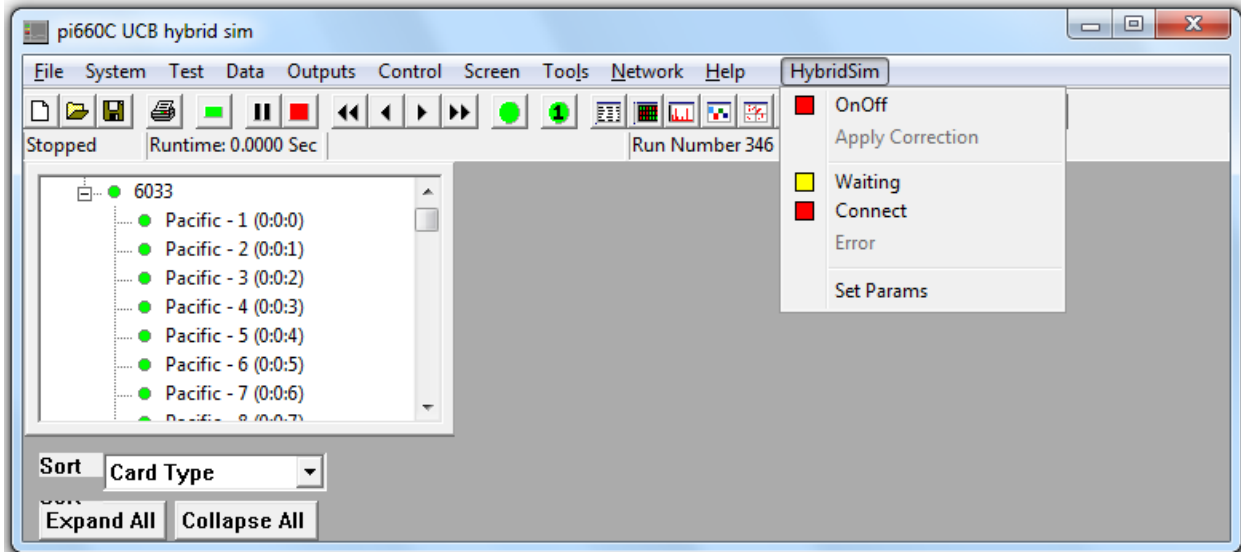
Figure 2.9 Screen shot of the developed new PI interface with the added HybridSim module and options.
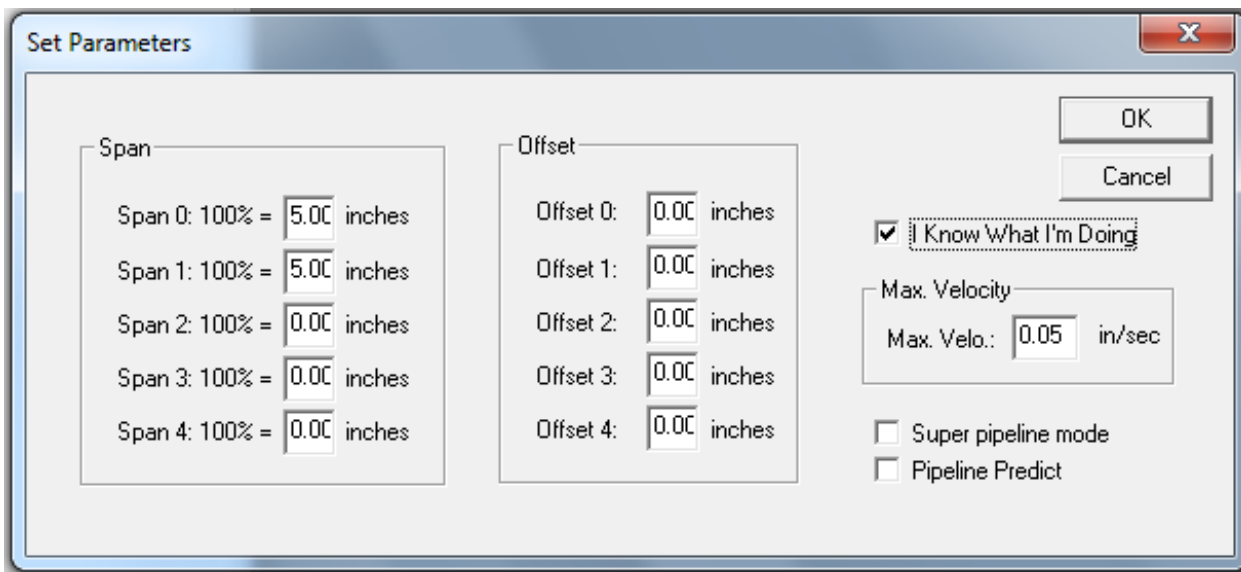
Figure 2.10 Screen shot of the HS parameters setting used in the new PI interface.

The PI6042 DSP routines were written in a Reversed Polish Notation (RPN), which is a close variant to both Assembly language and the Hewlett-Packard calculator macro-programming language. The RPN routines are executed once per data acquisition scan cycle at the requested sampling rate. For proper operation, the sampling rate required for defining the actuators path velocity was set to 10 millisec for the HS trials and tests conducted in this study. The RPN routines, called by the PI660C UCB HybridSim interface, are executed on the PI6042 DSP card sequentially at every data acquisition scan. One of the main functions of these routines is to interpolate the final end-displacement at a given time step, as received from OpenFresco via the new PI interface, and deliver the interpolated calculated signal to the MTS 407 controllers. The physical connection for the interpolated signal transfer to the controllers is a standard BNC

18

to BNC cable, where one end is connected to the DSP card in the PI chassis, and the other end is connected to the controller as shown in Figure 2.12. Note that the capabilities of the PI6042 DSP card were utilized by Mosalam and Günay [2014] in a previous study to conduct real-time HS tests on a shaking table configuration for electrical disconnect switch single post insulators. The specialized RPN routines documented in their study were successfully executed at 1 millisec intervals, which allowed the HS to take place in real-time.
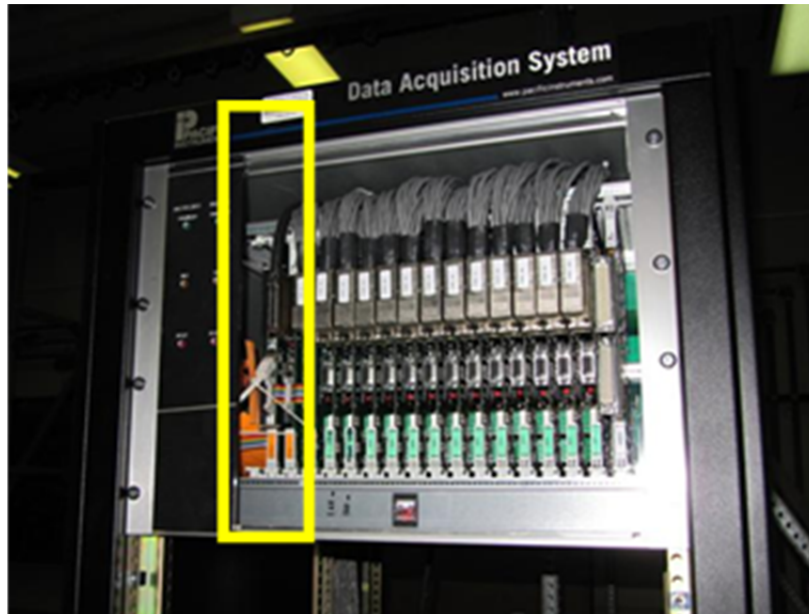
Figure 2.11 **PI data acquisition system and DSP card (identified by the light rectangle box) used in the HSS.**
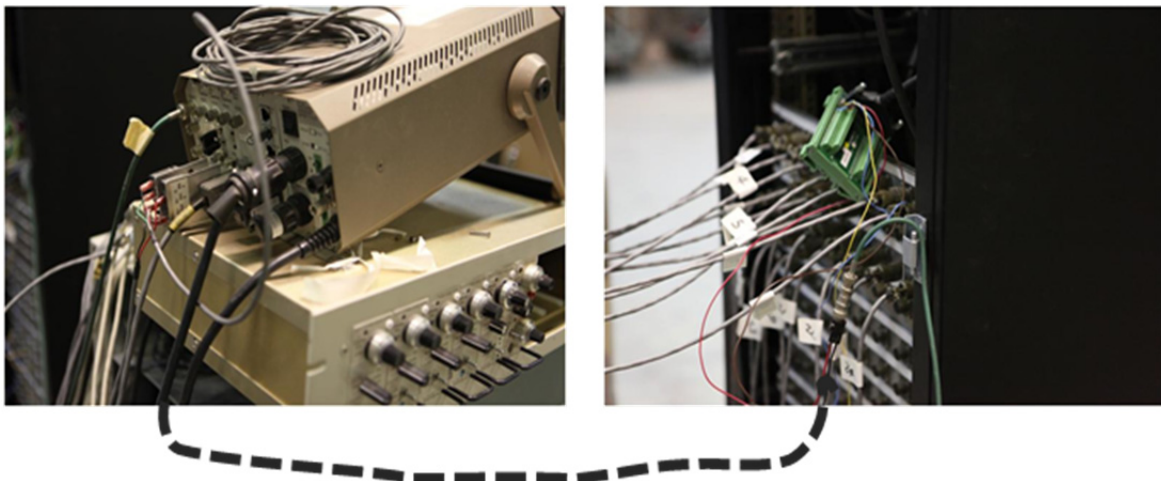
Figure 2.12 **Physical connection for sending the interpolated calculated displacement input from the DSP to the MTS 407 controller.**

2.4   HYBRID SIMULATION SYSTEM VERIFICATION TESTS

To confirm the performance of the implemented developments and validate the HSS for testing retrofitted Specimen No. 2, several trials and verification tests were conducted. The verification tests started with network protocol analysis and then utilized single and double free actuators, i.e., not attached to any physical specimens, as discussed in this section. Full HS tests that utilized the repaired Specimen No. 1 to validate the whole HSS were finally conducted as discussed next.

2.4.1 TCP/IP Network Stack

Numerous performance and characterization tests were performed on the TCP/IP performance between the OpenFresco/OpenSees platform and the new PI660C UCB HybridSim interface. These characterization tests were performed directly by using the Wireshark network protocol analyzer program [Orebaugh et al. 2006]. Wireshark attaches directly to the network software stack and records all the Ethernet packets traversing the Ethernet interface, which is commonly referred to as "sniffing." By looking at the timestamps and decoding the packet payloads, the traffic flow and timing were understood. A screenshot of the Wireshark sniffing of an established Ethernet TCP/IP connection in the developed HSS is shown in Figure 2.13.

The Ethernet TCP/IP network transactions flowing through a preliminary established connection between the OpenFresco platform and the new PI interface was analyzed. The timing data from the Ethernet transactions first indicated a latency of approximately 216 millisec. In order to reduce latency, the transmit buffer of OpenFresco was resized to be an integer multiple of the payload size of the Ethernet frame, i.e., the OpenFresco variable *OF_Network_dataSize* was modified from 256 to 365, such that on every network transaction, two totally filled Ethernet frames were utilized. Adjusting the OpenFresco packet size reduced the latency to 70 millisec. Due to the slow nature of the loading rate of the test in this study, the 70 millisec latency were found to be insignificant in altering the desired HS communication. For extension to real-time HS, this latency needs to be revisited.
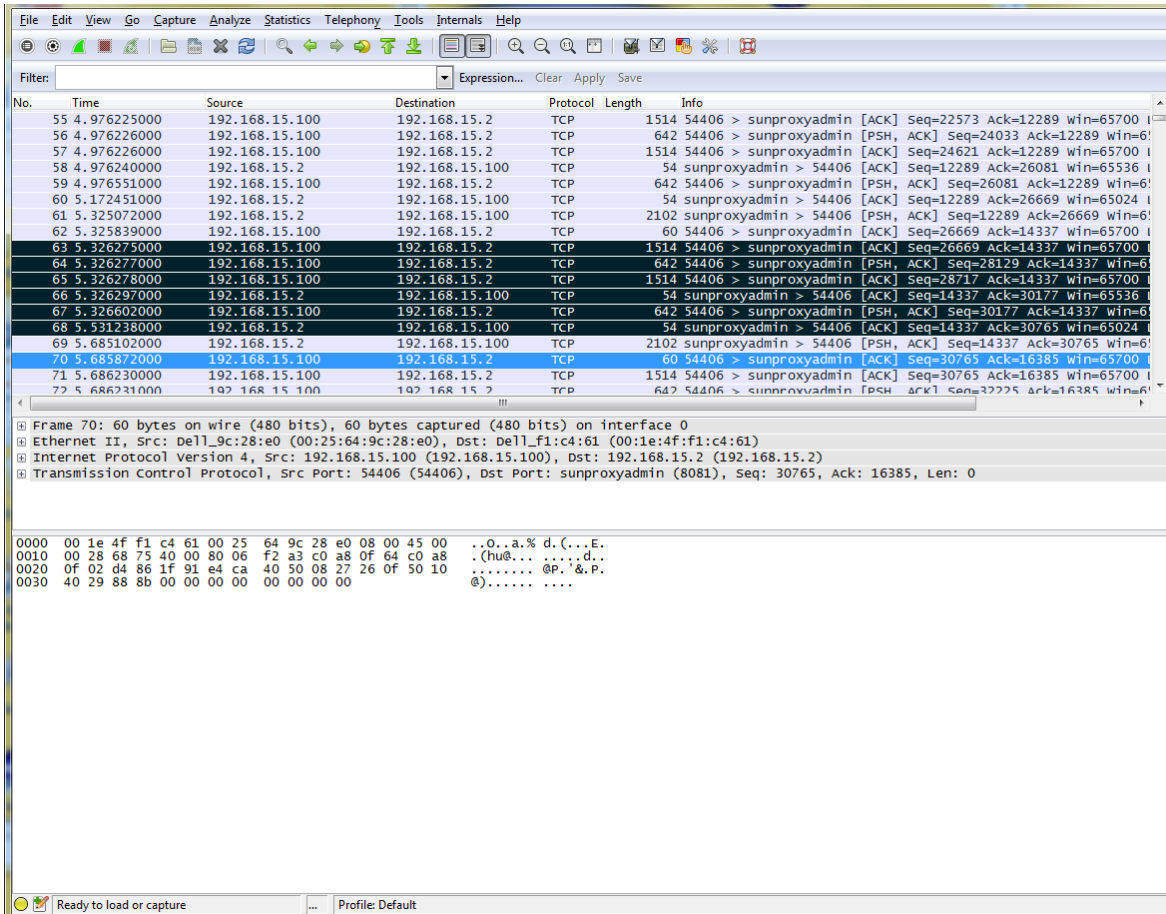
Figure 2.13   Screenshot of the Ethernet TCP/IP network packet analysis using Wireshark.

2.4.2 Single Actuator Tests

To verify the robustness of the communication between OpenFresco and the controllers via the newly developed PI interface and DSP routines, HS trial tests were conducted on free actuators detached from the specimen. A single actuator was used first along with a large multi-DOF computational model to test the communication loop between all components of the HSS. The set-up for the free actuators is shown in Figure 2.14. Two-way communication is necessary in HS; one way is for sending the displacement command and the other is for receiving the force feedback. A free actuator that is not attached to any specimen will report zero force feedback or only the load-cell noise. Thus, for the free actuator trials, a multiplier (stiffness) of the displacement command was feedback to the DSP and DAQ as a virtual force feedback. The constant multiplier reflected the stiffness of a hypothetical linear force-displacement relationship. The advantage of this virtual feedback is that it allows for comparison with pure simulation results where an elastic element with a constant stiffness replaces the actuator displacement/force feedback virtual experimental element. The computational model used for the free actuator trial was a multi-story multi-bay frame, represented schematically in Figure 2.15, where one column in the first story is modeled using either a linear elastic element or replaced by a generic simulation experimental element in HS tests. The El Centro ground-motion record was used for these trials as it contained several cycles with various amplitudes rather than a single large pulse.

For comparison with the pure simulation case, a multiplier of two was chosen for the displacement feedback to the DSP to reflect a hypothetical elastic element with 2 kip/in. stiffness, which was compatible with the other columns in the computational frame in the hybrid model.

Figure 2.14   **Actuators detached from the specimen for conducting trial HS tests.**
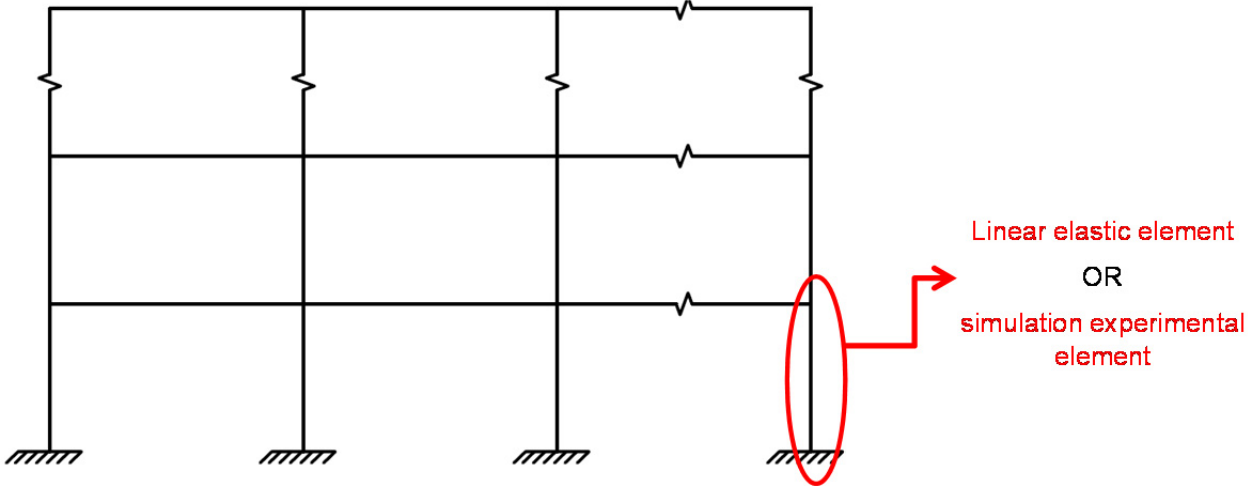
Figure 2.15   **Schematic representation of multi DOF frame computational model used for HS actuators trial tests.**

Figure 2.16 and Figure 2.17 compared the displacement and force histories from the pure simulation to those from the HS recorded data obtained from OpenSees and the PI DAQ,

respectively. OpenSees recorded the displacements obtained from the solution of the equation of motion at each time step along with the discrete force feedback at solution time steps only when received through the new PI interface. Meanwhile, the PI DAQ recorded the actual command data, i.e., actuator motion, and its multiplier when received at the DSP card. As shown in Figure 2.18, the force-displacement relationships are plotted for all cases to demonstrate the constant stiffness used for the model and the case with the hypothetical feedback. The comparison shows the perfect match between the simulation and the HS tests.
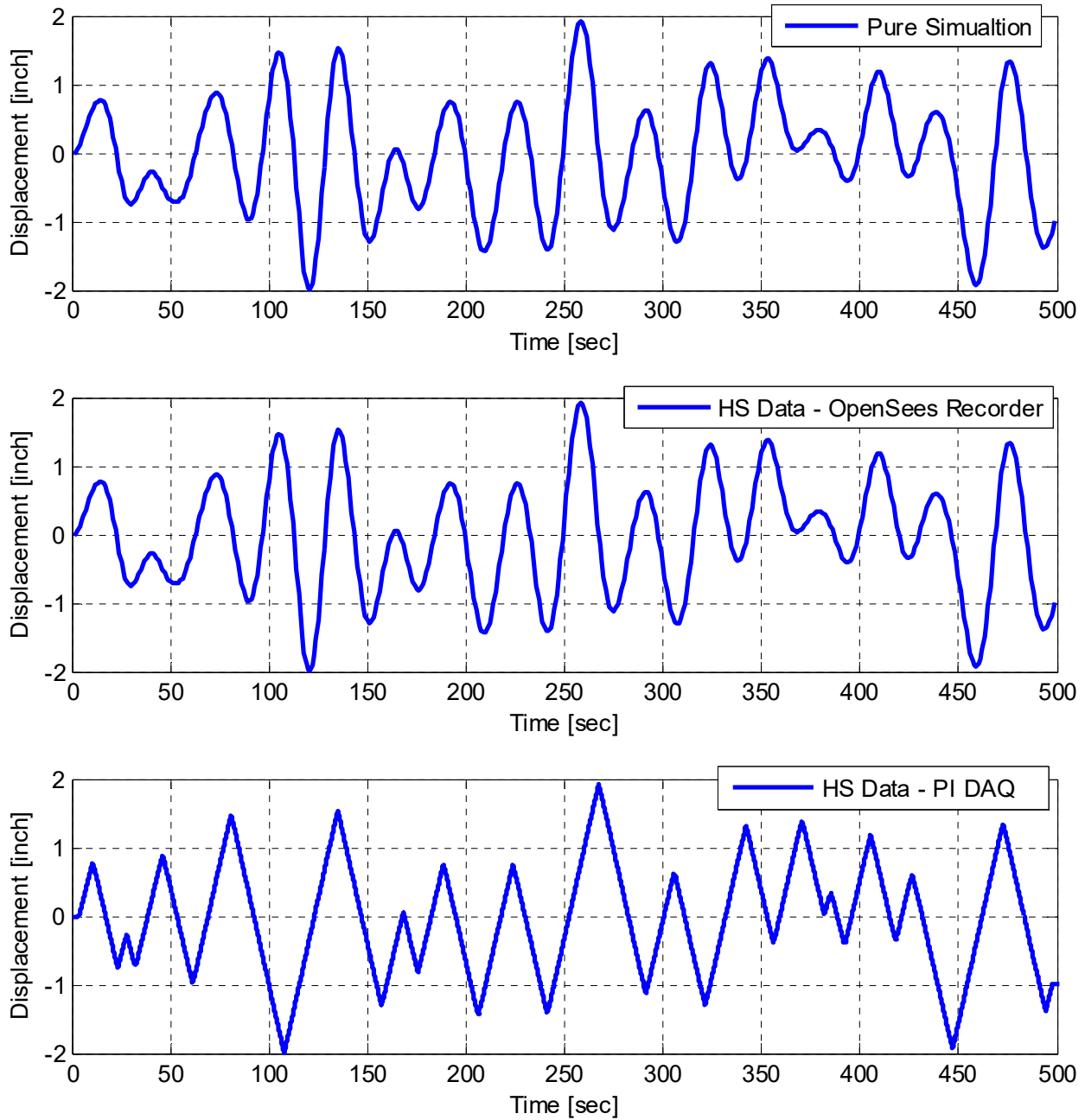
Figure 2.16 **Comparison of the displacement history obtained from the pure simulation, the computed OpenSees command for HS, and the actual actuators motion obtained from HS tests using single free actuator.**
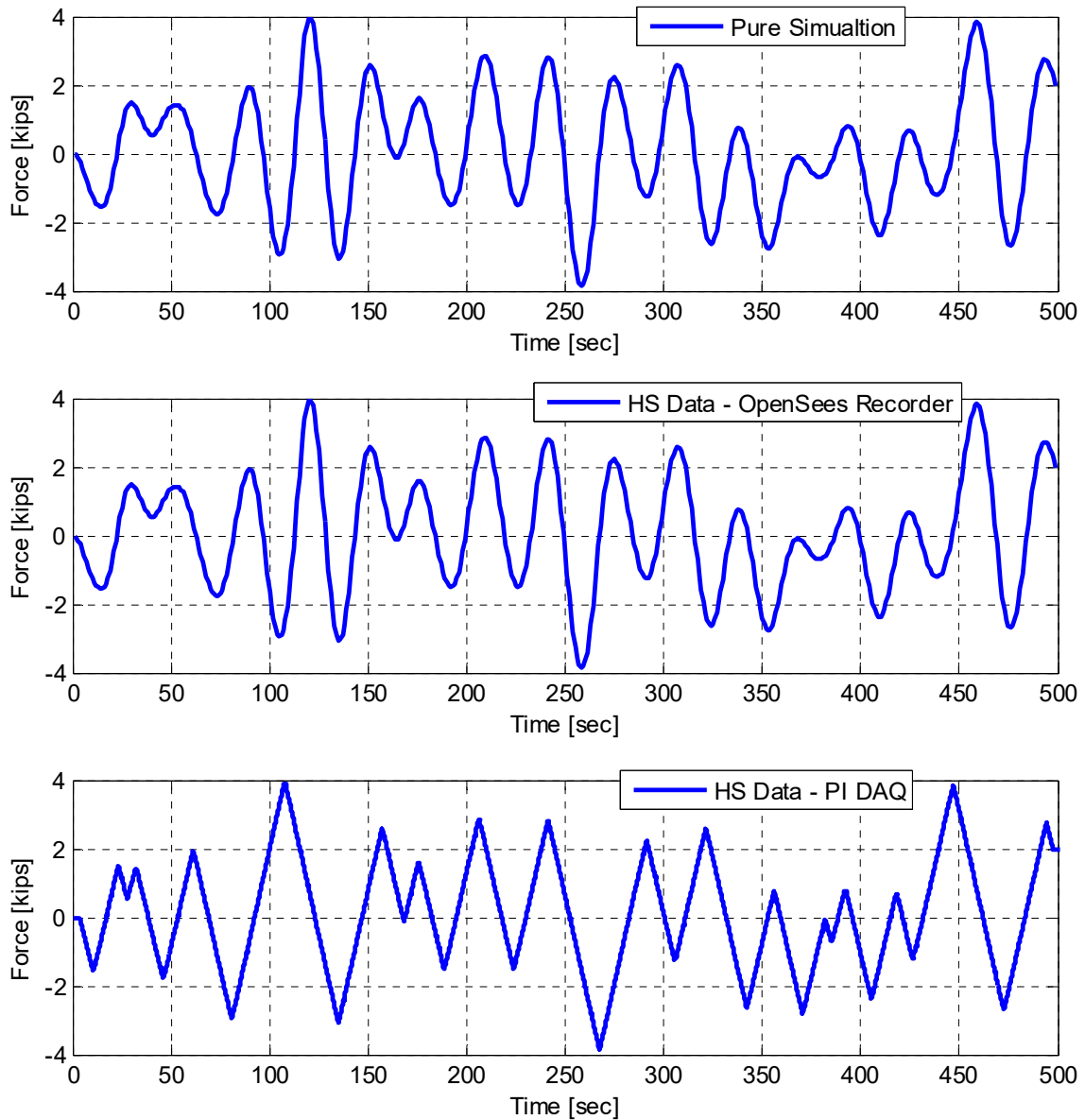
Figure 2.17 **Comparison of the force history obtained from the pure simulation, the received feedback at OpenSees, and multiple of the actual actuator displacement feedback as force as obtained from HS tests using single free actuator.**

Despite the perfect match in the displacement amplitudes, the progression with time was different from the actual actuator motion and the OpenSees command, or pure simulation case. This was expected and was attributed to the constant velocity or rate of loading used for commanding the actuator. The DSP routines were used to interpolate the received displacement command and apply it smoothly to the controller to pass it to the actuator. Thus, an obtained constant velocity would verify the communication loop and the DSP interpolation routines. Figure 2.19 shows the velocity history as calculated from the actual recorded interpolated commands. The constant velocity at 0.05 in./sec, which was the input rate through the PI660C UCB HybridSim parameters definition as shown previously in Figure 2.10, was successfully

achieved as calculated from the actual recorded data. Therefore, the good comparison between the HS tests that used a hypothetical feedback of a constant multiplier applied to the actual command and the pure simulation demonstrate the accuracy of the communication loop among the different HSS components.
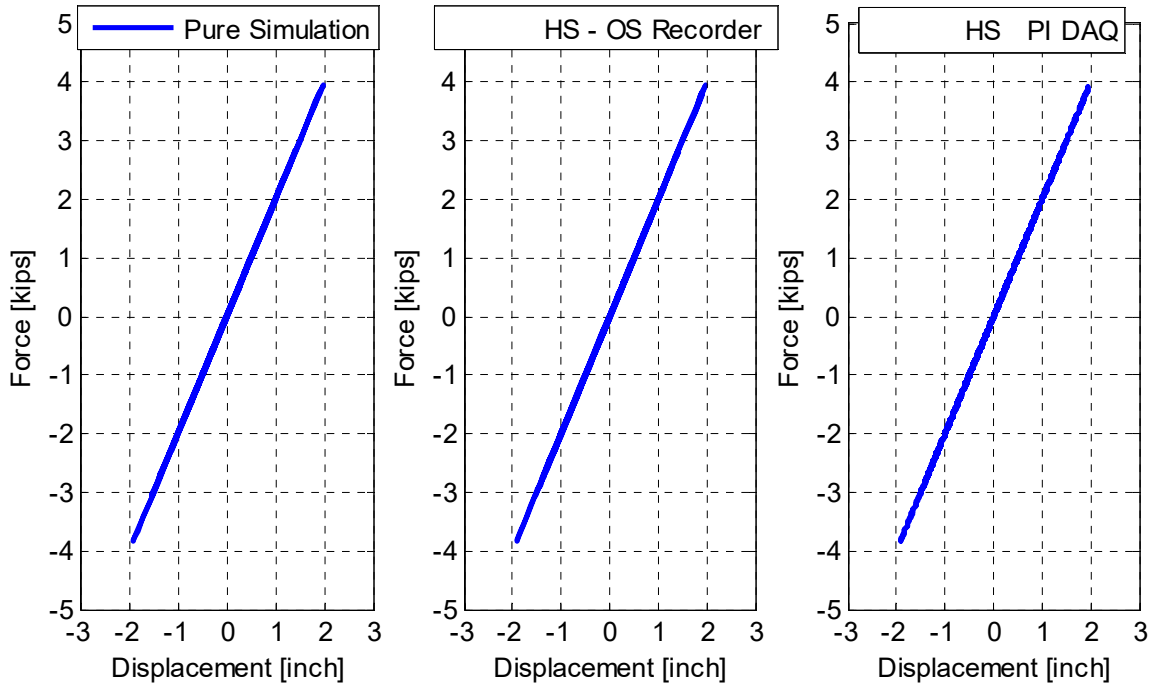
Figure 2.18   **Force-displacement relationships from pure simulation and HS test data recorded at OpenSees and using the PI DAQ from HS tests using single free actuator.**
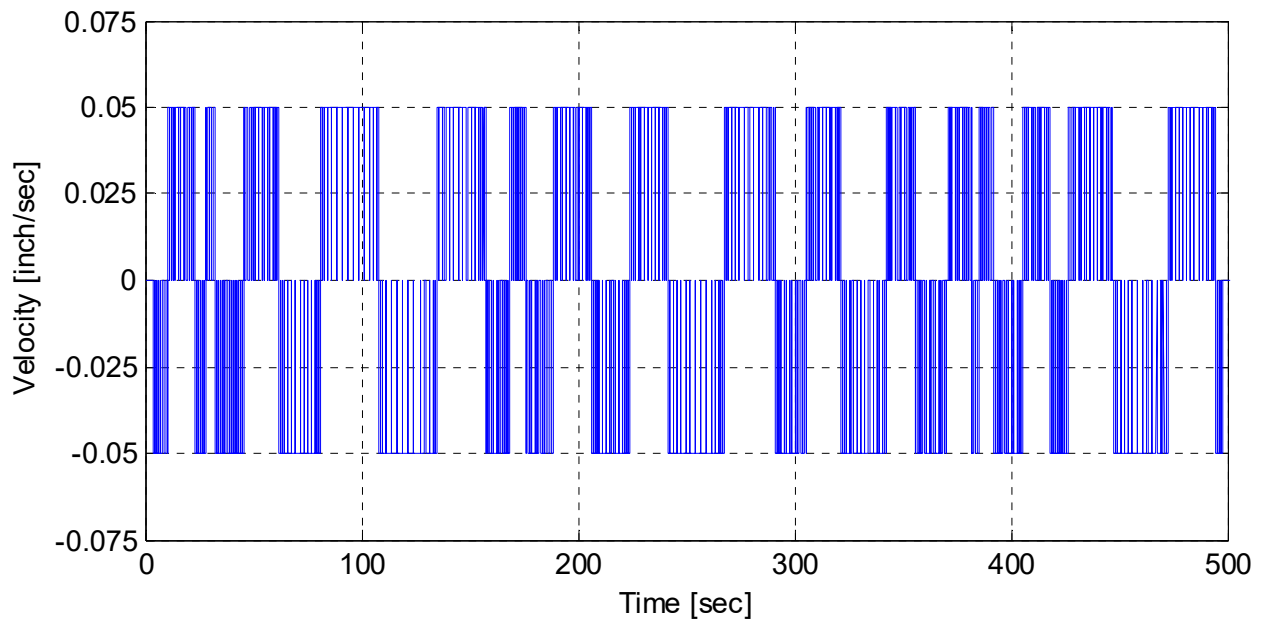
Figure 2.19   **Velocity history of the actual actuator motion from single actuator HS tests.**

2.4.3 Double Actuator Tests

Similar trial tests were conducted using two free actuators set-up with the actual computational model for the bridge sub-assemblage test specimen, i.e., utilizing the newly implemented geometric transformation set-up (the TriangularActuators *ExperimentalSetup* class) in the OpenFresco/OpenSees input file. In addition, the Rinaldi ground motion considered in the actual HS tests in this study was used in these trials. The same concept of feeding back a hypothetical force that is two times the actual displacement command was used in these trials as well. These tests aimed at verifying the correctness of the newly implemented geometric transformation and the DSP routines in interpolating the displacement command for two actuators simultaneously. To verify the geometric transformation, the input of the OpenFresco *TriangularActuator* command was set up in a way that rendered each of the actuators inclined with a 45° angle, e.g., *A1* and *B1* identified in Figure 2.8 were set to similar values. In this geometry, if a global transverse direction only motion (u_x in Figure 2.8) is required, the two actuators should have identical input along the local DOFs. On the other hand, if a longitudinal-only motion (u_y in Figure 2.8) is required, the two actuators should have same magnitude but opposite direction local DOFs input. This anticipated geometric transformation was verified as shown in Figure 2.20 through Figure 2.27. In subsection 2.4.3.1, the figures from the transverse direction only case are shown. Figure 2.20 and Figure 2.21 compare the OpenSees displacement command and received force feedback for the two actuators with the actual PI DAQ recorded data, respectively. The force-displacement relationships are also compared in Figure 2.22 to demonstrate the communication effectiveness reflected in the linear relationship shown in the figure. To emphasize that the two actuators had identical motion as intended, the velocities for both actuators were calculated and plotted in Figure 2.23. Both actuators moved with the input constant velocity of 0.05 in./sec, which verifies the capability of the DSP routines to interpolate the command for two actuators simultaneously.

Subsection 2.4.3.2 displays the plots for the longitudinal-only trial tests. The well-matching amplitudes from the OpenSees generated the displacement command; the actual motion of the actuators is shown in Figure 2.24. Similarly, the hypothetical force feedbacks that were twice the actual displacements are similar to what OpenSees eventually received at each time step for solving for the new time step, as illustrated in Figure 2.25. The force-displacement relationships are compared in Figure 2.26, and the calculated velocities for the two actuators are shown in Figure 2.27. The figures show that the two actuators had similar input along the local DOFs but with opposite direction (sign). This implies that the two components of the actuators motion in the transverse direction cancelled the effect of each other and hypothetically forced the actuators along a longitudinal path. Meanwhile, the velocities presented in Figure 2.27 show different signs but almost constant velocity for the two actuators as a similar magnitude of motion is "commanded" to each of them. While this preliminary tests verified the geometric transformation and DSP interpolation routines, a formal verification was obtained when a full HS test was conducted using the repaired Specimen No. 1 specimen as discussed in the next section.

One final trial test that used the two free actuators was a generic bi-directional test. This generic case was useful in the final verification of the DSP interpolation routines rather than the geometric transformation, as discussed in subsection 2.4.3.3. Figure 2.28 and Figure 2.29 show the displacement command and force feedback comparison, respectively. Figure 2.30 shows the force-displacement relationship, and Figure 2.31 shows the velocities of the actuators. The key

observation from this test is how the actuators change their velocities when one actuator has a longer displacement command to execute than the other. In this case, only the actuator with larger interpolated command moves at the maximum set velocity, while the other actuator slows its velocity to stay on the same spatial path of the anticipated column head where the actuators would be eventually connected. Figure 2.31 denotes when the two actuators had different command magnitude; actuator 2 moved at a slower velocity when actuator 1 was moving with the maximum 0.05 in./sec and vice versa. This ultimately verified the DSP interpolation routines and the DSP/PI DAQ communication loop.

2.4.3.1 Transverse direction only Ground-Motion Input
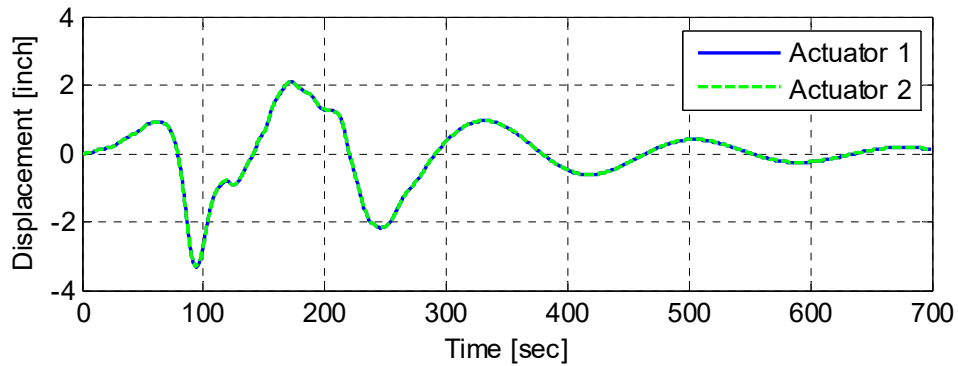
(a)
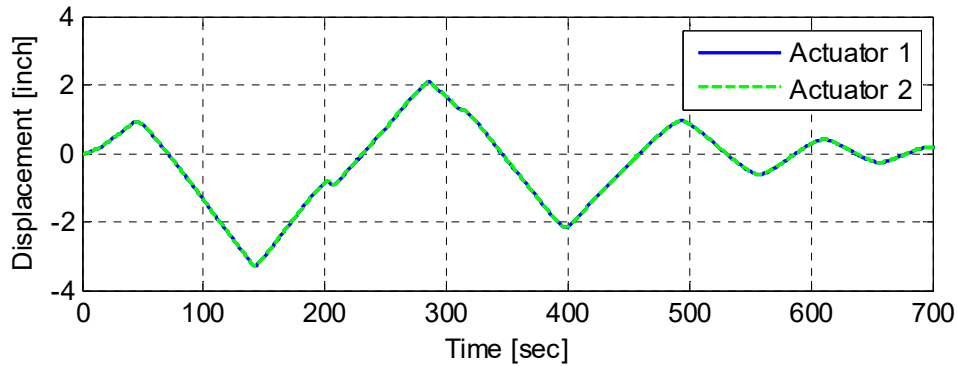
(b)

Figure 2.20   **(a) Actuators displacement history from the HS computed OpenSees signal; and (b) actuators feedback from the DAQ (bottom) for transverse direction only ground motion test.**
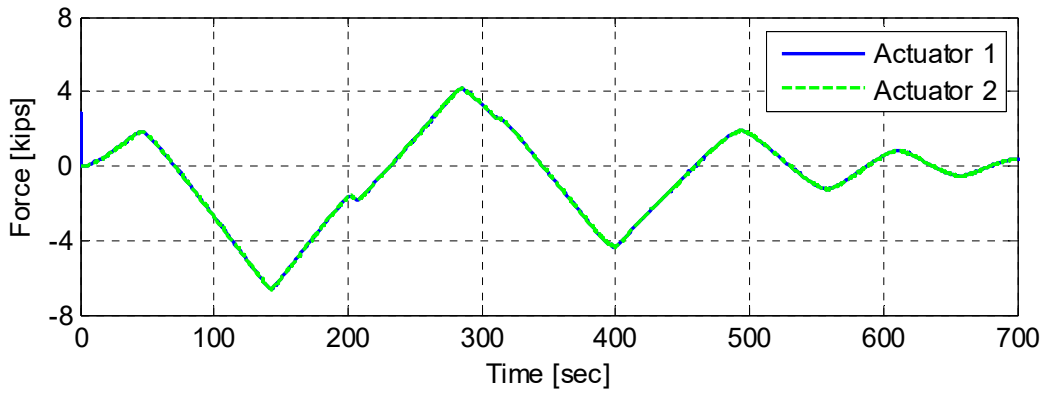
Figure 2.21   Actuators force history from load cell DAQ data for transverse direction only ground motion test.
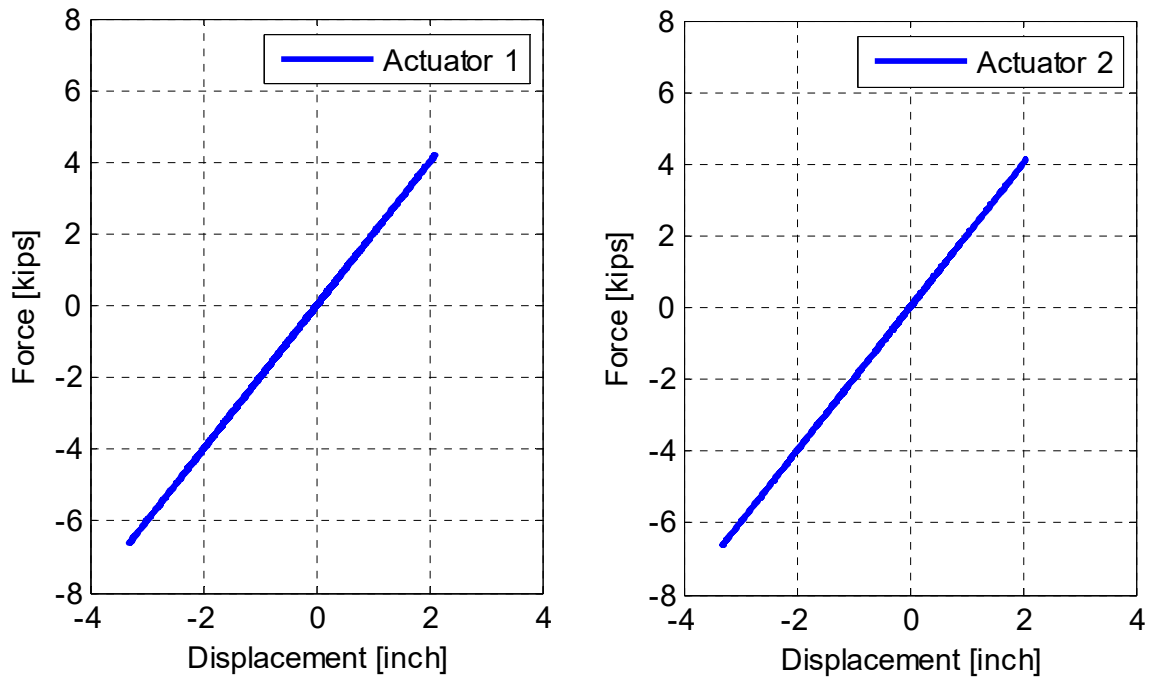
Figure 2.22   Actual force-displacement relationships obtained from the DAQ data for transverse direction only ground-motion test.

28
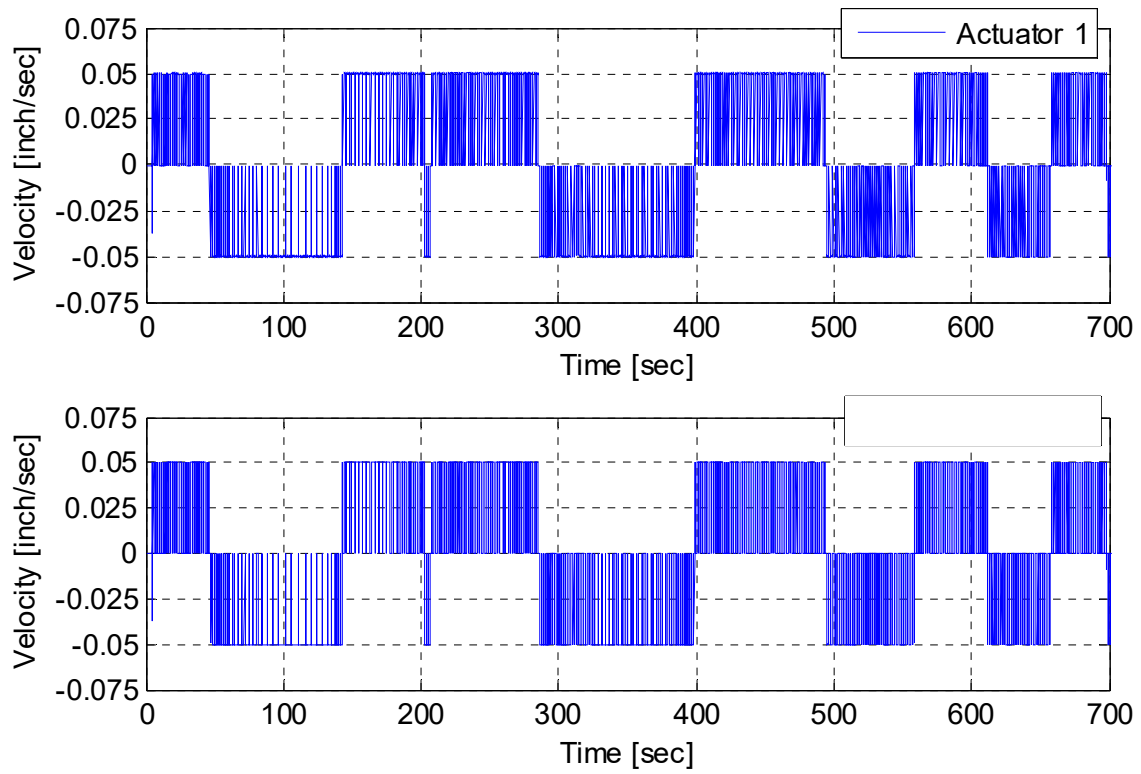
Figure 2.23 Actuators velocity as calculated from the obtained feedbacks from the DAQ data for transverse direction only ground-motion test.

2.4.3.2 Longitudinal-only Ground-Motion Input
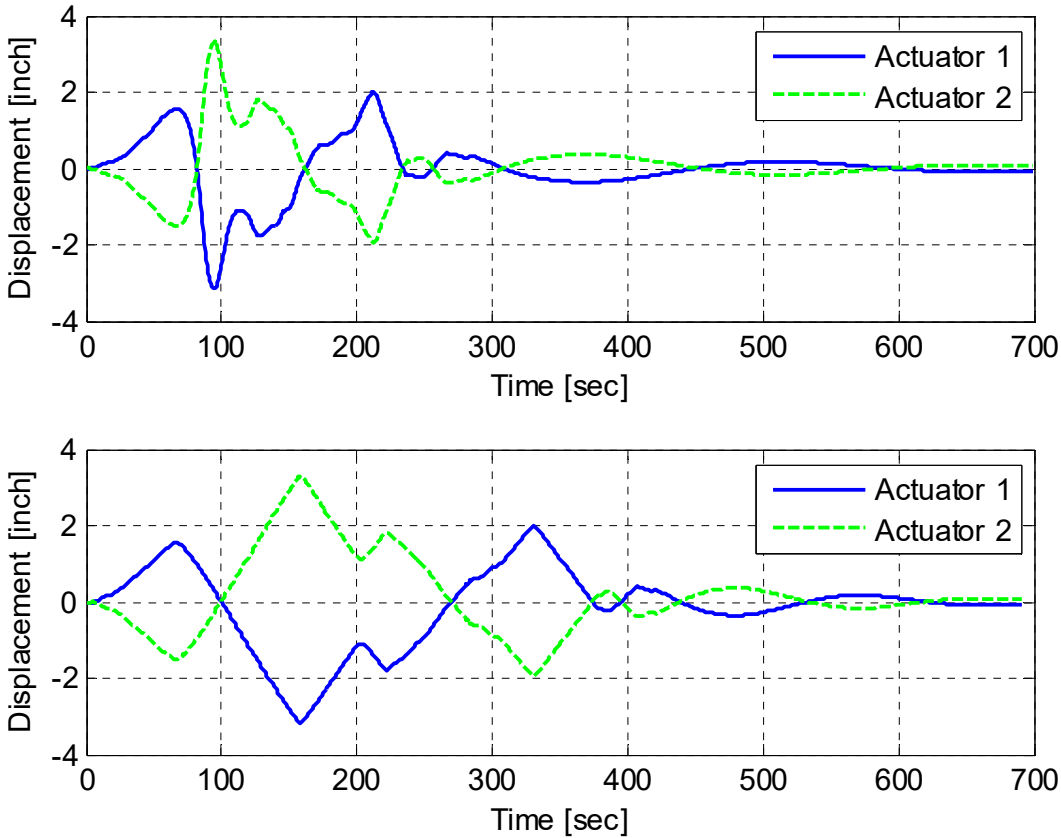
Figure 2.24 **Actuators displacement history from the HS computed OpenSees signal (top) and actuators feedback from the DAQ (bottom) for longitudinal direction only ground-motion test.**
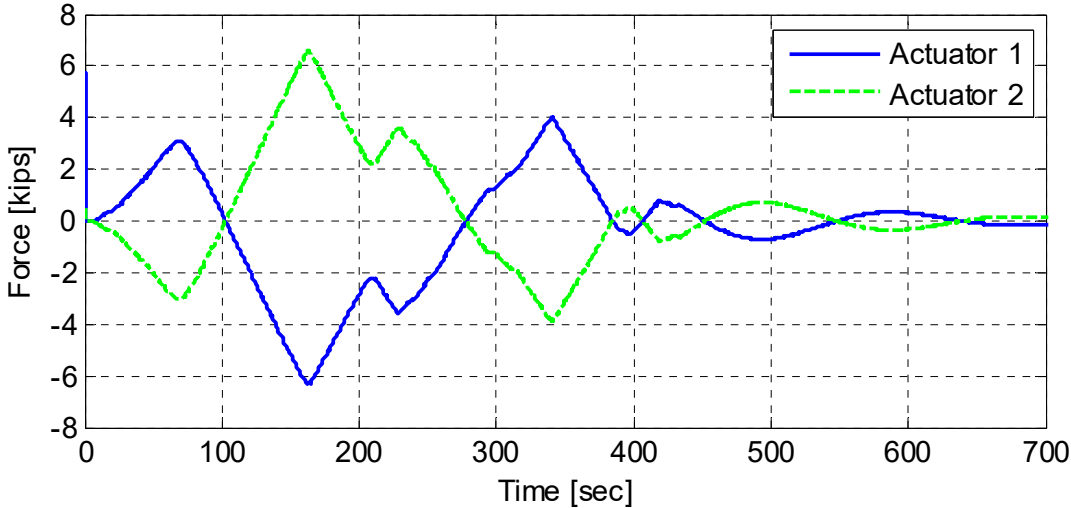
Figure 2.25 **Actuators force history from load cell DAQ data for longitudinal direction only ground-motion test.**
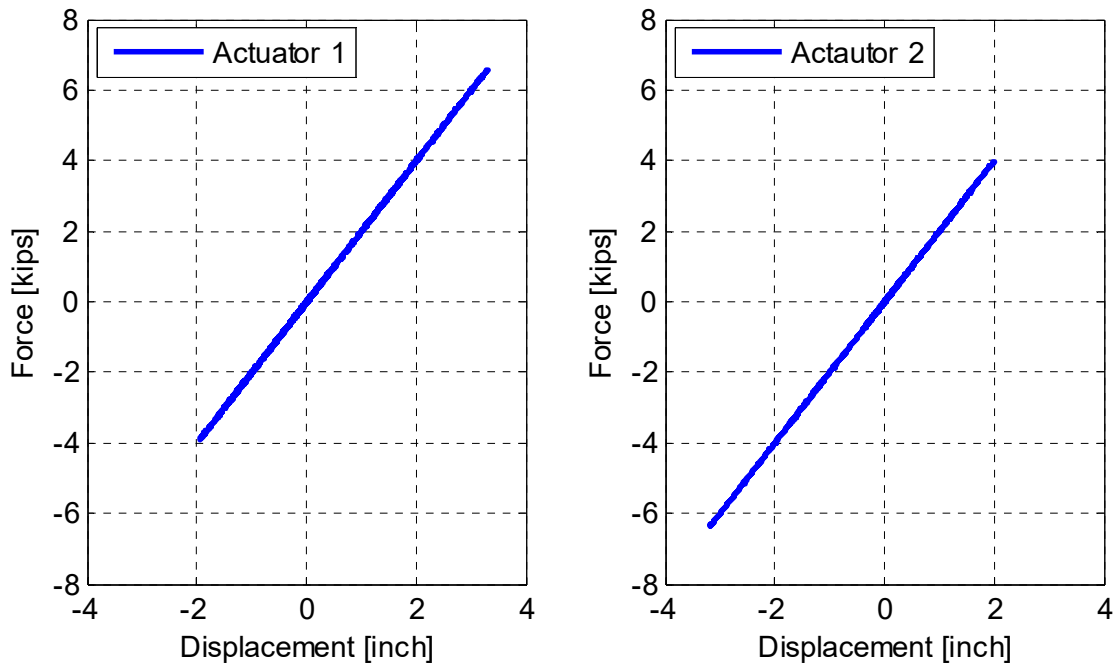
Figure 2.26 Actual force-displacement relationships obtained from the DAQ data for longitudinal direction only ground-motion test.
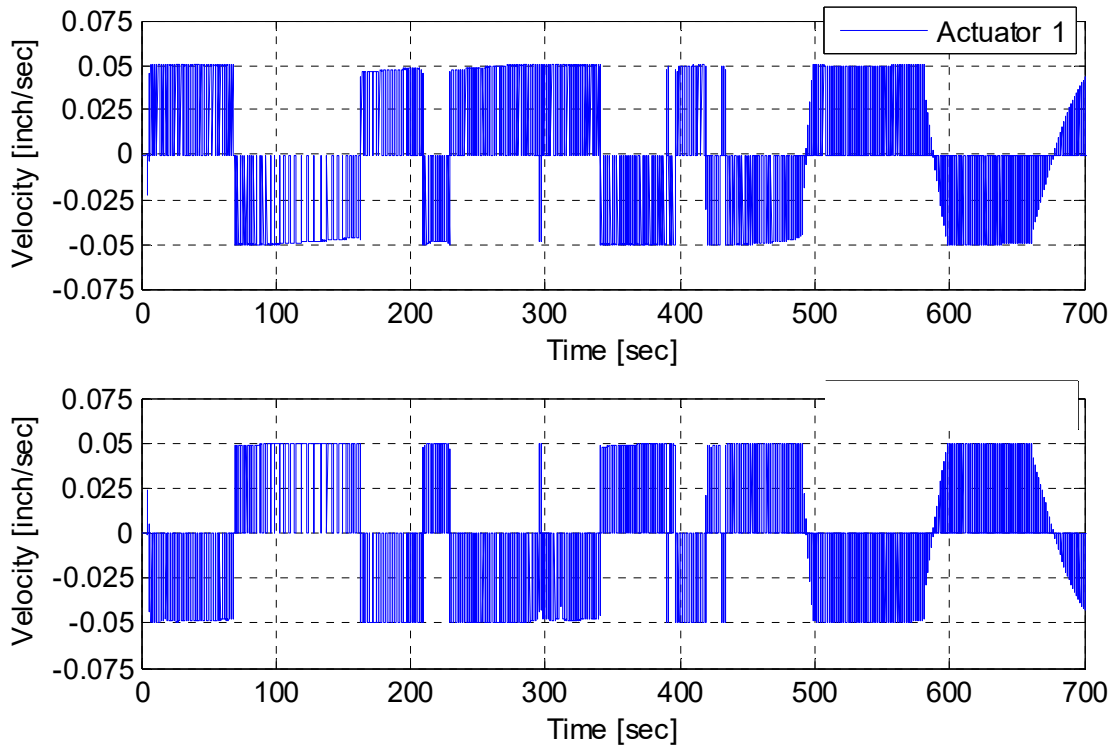
Figure 2.27 Actuators velocity as calculated from the obtained feedbacks from the DAQ data for longitudinal direction only ground-motion test.

2.4.3.3 Bi-directional Ground-Motion Input
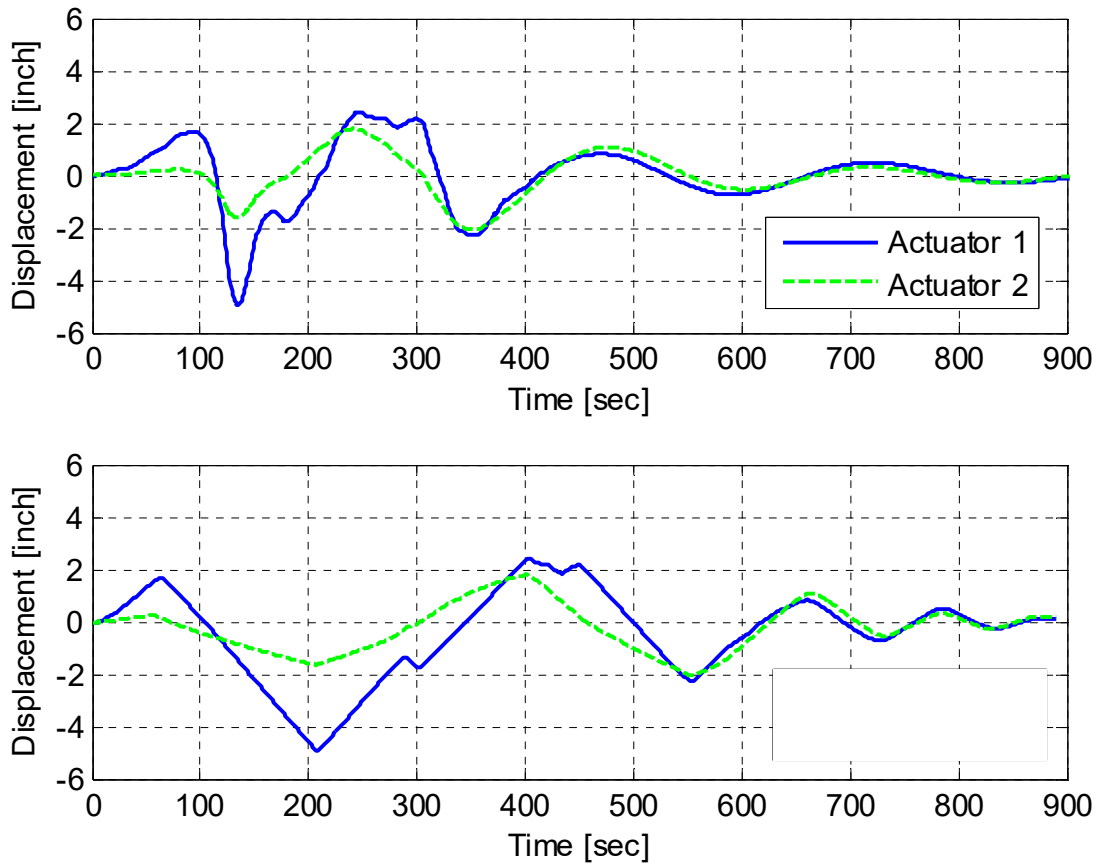
Figure 2.28 **Actuators displacement history from the HS computed OpenSees signal (top) and actuators feedback from the DAQ (bottom) for bi-directional ground-motion test.**
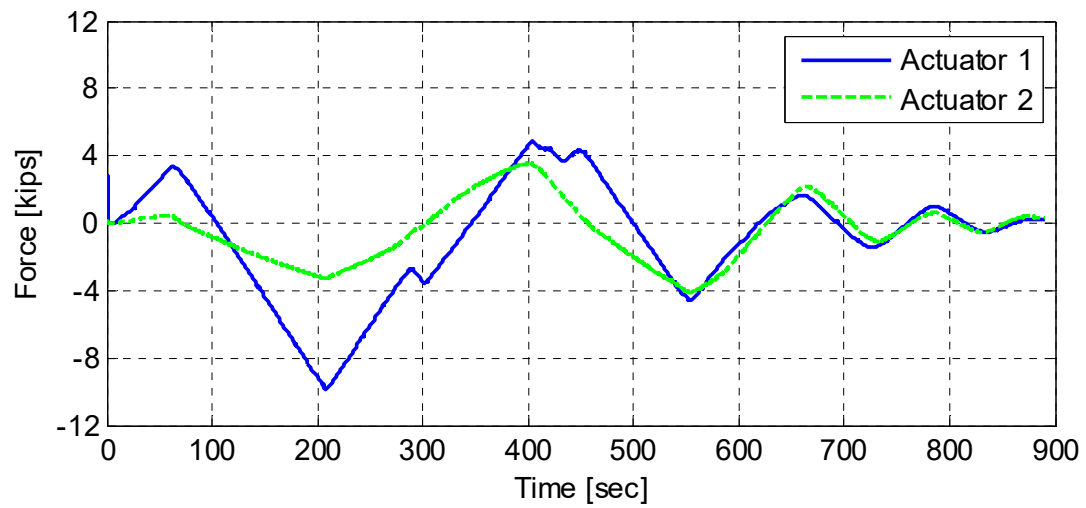
Figure 2.29 **Actuators force history from load cell DAQ data for bi-directional ground-motion test.**
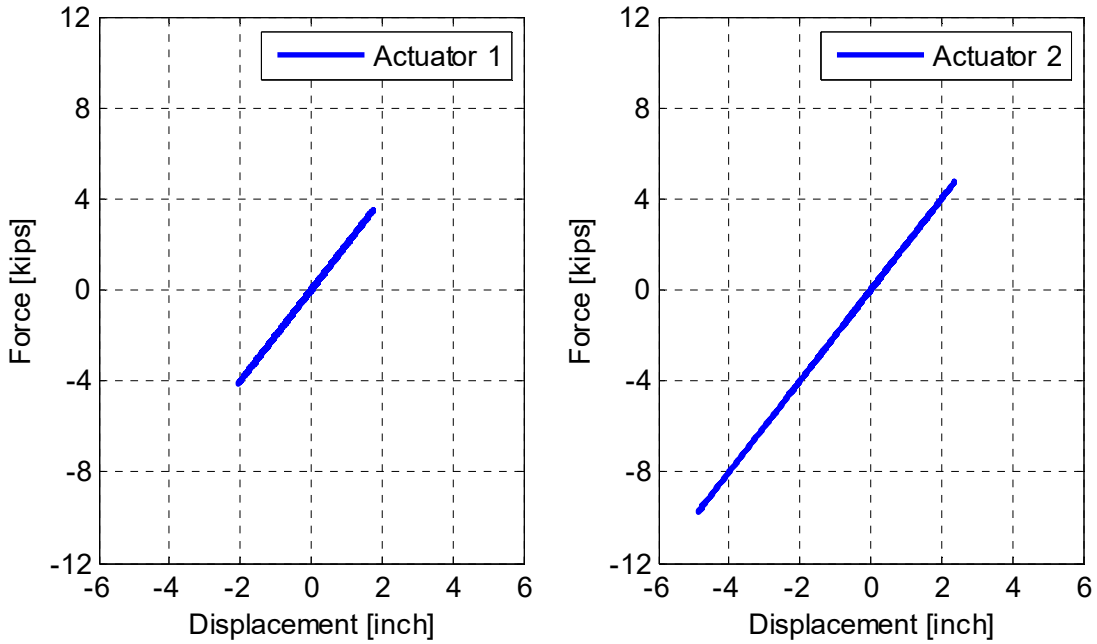
Figure 2.30   Actual force-displacement relationship obtained from the DAQ data for bi-directional ground-motion test.
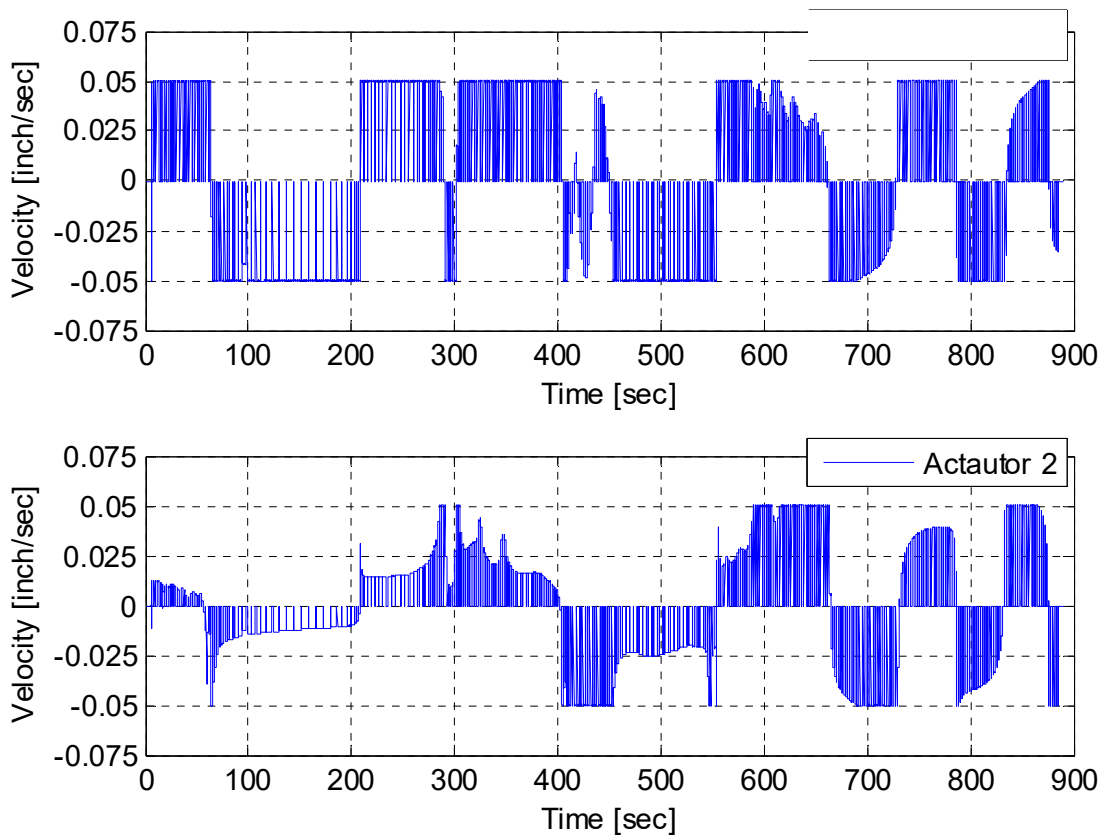
Figure 2.31   Actuators velocity as calculated from the obtained feedbacks from the DAQ data for bi-directional ground-motion test.

2.5   REPAIRED SPECIMEN NO. 1 HYBRID SIMULATION TESTS

To complete the validation of the integrated HSS, a full specimen HS test was conducted at the Structures Laboratory at UCB using the repaired Specimen No. 1, as shown in Figure 2.32. Several HS trials with and without gravity loads and using different ground-motion scales and components were conducted, as summarized in Table 2.2. The main benefit of the full specimen HS tests was to validate the whole system using a true specimen with inelastic nonlinear behavior. Selected results from the Specimen No. 1 HS trials that serve the purpose of the HSS validation are presented here.

Figure 2.32   Test set-up used for conducting HS trial tests for the repaired Specimen No. 1.

Table 2.2   Summary of repaired Specimen No. 1 HS tests.

Test ID	Gravity-load level	Ground motion	Ground-motion scale	Components
1	0	Rinaldi	20%	Transverse direction only
2	0	Rinaldi	20%	Longitudinal direction only
3	0	Rinaldi	20%	Bi-directional
4	0	Rinaldi	50%	Bi-directional
5	10%	Rinaldi	50%	Bi-directional
6	10%	Rinaldi	80%	Transverse direction only
7	10%	Rinaldi	80%	Longitudinal only
8	10%	Rinaldi	80%	Bi-directional

2.5.1 50% Scale Bi-Directional Hybrid Simulation Tests

The first objective from the HS full specimen tests was to check the robustness of the developed HSS in different stability and loading conditions. For this purpose, a 50% Rinaldi bi-directional HS tests were conducted before (Test ID 4) and after (Test ID 5) applying the gravity load. The repaired Specimen No. 1 was heavily tested under quasi-static cyclic loading in as-built and repaired conditions. Thus, the developed plastic hinge might result in instability if lateral loading is applied, which was checked by comparing the HS test results. For brevity, only the recorded data from OpenSees are presented.

The displacement and force responses from the 50% scale bi-directional HS tests with and without the applied gravity load are compared. Figure 2.33 compares the computed displacement in both of the transverse (u_x) and longitudinal (u_y) directions with and without gravity load application. Additionally, the transverse (f_x) and longitudinal (f_y) force feedbacks received at the OpenSees side after they went through the PI interface and the OpenFresco geometric transformation are shown in Figure 2.34. The displacement history suggests that when the gravity load was not applied, the system oscillated around a shifted displacement due to the almost zero force feedback received. The HS computational model solution and load application from a full test gave confidence about the robustness of the HSS system even with almost zero feedback. Such zero force feedback can be seen in Figure 2.34, where the damaged column did not provide any resistance before the gravity load was applied.
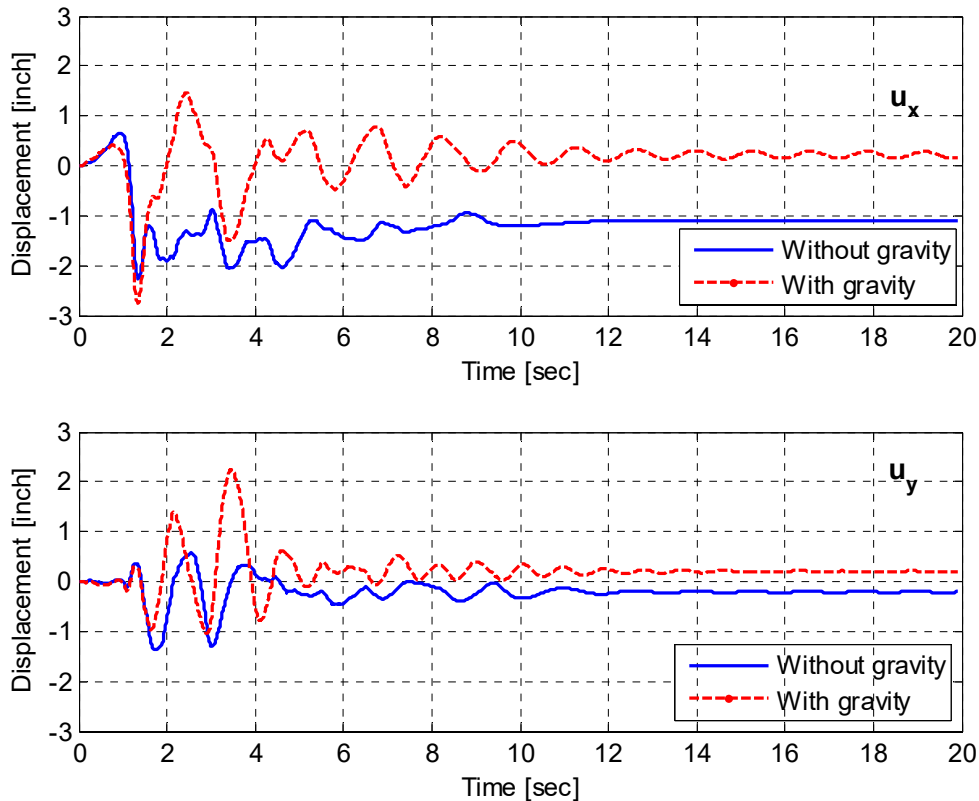
Figure 2.33   **Comparison of the OpenSees computed displacements for Specimen No. 1 HS subjected 50% Rinaldi bi-directional loading with and without the gravity load applied.**
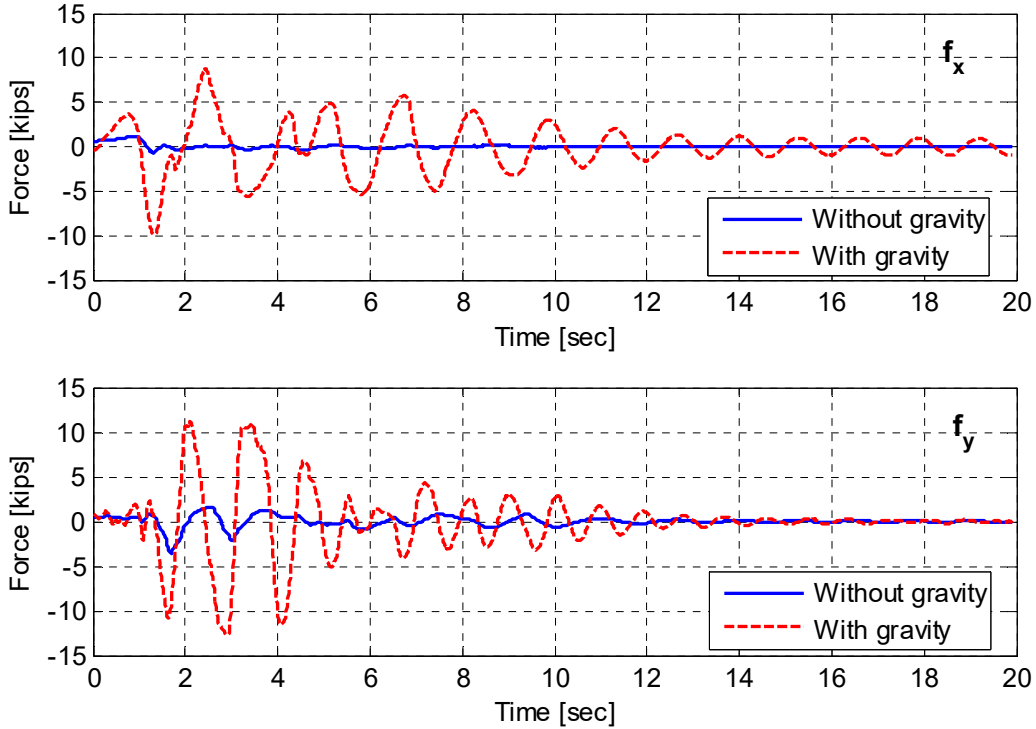
Figure 2.34   Comparison of the force feedbacks received at OpenSees for Specimen No. 1 HS subjected to 50% Rinaldi bi-directional loading with and without the gravity load applied.

As illustrated in Figure 2.34, when the gravity load was applied the increased compressive stresses in the column led to engaging partial lateral resistance from the column again. Reasonable maximum force feedbacks of about 10 kips in the transverse direction and about 12 kips in the longitudinal direction were measured when the gravity load was applied. These force feedback values are comparable with the residual forces after the repaired Specimen No. 1 cyclic tests were completed (see the companion report).

2.5.2 80% Scale Bi-directional Hybrid Simulation Tests

When a 10% gravity load was applied to the repaired Specimen No. 1, the 50% scale HS tests demonstrated that the test specimen sub-assemblage preserved reasonable force capacity. Thus, a larger 80% scale bi-directional test (Test ID 8) was conducted, and the data from the OpenSees side were compared to the actual recorded data at the PI DAQ. The directly measured responses in the global *x* and *y* directions were compared to the intended OpenSees commands to perform a final check of the geometric transformation. Moreover, the actuators performance was checked again to verify the DSP interpolation routines.

The actuators commands adopted from the OpenSees computations but after applying the OpenFresco geometric transformation were compared to the temposonic measurements of the actual actuators' motion as previously conducted in the free actuators tests. Figure 2.35 and Figure 2.36 show such comparison for both the north and south actuators, respectively. These figures represent the transformed OpenSees commands, which were basically the commands sent to the DSP card to interpolate and send to the controllers versus the actual achieved commands, which progressed in time based on the set velocity and loading rate. Thus, only the amplitudes

were useful in comparing these plots as a final check of the HSS; as shown in the figures, the plots match closely. The temposonic displacements also feature the constant slopes representing the velocities, which were computed and shown in Figure 2.37 for the two actuators. The velocity history demonstrates how each of the two connected actuators at the specimen's column head adjusted their speed to keep up with one another during bi-directional loading. The maximum velocity set as one of the PI660C UCB HybridSim interface parameters at 0.05 in./sec was maintained during the HS tests, i.e., the actuator that received a smaller displacement command slowed its rate of loading according to the developed DSP routines. This observation is similar to what the two free actuators trial tests showed earlier. However, the full specimen actual HS test is more of a confirmation because the correct displacement orbit of the physical column head was verified, which in turn successfully verified the DSP interpolation routines.

A final check for the HSS verification is to compare the intended computed displacement commands and received force feedbacks in the global DOFs versus what was actually obtained from the tests, i.e., verifying the newly implemented OpenFresco geometric transformation. For this purpose, wirepots were set up to measure the global x and y displacements using proper triangulation relationships. Figure 2.38 and Figure 2.39 show the comparison of the command history in global DOFs, as directly calculated in OpenSees before any geometric transformation, and from the wirepots measurements. The amplitude closely matched with only less than 2.5% difference, which verified the geometric transformation in the displacement command. Furthermore, the backward transformation of the actuator load cell forces was also verified by comparing the overall force-displacement relationship (Figure 2.40) from OpenSees versus that where the global force calculated from the local load-cell measurements along with the actual displacements from the wirepots.
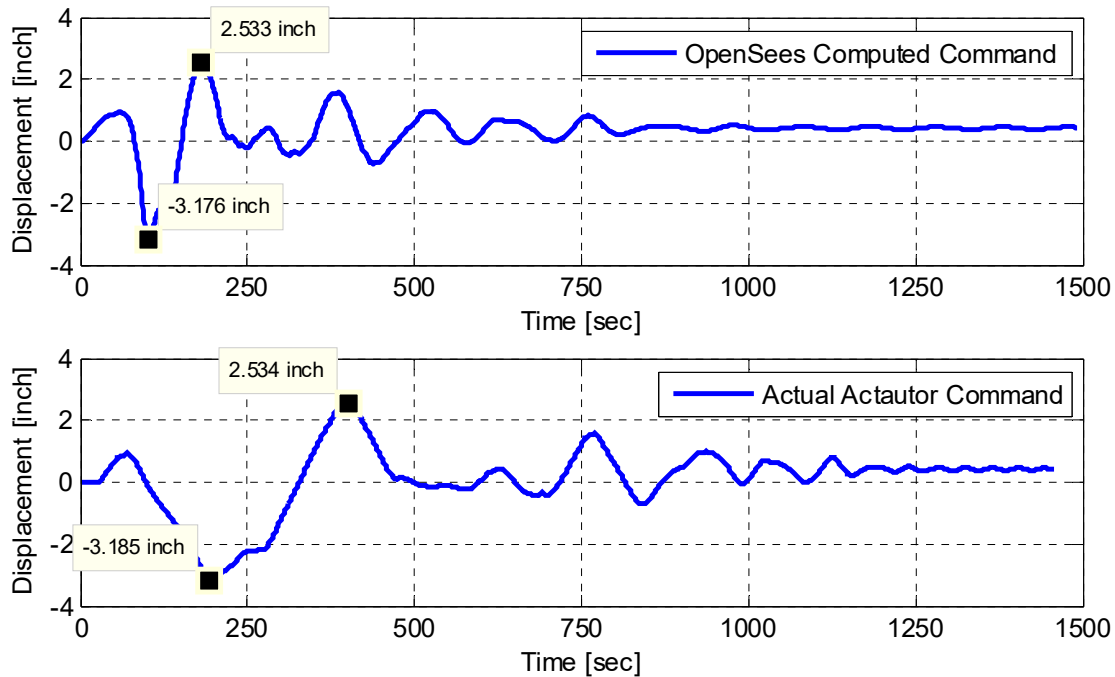
Figure 2.35   **North actuator (u_1) generated command and actual motion history for the repaired Specimen No. 1 80% Rinaldi bi-directional HS test.**
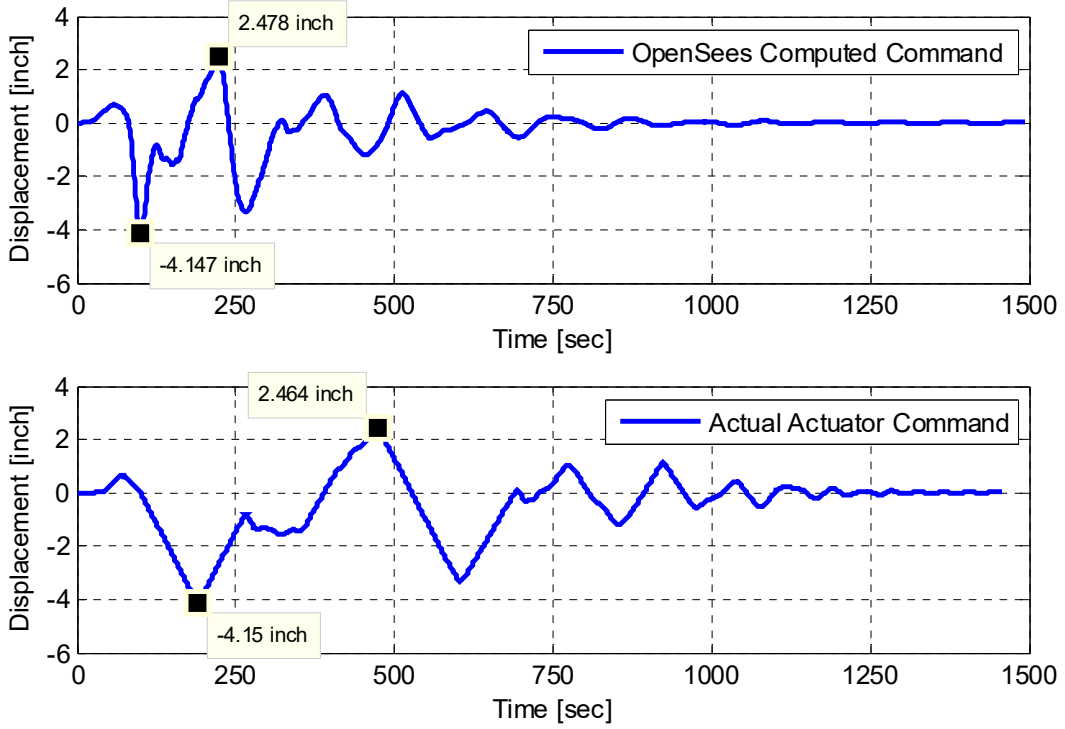
Figure 2.36 South actuator (u_2) generated command and actual motion history for the repaired Specimen No. 1 80% Rinaldi bi-directional HS test.
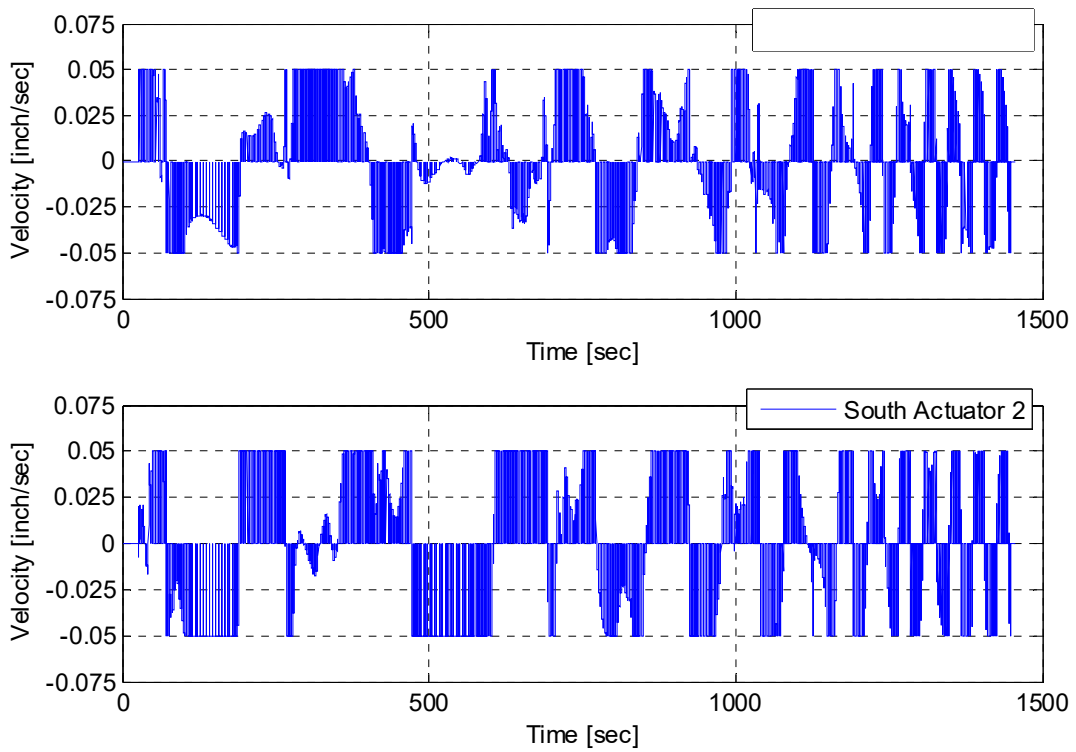
Figure 2.37 Actuators velocity as calculated from the obtained displacement measurements from the DAQ data for the repaired Specimen No. 1 80% Rinaldi bi-directional HS test.
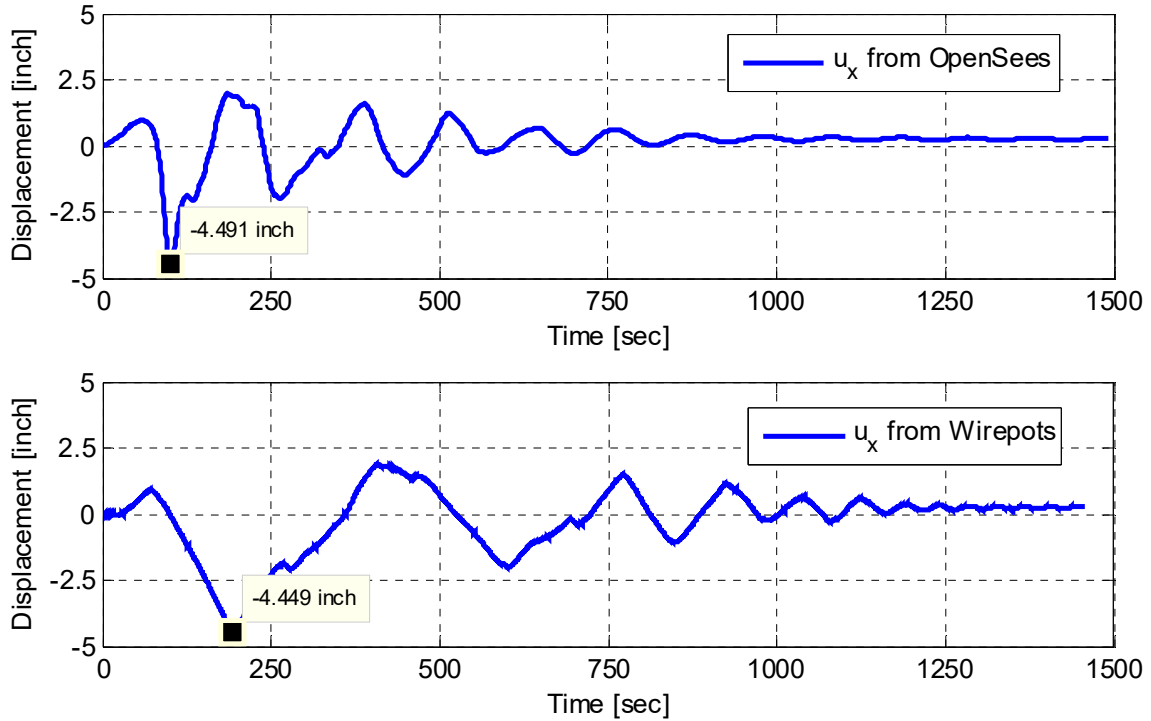
Figure 2.38 Global transverse displacement history (u_x) obtained from the OpenSees solution and that actually measured from wirepots for the repaired Specimen No. 1 80% Rinaldi bi-directional HS test.
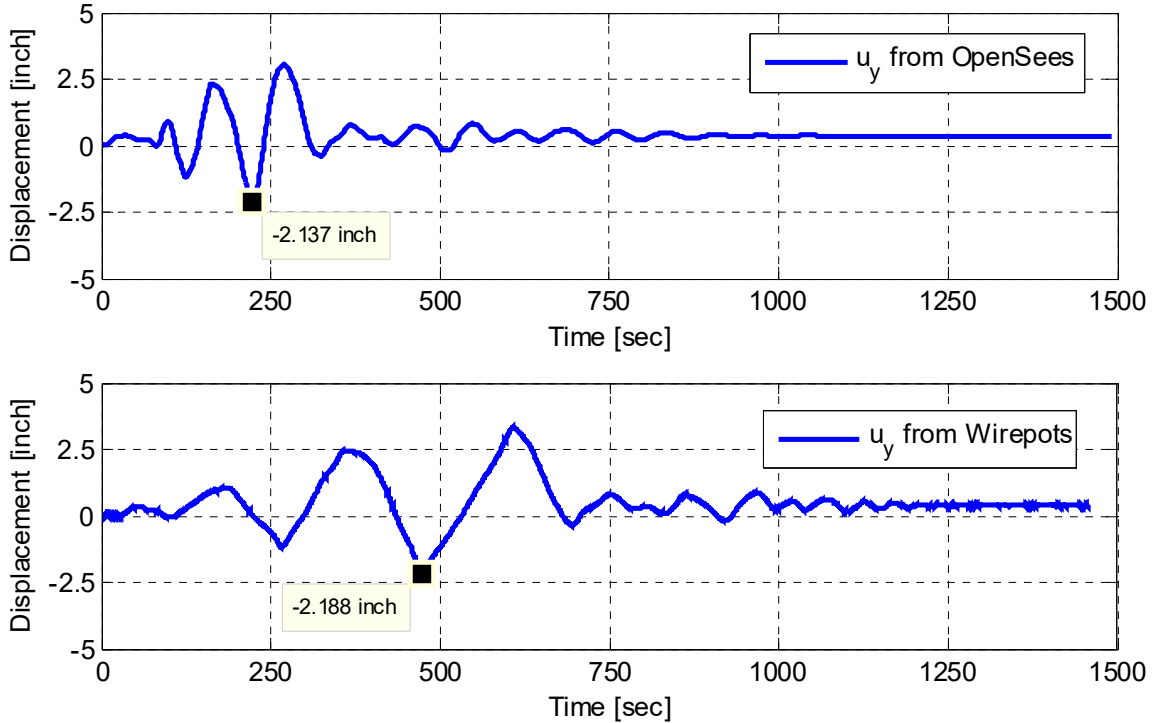
Figure 2.39 Global longitudinal displacement history (u_y) obtained from the OpenSees solution and that actually measured from wirepots for the repaired Specimen No. 1 80% Rinaldi bi-directional HS test.
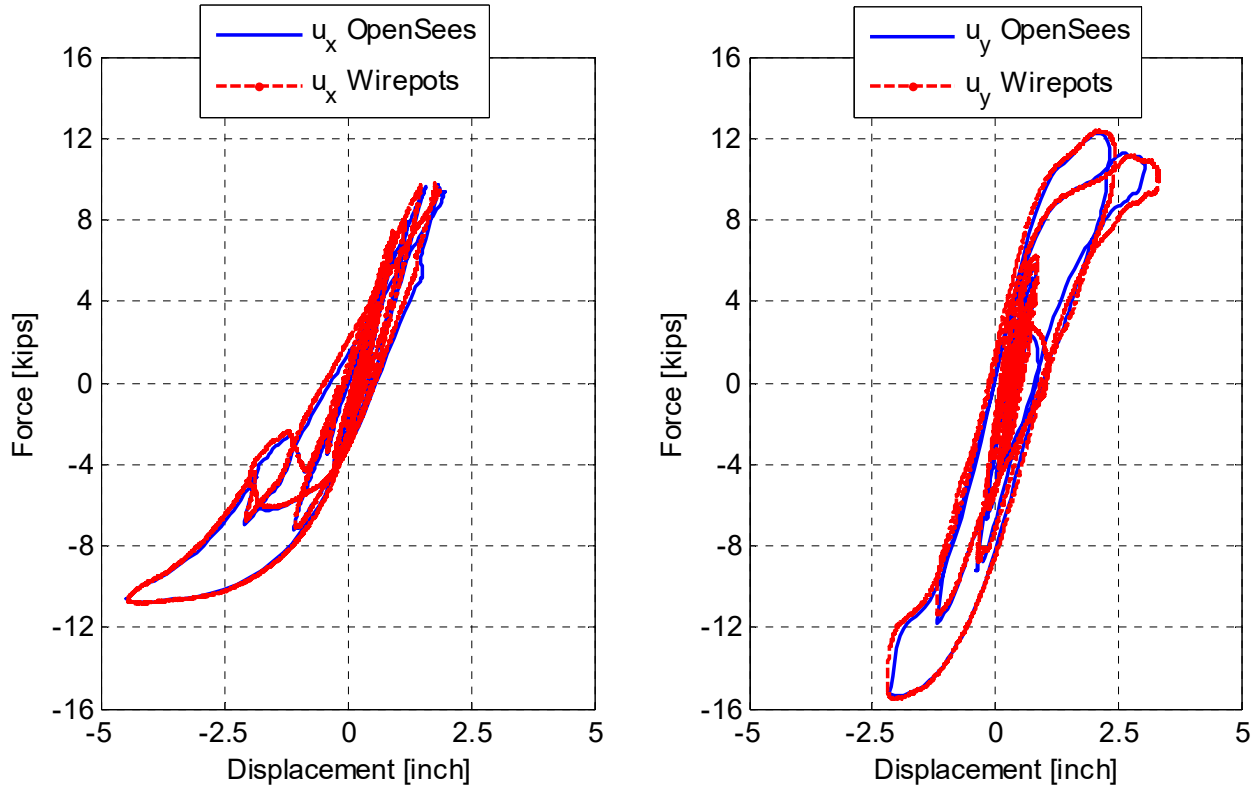
Figure 2.40   Comparison of force-displacement relationship in transverse (left) and longitudinal (right) directions from the recorded OpenSees data and actual load cells and wirepots DAQ data for the repaired Specimen No. 1 80% Rinaldi bi-directional HS test.

Based on all the verification tests from the free actuators and the repaired Specimen No. 1 full specimen HS test, it was concluded that the HSS developed herein is reliable and performed as expected. In particular, the new PI660C UCB HybridSim application (interface) successfully communicated the displacement and force feedback vectors between OpenFresco and the experimental hardware. The associated DSP routines developed within the PI660C UCB HybridSim successfully interpolated the commands for multi-actuators simultaneously, and communicated the DAQ actuators load cell measurements back to the PI interface. Finally, the newly implemented OpenFresco experimental set-up object correctly performed displacement and force geometric transformation between the global DOFs and the two actuators in a triangular arrangement local DOFs. The HSS was then used with confidence to test Specimen No. 2, as discussed in the next chapter.

3 Hybrid Simulation: Retrofitted Specimen Two Tests

The experimental program conducted in this study comprised mainly of two specimens that were tested using different loading protocols and under different conditions. The first specimen was tested as-built under cyclic loading and then was repaired and retested under cyclic loading as discussed in Part I of this report. The repaired Specimen No. 1 was also utilized in HS test trials for HS system verification, as presented in Chapter 2 of this report. Specimen No. 2 was retrofitted before any testing and was only tested using HS. Discussions of Specimen No. 2 test results are the focus of this chapter. The chapter presents the retrofit procedure, the tests and damage progression, the global behavior, the column and bent cap beam local behavior, and effective width discussion. The chapter concludes with a brief discussion of the effectiveness of the retrofit through comparison of various behavior metrics against the corresponding quantities from the identical as-built Specimen No. 1 Tests.

3.1 RETROFIT PROCEDURE

The objective of the retrofit considered in this part of the study was to increase the moment capacity of the column such that the bent cap beam could experience higher moment demands. For this purpose, three layers of CFRP were used to wrap the column to improve the confinement behavior and, in turn, increase its flexural capacity. Each of the three layers was 0.04 in. thick and the total thickness of the jacket was 0.12 in. A brief discussion of the material properties of the carbon sheets and the structural epoxy used for creating the jacket layers is included in Part I of this report. A similar procedure of wrapping the repaired column of Specimen No. 1 with CFRP layers was followed for the untested column of Specimen No. 2. A summary of the procedure is shown in Figure 3.1 through Figure 3.5.

The second specimen retrofit was carried out at a later stage after the construction of the specimen. A view of the as-built Specimen No. 2 before the column retrofit is shown in Figure 3.1. The first step in preparation for the retrofit was cleaning and smoothing the concrete surface, Figure 3.1, for efficient wrapping. The surface was then wet with a layer of the primer epoxy and the carbon sheets were cut to the required length as shown in Figure 3.2. Each layer of the carbon sheets was generously coated from both sides with the primer epoxy as illustrated in Figure 3.3. All the wet carbon sheets were rolled and left for a short time to make sure the epoxy is well-immersed. The following stage was to apply the wet carbon sheets to the column in a circumferential manner to create the three-layer jacket one layer at a time. Note that the sought

CFRP jacket extended to the mid height of the column. That was to guarantee that the moment demand in the unwrapped portion of the column did not exceed its capacity and that the plastic hinge did not migrate to an undesired upper location of the column in its inverted position, i.e., closer to the pin support. Thus, each layer of the jacket comprised two adjacent sheets provided in standard 24-in.-wide rolls with no overlap. Figure 3.4 shows the application of the lower and upper parts of the first jacket's layer. The final retrofitted column is shown in Figure 3.5.

(a)   (b)
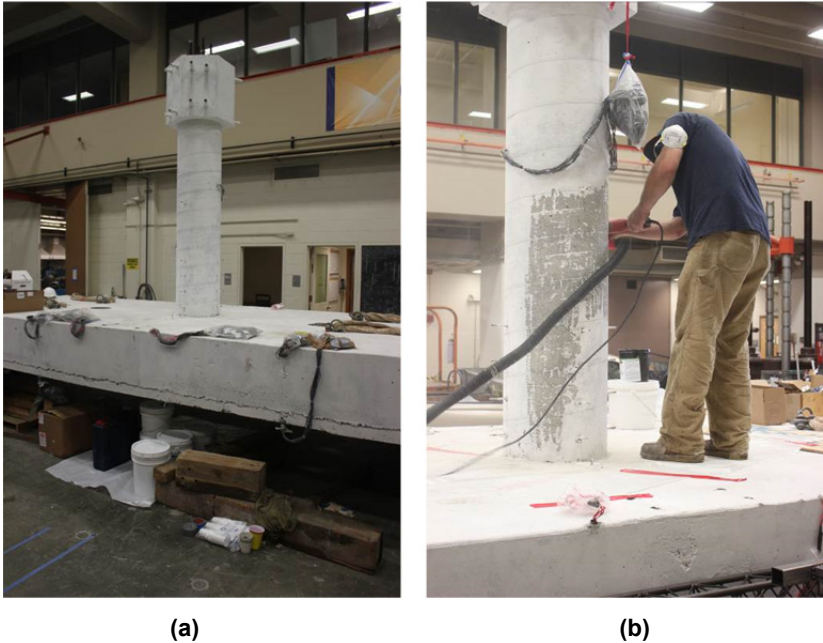
Figure 3.1   **The as-built Specimen No. 2 (a) before retrofit (left); and (b) preparing the column surface for CFRP wrapping.**

(a)   (b)

Figure 3.2   **(a) Applying a primer epoxy coat to the column surface before applying the CFRP layers; and (b) preparing a single layer of a carbon fibers sheet and cutting the sheet to the desired length.**

Figure 3.3   Coating the carbon sheets with epoxy resin and rolling the wet sheets in preparation for wrapping.

(a)   (b)
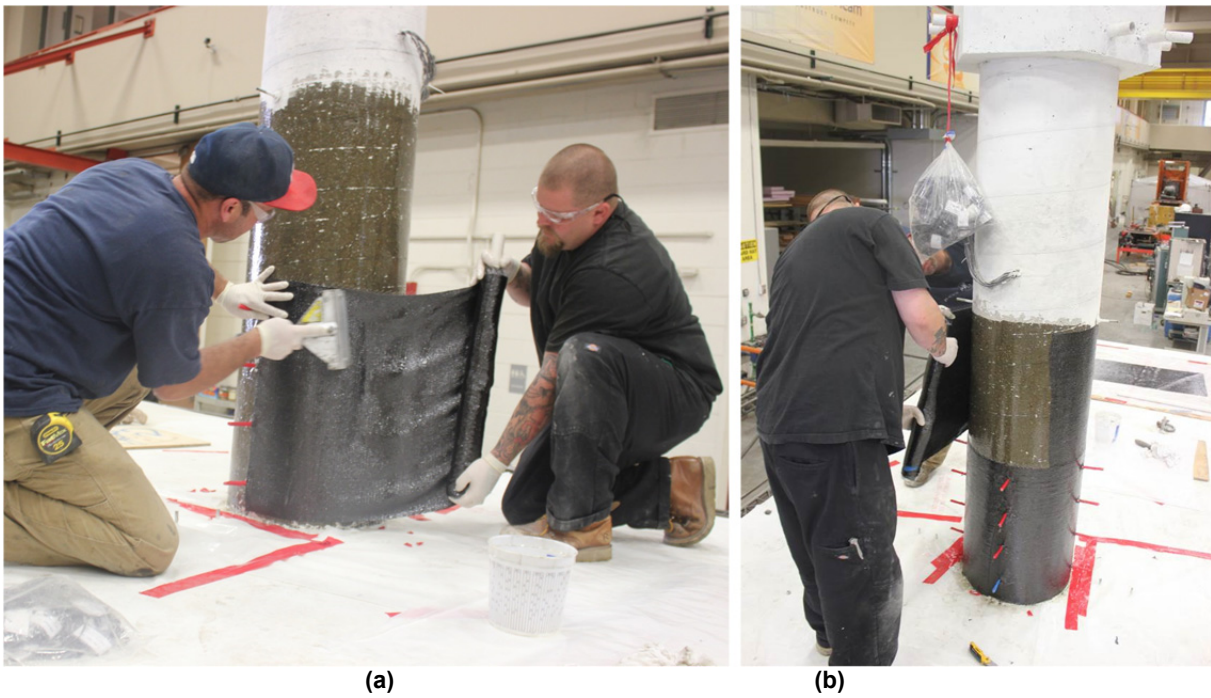
Figure 3.4   Applying the first CFRP layer of (a) the lower part of the jacket and (b) the upper part of the jacket of the column using the ready CFRP wet rolls.

	(a)			(b)	
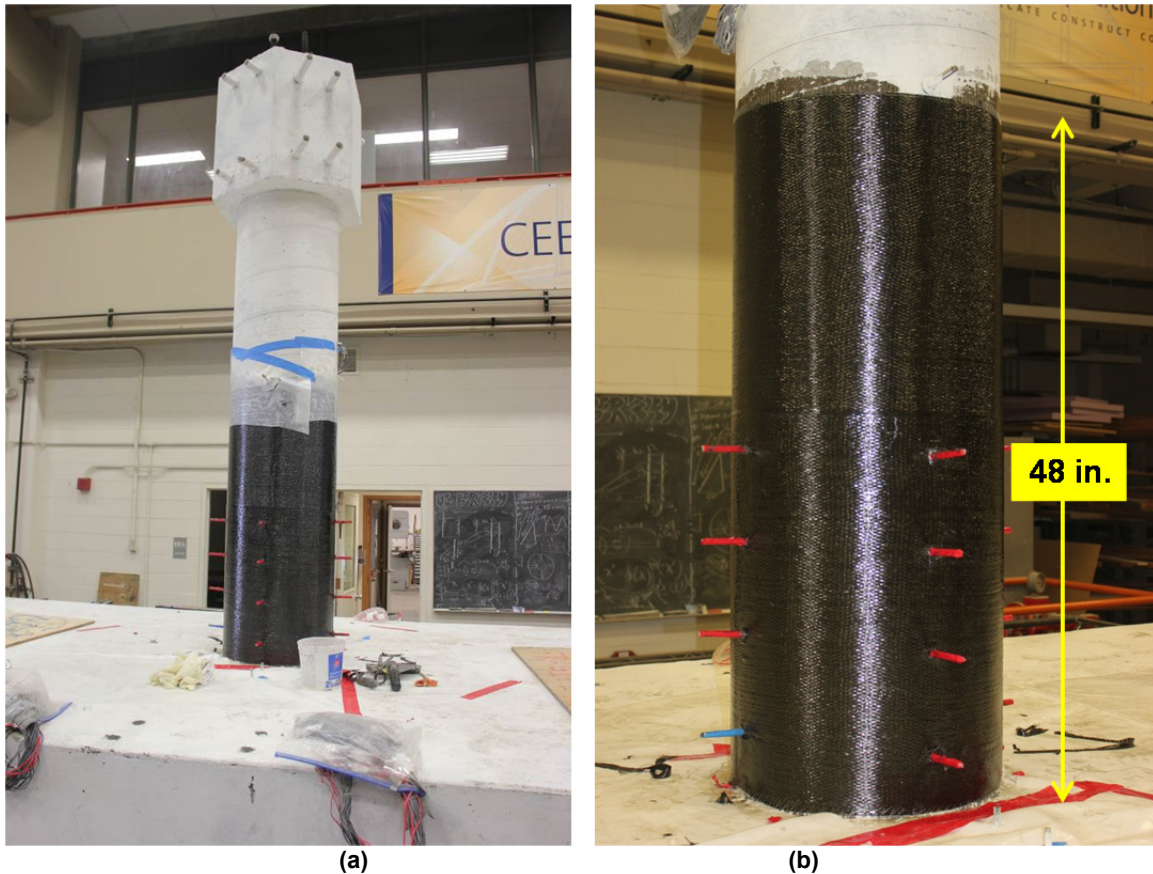
Figure 3.5   **(a) An overview and (b) close-up view of the final retrofitted column of Specimen No. 2.**

3.2   PROGRESSION OF TESTING AND DAMAGE

As discussed earlier, a similar test set-up to Specimen No. 1 tests was used for conducting the Specimen No. 2 HS tests. The main difference is that for Specimen 2 tests, the displacement response of the column subjected to ground motion computed during the test used the forces feedback measured from the actuators rather than using a prescribed cyclic loading pattern as used in Specimen No. 1 quasi-static tests. In addition, the bi-directional loading was conducted in both of the transverse and longitudinal directions simultaneously in case of Specimen No. 2 HS tests rather than separately as in the Specimen No. 1 cross-orbit cyclic loading tests. An overview of the test set-up and load progression during one of the HS tests is shown in Figure 3.6. Several HS tests were performed that varied in ground-motion scale, components, and direction. Only the test runs that utilized the Rinaldi ground motion at 50% scale or higher were included in the test processing and discussion herein. Other smaller scale tests were mainly utilized to decide on a suitable loading rate with minimal error and are not included here for brevity. A summary of the 15 tests conducted are listed in Table 3.1. The test runs of 100% scale or higher were conducted in two opposite directions of shaking, i.e., the ground motion direction in the HS input file was used twice: (1) positive (original) and (2) negative (inverted polarity). That is because the pulse nature of the Rinaldi ground-motion record caused large inelastic deformations in one direction but did not have the same effect in the opposite direction because

44

the pulse did have large enough reversal. More details are presented in the global behavior discussion in the next section.

Figure 3.6   Retrofitted Specimen No. 2 HS test set-up during a bi-directional run.

Table 3.1   Summary of different Specimen No. 2 HS runs.

Test ID	Grvaity load level	Ground-motion scale	Components	Direction	*P*-delta correction
1	10%	50%	Bi-directional	Positive	Yes
2	10%	50%	Bi-directional	Positive	No
3	10%	50%	Transverse only	Positive	Yes
4	10%	50%	Longitudinal only	Positive	Yes
5	10%	75%	Bi-directional	Positive	Yes
6	10%	100%	Bi-directional	Positive	Yes
7	10%	-100%	Bi-directional	Negative	Yes
8	15%	125%	Transverse only	Positive	No
9	15%	-125%	Transverse only	Negative	No
10	15%	150%	Transverse only	Positive	No
11	15%	-150%	Transverse only	Negative	No
12	15%	175%	Transverse only	Positive	No
13	15%	-175%	Transverse only	Negative	No
14	15%	200%	Transverse only	Positive	No
15	15%	-200%	Transverse only	Negative	No

The observed global damage and overall mode of failure for the retrofitted Specimen No. 2 was much different from that of the identical as-built Specimen No. 1. The retrofitted column in Specimen No. 2 did not experience extensive damage, i.e., no bar buckling or rupture occurred because of the CFRP jacket confinement. Instead, slight damage was observed in the bent cap in the compression zone at one of the column sides; see Figure 3.7. To better investigate the final damage state of the specimen, the CFRP jacket was carefully removed after all test runs were concluded. Figure 3.8 shows the procedure for removing the jacket and an overview of the column and cap beam damage state. A uniform pattern of flexural cracks that were almost equally spaced within the anticipated plastic hinge zone was observed in the column after the jacket removal. All the loose concrete and dust were cleaned after the jacket removal to identify the final damage state. Figure 3.9 shows a close-up view of the column flexural circumferential cracks and bent cap beam concrete crushing. The first column hoop inside the column-bent cap joint and the bent cap transverse stirrups were exposed (Figure 3.9). This indicates that the mode of failure was indeed cap beam compression crushing manifested by cover spalling rather than a column plastic hinging. This confirms the accuracy of the estimation of the bent cap beam capacity by subjecting it experimentally by jacketing the column using CFRP to increase its capacity and accordingly the demand on the cap beam.

(a)   (b)

Figure 3.7   **Damaged state of Specimen No. 2 (a) after all HS tests and (b) final view of this damage state after all loose concrete were removed.**

(a)   (b)
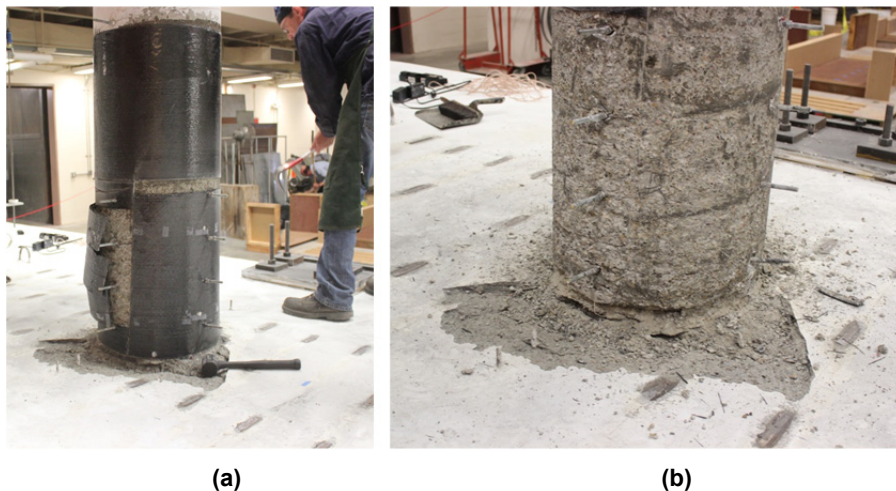
Figure 3.8   **Procedure of (a) removing the CFRP jacket after the retrofitted Specimen No. 2 tests were concluded and (b) final view of the column after the jacket removal.**

Figure 3.9 A close-up view of Specimen No. 2 column flexural cracks (CFRP jacket was removed) and bent cap beam concrete cover spalling after HS tests.

3.3 GLOBAL BEHAVIOR

Post-processing and presenting the experimental test results of Specimen No. 2 followed similar framework to that of Specimen No. 1 quasi-static tests (Part I of this report). This includes a discussion of the global behavior, which is presented in this section, followed by a discussion of the column and bent cap beam local behaviors, and the effective width. For the global behavior, the observed displacement and force histories, and force-displacement relationships are discussed.

3.3.1 Displacement History

Monitoring displacements are central to HS tests because displacements are computed and updated online during the test based on the measured force feedback, i.e., applied displacements are not known beforehand. Similar to the quasi-static cyclic tests, displacements were measured using wire potentiometers to capture the global specimen displacements, and temposonics were installed along the actuators axes to capture and control the actual input motion at each actuator. The actuators displacements were geometrically transformed to the global directions and compared to the wirepots measurements. The geometric transformation was reliable and was used to deduce the motion of the column head in the transverse and longitudinal directions. Table 3.1 summarizes the entire displacement history that was computed and applied to the retrofitted Specimen No. 2 during the 15 HS tests; the global transverse and longitudinal directions are shown in Figure 3.10. Figure 3.11 compares the transverse and longitudinal displacements to the two actuator local displacements for the full history of the 15 HS tests. This figure gives an overview of the different components of the conducted tests and the sequence of the increased ground-motion scales and reversed directions. Zoomed-in views of the displacement histories in

47

the 50%-scale tests in bi-directional, transverse direction only, and longitudinal direction only tests are shown in Figure 3.12, Figure 3.13, and Figure 3.14, respectively.

Figure 3.12 shows that for the case of simultaneous bi-directional loading, one of the actuators consistently experienced much lower displacements, which is attributed to the fact that the resultant of the nearly similar transverse and longitudinal components was almost aligned with the south-inclined actuator direction. Figure 3.13 shows that both actuators had almost symmetric (same magnitude and direction) displacements when only transverse loading was applied. Figure 3.14 shows that both actuators had almost anti-symmetric (same magnitude but opposite directions) displacements when only a longitudinal loading was in progress. Moreover, Figure 3.12 to Figure 3.14 show constant slope lines (especially for large displacements) for all the global and local displacements. This is attributed to the conducted constant velocity slow rate HS tests. Obtaining this constant velocity for the displacement input was a fundamental criterion to verify the performance of the HSS and the communication between its components. More details were presented in Chapter 2 about the validation of the developed HSS. Another important observation from the displacement history figures, especially the full history demonstrated in Figure 3.10 and Figure 3.11, is the residual displacements at the end of each of the HS tests. For the small-scale tests, a small residual displacement was observed due to the minimal damage. However, much higher residual displacements were observed in the transverse direction only large-scale tests that reached a final residual displacement of about 2 in. (drift ratio of 2.2%) after all the tests were concluded.
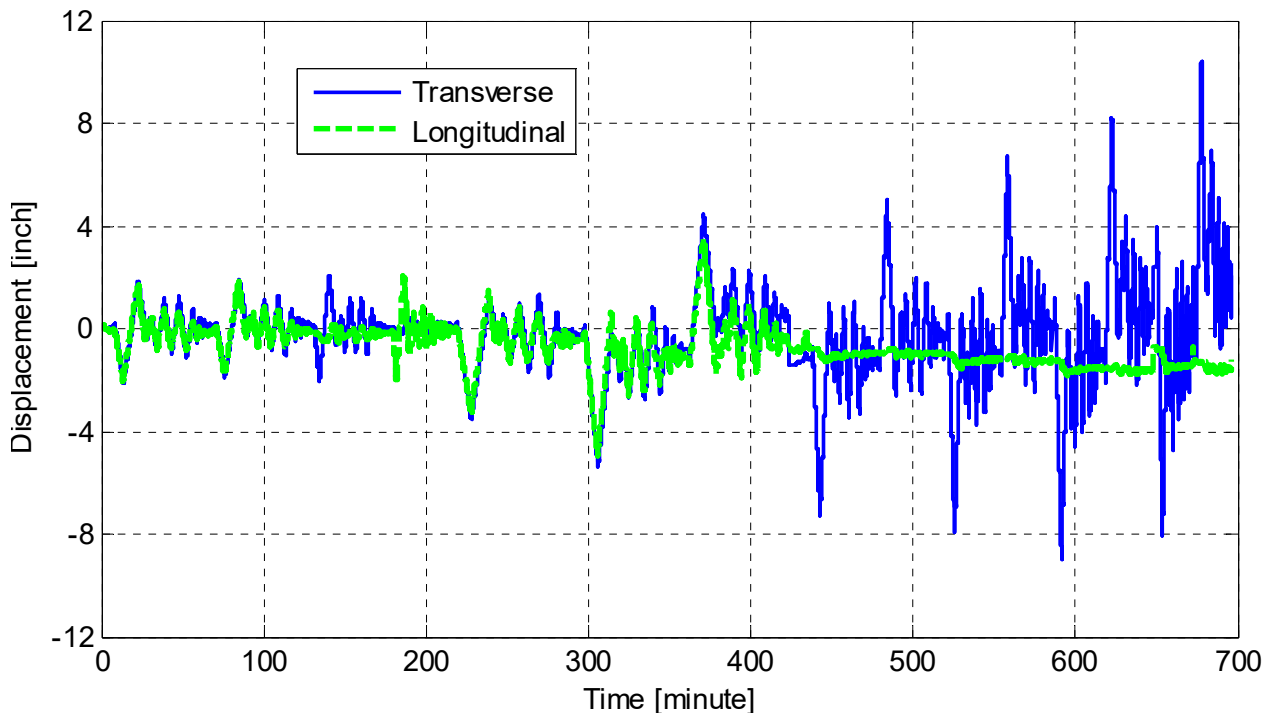
Figure 3.10   History of the online computed (and applied) displacements in the global transverse and longitudinal directions throughout all 15 HS test runs of the retrofitted specimen (Specimen No. 2).
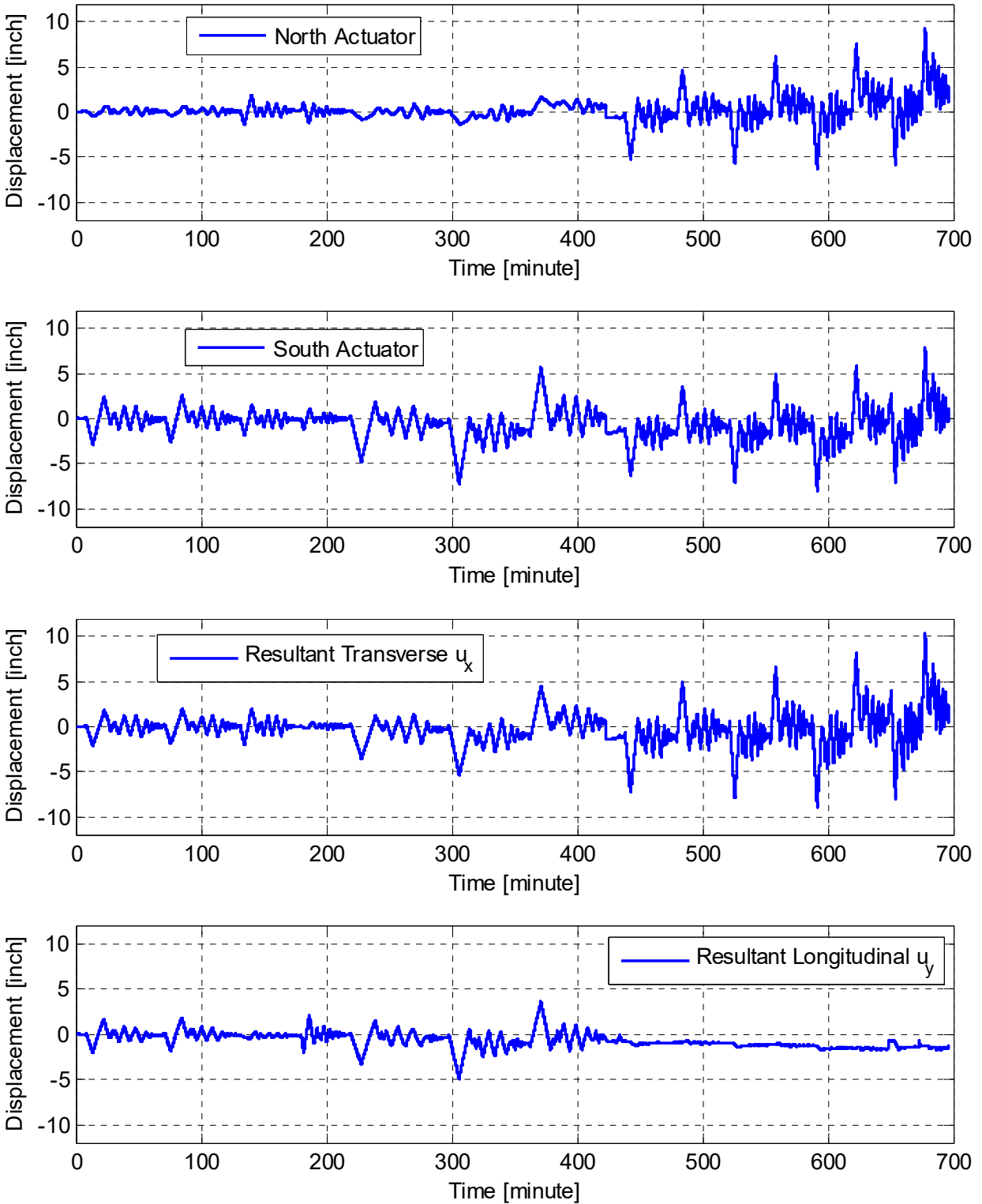
Figure 3.11 History of north and south lateral actuators temposonics measurements and the corresponding resultant displacements in transverse (u_x) and longitudinal (u_y) directions for all 15 HS test runs of Specimen No. 2.
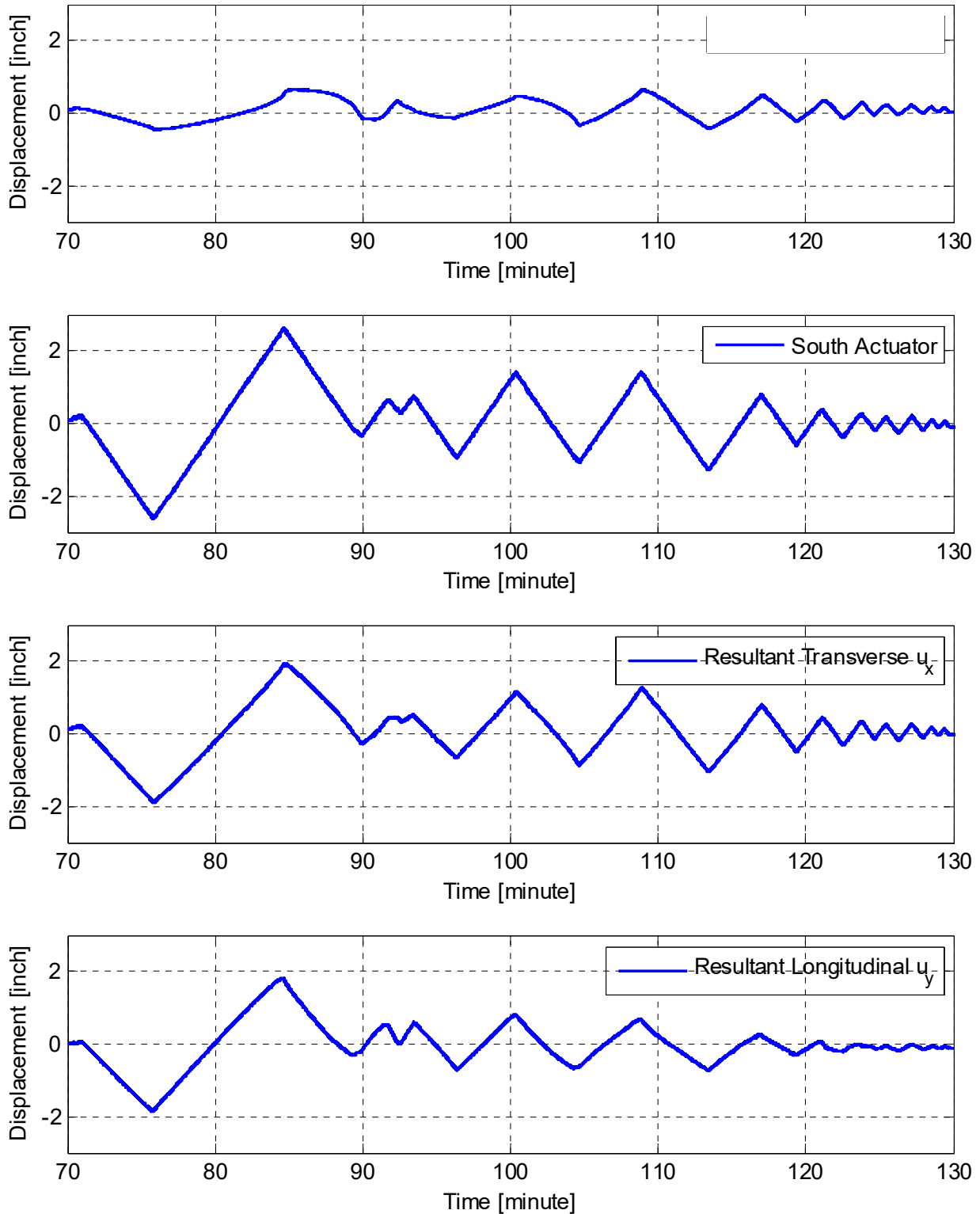
Figure 3.12 Zoomed-in view of the history of north and south lateral actuators temposonics measurements and the corresponding resultant displacements in transverse (u_x) and longitudinal (u_y) directions for the 50% scale bi-directional HS test.
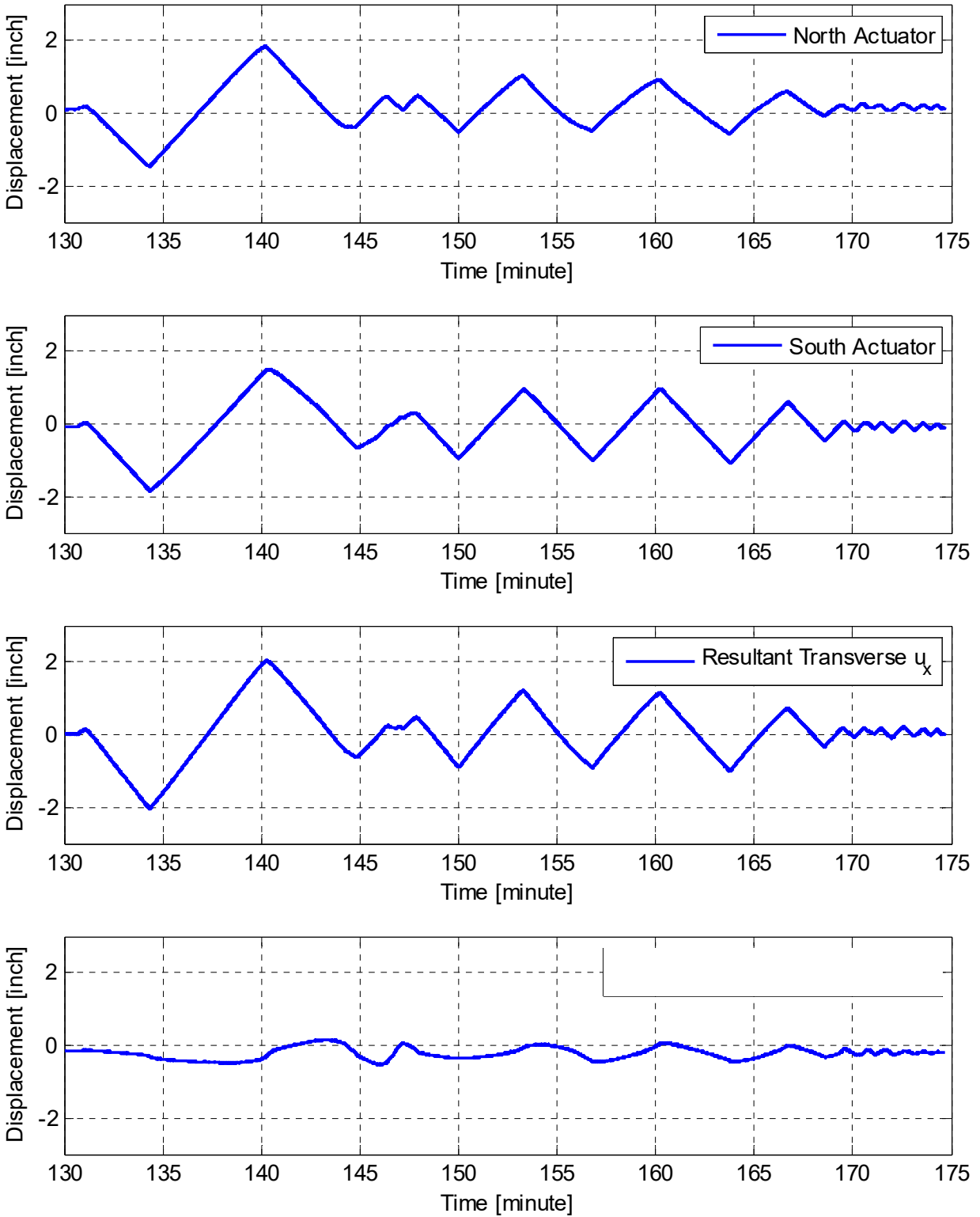
Figure 3.13 Zoomed-in view of the history of north and south lateral actuators temposonics measurements and the corresponding resultant displacements in transverse (u_x) and longitudinal (u_y) directions for the 50% scale transverse direction only HS test.
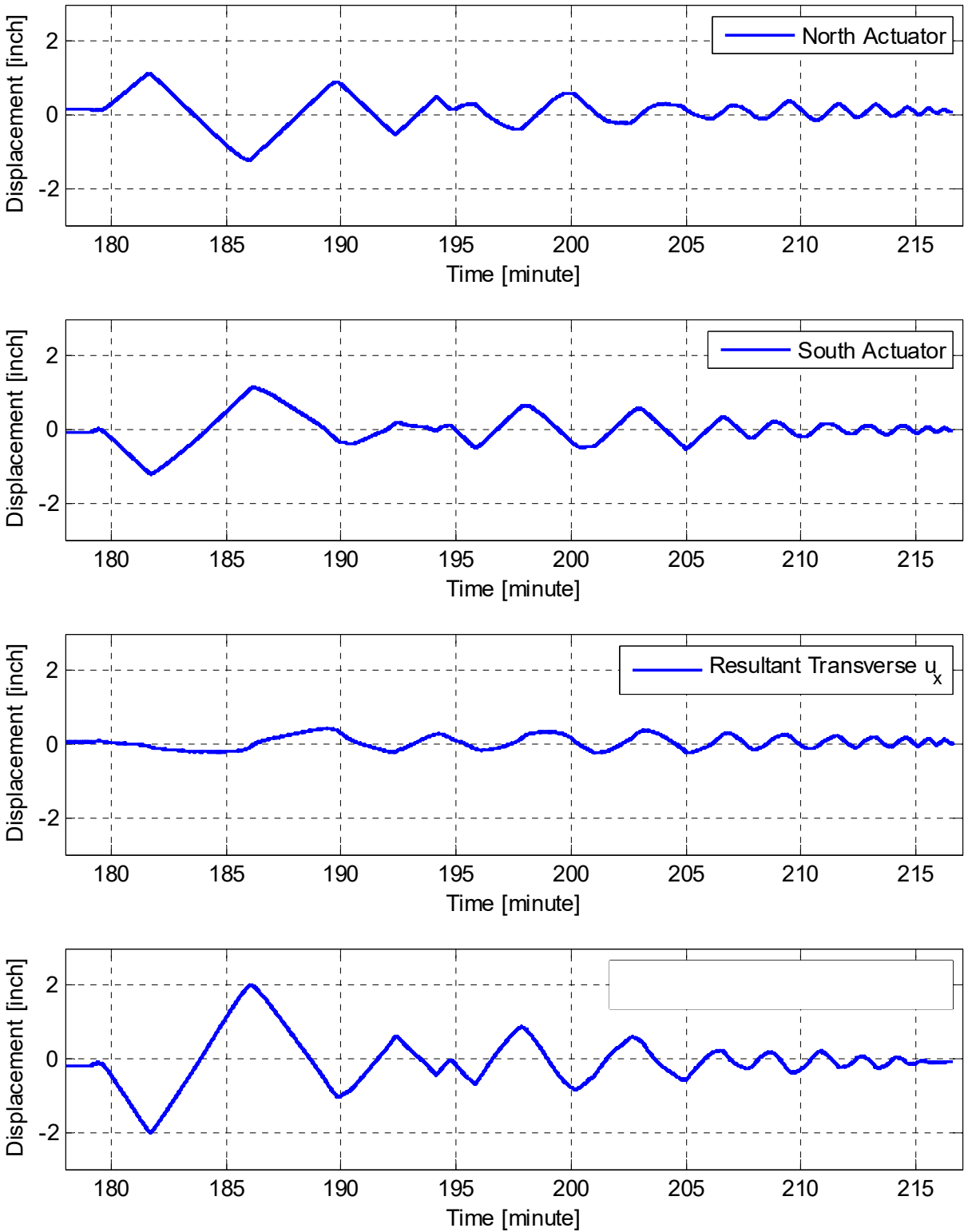
Figure 3.14 Zoomed-in view of the history of north and south lateral actuators temposonics measurements and the corresponding resultant displacements in transverse (u_x) and longitudinal (u_y) directions for the 50% scale longitudinal-only HS test.

3.3.2 Force History

Displacements are crucial to monitor during displacement-controlled HS tests because that is the only way to know what deformations the specimen has gone through during HS testing. However, lateral forces are even more important to monitor because it is the force feedback that influences the next solution of the governing equations of motion, Equation (2.1) in Chapter 2, and, in turn, the new displacement input. A constant vertical gravity load was applied and maintained throughout the tests under force-control, which also needed to be monitored to make sure it remained constant during the test. The gravity load history is shown in Figure 3.15 for all the 15 HS test runs. The total vertical reaction as the sum of the two strut forces is shown as well in Figure 3.15 to compare the total portion of the gravity load transmitted directly to the bent cap beam at its two supported ends by the two struts. The ratio between the total strut reactions and the gravity load was observed to be consistently around 70%, which agrees with the observation from Specimen No. 1 cyclic tests as well. Note that the sudden drop and consequent increase at the beginning of the second gravity load level, which was 15% corresponding to ~240 kips, reflects the unloading and reloading again since testing was conducted during two separate days. The total gravity load values that was measured continuously was utilized along with the lateral displacement values and the prescribed numerical component of the vertical earthquake excitation by the computational model to estimate the equivalent lateral force considering the P-delta effect. Accordingly, the lateral force feedback was corrected before sending it to the computational model for the computation of the next displacement input, as discussed in Chapter 2. Only the bi-directional runs had the correction involving the P-delta effect considering both the time-varying vertical earthquake excitation and the applied constant gravity load. However, no such correction was applied during the large-scale transverse direction only HS runs. That is because the corresponding axial load variation considering the large-scale runs with vertical excitation would experience tension at some time steps, thus increasing the corrected lateral force value and affecting the computed displacement input in a somewhat unpredictable way because of possible column tension. Although this scheme might be realistic in some cases, it was decided to proceed with the transverse direction only runs of scales 100% and higher 200% without accounting for the P-delta correction to limit the scope of the study to no-tension gravity load in combination with the applied lateral earthquake excitations.

The entire history of the measured force feedback in both transverse and longitudinal directions is shown in Figure 3.16. The force that was sent to the computational model for solving the equations of motion is slightly different as it incorporated the P-delta corrections for those runs that had that correction scheme applied. A more detailed discussion is presented in a following subsection. Similar to the displacements discussion, the local force measured at the actuators load cells was compared to the resulting force in the two intended transverse and longitudinal global directions. Figure 3.17 shows the full history of north and south actuator forces along with transverse and longitudinal force resultant for all the 15 HS test runs. A zoomed-in view for the 50%-scale bi-directional, transverse-only, and longitudinal-only tests are shown in Figure 3.18, Figure 3.19, and Figure 3.20, respectively. The force residual at the end of each test was adjusted and reduced to zero before the start of a subsequent test to avoid any unrealistic force feedback at the start of the subsequent HS test. Zeroing the forces also allowed the determination of the corresponding residual displacements. However, due to the effect of the residual displacements, a minor force feedback was generated in the longitudinal direction when testing took place in the transverse direction only, as seen from the noise around the zero force

value in the longitudinal force history in Figure 3.16. Also worth noting is that the constant slope mentioned above for the displacement histories could be observed only in the small runs where the behavior was still in the linear elastic range. However, for the large-scale tests, the constant slope in the force history plots was no longer observed because of the inelastic and hysteresis damage behavior.
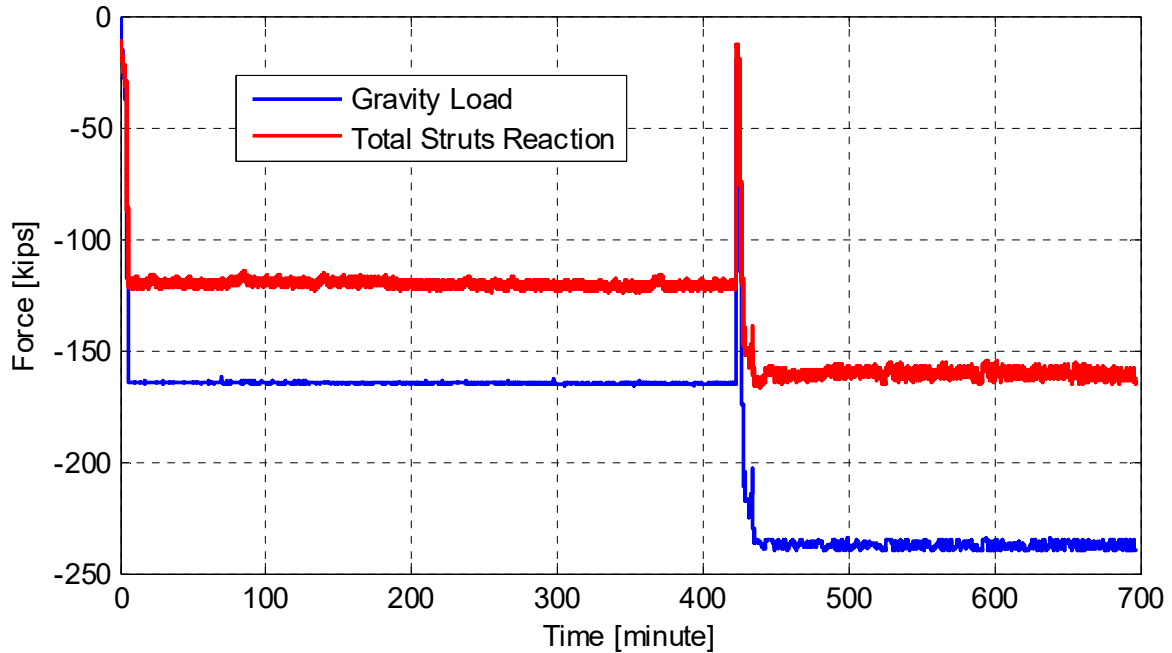
Figure 3.15   Gravity load history and corresponding two vertical strut reactions for all 15 HS test runs of Specimen No. 2.
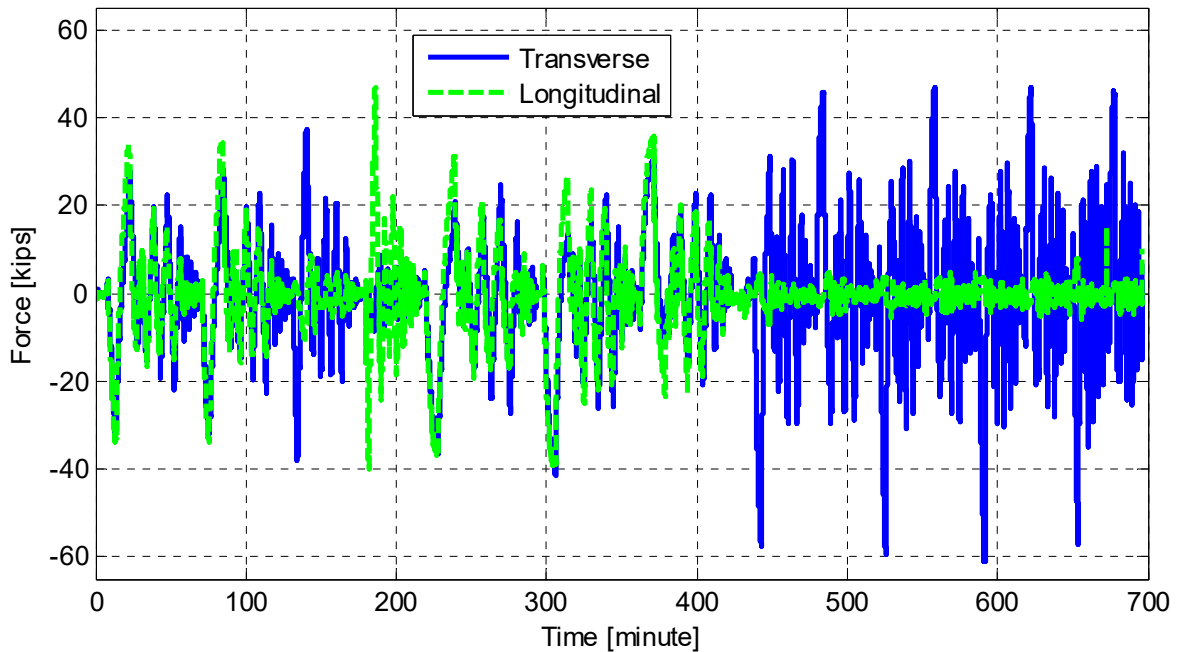
Figure 3.16   History of the force feedback in the transverse (f_x) and the longitudinal (f_y) directions for all 15 HS test runs of Specimen No. 2.
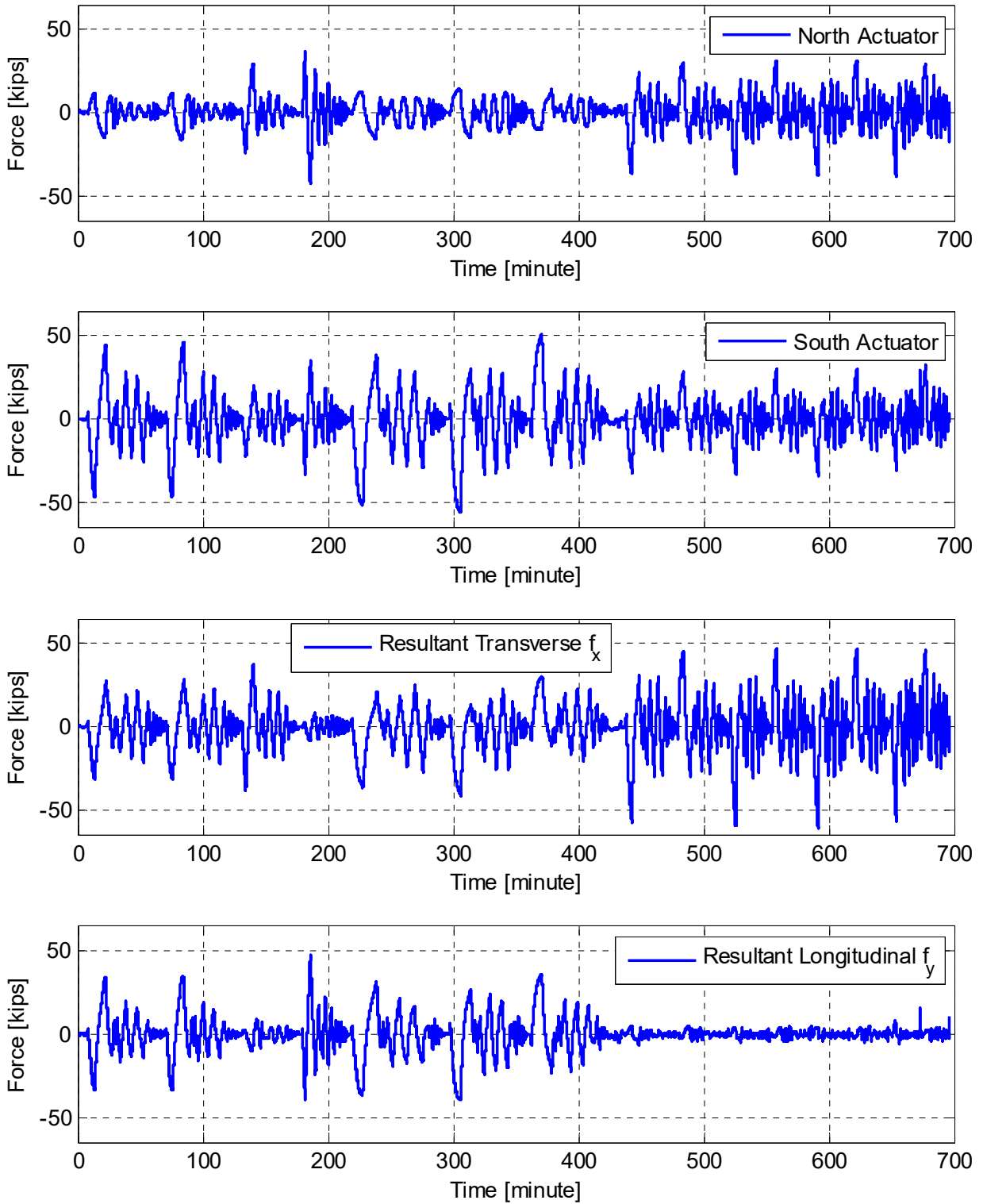
Figure 3.17 History of north and south lateral actuators load cells measurements and the corresponding resultant forces in the transverse (f_x) and the longitudinal (f_y) directions for all 15 HS test runs of Specimen No. 2.
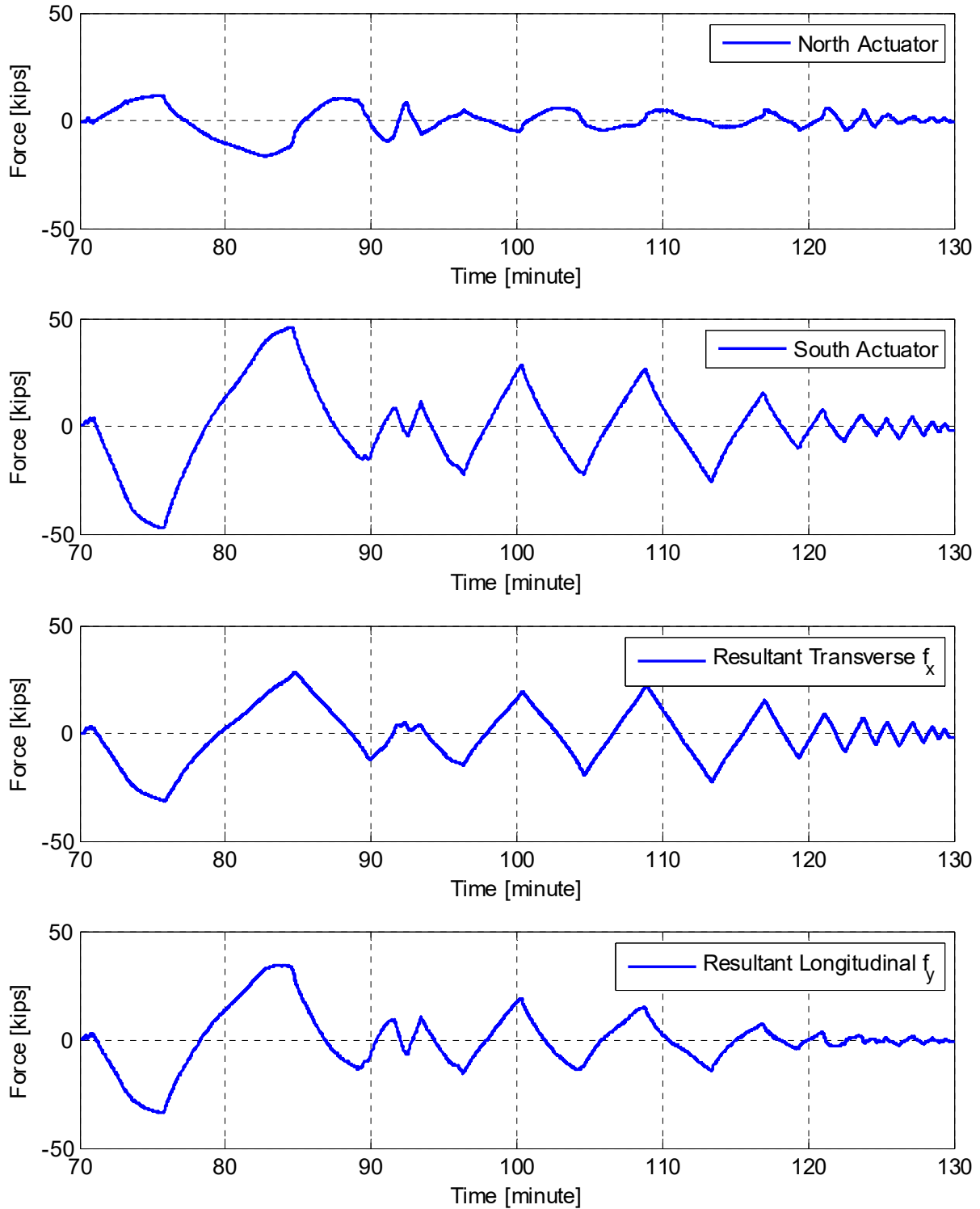
Figure 3.18   Zoomed-in view of the history of north and south lateral actuators load cells measurements and the corresponding resultant forces in the transverse (f_x) and the longitudinal (f_y) directions for the 50%-scale bidirectional HS test.
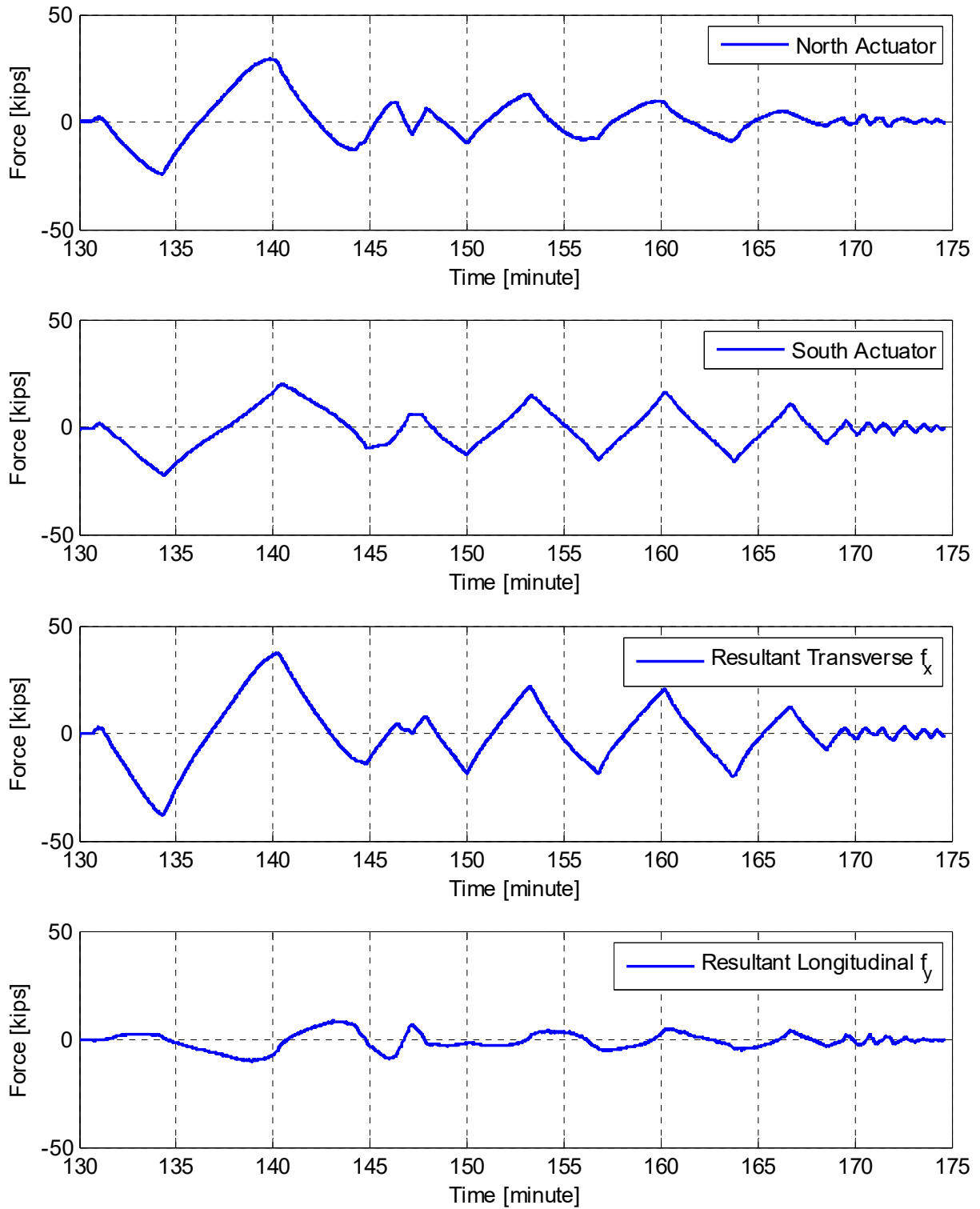
Figure 3.19 Zoomed-in view of the history of north and south lateral actuators load cells measurements and the corresponding resultant forces in the transverse (f_x) and the longitudinal (f_y) directions for the 50%-scale transverse direction only HS test.
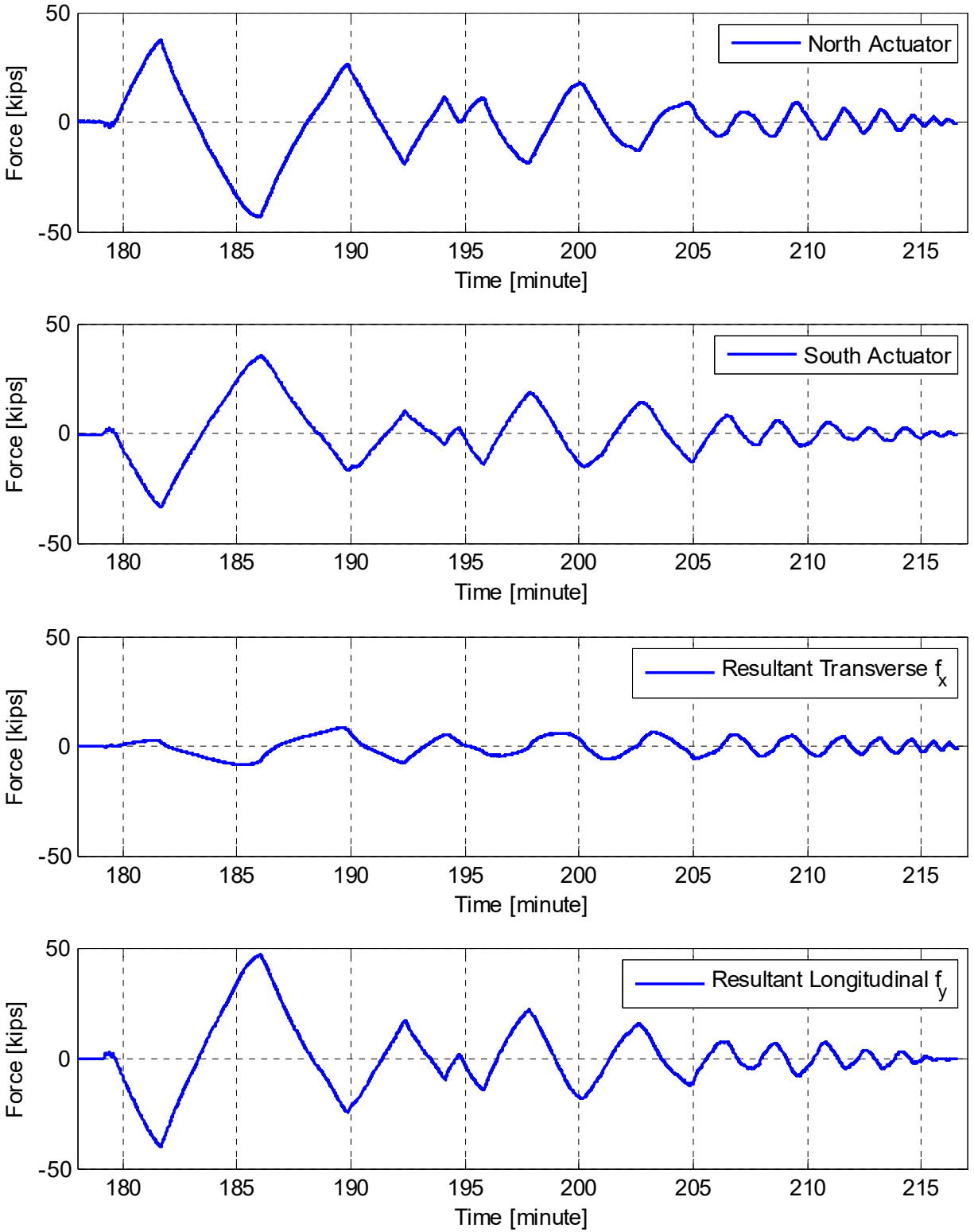
Figure 3.20 Zoomed-in view of the history of north and south lateral actuators load cells measurements and the corresponding resultant forces in the transverse (f_x) and the longitudinal (f_y) directions for the 50%-scale longitudinal direction only HS test.

3.3.3 Force-Displacement Relationship

The final global feedback forces and applied displacements in the specimen's transverse and longitudinal directions are plotted for the tested retrofitted bridge sub-assembly Specimen No. 2. The force-displacement response considered a whole system response rather than a single column response because of the nature of the column-to-superstructure connection, especially where the contribution of the full superstructure to the column stiffness is engaged during bi-directional loading. The concatenated force-displacement relationships for all the 15 HS test runs in both transverse (f_x versus u_x) and longitudinal (f_y versus u_y) directions are shown in Figure 3.21 and Figure 3.22, respectively. As shown in the figures, the force capacity was reached only in the transverse direction where the stroke capacity of the actuators limited reaching the specimen capacity while testing bi-directionally or longitudinally. For the large-scale transverse direction only runs, the force capacity was reached as evidenced by the capped value of the force, regardless of the increased input ground-motion scale. However, the force capacity reached was higher in one direction than the other, which is attributed to the pulse nature of the ground motion that concentrated the initial damage on one side; this damage propagated asymmetrically even when the input ground motion direction was reversed. As previously observed in the damage photographs in Figure 3.7 and Figure 3.9, the cap beam concrete crushing represented by cover spalling was the likely mode of failure that caused the bridge system force capacity to be reached, as observed in the force-displacement relationship in the transverse direction. In addition, the revealed column surface underneath the CFRP jacked showed only flexural cracks without concrete crushing, which supports the argument that the force capacity was reached as the bent cap reached its capacity rather than the column reaching its capacity.
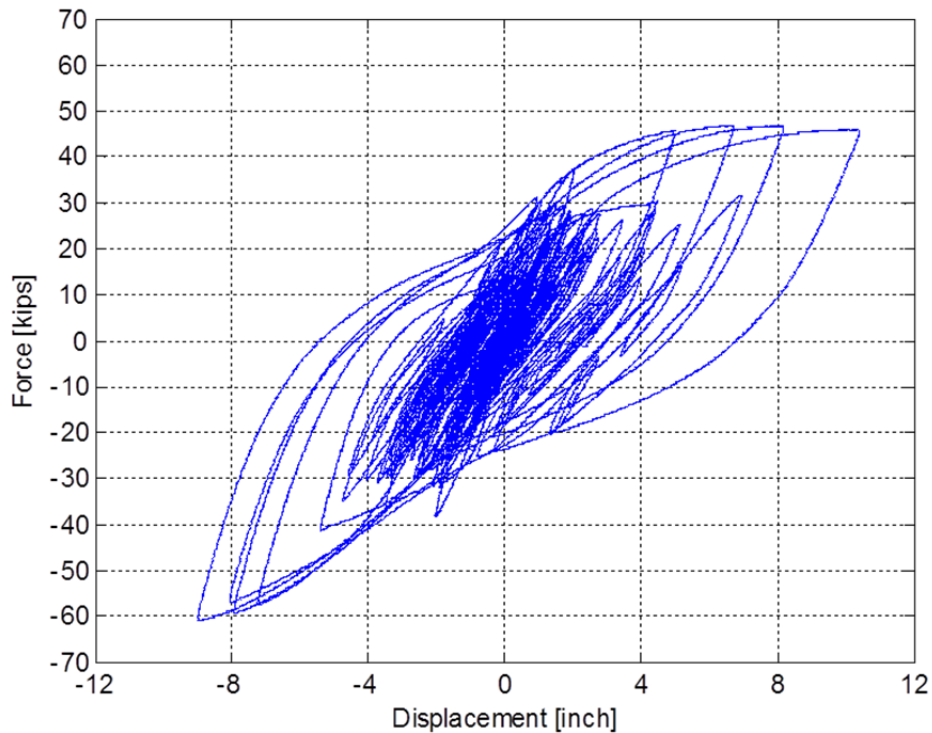
Figure 3.21   **Force-displacement relationship in the transverse direction for all Specimen No. 2 HS test runs.**
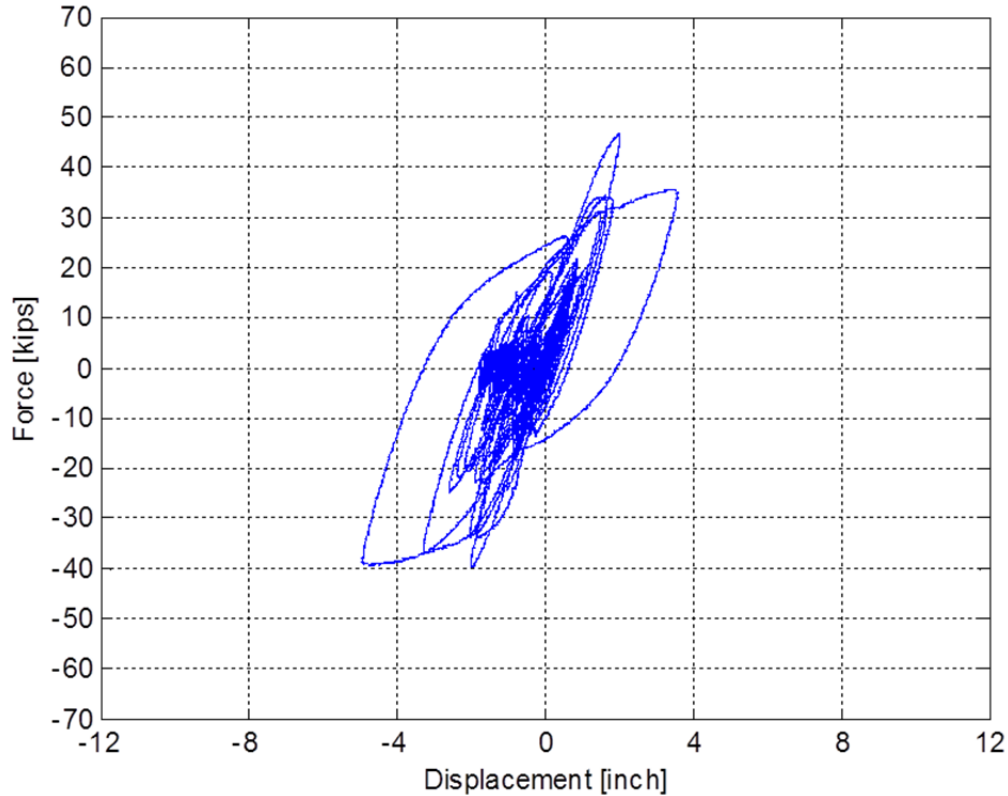
Figure 3.22   **Force-displacement relationship in the longitudinal direction for all Specimen No. 2 HS test runs.**

A closer look at the behavior during individual test runs is given in Figure 3.23 through Figure 3.25. The force-displacement relationship due to the 100% bi-directional only tests is shown in Figure 3.23 and Figure 3.24 when the ground motion was input in the positive direction and reversed in the negative direction, respectively, for both the transverse and longitudinal directions. These resolved force and displacement components revealed a slightly different response in each direction. Moreover, the initiation of damage and hysteretic inelastic behavior led to a different asymmetric response when the ground-motion direction was reversed, irrespective of the column symmetry and the similarity of the input motion. A maximum value of about 30 kips for the transverse force value was observed in one direction versus a maximum of almost 40 kips when loading was reversed in the other direction. The same observation was pronounced in Figure 3.25 where the force-displacement relationship obtained from the positive 175% transverse direction only HS test is compared against the one obtained from the negative 175% test, i.e., the reversed direction.
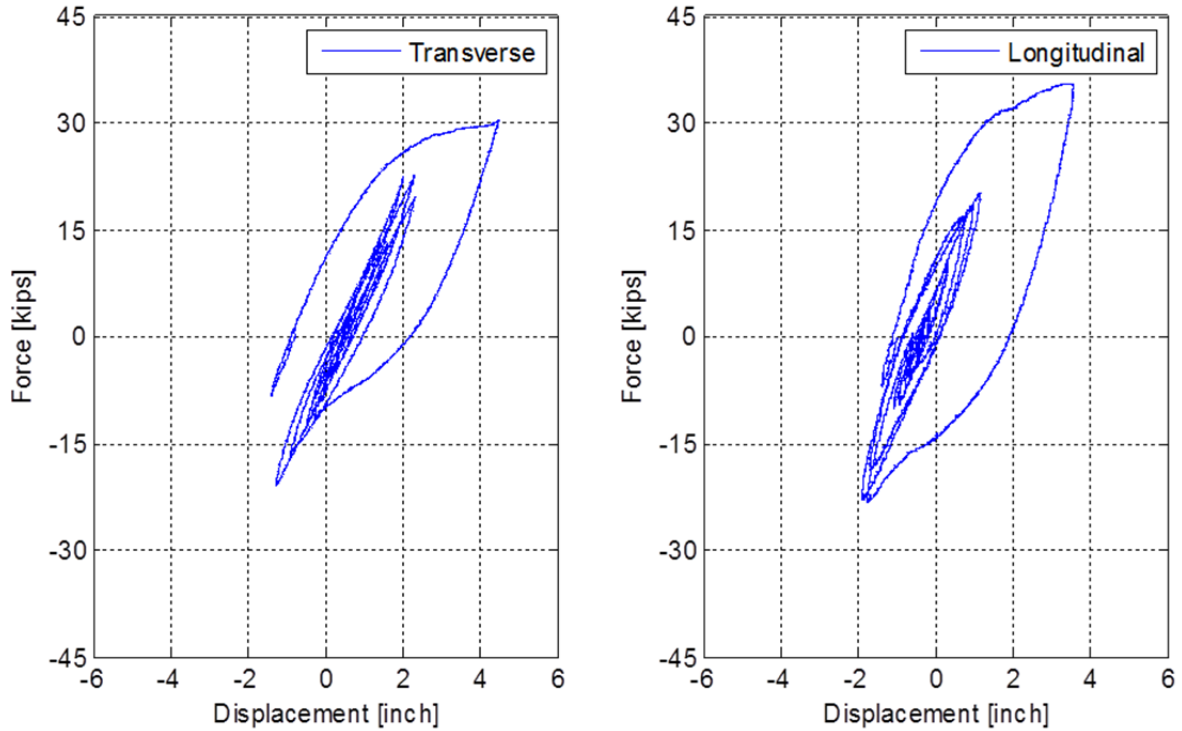
Figure 3.23   Force-displacement relationship in both transverse and longitudinal directions for the 100% bi-directional HS test with positive direction ground-motion input.
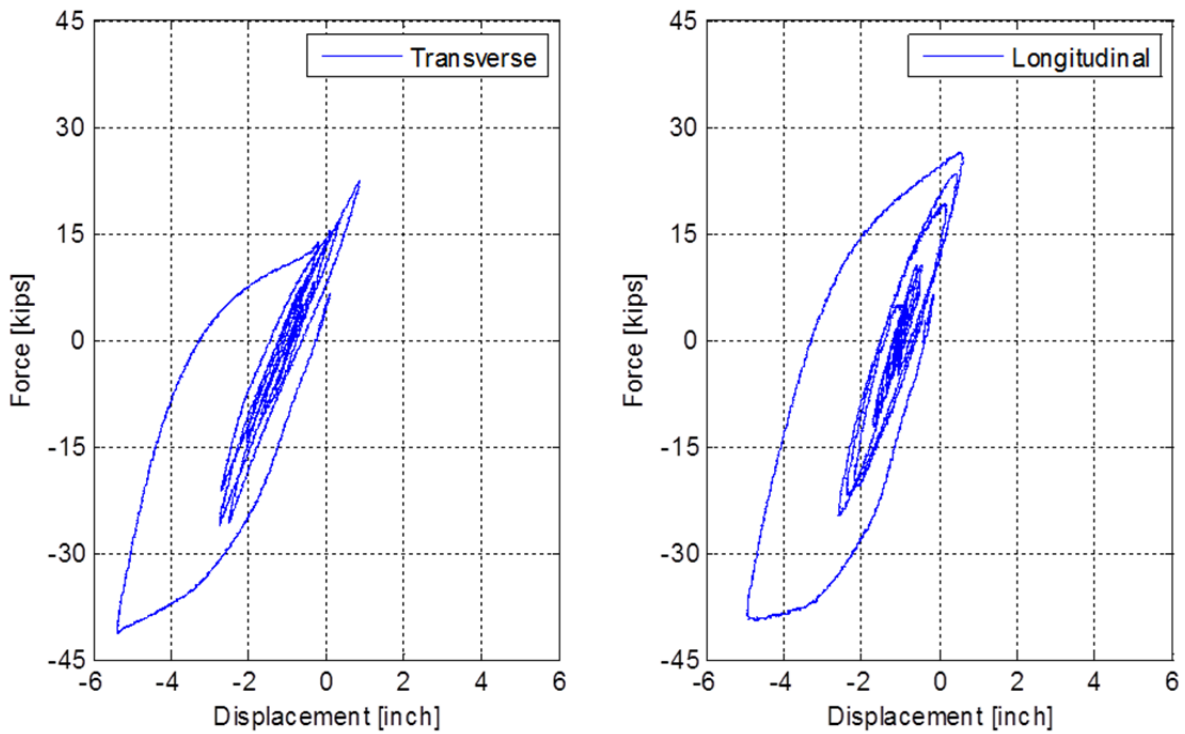
Figure 3.24   Force-displacement relationship in both transverse and longitudinal directions for the 100% bi-directional HS test with negative direction ground-motion input.

(a)

(b)
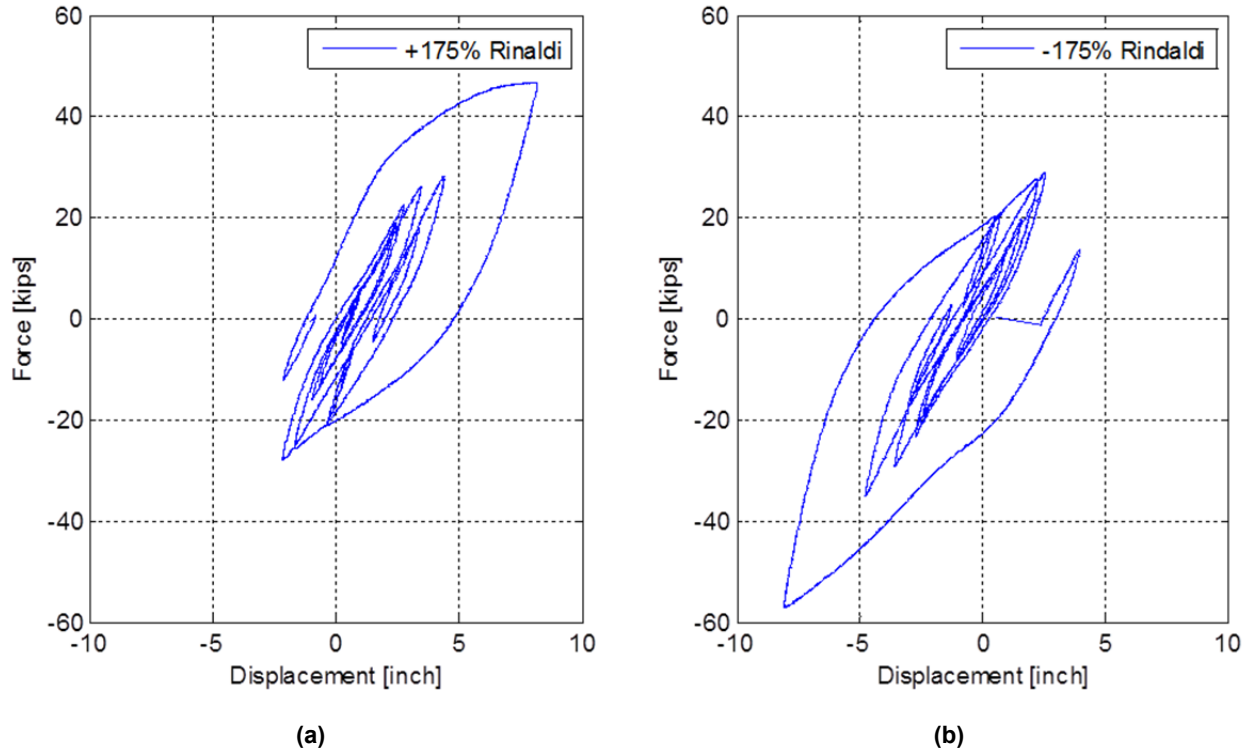
Figure 3.25 **Force-displacement relationship in the transverse direction for the 175% transverse direction only HS test with (a) positive and (b) negative ground-motion inputs.**

3.3.4 Comparison with OpenSees Data

One of the advantages of utilizing OpenSees and OpenFresco for conducting the HS tests is the ability to record the received force feedback and the computed displacements. Ideally, if the HSS does not have any delays or errors, the applied displacement should match perfectly the computed displacement at the computational platform end. Figure 3.26 and Figure 3.27 show the force-displacement relationships in the transverse and longitudinal directions, respectively, which compare the measured test data and the OpenSees recorders for all 15 HS test runs. Although the effect of experimental errors and delays should be minimal, as verified from the HSS development and validation trials discussed in Chapter 2, a large discrepancy can be observed. This is because the computed displacements in OpenSees started from zero each time a new test was conducted without recording the residual displacement from the previous test. Thus, a better comparison would be achieved if the residual displacement at the start of each test is added to the OpenSees data; however, this would not have added much benefit. The force comparison is more desirable in that it assures that the measured load cells values are comparable to what OpenSees used in solving the equations of motion.

To exclude the discrepancy in the displacements, only the force values in the transverse direction were plotted against the forces in the longitudinal direction; comparisons between the measured test data and the OpenSees recorders are shown in Figure 3.28. Note that although some runs incorporated *P*-delta corrections for the force feedbacks sent to OpenSees, the two plots compare reasonably well and give confidence that the correct measured forces were utilized in the displacement calculations. The difference due to the *P*-delta correction should be minimal

as the largest correction force value did not exceed 10% of the actual measured value. Therefore, only the bi-directional runs included the *P*-delta correction, while the transverse direction only large-scale runs did not include the correction. Thus, for these large-scale runs, the measured force feedback was directly sent to the computational platform without any modification.
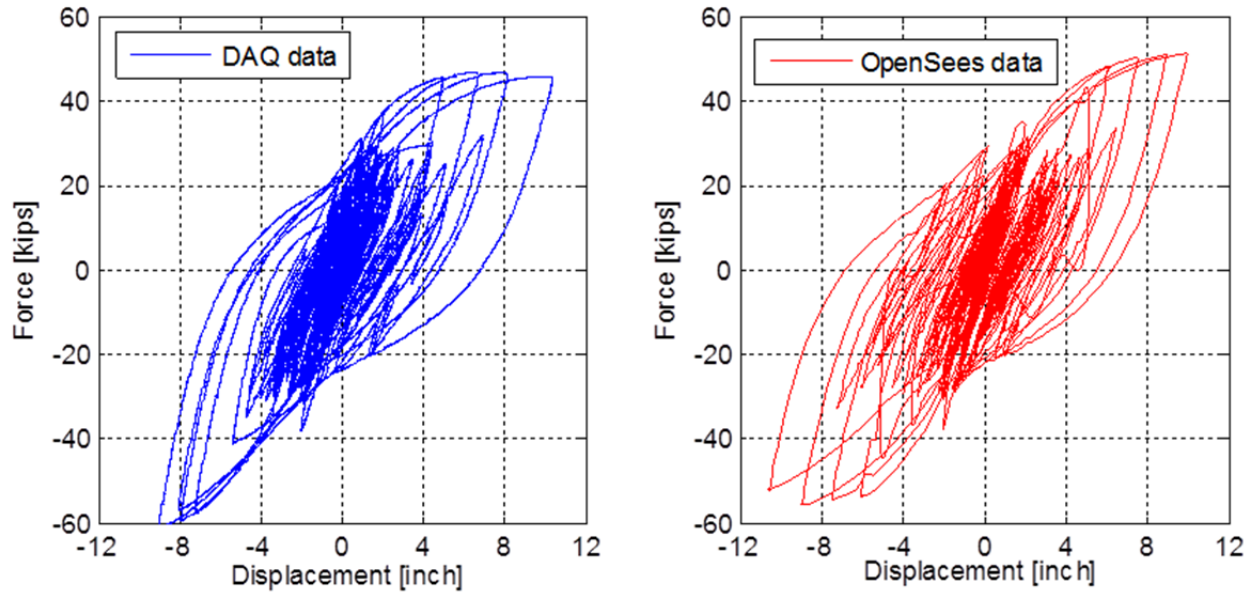
Figure 3.26   Comparison of force-displacement relationship for all HS test runs as obtained from the observed data acquisition (DAQ) experimental test data and the recorded OpenSees data in the transverse direction.
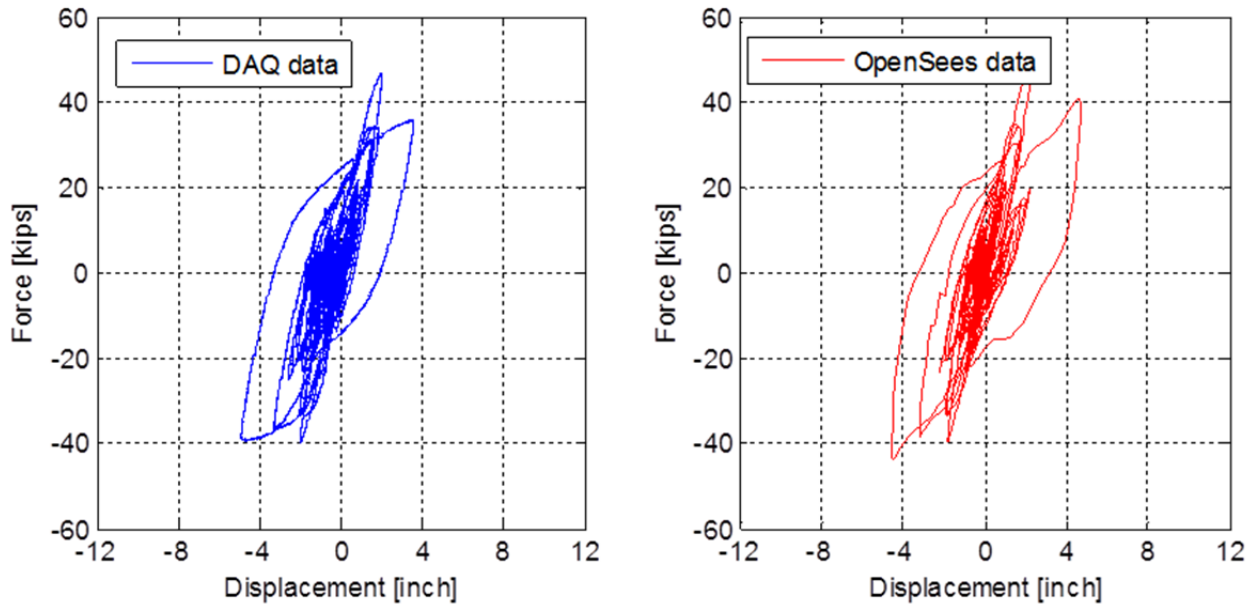
Figure 3.27   Comparison of force-displacement relationship for all HS test runs as obtained from the observed DAQ experimental test data and the recorded OpenSees data in the longitudinal direction.

63
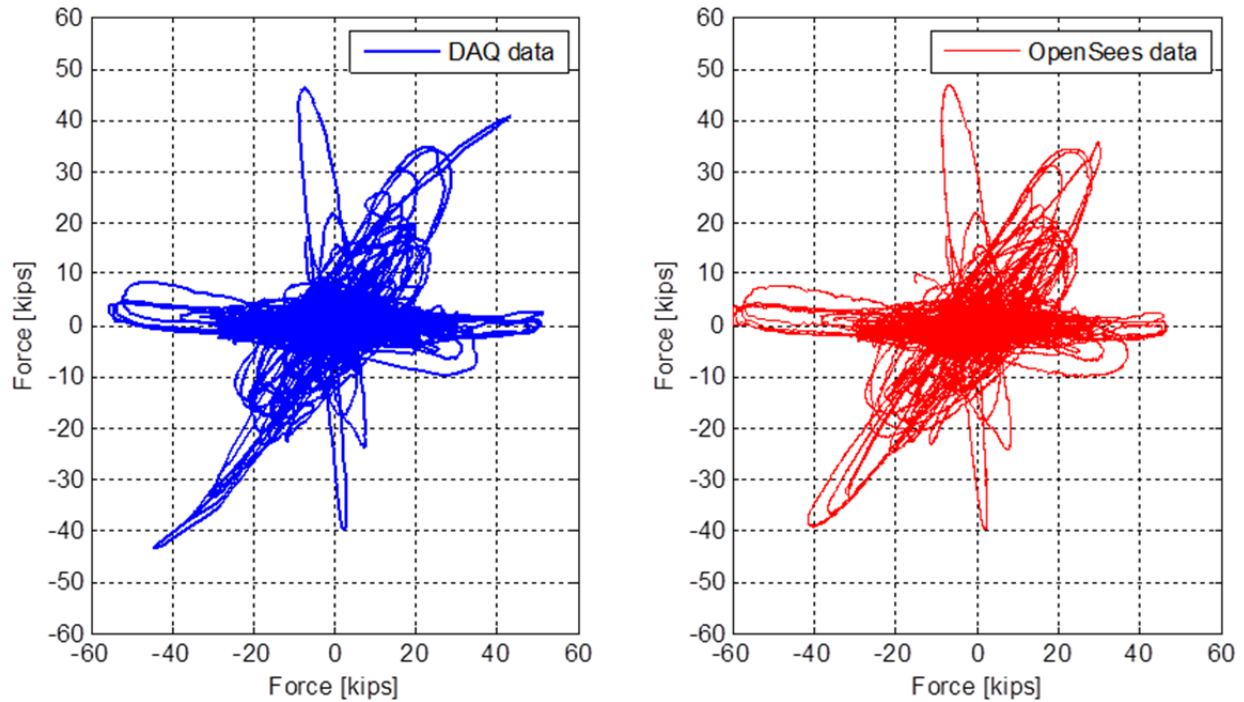
Figure 3.28 Comparison of the transverse-longitudinal force relationship for all HS test runs as obtained from the observed DAQ experimental test data and the recorded OpenSees data.

3.4 LOCAL BEHAVIOR OF COLUMN

The main objective of the experimental program is to evaluate the bent cap beam behavior and the effective slab width. The column local behavior from the as-built Specimen No. 1 tests was extensively discussed in the companion report; therefore only brief discussion of the column in the Specimen No. 2 HS tests is presented here in relation to the column reinforcement strain history, section moments and curvatures, and the CFRP jacket strains. A complementary discussion is presented in Section 3.7 where a comparison is made between the as-built and retrofitted behavior to evaluate the effectiveness of the retrofitting technique.

3.4.1 Strain History

No bar buckling or rupture took place during the HS test runs due to the confinement provided by the CFRP jacket. However, extensive yielding was observed in the instrumented column longitudinal reinforcement within the plastic hinge zone. Before presenting the strain history at the maximum strain location, the response of the four-column instrumented bars as they relate to the loading direction is presented in Figure 3.29. Figure 3.30 shows the strain history in the two bars that experienced the highest strain for all 15 Specimen No. 2 HS tests in the north and south directions. Similarly, Figure 3.31 shows the strain history for the east and west sides, where the strain in the east and west sides of the column reached much higher strain levels (as that was the direction where the transverse direction only large-scale runs were applied).

To study the extent of extensive yielding in the column in the transverse direction, the strain history in the east and west sides is plotted at two levels in addition to the level of maximum strain shown in Figure 3.31. One level is 18 in. from the face of the bent cap beam, which corresponds to the end of the anticipated plastic hinge zone in a conventional column without the CFRP jacket, as shown in Figure 3.32. The second level is at the column mid-height, as shown in Figure 3.33. Extensive yielding was observed throughout the anticipated plastic hinge region, while the column mid-height remained elastic as expected.
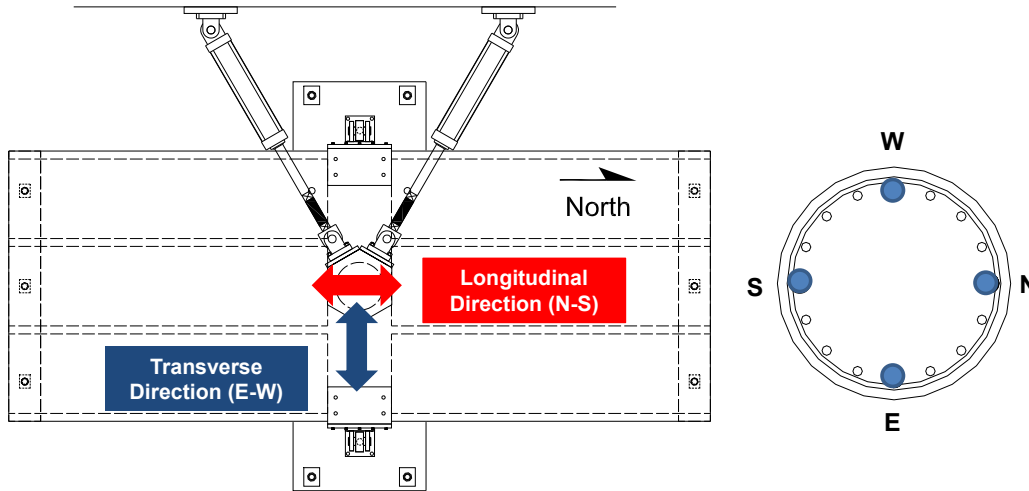
Figure 3.29 Layout of the instrumented column rebars in Specimen No. 2 as related to the loading directions.
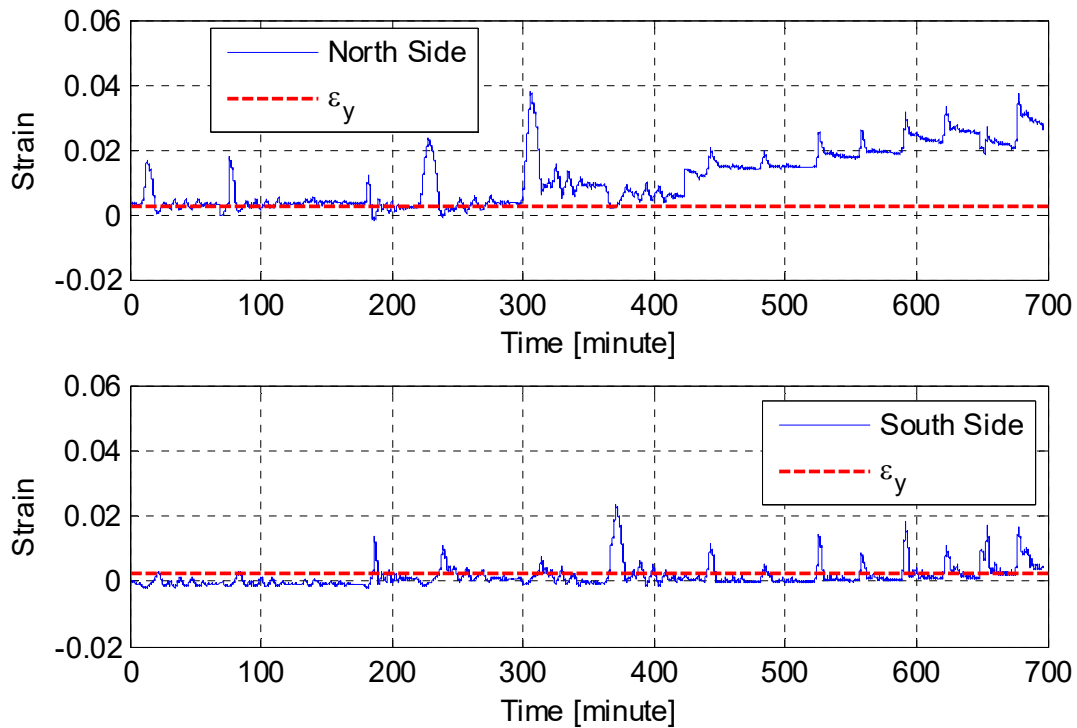
Figure 3.30 Strain history in north and south side column bars due to all HS tests at maximum strain location (close to the cap beam face).
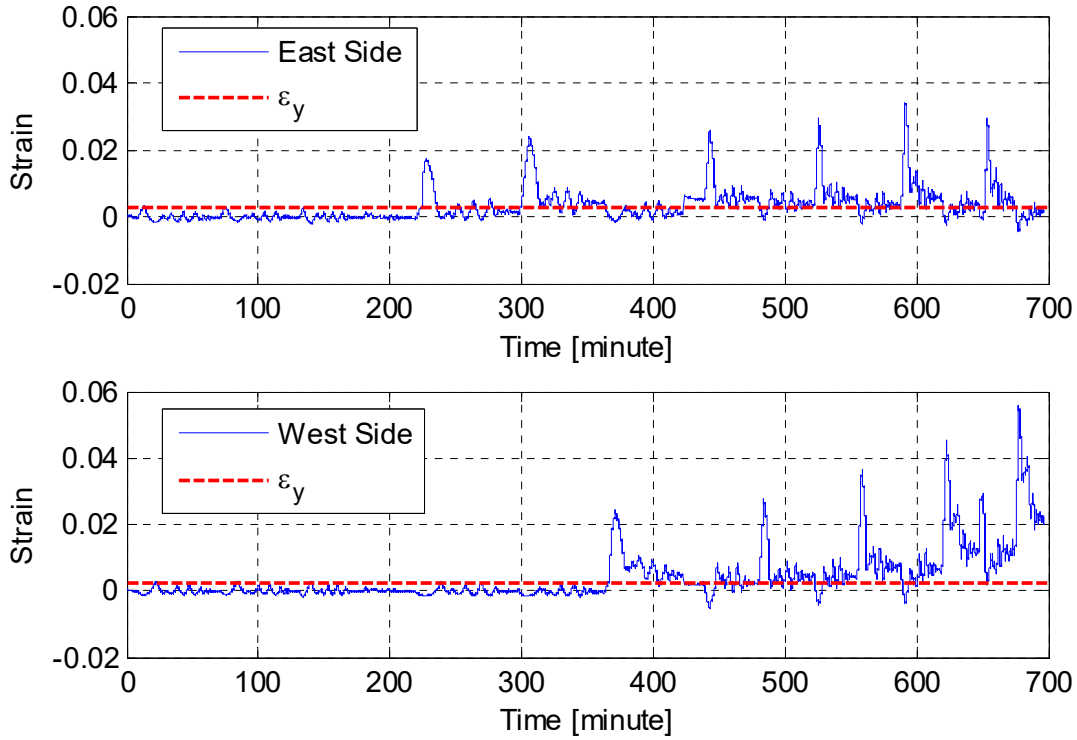
Figure 3.31   Strain history in the east and west side column bars due to all HS tests at maximum strain location (close to the cap beam face).
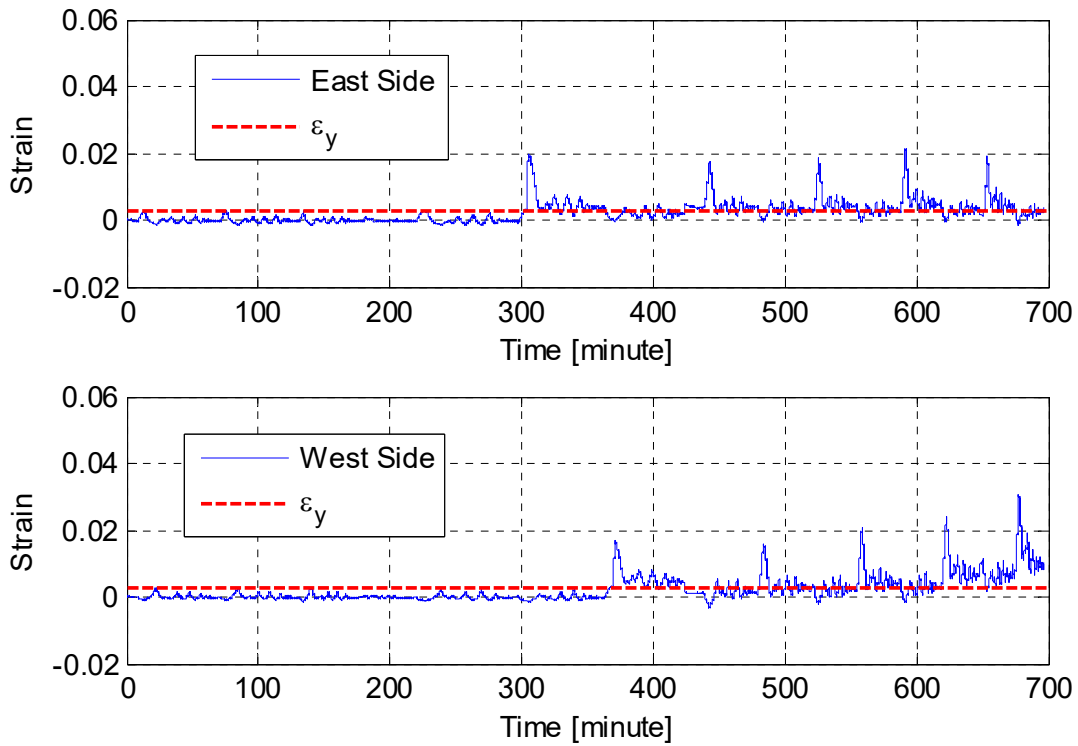
Figure 3.32   Strain history in the east and west side column bars due to all HS tests at height of 18 in. from the cap beam face.

66
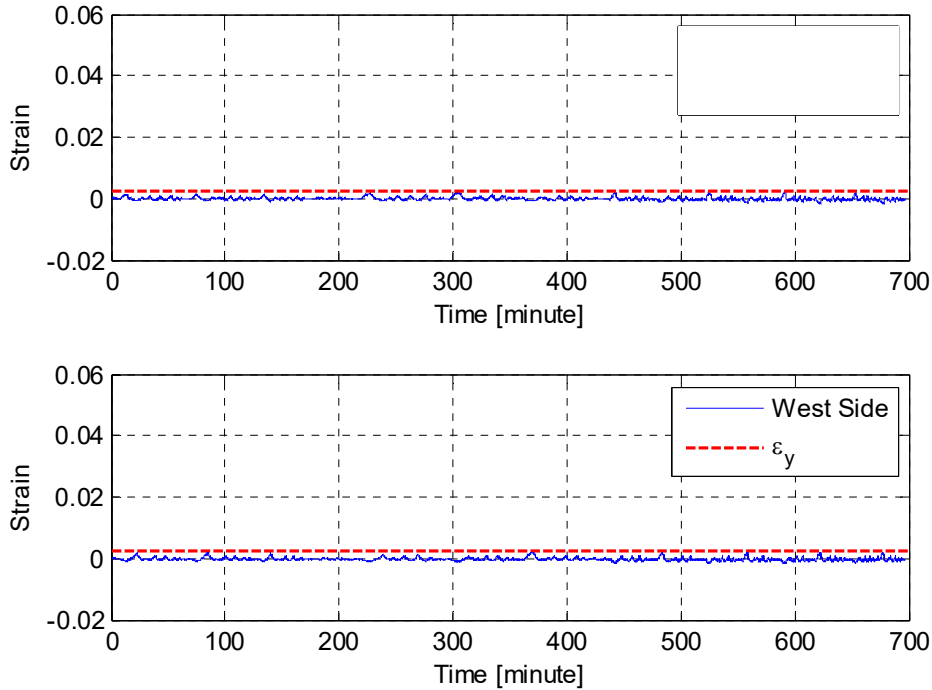
Figure 3.33   **Strain history in the east and west side column bars due to all HS tests at the column mid-height (51 in. from the bent cap beam face).**

3.4.2 Moment and Curvature History

The bending moment at the column-bent cap interface, where the maximum moment was expected, was estimated from the applied lateral force. Figure 3.34 shows the full history of the calculated column moment in both the transverse and longitudinal directions. A zoomed-in view of the column moment due to the large-scale transverse direction only HS tests is shown in Figure 3.35. (The maximum observed moment is compared to that of the as-built column in Section 3.7. Although the maximum moment can be considered larger than the yield moment, it cannot be claimed that this higher moment represented the retrofitted column moment capacity. The observed visual damage suggests that the system capacity was capped due to the bent cap beam concrete crushing manifested in the form of concrete cover spalling in the vicinity of the column.

The curvatures at various column sections were estimated during the HS test runs. A detailed discussion of the curvature distribution along the column height and a comparison between the strain-based versus the LVDT-based curvatures was previously presented in the companion report for the as-built Specimen No. 1 specimen. Thus, only the LVDT-based curvature history at the location of maximum expected curvature is shown in Figure 3.36 for all 15 Specimen No. 2 HS test runs in the transverse and longitudinal directions; a zoomed-in view of the curvature history for the transverse direction only large-scale runs is shown in Figure 3.37. As shown in this figure, the column section responded somewhat in the longitudinal direction, although loading was only applied in the transverse direction. That is attributed to the residual displacements (discussed earlier) that led a portion of the transverse loading to be accompanied with some loading in the longitudinal direction. The obtained curvatures at other column-height levels are presented in the next subsection.
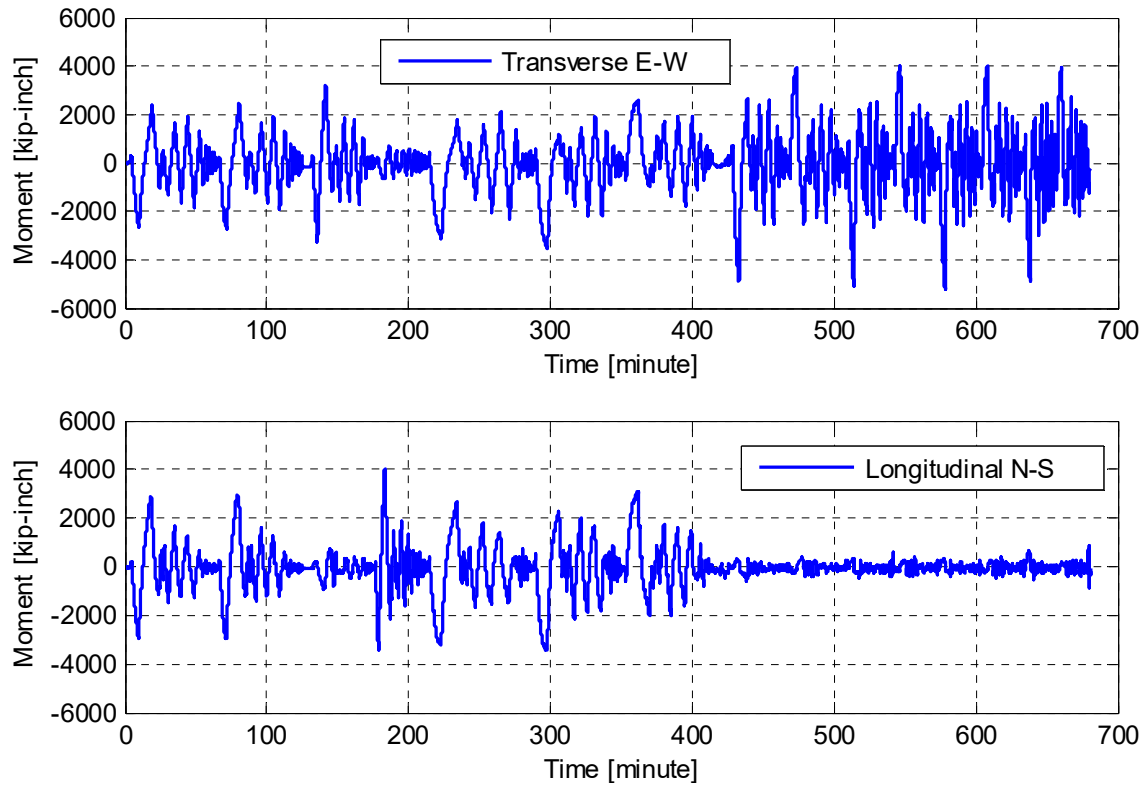
Figure 3.34 Column moment history at maximum location for all HS test runs.
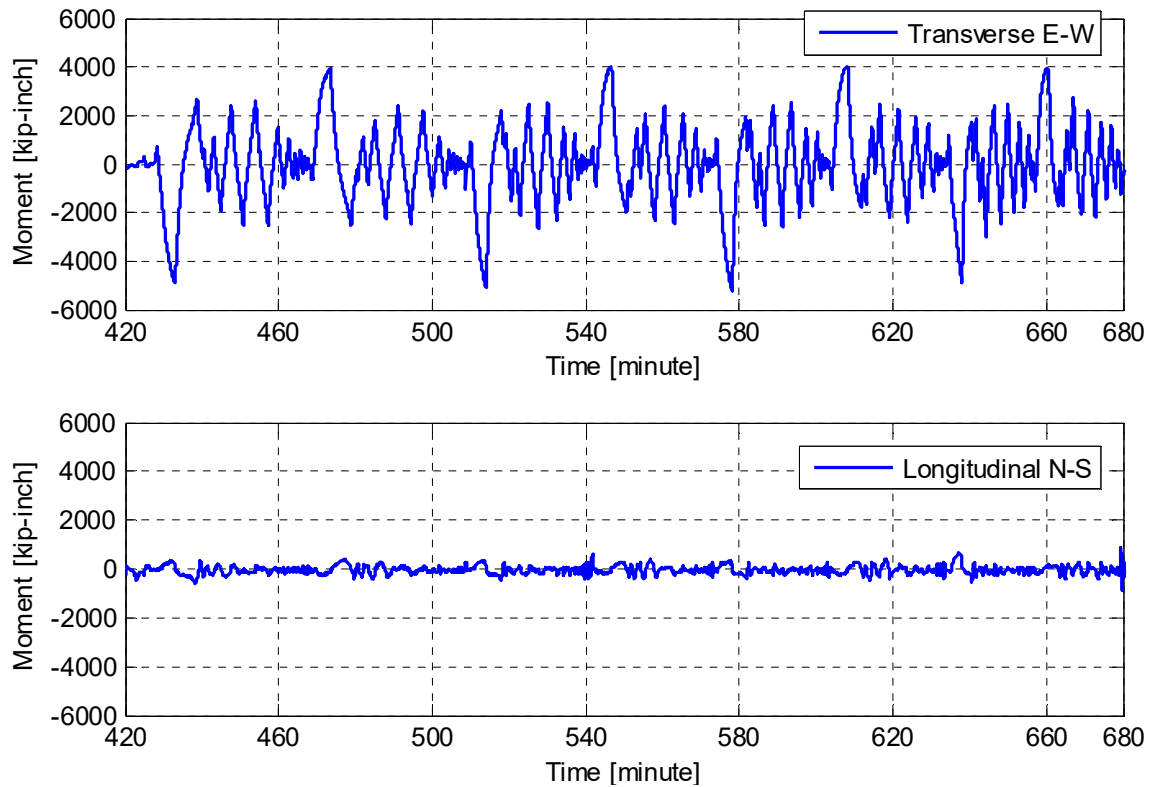
Figure 3.35 Zoomed-in view of the column moment history at maximum location for the large-scale transverse direction only HS test runs.
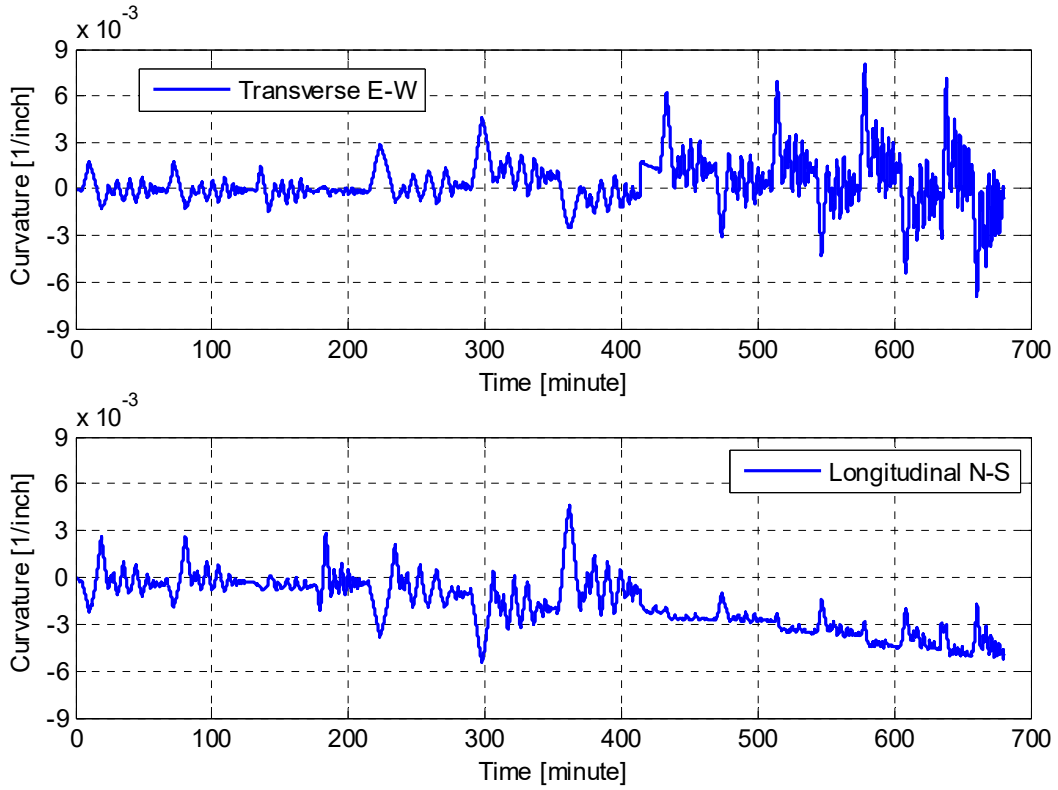
Figure 3.36 Column curvature history at maximum location for all HS test runs.
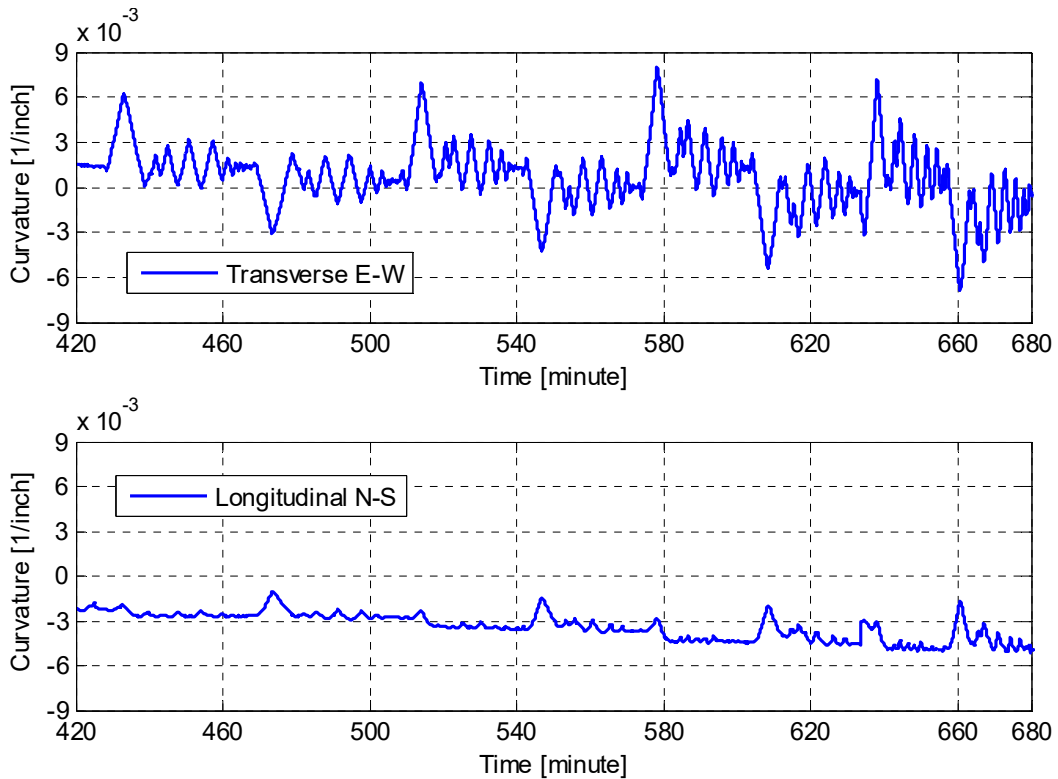
Figure 3.37 Zoomed-in view of the column curvature history at maximum location for the large-scale transverse direction only HS test runs.

3.4.3 Moment-Curvature Relationships

As previously mentioned, all the presented curvature measurements for the HS tests are based on the LVDTs measurements rather than strain measurements. As shown in Part I of this report, strain-based curvature calculations are not very reliable, especially at higher deformation levels. The moment-curvature relationships from bi-directional HS tests are presented separately from the large-scale transverse direction only runs to keep the plots simpler and more informative.

3.4.3.1 Bi-Directional Tests

Bi-directional HS tests applied loading in both the transverse and longitudinal directions simultaneously as a result of solving the MDOF computational model under two-component horizontal excitation. The moment-curvature relationship is compared for all bi-directional runs in the transverse and longitudinal directions at different levels along the column's anticipated plastic hinge zone. Figure 3.38 shows the moment-curvature relationship at the section of the anticipated largest moment and curvature, i.e., 4 in. from the cap beam face. Figure 3.39, Figure 3.40, and Figure 3.41 show the moment-curvature relationships at sections that were 10, 16, and 22 in. away from the bent cap beam face, respectively. Although the largest bi-directional HS test was conducted at 100%-scale, the column hysteresis was only pronounced within 10 in. from the cap beam face, i.e., no column damage extended through the entire conventional plastic hinge region up to the 100%-scale runs. As discussed below, when larger ground motion scales were applied, the hysteretic damage extended to larger height of the column.

In addition, the curvature values were slightly higher in the longitudinal direction than in the transverse direction for comparable moment demands. This led to wider hysteresis moment-curvature loops in the longitudinal direction and more energy dissipation than the transverse direction; see Figure 3.38.
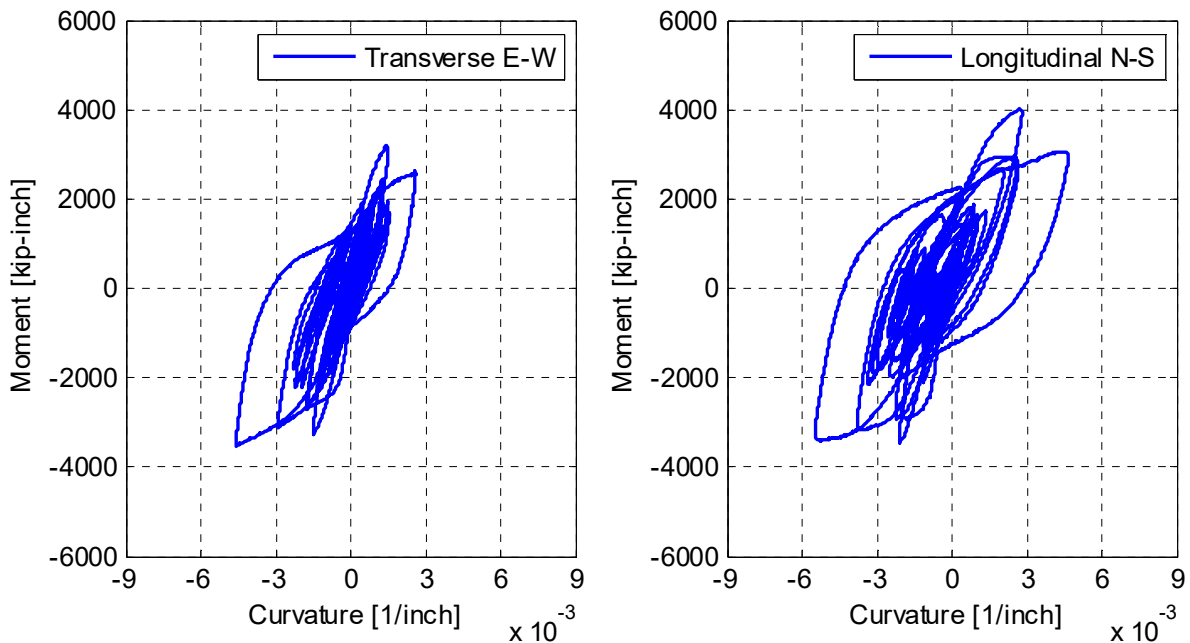
Figure 3.38   Column moment-curvature relationship in transverse and longitudinal directions at 4 in. from the cap beam face for all bi-directional HS test runs.
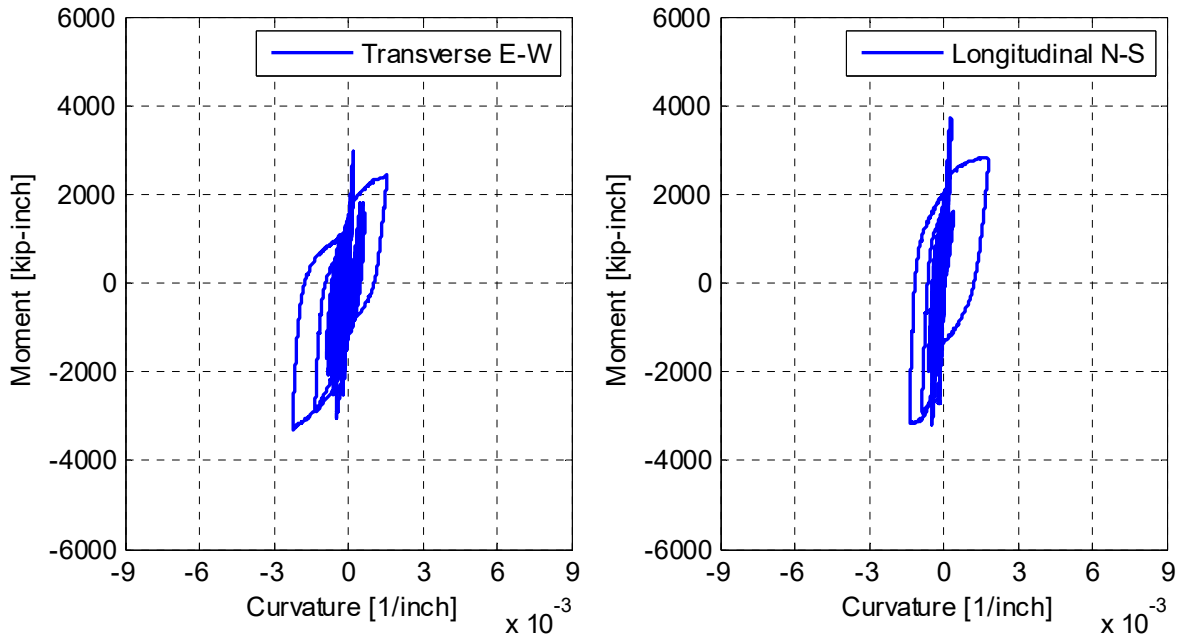
Figure 3.39   Column moment-curvature relationship in transverse and longitudinal directions at 10 in. from the cap beam face for all bi-directional HS test runs.
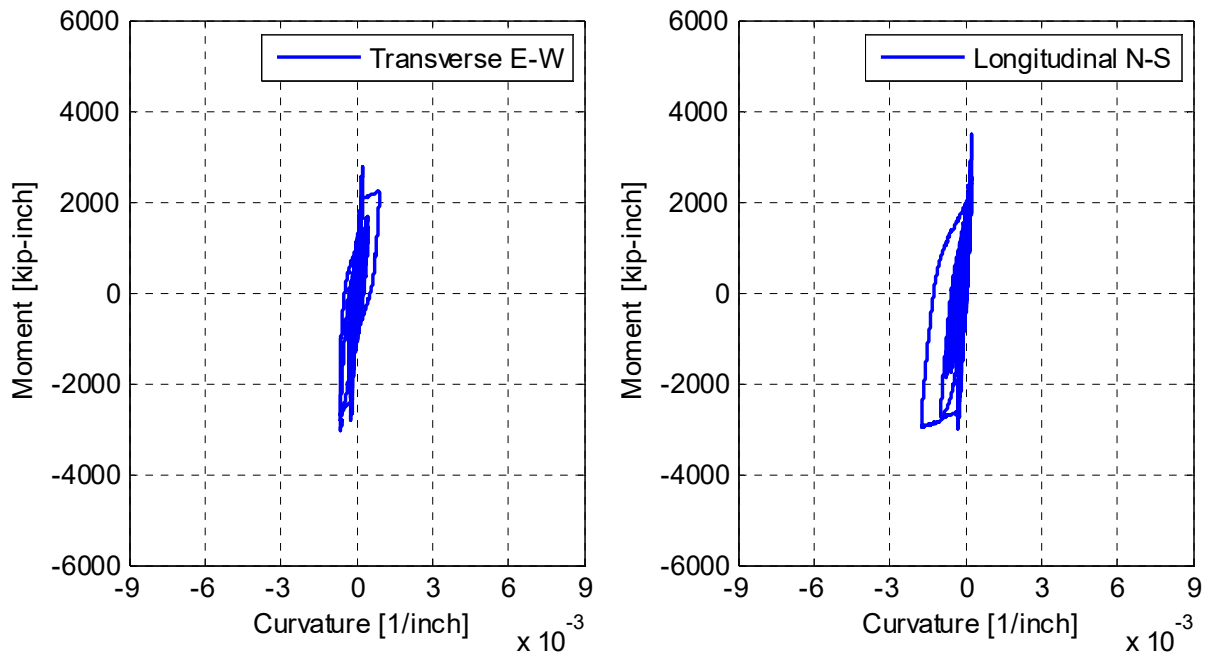
Figure 3.40   Column moment-curvature relationship in transverse and longitudinal directions at 16 in. from the cap beam face for all bi-directional HS test runs.
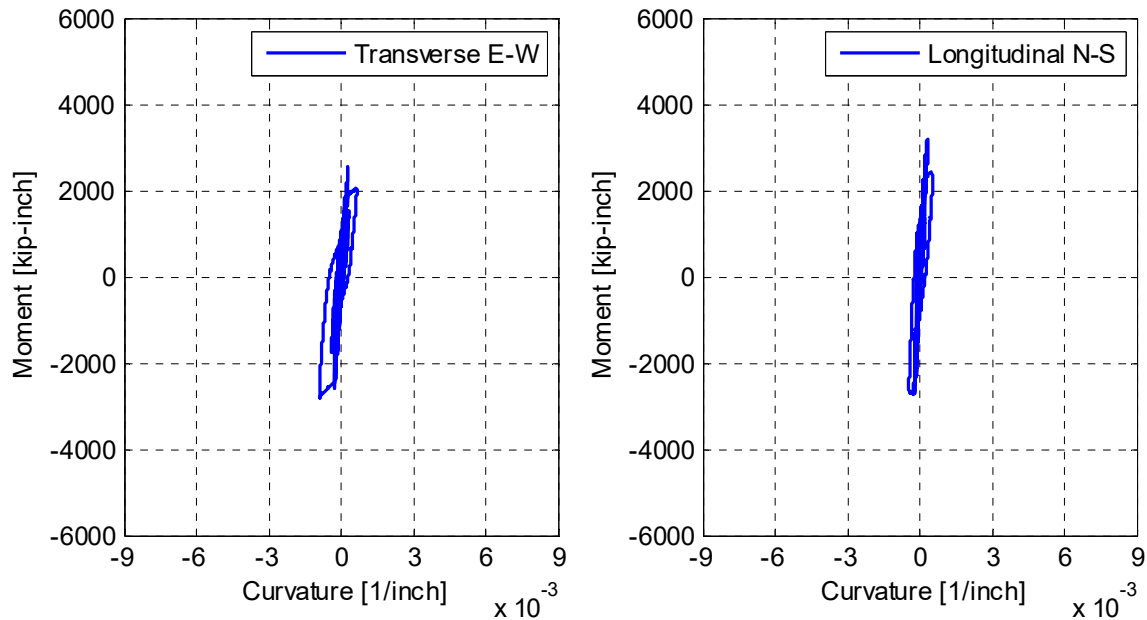
Figure 3.41   **Column moment-curvature relationship in transverse and longitudinal directions at 22 in. from the cap beam face for all bi-directional HS test runs.**

3.4.3.2 Transverse direction only Tests

The moment-curvature relationships for the large-scale eight HS runs that applied the transverse direction only Rinaldi ground motion scaled at 125% through 200% in positive and negative directions are shown here (Figure 3.42 through Figure 3.46). Since the ground motion was applied only in the transverse direction, the moment-curvature in the transverse direction only is discussed. As above, the moment-curvature relationship is plotted at various sections along the column height to explore the extent of the hysteresis damage in the column; this was done because visual evidence was not possible because of the confining CFRP jacket. Five levels at 4, 10, 16, 22, and 51 in. away from the cap beam face were used to generate the moment-curvature relationship in the transverse direction, as presented in Figure 3.42 to Figure 3.46, respectively.

Note that the hysteresis damage was extensive at the largest measured moment and curvature location, i.e., 4 in. from the cap beam face. In addition, Figure 3.42 shows that higher moments were reached in one side of the column than the other; this is attributed to the nature of the HS loading along with the accumulated residual displacement in a certain direction, which generated displacement input loading of less value in one direction than the opposite one. It is unclear from the observed moment values that the column reached its capacity, as visual evidence during the test suggested that the system force capacity was capped due to the onset of the concrete crushing in the compression zone of the bent cap beam, as previously stated. More details about the observed damage were presented earlier in Section 3.2.

When the CFRP jacket was removed, only a uniform pattern of flexural cracks were observed that extended to a region of almost 20 in., which roughly corresponded to the conventional plastic-hinge length in columns without CFRP jackets. The moment-curvature relationships confirm that the hysteresis damage extended throughout the plastic-hinge length, as

shown in Figure 3.42 through Figure 3.45; as shown in Figure 3.46, however, the column remained elastic at the mid-height, as previously observed from the strain values.
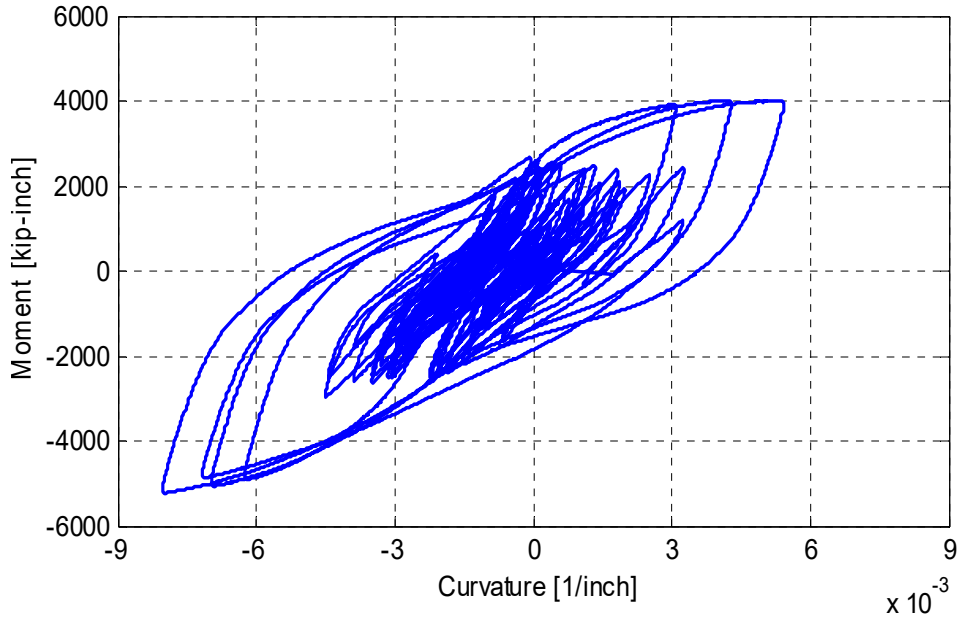
Figure 3.42 Column moment-curvature relationship in the transverse direction at 4 in. from the cap beam face for the large-scale transverse direction only HS test runs.
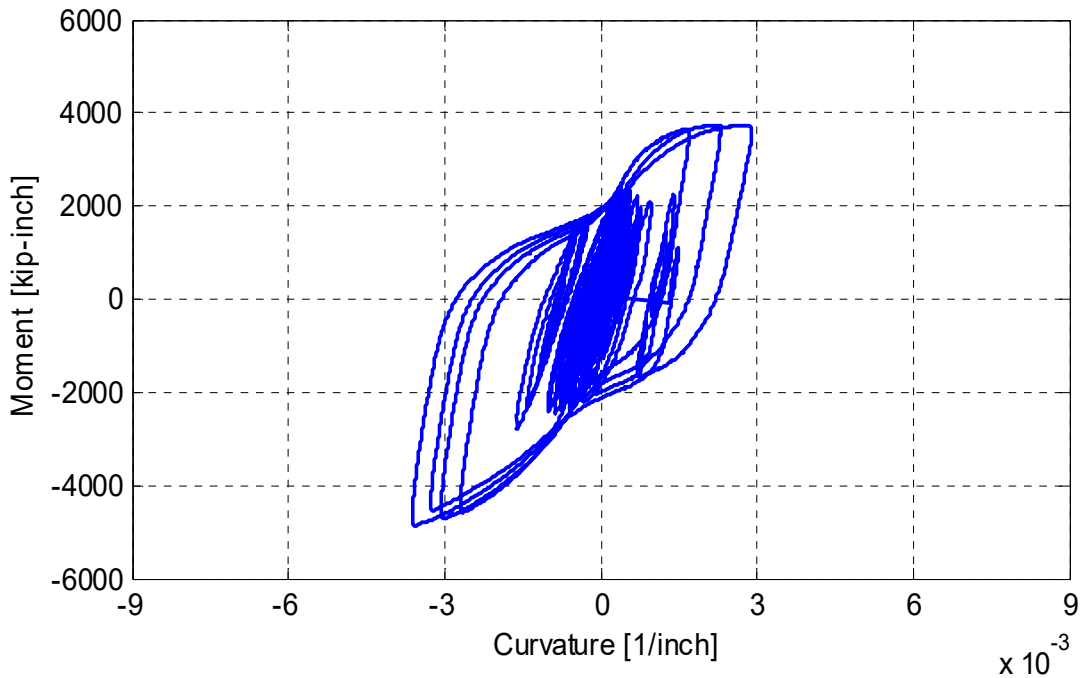
Figure 3.43 Column moment-curvature relationship in the transverse direction only at 10 in. from the cap beam face for the large-scale transverse direction only HS test runs.
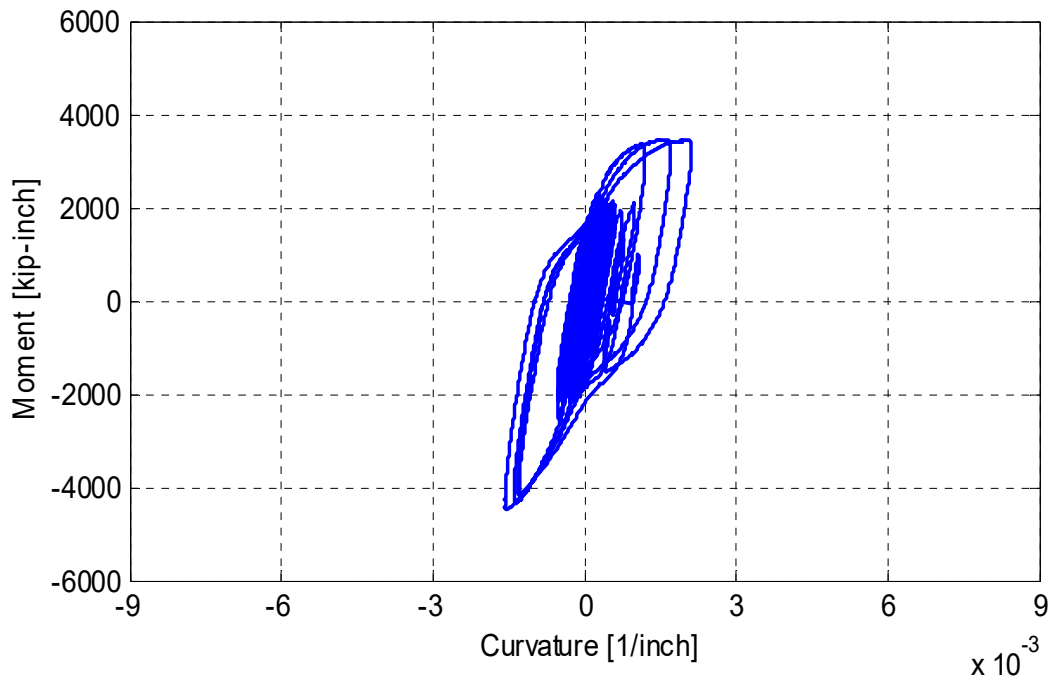
Figure 3.44   Column moment-curvature relationship in the transverse direction only at 16 in. from the cap beam face for the large-scale transverse direction only HS test runs.
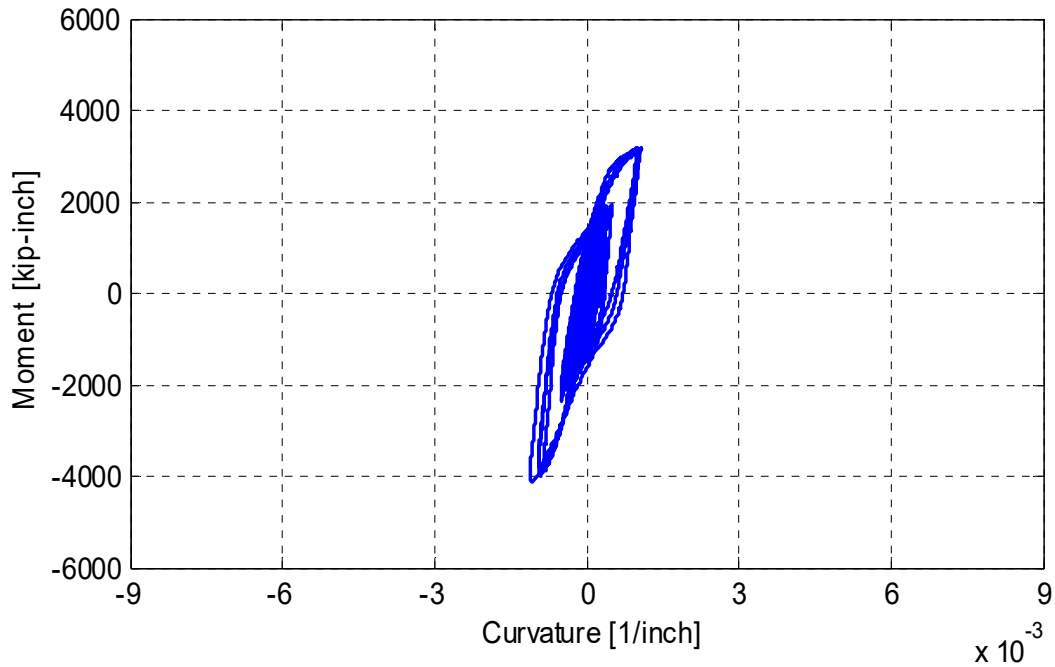
Figure 3.45   Column moment-curvature relationship in the transverse direction only at 22 in. from the cap beam face for the large-scale transverse direction only HS test runs.
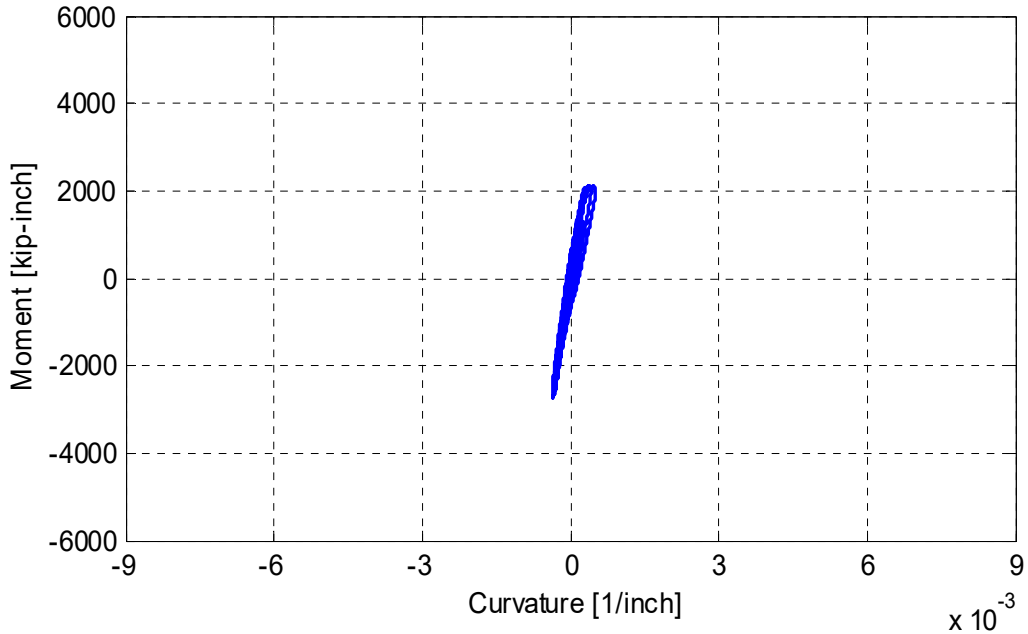
Figure 3.46 Column moment-curvature relationship in the transverse direction at the column mid-height for the large-scale transverse direction only HS test runs.

3.4.4 CFRP Jacket Strain

The second specimen differed from the originally identical first specimen because of the CFRP retrofit of the column. One central response quantity of interest for column retrofitted using CFRP jacket is the confinement effectiveness due to the jacket. For this reason, several strain gages were installed around the circumference of the jacket at two levels 18 in. apart within the typical plastic-hinge length. The first level was at 2 in. from the cap beam face. Each level was instrumented with 12 strain gages, as shown in Figure 3.47.
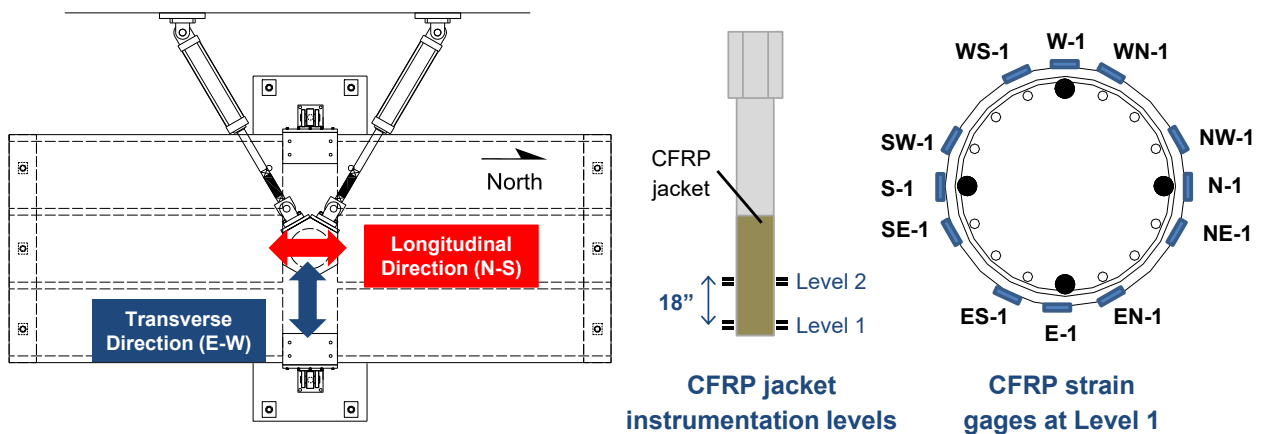
Figure 3.47 Layout of the CFRP jacket strain gages as related to the loading directions.

75

The confining strain history at the outermost east and west sides of the first instrumentation level of the CFRP jacket, designated as E-1 and W-1 in Figure 3.47, is shown for all 15 HS test runs in Figure 3.48. Similarly, the strain history at the north and south strain gages, designated as N-1 and S-1, is shown in Figure 3.49 for all HS test runs. The peaks observed in the confining strain history suggest that the jacket responded effectively to the loading when a larger confining strain developed at the compression side of the column relative to a certain loading direction. This is because as the increase in the compressive stress in one column side under combined axial and bending action might cause bar buckling, which was restrained by the concrete cover, that in turn was well-confined by the CFRP jacket. Thus, any desired expansion in the concrete cover is outweighed by the confining CFRP jacket as long as the jacket remains intact and effective.

A similar observation can be better demonstrated if the strain profile at a certain time instant at a given section in the CFRP jacket is graphically presented. Kumar et al. [2014] provided a novel approach to plot the recorded strain values at a given time instant for all strain gages in a given instrumentation level. The same approach is used to produce polar profiles of the confining strain around the entire jacket circumference, as shown in Figure 3.50 to Figure 3.52. Figure 3.50 shows the confining strain profiles from each of the 12 installed strain gages at the two instrumentation levels when the displacement amplitude was reached during the negative 100% bi-directional test (ID 7); however, Figure 3.51 and Figure 3.52 show the strain profiles at the displacement amplitude of the positive 175% (ID 12) and 200% (ID 14) transverse direction only HS tests, respectively. Note that the confining strain was much less at the second instrumentation level, i.e., as expected, the confining strain decreased with the decrease of the moment and stress demands. The profiles also point in a certain direction where the maximum compressive stress developed. In the bi-directional tests, it is implied that concrete expansion took place at both of the transverse and longitudinal directions, whereas the maximum strain at concrete expansion was aligned with the uni-directional transverse direction loading tests.
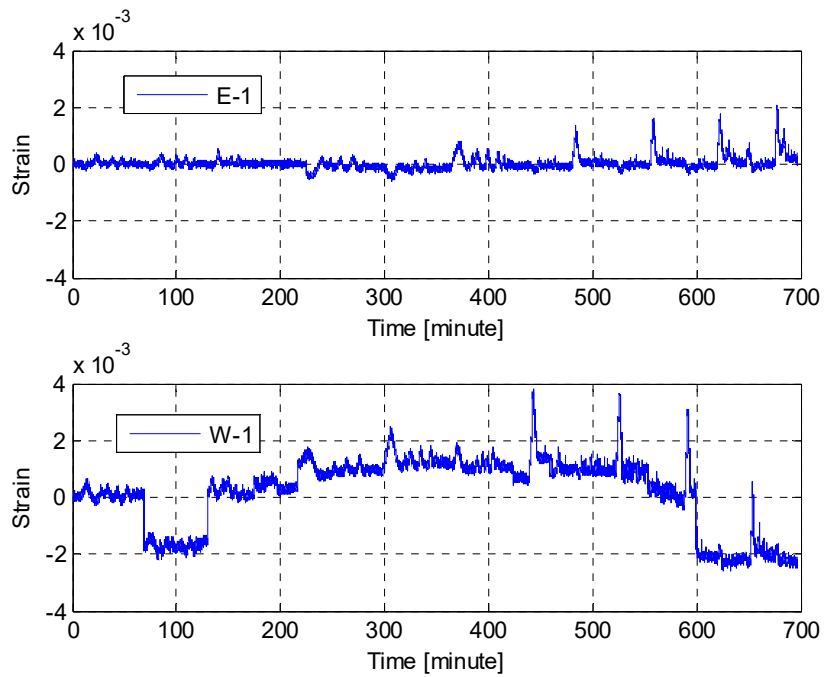
Figure 3.48   Confining strain history in the CFRP jacket east and west sides for all HS test runs.
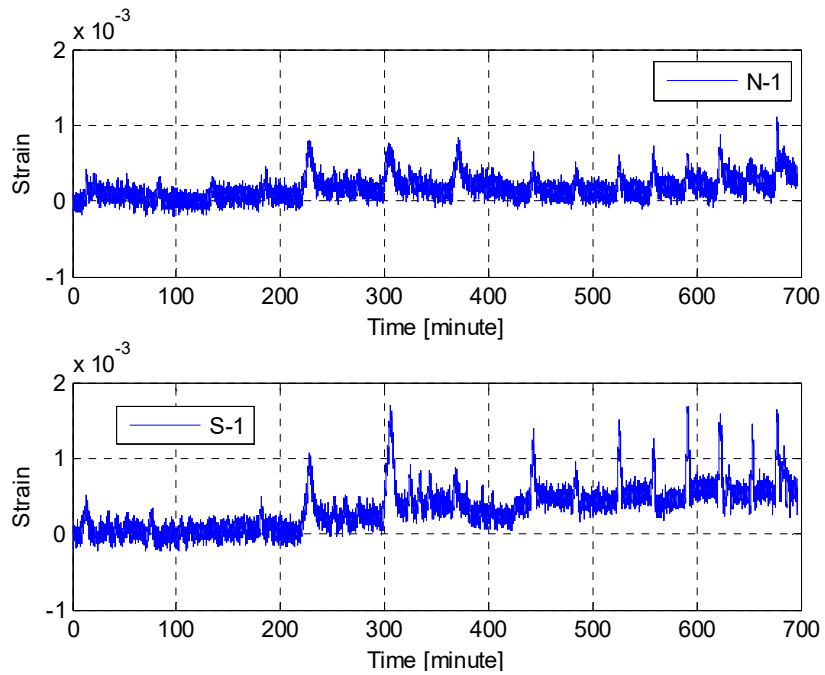
Figure 3.49   Confining strain history in the CFRP jacket north and south sides for HS test runs.
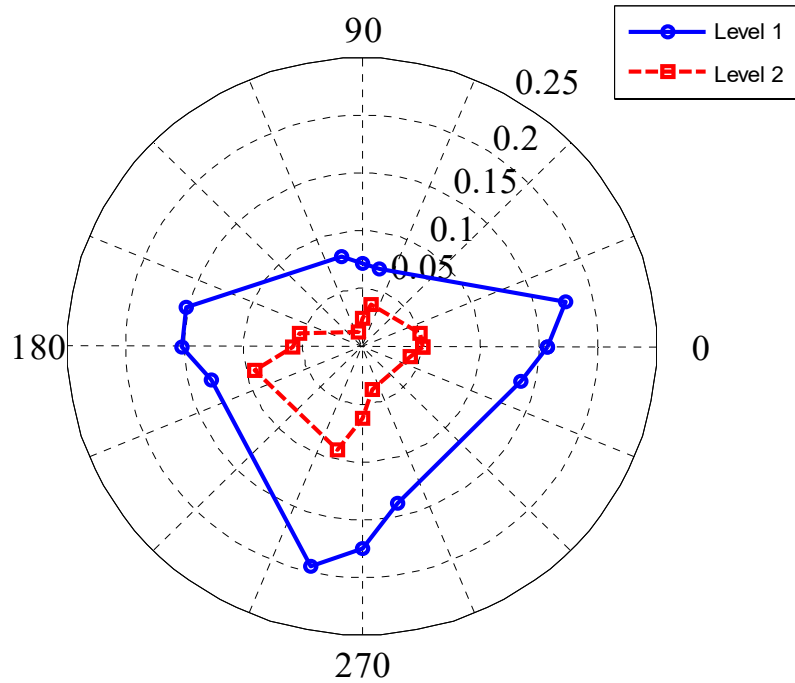
Figure 3.50   CFRP jacket confining strain profile [%] at the instant of displacement amplitude due to the 100%-scale bi-directional HS test (ID 7) for the two instrumented levels.
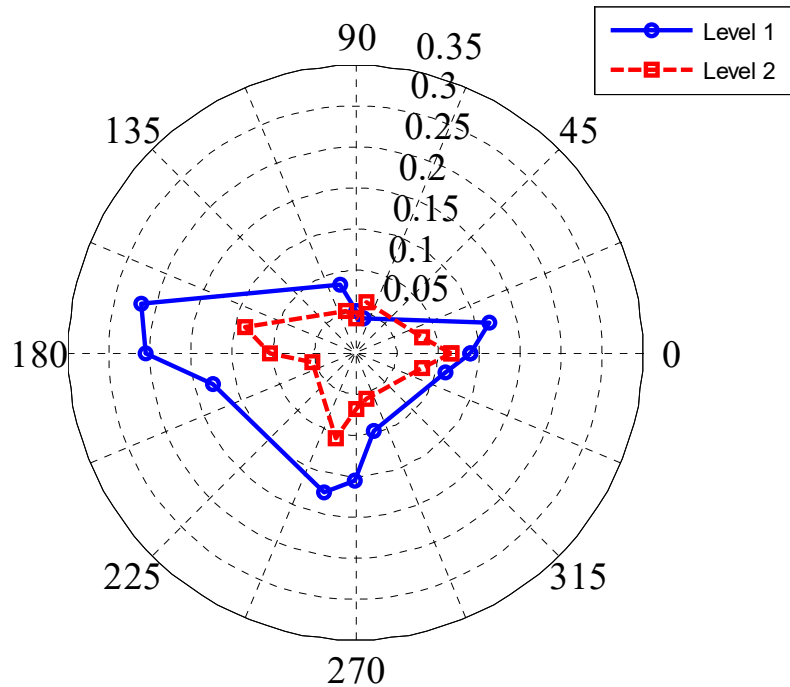
Figure 3.51   CFRP jacket confining strain profile [%] at the instant of displacement amplitude due to 175%-scale transverse direction only HS test (ID 12) for the two instrumented levels.
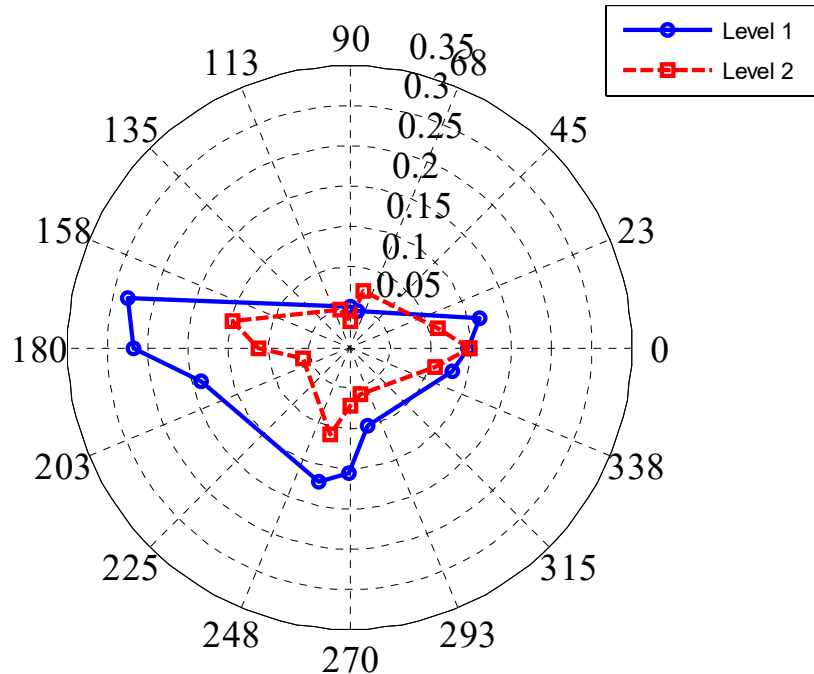
Figure 3.52   **CFRP jacket confining strain profile [%] at the instant of displacement amplitude due to 200%-scale transverse direction only HS test (ID 14) for the two instrumented levels.**

3.5 BENT CAP LOCAL BEHAVIOR

The main objective of this study is to evaluate the contribution of the box-girder slabs to the cap beam behavior and the capacity of the cap beam and its mode of failure. Thus, the strain, moment, and curvature histories at both Sections B and D are discussed in this section. In addition, the moment-curvature relationship is presented where the cap beam moment capacity is estimated.

3.5.1 Strain History

Extensive yielding was observed in the bent cap beam during the HS test runs. A sample of the strain history in one of the instrumented cap beam bottom rebars at Sections B and D, where maximum strains along the beam length were recorded, is shown in Figure 3.53 and Figure 3.54, respectively, for all 15 HS test runs. Figure 3.53 relates the strain evolution to the main phases of the bi-directional testing, increasing the gravity load to the 15% level, and the large-scale transverse direction only HS testing. It is shown that the bi-directional tests led to the onset of the bent cap beam yielding, i.e., the observed strain values exceeded the 0.0026 yielding strain of the used reinforcing bars. An immediate significant increase in the strains at Section B were observed as the 15% gravity load level was applied, whereas a more gradual increase was observed at Section D. Testing was conducted in two days, where the specimen was unloaded after the set of the bi-directional HS test runs was concluded in the first day of testing. For the second day of testing, the application of the 15% gravity load started from zero and was then followed by the eight large-scale transverse direction only HS test runs. A comparison of Figure

3.53 and Figure 3.54 show increased the strain values more significantly at Section D than Section B. Note that up to 2% strain was observed in the bent cap reinforcement in the tension side during the retrofitted Specimen No. 2 HS test runs, whereas only up to 1.3% strain was observed during the as-built Specimen No. 1 cyclic tests. This reflects the higher moment demands in the case of the HS tests of Specimen No. 2 compared to the cyclic tests of Specimen No. 1.

Another way of looking at the measured strains in the cap beam is to plot it against the progressing lateral load. The maximum strain measured at Sections B and D is plotted against the lateral transverse force in Figure 3.55 and Figure 3.56, respectively. The strain evolving at zero lateral force corresponds to the strains resulting from the gravity load application, as illustrated in Figure 3.55 and Figure 3.56; note that the application of the 15% gravity load level on the already yielded cap beam increased the strains significantly. Figure 3.53 and Figure 3.54 also show that a jump in the strain took place at the start of each new HS test run. This was mainly attributed to the pulse-nature of the used Rinaldi ground motion where a large pulse was applied, causing the strain value to increase significantly, which was then followed by small cycles that followed an almost bilinear path as the loading progressed and reversed.
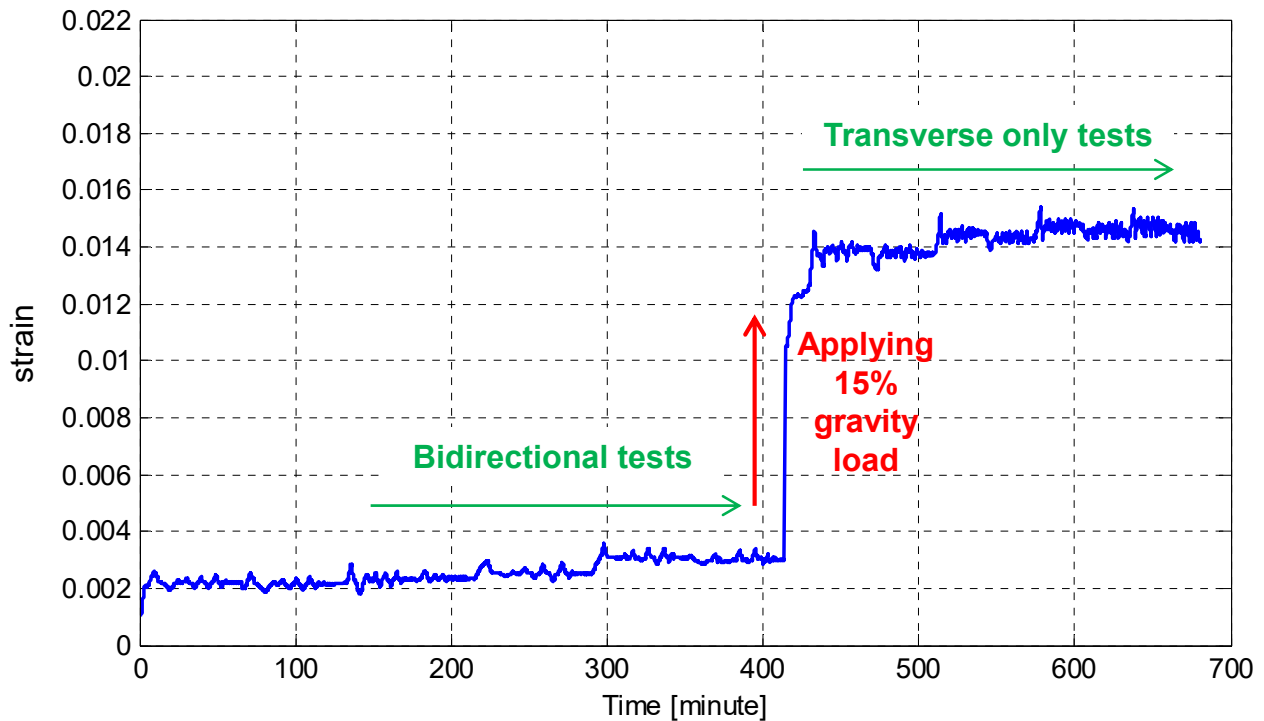
Figure 3.53   Bent cap beam strain history at Section B due to all HS runs.
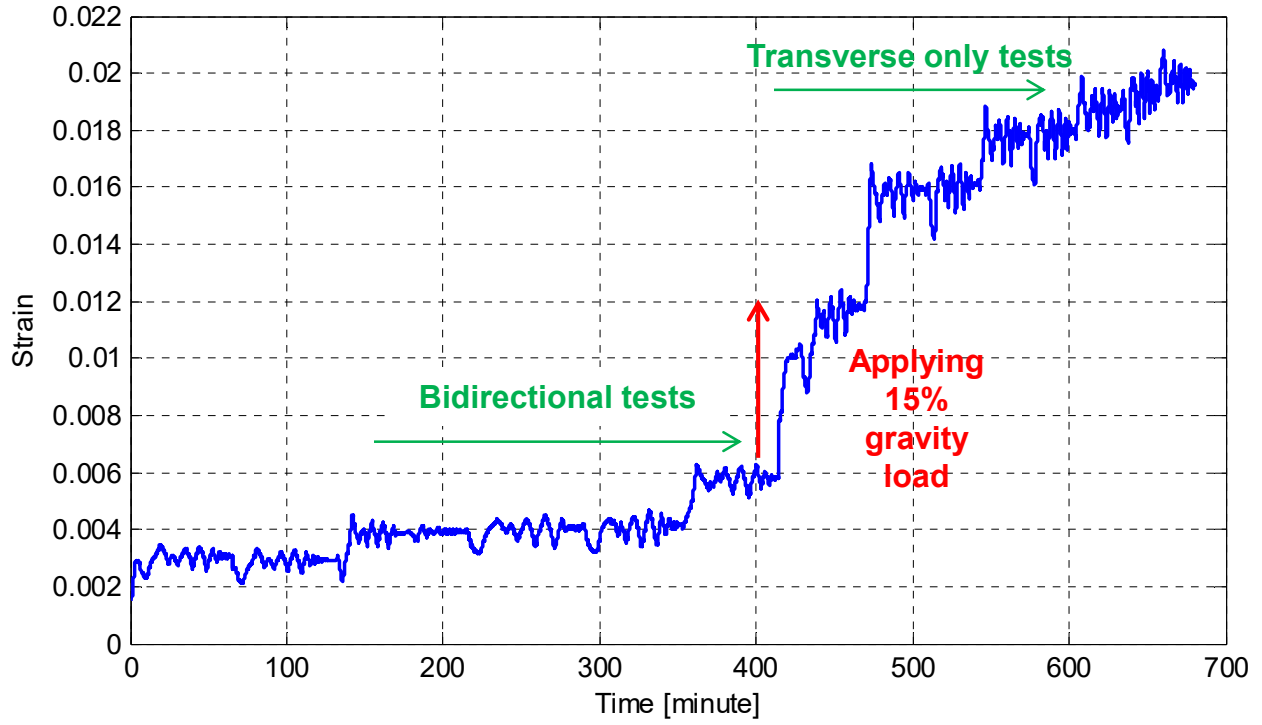
Figure 3.54   **Bent cap beam strain history at Section D due to all HS runs.**
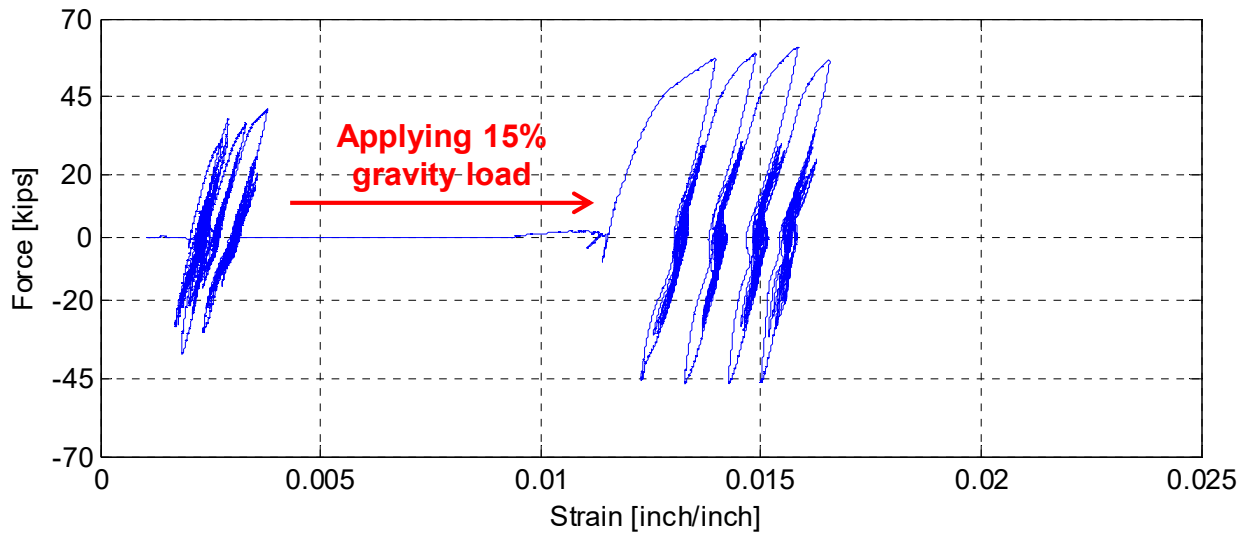
Figure 3.55   **Global lateral force-strain relationship at Section B of the bent cap beam due to all HS runs.**
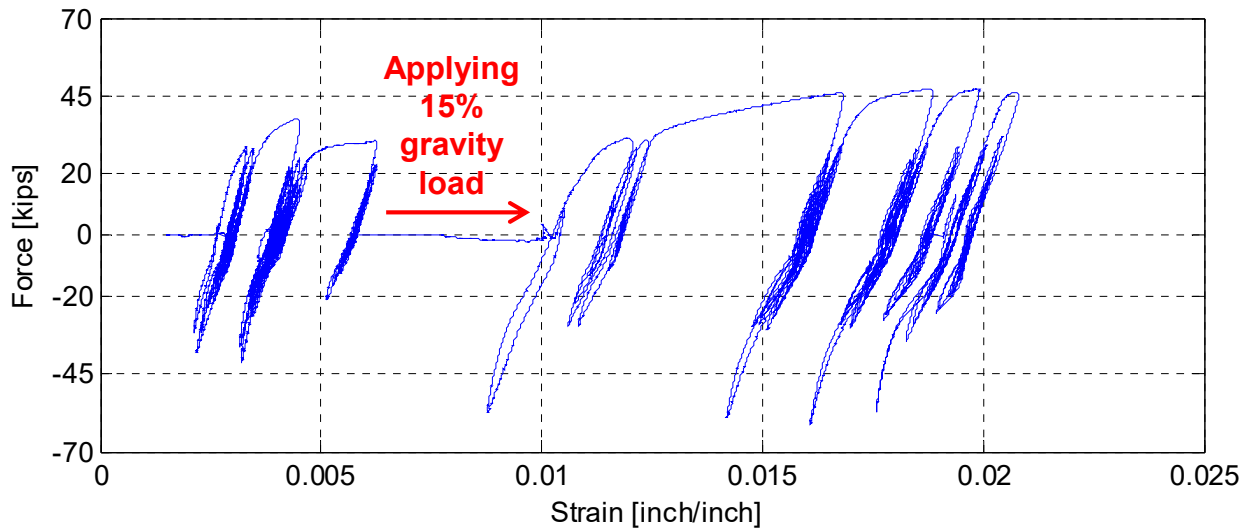
Figure 3.56 **Global lateral force-strain relationship at Section D of the bent cap beam due to all HS runs.**

3.5.2 Moment and Curvature History

Although the strains are important to investigate partial section or localized behavior of the bent cap beam, the bending moments are more descriptive of the full bent cap section behavior. The bending moments in the bent cap beam were estimated using the calibrated end struts; see Part 1. The bent cap beam moment history at Sections B and D for all the HS test runs is shown in Figure 3.57. Much higher moments were observed in the bent cap beam in the HS test runs when compared to the case of the first specimen's cyclic tests. The bent cap was subjected to higher bending moment demands using higher gravity load level and the undertaken retrofit scheme; this successfully increased the column capacity and, in turn, the bent cap demands. The observed capped value of the bent cap moment of approximately 6500 kip-in., along with the compression zone concrete crushing, suggests that this moment value can be reasonably considered the overall bent cap beam capacity. The exact value of 6535 kip-in. was considered the experimentally-determined bent cap beam flexural capacity.

As standard practice in this study, the total bent cap beam moment combined from Sections B and D was compared to the column bending moment; see Figure 3.58. This verifies the results obtained from bent cap beam bending moments based on the observation that the box-girder torsional stiffness in the cracked status after loading attracted small part of the moments applied to the superstructure through the column. In other words, almost the whole lateral transverse column moment was transferred as flexural moment to the bent cap beam only.
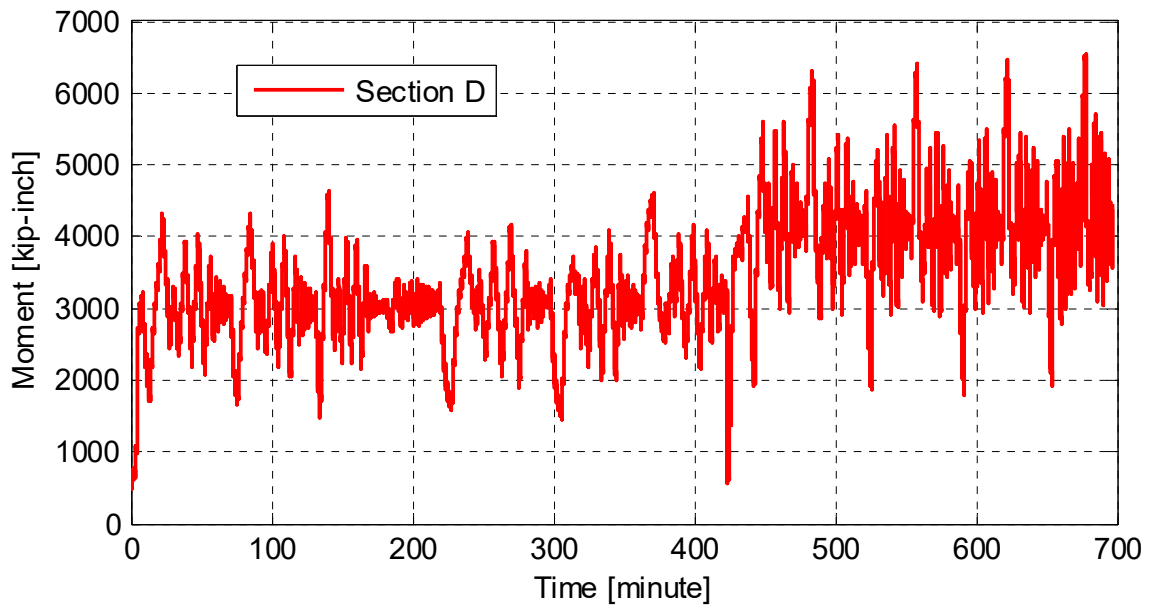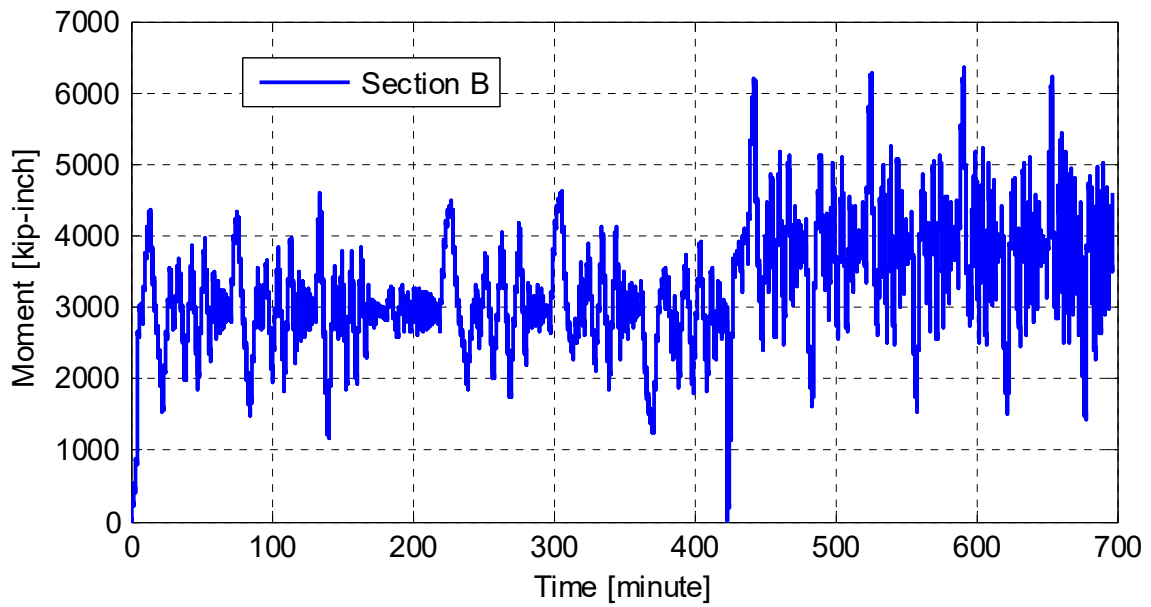
Figure 3.57   Bent cap beam moment history at Sections B and D for all HS runs.
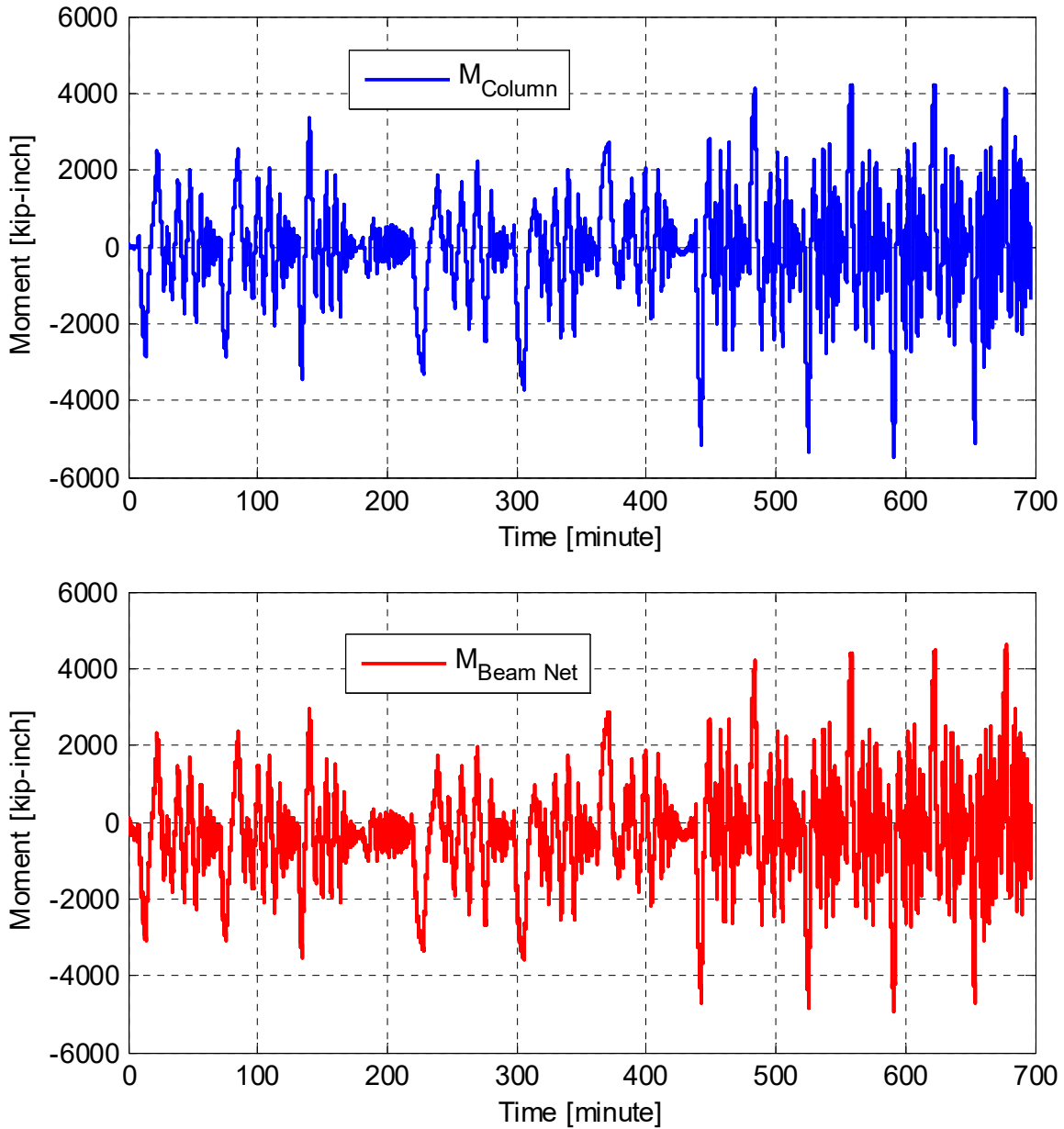
Figure 3.58 Comparison of the total bent cap beam moment at both Sections B and D combined versus the column moment history.

For a complete description of the bent cap Section Behavior, the curvature values were deduced from the observed strain in the bent cap top and bottom instrumented rebars. The procedure for estimating strain-based curvatures was previously discussed in Part 1. Note that the more accurate method of estimating a given section's curvature using LVDTs was not practical in the case of the bent cap. The history of the estimated curvatures from using one set of rebars at Sections B and D is shown in Figure 3.59 and Figure 3.60, respectively. The estimated moments and curvatures were used to generate the moment-curvature relationships at both Sections B and D, as discussed next.
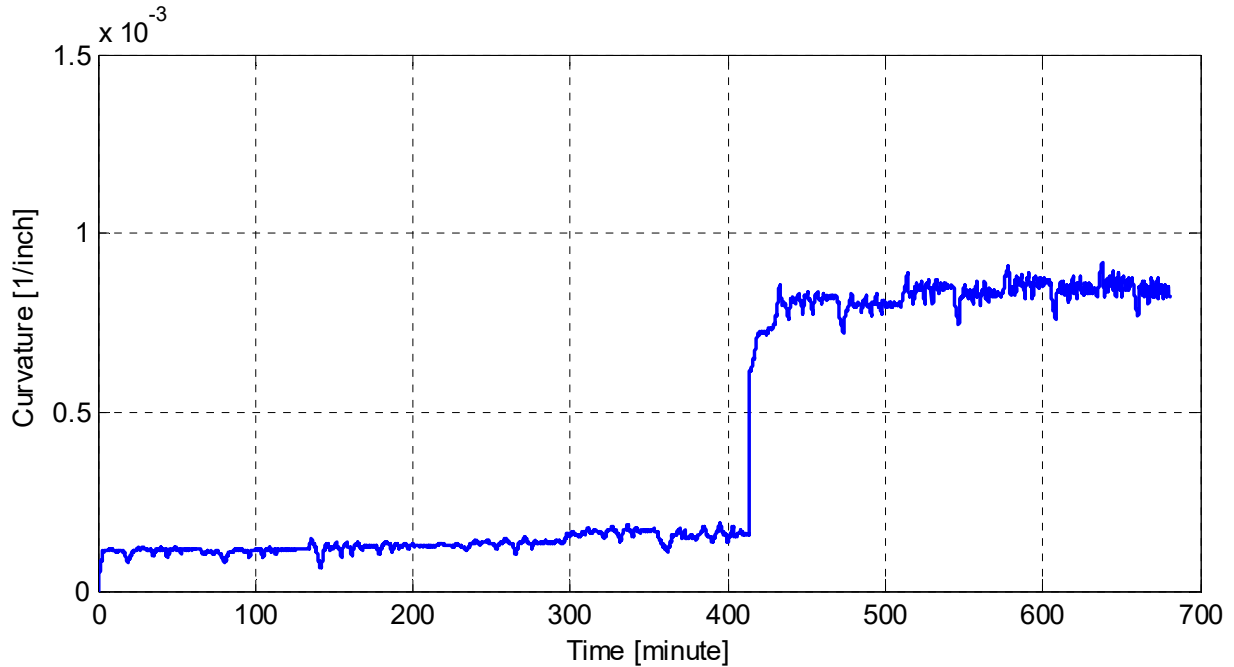
Figure 3.59   Bent cap beam curvature history at Section B due to all HS runs.
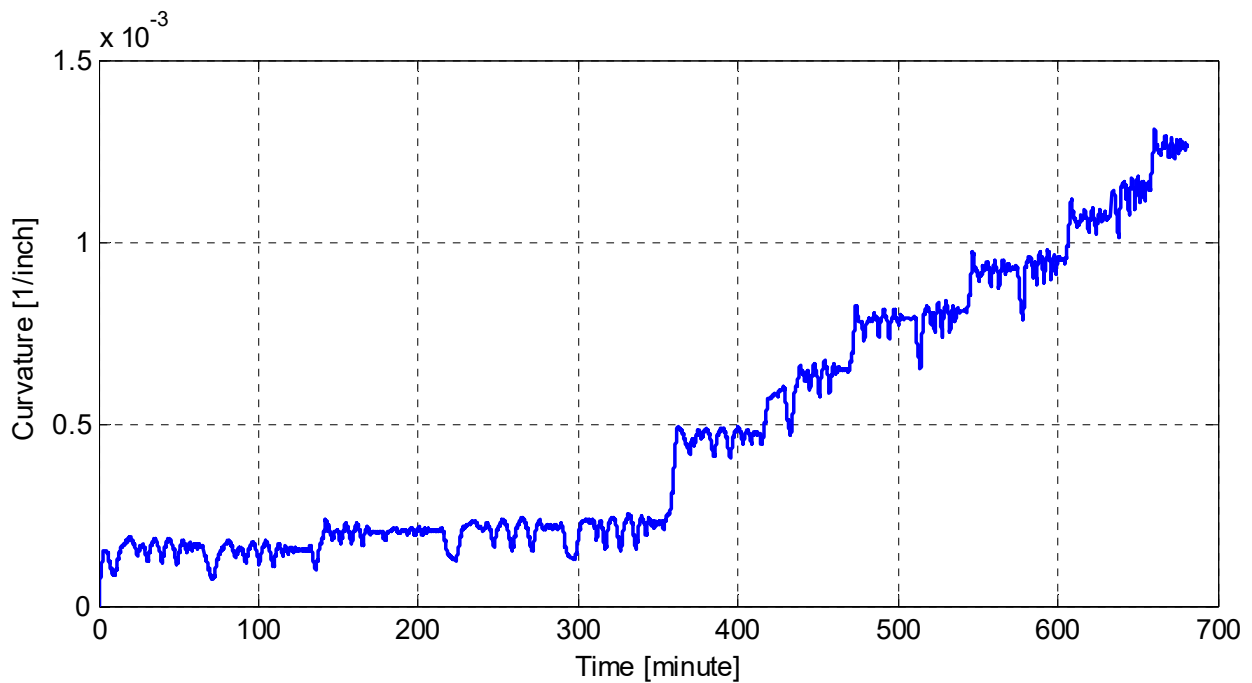
Figure 3.60   Bent cap beam curvature history at Section D due to all HS runs.

3.5.3 Moment-Curvature Relationship

Once the bending moment is obtained, it is useful to investigate the overall bent cap response by plotting it against the section curvatures estimated earlier. Figure 3.61 and Figure 3.62 show the moment-curvature relationship for the bent cap beam for all 15 HS test runs at Sections B and D, respectively. Similar to the moment history plot, the moment-curvature relationship plots show

that the moment was capped at the bent cap capacity: about 6500 kip-in. The analytical nominal moment-curvature relationship obtained from a classical sectional analysis was shown together with the bent cap beam local behavior in Part 1. The sectional analysis performed based on the Caltrans SDC [2013] provisions shown that the bent cap beam capacity is 5024 kip-in.; however, the observed experimental value for the beam capacity of 6535 kip-in. demonstrates that the Caltrans provisions underestimate the bent cap capacity.

This particular conclusion is an important outcome of this study. The design implications of the bent cap capacity underestimation are discussed along with the post-test analysis in Chapter 4. Note that the shown moment values in the moment-curvature relationships in Figure 3.61 and Figure 3.62 are slightly different from the moment history previously shown in Figure 3.57. This is because the moment values used in the moment-curvature relationships, unlike the exact moment values shown in the moment history plots, were approximately reproduced from the column moments. This difference is attributed to the curvature data being collected by the NEFF data acquisition system, while the strut forces used for moment calculations were collected at a totally different sampling rate at the PI. Only the global forces used in the column moment calculations were recorded by both data acquisition systems, thus enabling approximate reproduction of the bent cap moments at the curvatures sampling rate and plotting them together.
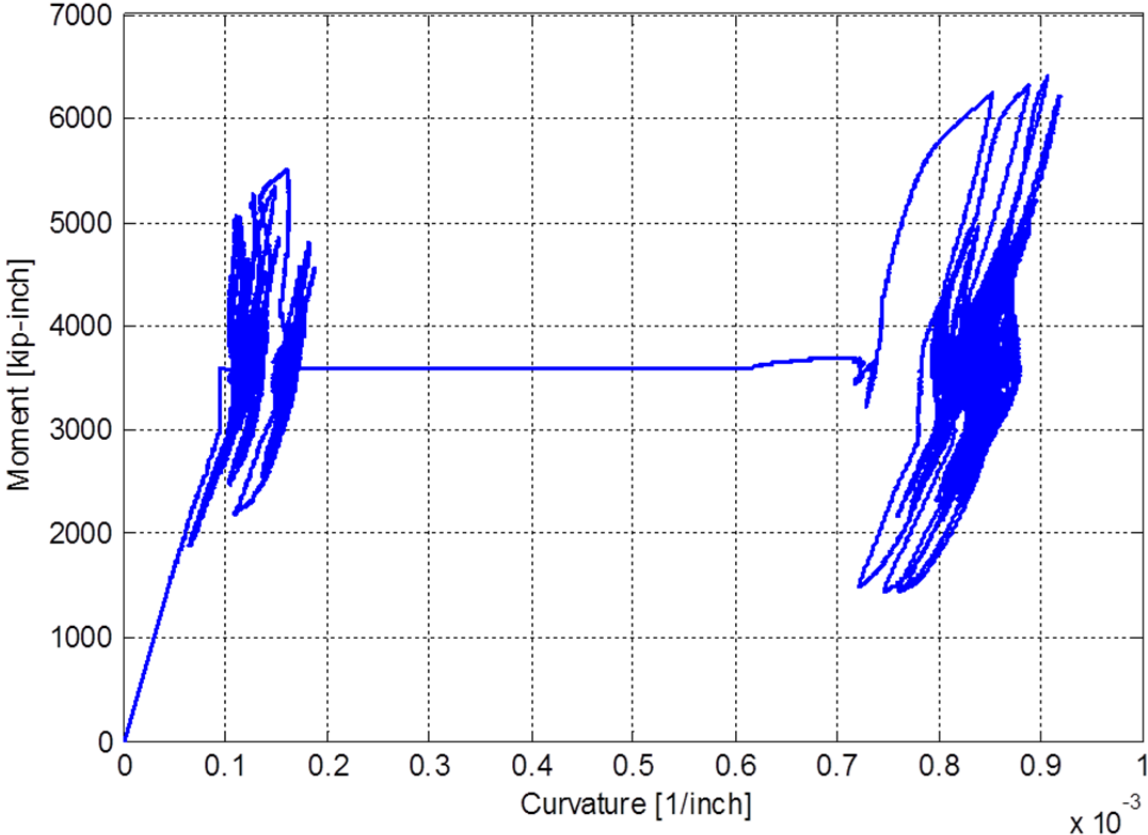
Figure 3.61   **Moment-curvature relationship for the bent cap beam at Section B for all the 15 HS bi-directional and transverse direction only test runs.**
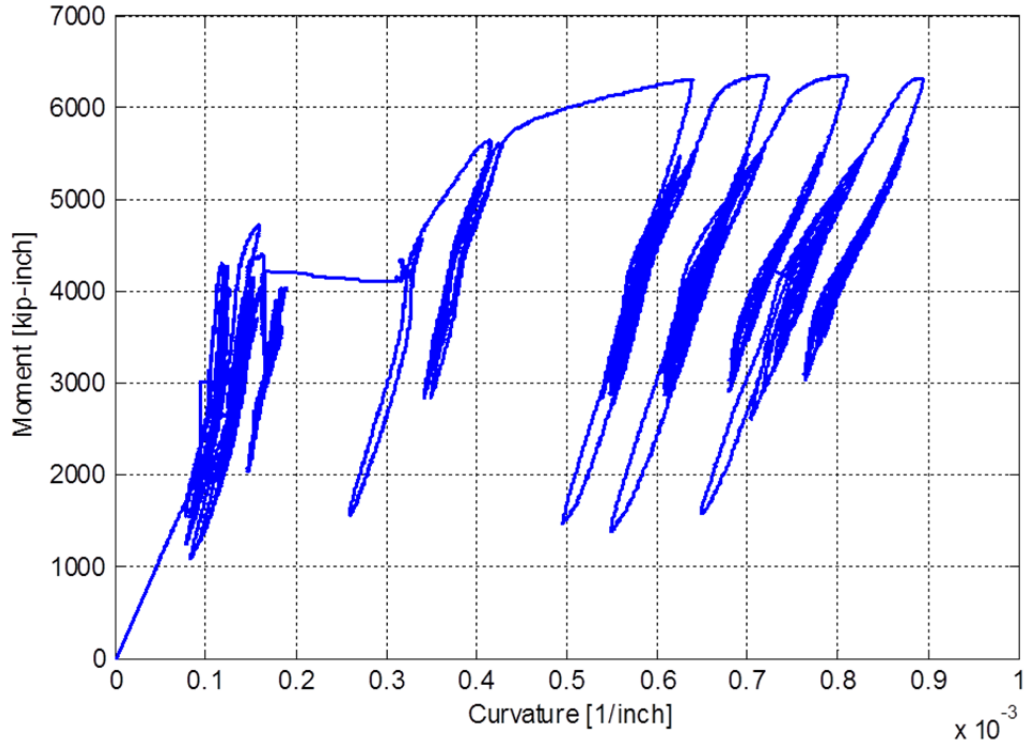
Figure 3.62 **Moment-curvature relationship for the bent cap beam at Section D for all the 15 HS bi-directional and transverse direction only test runs.**

3.6 EFFECTIVE SLAB WIDTH

Besides the bent cap beam capacity estimation, understanding the box-girder slab contribution to the bent cap and accurately quantifying the effective slab width is another important goal of this study. As mentioned before, the Caltrans SDC and AASHTO LRFD guidelines for seismic design require considering a flanged section with an effective slab width $12t_s$ for the integral RC bent cap beams balanced stiffness check and seismic capacity check. The effective slab width, which is typically based on the equivalent strain block concept, was revisited in this study. Similar to what was performed in the case of the as-built Specimen No. 1 cyclic tests, the strain distribution in the bent cap beam reinforcement and the adjacent transverse slab reinforcement from both sides of the beam was determined for all retrofitted Specimen No. 2 HS test runs. Because only the strain distribution in the tension side was found to be more reliable and, therefore, was utilized in this study. Note that the compression side was found to be very sensitive to the concentrated gravity load applied through the column; see in Part I. The results from the tension side strain distribution and the revisited effective slab width from the HS tests are presented in this section. A brief discussion of the surface concrete strain gages is also included.

The same procedure devised and used in Part I of this report to find the equivalent strain block and effective width was used again in this part of the study. The reader is referred to Figure 5.22 in Chapter 5 in the companion report for an overview of such procedure. To consider as many cases as possible from the full set of HS test runs, the strain distribution and effective width were investigated at both Sections B and D, and at nine positive and negative loading

levels. The chosen levels were the ascending sequence of the peak displacements in the positive and negative transverse loading directions, identified in Figure 3.63 in terms of the corresponding ductility levels. Table 3.2 summaries those nine positive and negative loading levels, where all the effective slab width results were produced along with the corresponding drift ratios and ductility levels.

(a)

(b)
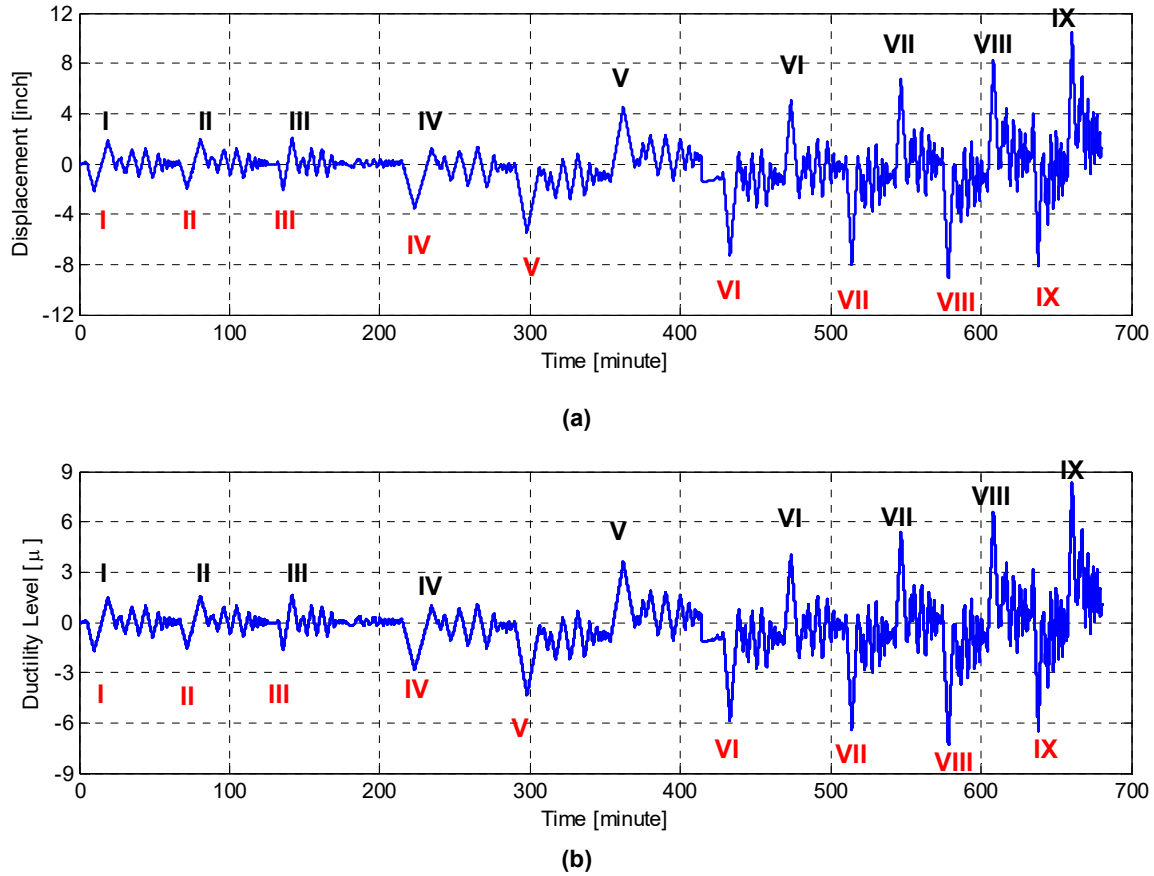
Figure 3.63 **(a) The main nine positive and negative displacement amplitudes; and (b) the corresponding ductility levels (bottom) used for investigating the effective slab width for retrofitted Specimen No. 2 tested using HS.**

Table 3.2   Summary of the peak displacements of the HS test runs in the transverse direction and their corresponding drift ratios and ductility levels.

Positive Transverse Loading				Negative Transverse Loading			
Group ID	Displacement (in.)	Drift ratio (%)	Ductility level (μ)	Group ID	Displacement (in.)	Drift ratio (%)	Ductility level (μ)
I	1.83	2.0	1.47	I	-2.12	-2.4	-1.70
II	1.92	2.1	1.54	II	-1.92	-2.1	-1.54
III	1.99	2.2	1.59	III	-2.01	-2.2	-1.61
IV	1.22	1.4	0.98	IV	-3.53	-3.9	-2.82
V	4.49	5.0	3.59	V	-5.40	-6.0	-4.32
VI	5.01	5.6	4.00	VI	-7.28	-8.1	-5.82
VII	6.72	7.5	5.38	VII	-7.94	-8.8	-6.35
VIII	8.16	9.1	6.53	VIII	-8.98	-10.0	-7.19
IX	10.43	11.6	8.35	IX	-8.02	-8.9	-6.41

3.6.1 Strain Distribution

The strain distributions at different sections across the bent cap and transverse slab reinforcement based on different strain gages readings were recorded continuously throughout all the HS test runs; however, only strain values acquired at the loading peaks, previously identified in Figure 3.63 and summarized in Table 3.2, were considered. The strain distribution was compiled at Sections B and D and was related to the drift ratio and ductility level (μ). Note that the distributions and the effective width were mainly considered under transverse loading in the cyclic tests. However, several cases of the strain distribution and effective width estimated from the HS test runs were determined from the more realistic concurrent bi-directional loading. Thus, the results are presented for the bi-directional tests separately from the large-scale HS transverse direction only test runs.

First, the strain distribution plots at Section B from the bi-directional tests and the transverse direction only tests are presented under subsections 3.6.1.1 and 3.6.1.2, respectively. Next, the results for Section D are shown for bi-directional and transverse direction only tests under subsections 3.6.1.3 and 3.6.1.4. Figure 3.64 and Figure 3.65 show the strain distribution in the tension side at Section B for the five different loading levels that corresponds to the bi-directional tests at the positive and negative peaks, respectively. Note that the bi-directional tests at 50%-scale were repeated twice, with and without the *P*-delta correction. In addition, a small transverse direction only and longitudinal direction only tests were conducted at 50%-scale and still included under the bi-directional tests discussion for simplicity. Because of some impractical strain distributions obtained during the test, the results from the longitudinal direction only test were shortened., Thus, the five loading levels in this case corresponded to drift ratios of 2.0%, 2.1%, 2.2%, 1.4%, and 50% at the positive peaks and 2.4%, 2.1%, 2.2%, 3.9%, and 6.0% at the negative peaks; see Table 3.2 for the equivalent ductility levels.

As previously noted, a significant jump in the strain values at Section B was observed when the 15% gravity load was applied to the already yielded cap beam. Figure 3.66 and Figure

3.68 capture the jump in the strain distribution at Section B at the first big transverse direction only run for positive and negative peaks, respectively, when the 15% gravity load was applied. The immediate adjacent transverse bars in the north side of the bent cap beam experienced a similar behavior. The distribution for the four large-scale transverse direction only runs at the positive and negative amplitudes are shown in Figure 3.67 and Figure 3.69, respectively.

Similar to the strain distribution shown at Section B, different loading levels and loading direction were considered to plot the strain distribution at Section D. Figure 3.70 and Figure 3.71 show the distribution for the five bi-directional tests at the positive and negative peak, respectively. Figure 3.72 and Figure 3.74, respectively, capture the change in the distribution as the first large-scale positive and negative transverse direction only tests were conducted after the 15% gravity load was applied. The overall strain distribution for all of the four positive and negative large-scale transverse direction only tests is shown in Figure 3.73 and Figure 3.75, respectively. Note that all plots in this subsection captured all the spatially extended distribution tails where the intercept at zero strain was determined as part of the effective slab width evaluation.

3.6.1.1 Section B – Bi-directional Runs
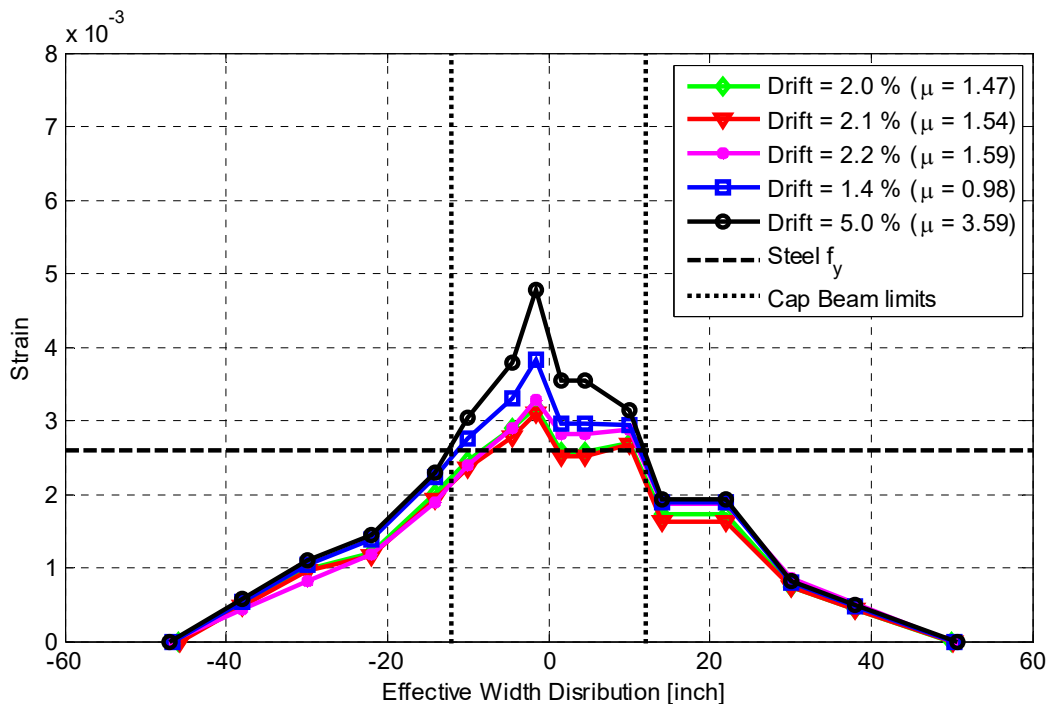
Figure 3.64   **Strain distribution in the tension side at Section B for all bi-directional HS test runs at the positive loading peak (expressed in terms of drift ratio and *µ*).**
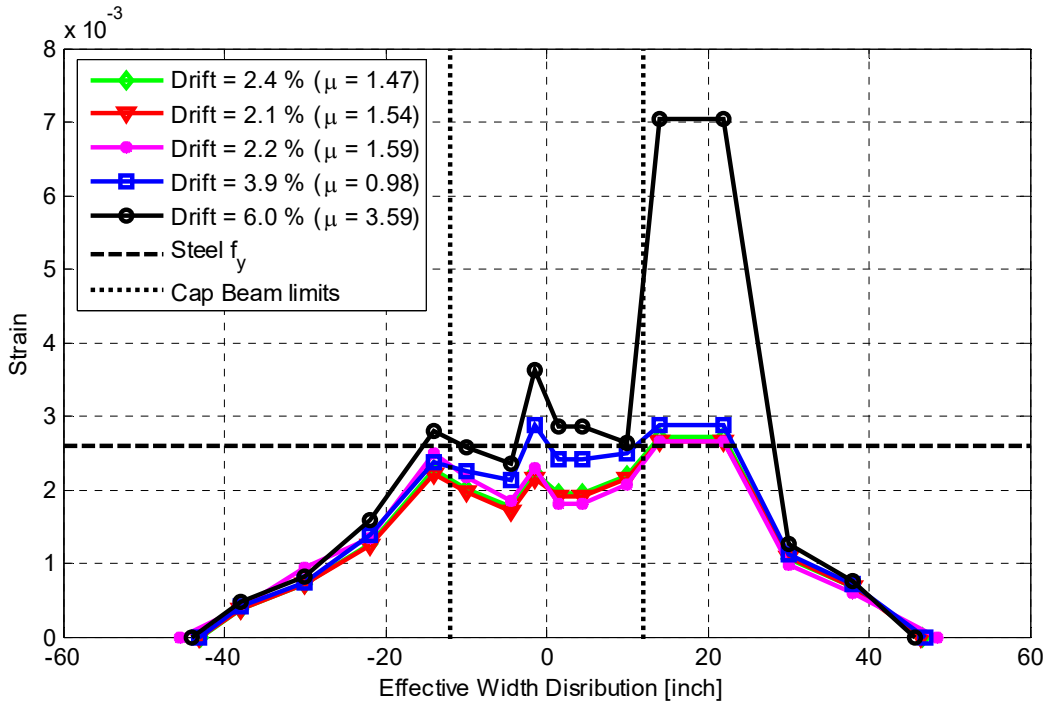
Figure 3.65 **Strain distribution in the tension side at Section B for all bi-directional HS test runs at the negative loading peak (expressed in terms of drift ratio and *μ*).**

3.6.1.2 Section B – Transverse direction only Runs
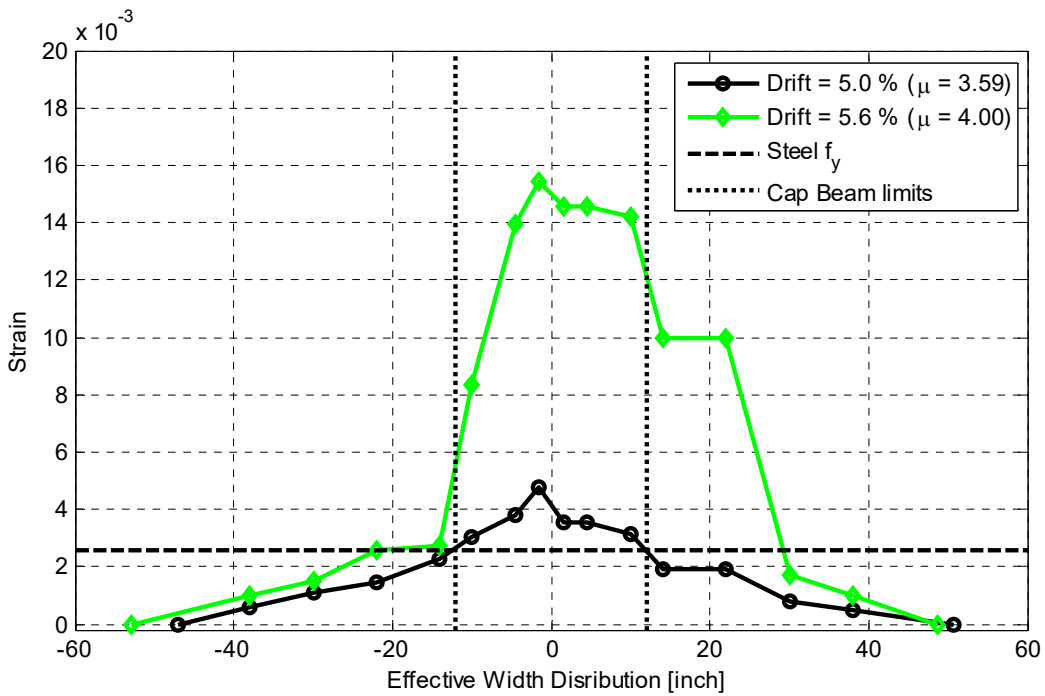
Figure 3.66 **Strain distribution change at Section B due to the increased gravity load and at the first large-scale transverse direction only HS test run at positive loading peak.**
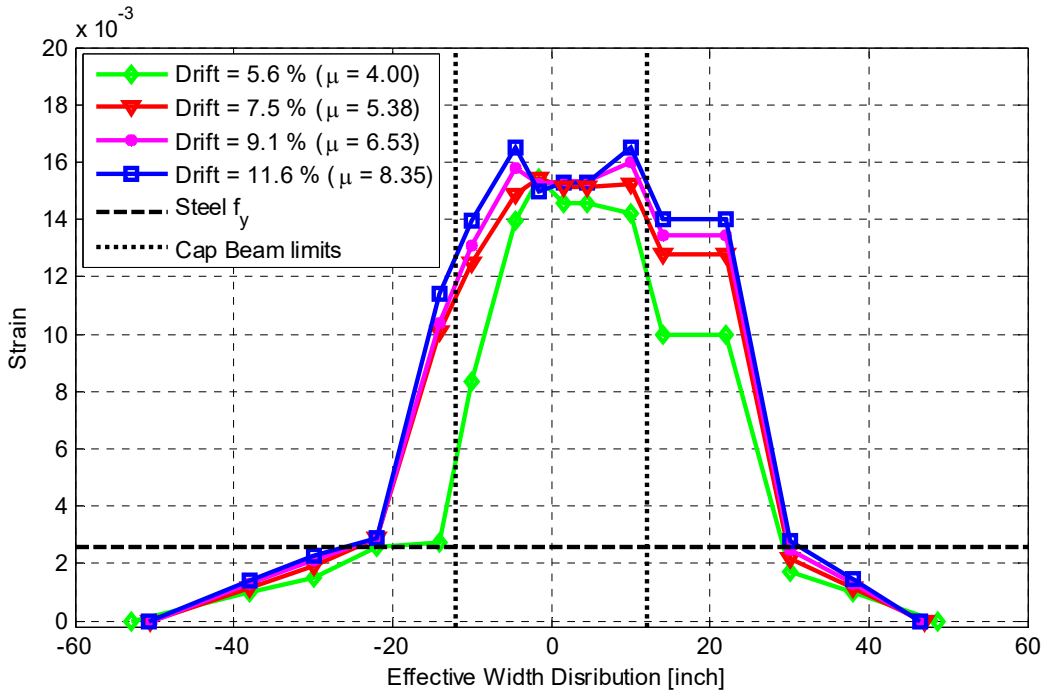
Figure 3.67 Strain distribution in the tension side at Section B for the four large-scale transverse direction only HS test runs at the positive loading peak (expressed in terms of drift ratio and *μ*).
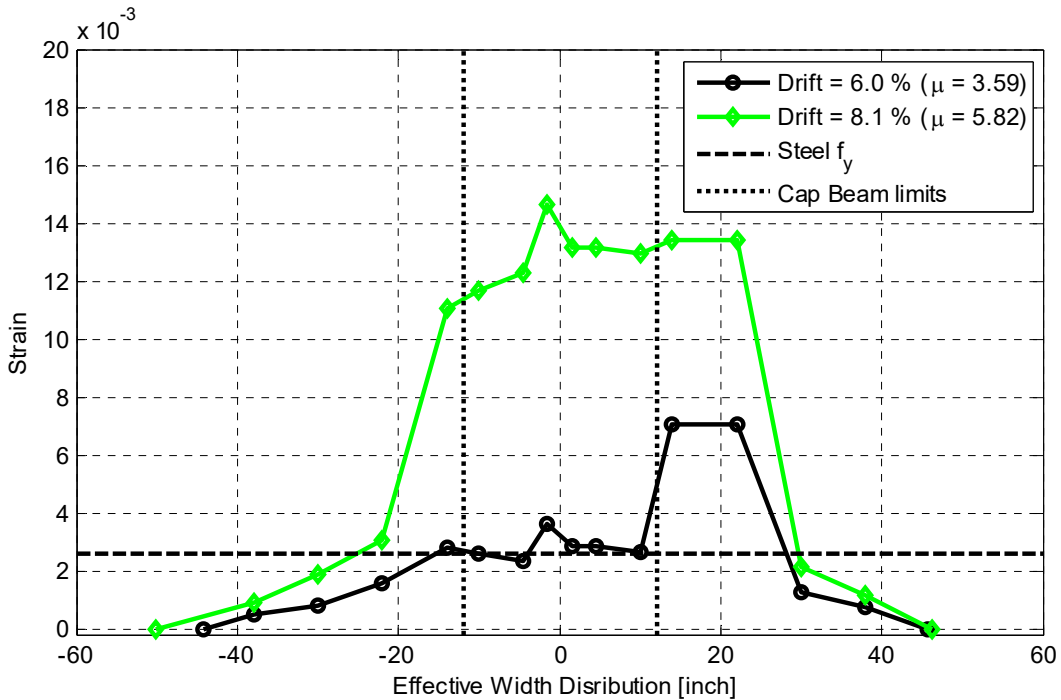
Figure 3.68 Strain distribution change at Section B due to the increased gravity load and at the first large-scale transverse direction only HS test run at negative loading peak.
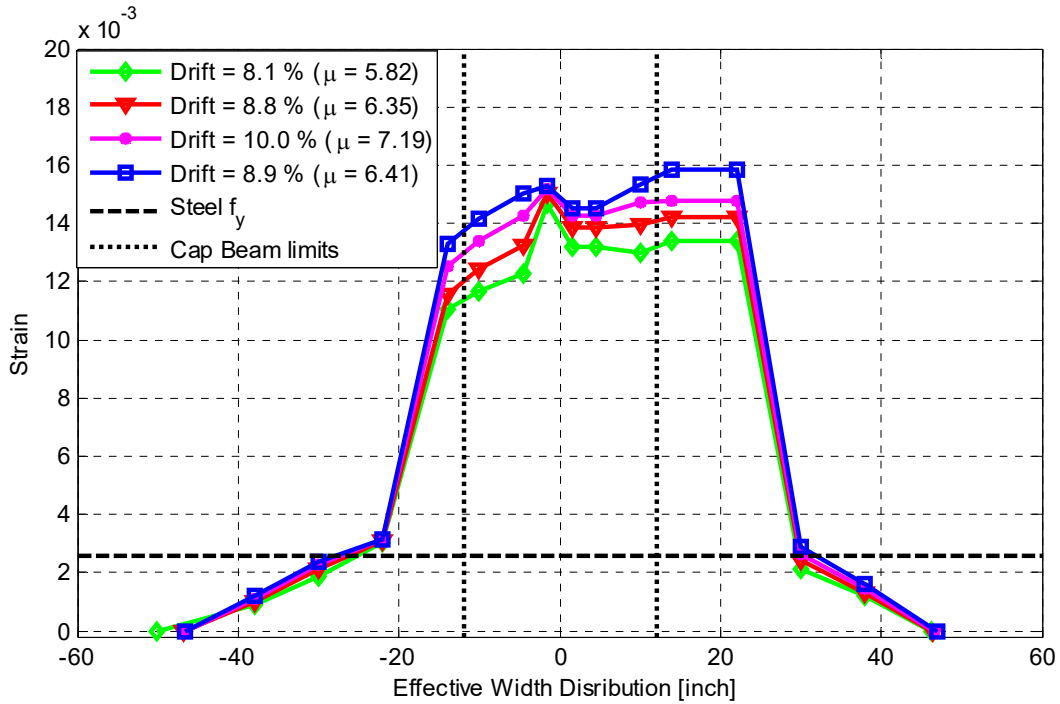
Figure 3.69 Strain distribution in the tension side at Section B for the four large-scale transverse direction only HS test runs at the negative loading peak (expressed in terms of drift ratio and *μ*).

3.6.1.3 Section D – Bi-directional Runs
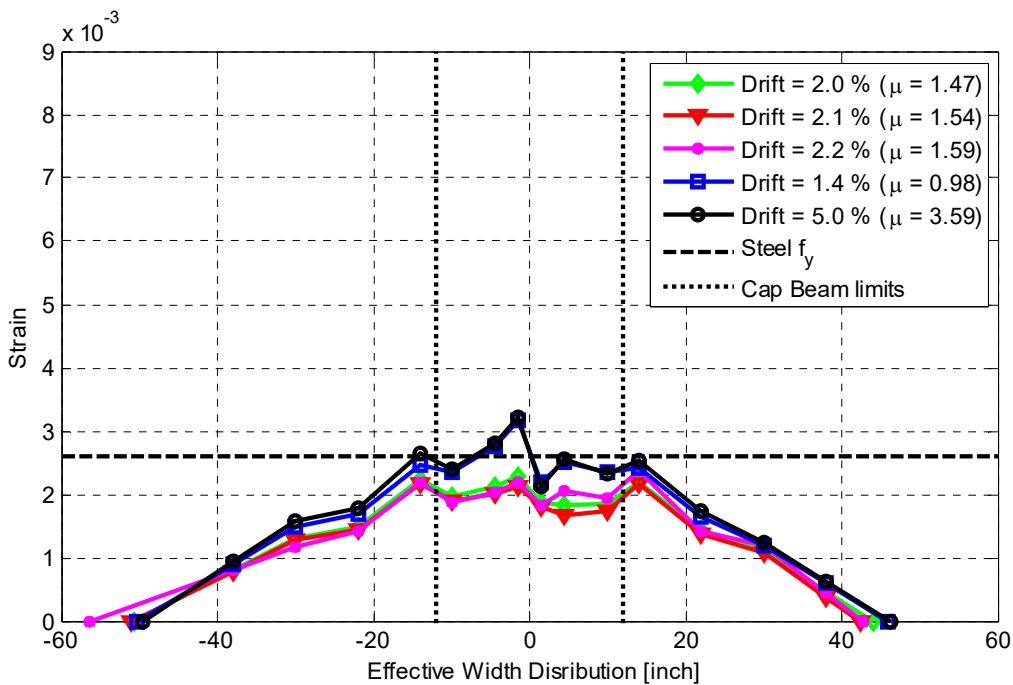
Figure 3.70 Strain distribution in the tension side at Section D for all bi-directional HS test runs at the positive loading peak (expressed in terms of drift ratio and *μ*).
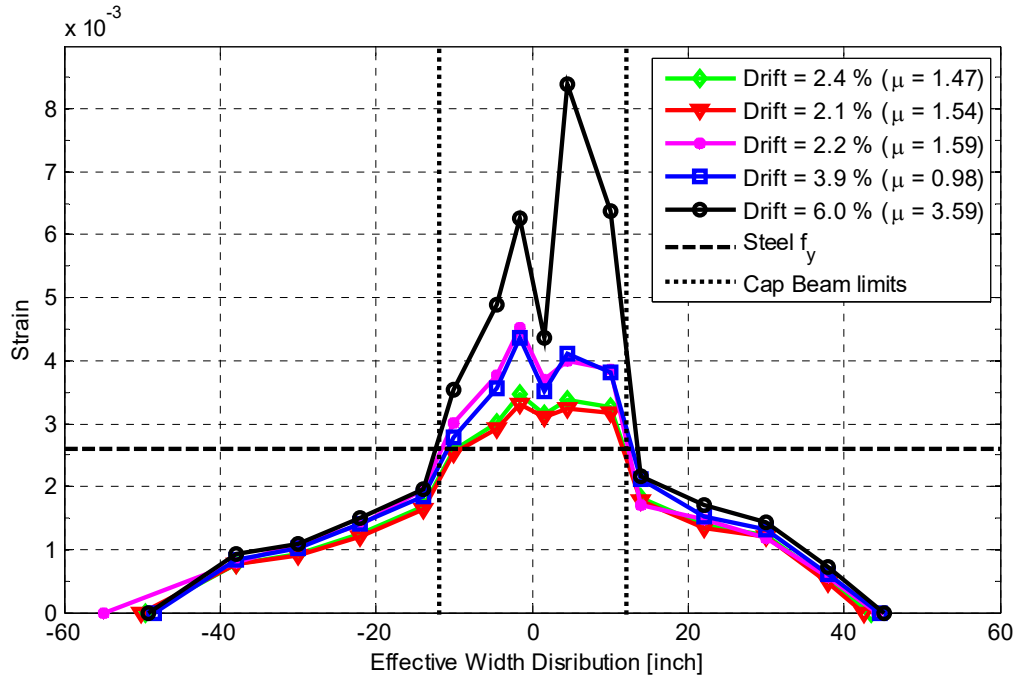
Figure 3.71 Strain distribution in the tension side at Section D for all bi-directional HS test runs at the negative loading peak (expressed in terms of drift ratio and *μ*).

3.6.1.4 Section D – Transverse Direction Only Runs
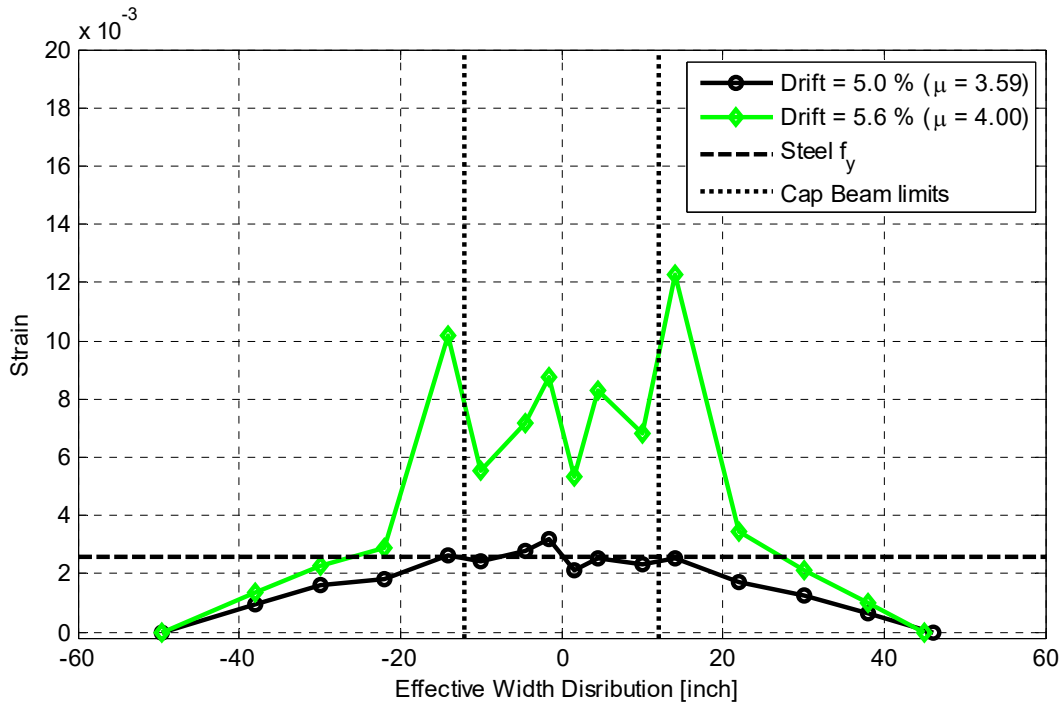
Figure 3.72 Strain distribution change at Section D due to the increased gravity load and at the first large-scale transverse direction only HS test run at positive loading peak.
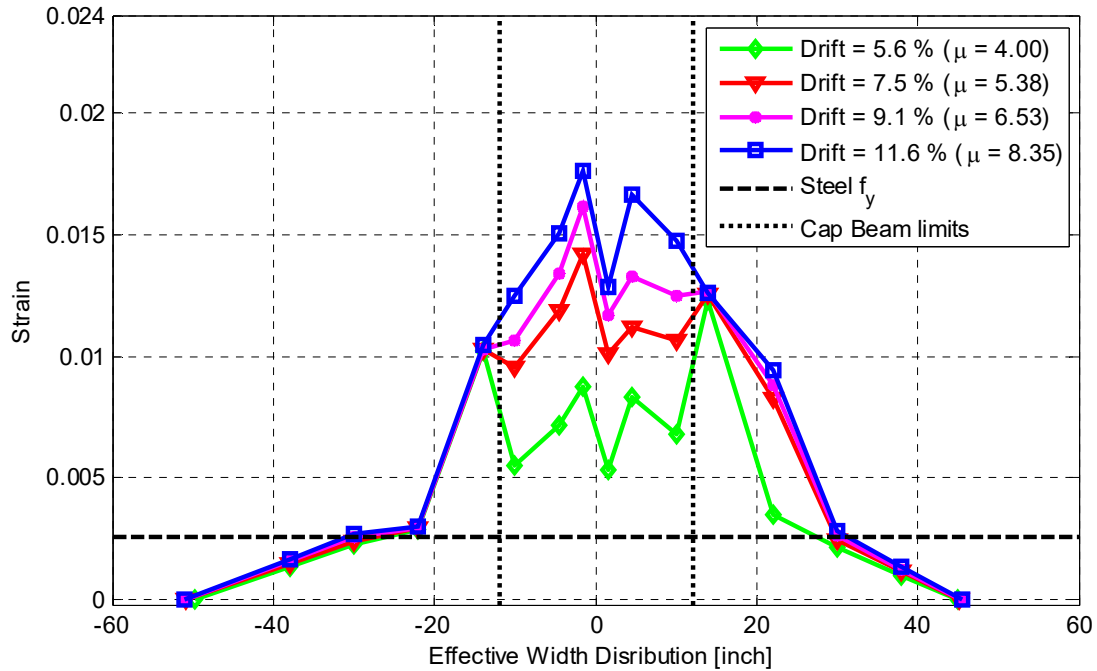
Figure 3.73 Strain distribution in the tension side at Section D for the four large-scale transverse direction only HS test runs at the positive loading peak (expressed in terms of drift ratio and μ).
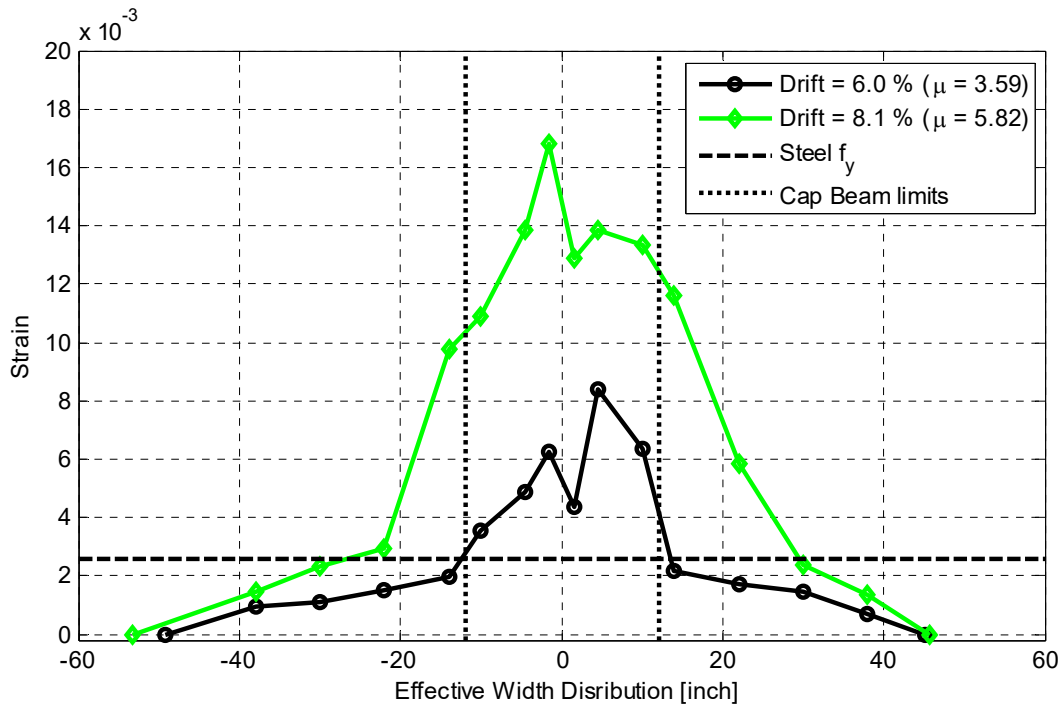
Figure 3.74 Strain distribution change at Section D due to the increased gravity load and at the first large-scale transverse direction only HS test run at negative loading peak.
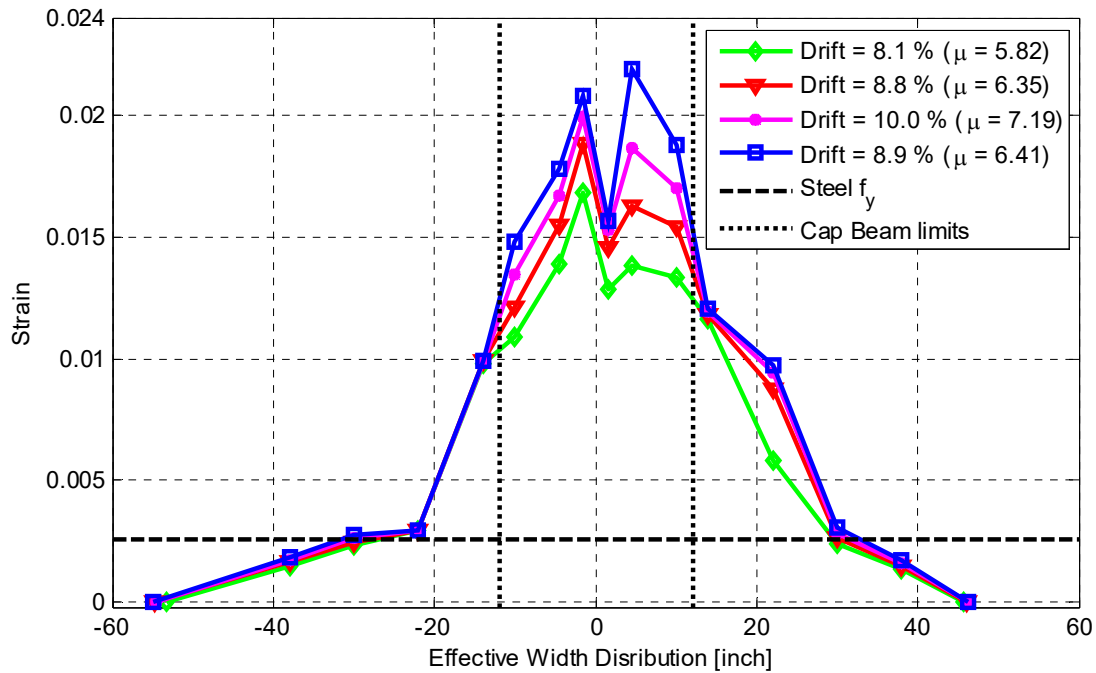
Figure 3.75 **Strain distribution in the tension side at Section B for the four large-scale transverse direction only HS test runs at the negative loading peak (expressed in terms of drift ratio and _μ_).**

3.6.2 Effective Slab Width Estimation

As previously mentioned, the effective slab width was determined using the equivalent strain block concept and the simple procedure devised in Chapter 5 of the companion report. The strain distributions presented in the previous subsection were utilized here to estimate the effective slab width at Sections B and D at different loading levels and directions. Similar to the framework adopted, two values for the bent cap beam strain value were used to define the equivalent strain block (B_{eff}). These are the minimum and the mean of the six instrumented rebars strain gage readings at a given cross section in the cap beam.

3.6.2.1 Section B

An example of how the strain block was determined using the strain distribution at Section B and using the minimum and mean cap beam strain values is shown in Figure 3.76. The total flange effective slab width, i.e., the equivalent strain block width B_{eff}, was calculated for the different nine loading levels at the positive and negative amplitudes; see Figure 3.63 and Table 3.2.
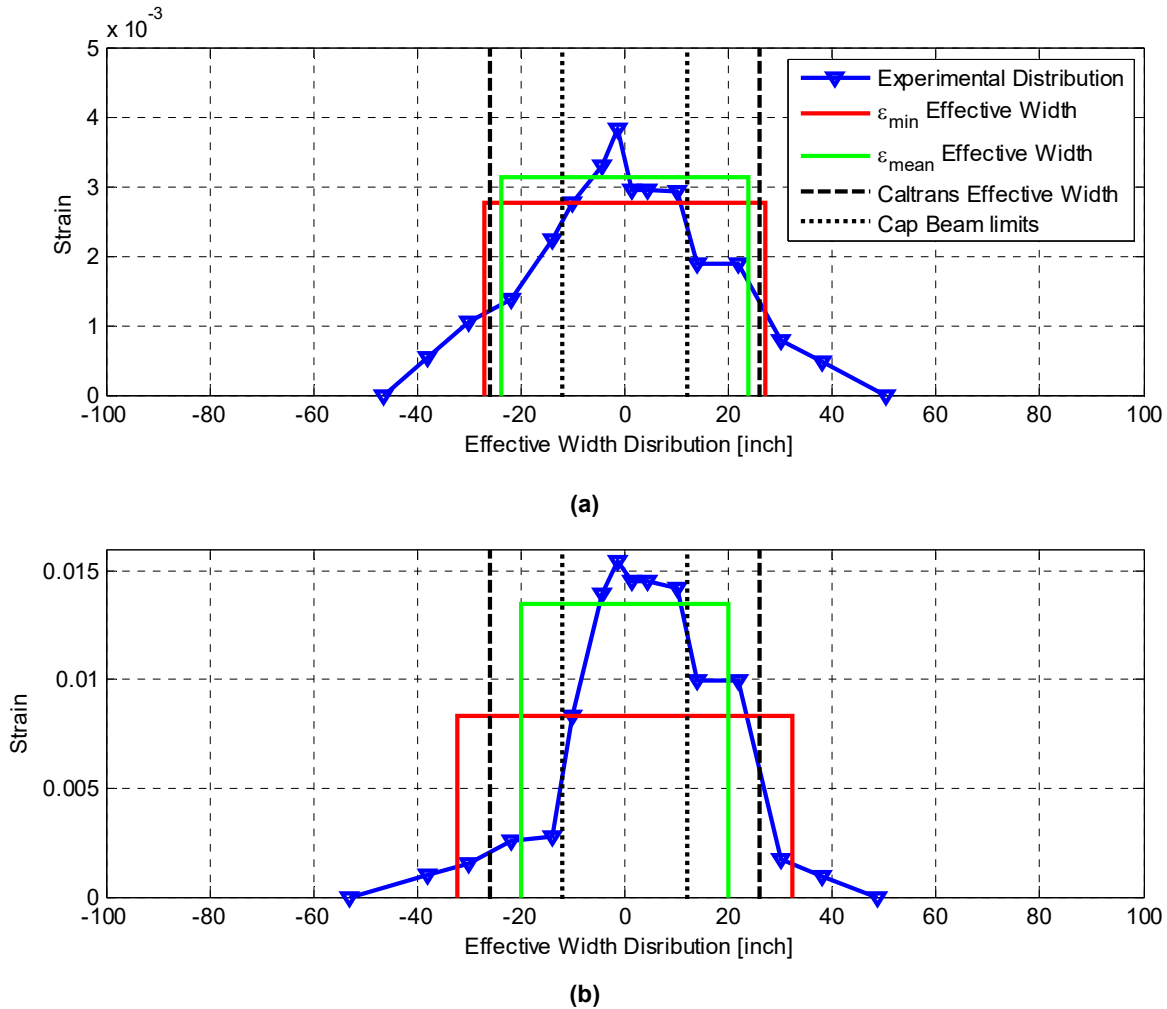
Figure 3.76 **(a) An example of the equivalent strain block at Section B from a bi-directional; and (b) a transverse direction only (bottom) HS test runs.**

A summary of the calculated B_{eff}, as related to the drift ratios, at Section B using both cap beam minimum (ε_{min}) and mean (ε_{mean}) strain values is shown in Figure 3.77 and Figure 3.78 for the positive and negative amplitudes, respectively. The figures also show the B_{eff} that was estimated in light of the Caltrans SDC provisions for the integral bent cap beam flanged section, which is referred to as a Caltrans value. The overall average of the nine positive and negative loading cases is summarized in Figure 3.79.

Figure 3.79 shows that the effective width estimated at the negative loading amplitudes was less than that calculated at the positive loading amplitudes. Note that the overall average from all cases, shown as dashed lines in Figure 3.79, is higher than the Caltrans estimate. Moreover, the determined effective width could be related to the slab thickness (t_s) and bent cap beam width (b_{beam}), as previously reported in the companion report, through a slab contribution constant (C), which quantifies the slab contribution as multiples of t_s. However, this step was skipped here for brevity; in the next section, only the final overall mean value from all HS tests is related to t_s.
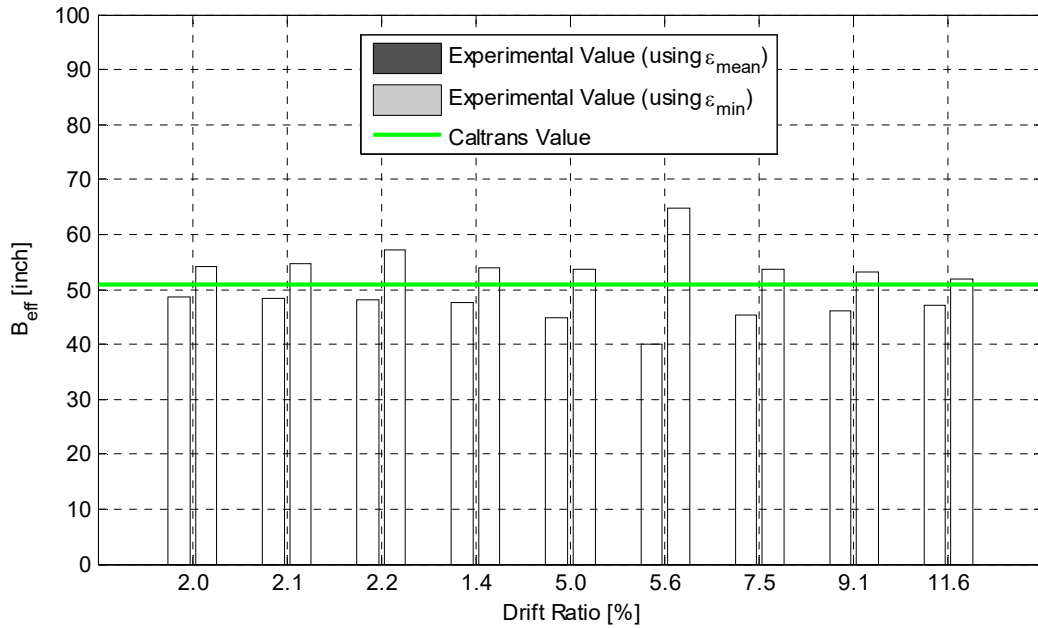
Figure 3.77   Summary of the estimated bent cap effective flange width at Section B from all HS test runs at nine positive loading peaks.
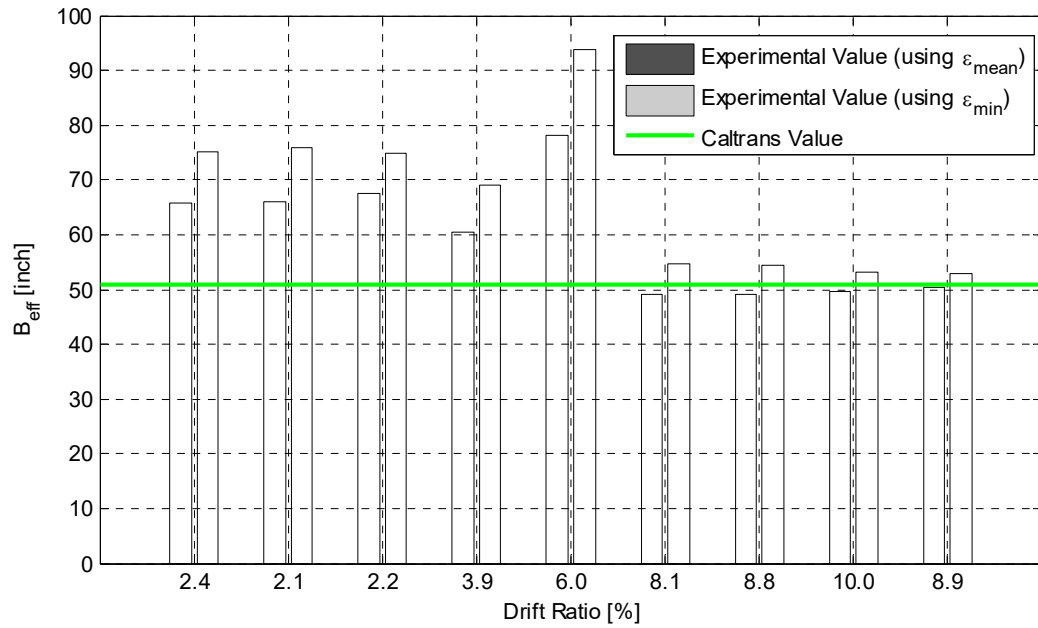
Figure 3.78   Summary of the estimated bent cap effective flange width at Section B from all HS test runs at nine negative loading peaks.
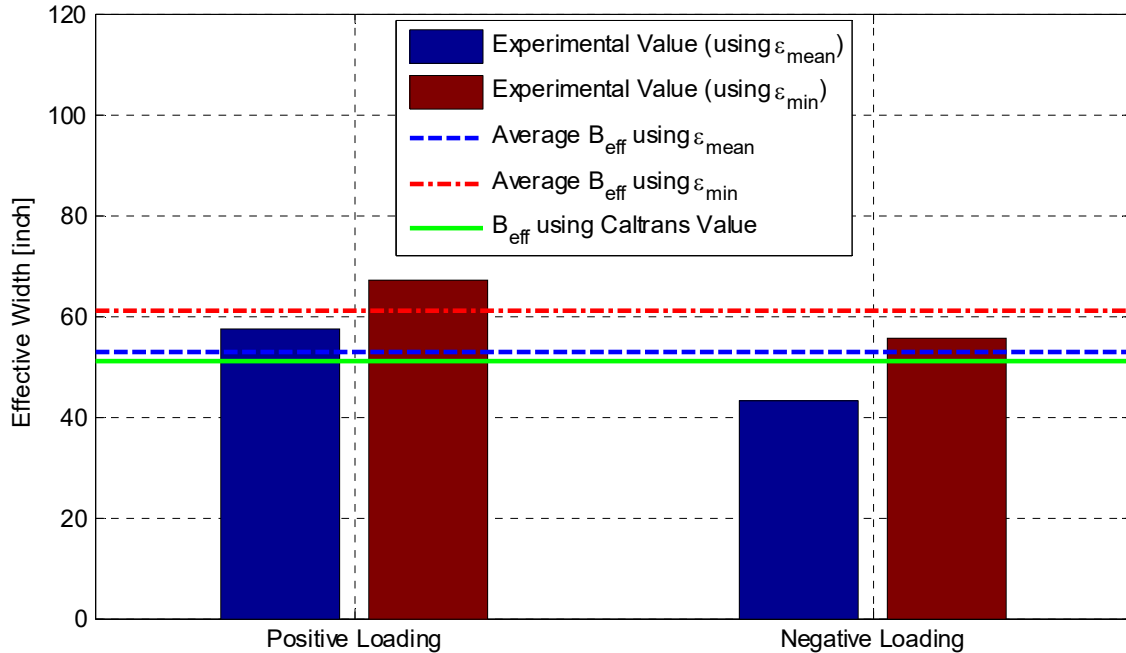
Figure 3.79 **Mean effective width from HS test runs from positive and negative loading (bar chart) and overall average effective width from all HS test runs (dashed lines) at Section B as compared to Caltrans SDC effective width value.**

3.6.2.2 Section D

A similar framework as before is used to present the effective slab width results at Section D. One example of how the strain block was determined using the strain distribution at Section D using the minimum and mean cap beam strain values is shown in Figure 3.80 for typical bi-directional and large-scale transverse direction only HS test runs. A summary of the calculated B_{eff} at Section D using both cap beam minimum and mean strain values is shown in Figure 3.81 and Figure 3.82 at all nine positive and negative amplitudes, respectively. Both figures express the loading level in terms of the drift ratios; the reader is referred to Table 3.2 for the corresponding displacement values or ductility levels. The Caltrans value for B_{eff} is also shown in Figure 3.81 and Figure 3.82 for comparison. Figure 3.83 summarizes the average value of each of the positive and negative loading sets, and the overall average for all cases combined. As was determined for Section B, the estimated effective flange width using the mean strain for Section D was higher than the Caltrans value. Note that contrary to the results obtained for Section B, the average effective width from the positive loading cases was less than that from the negative loading at Section D.
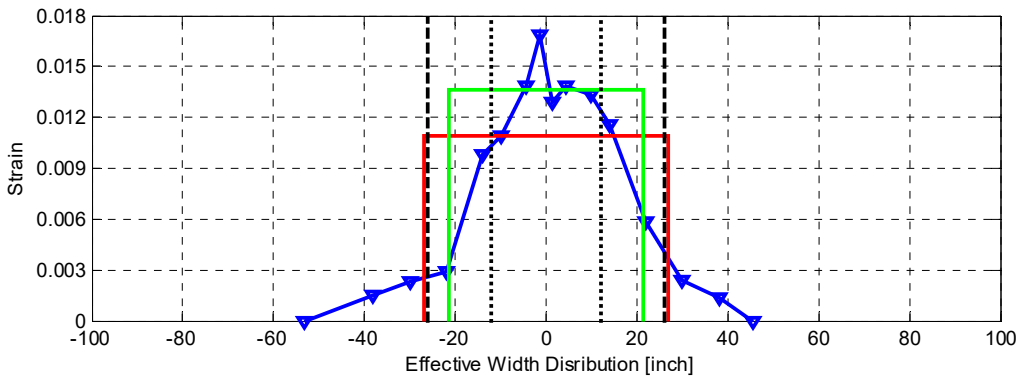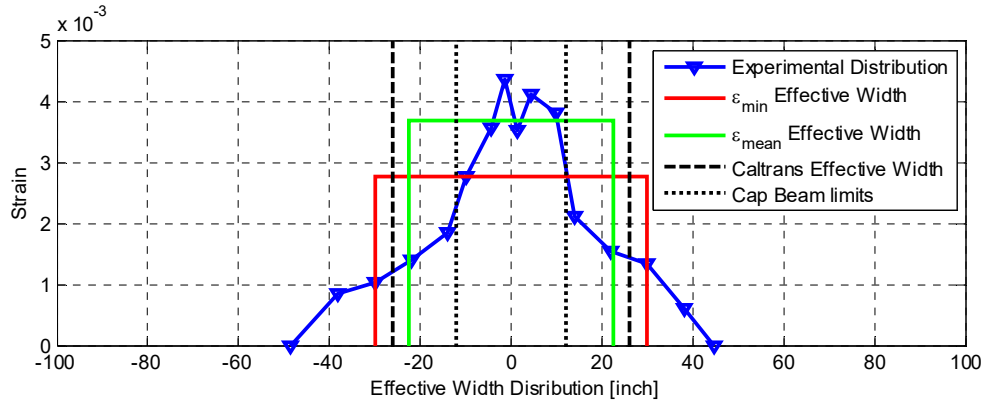
Figure 3.80 An example of the equivalent strain block at Section D from a bi-directional (top) and a transverse direction only (bottom) HS test runs.
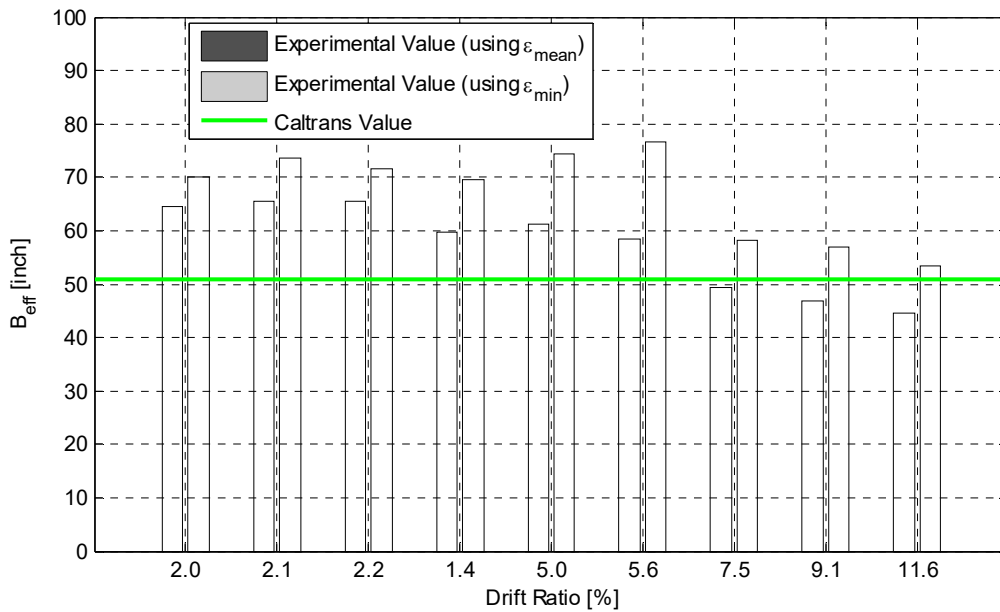
Figure 3.81 Summary of the estimated bent cap effective flange width at Section D from all HS test runs at nine positive loading peaks.
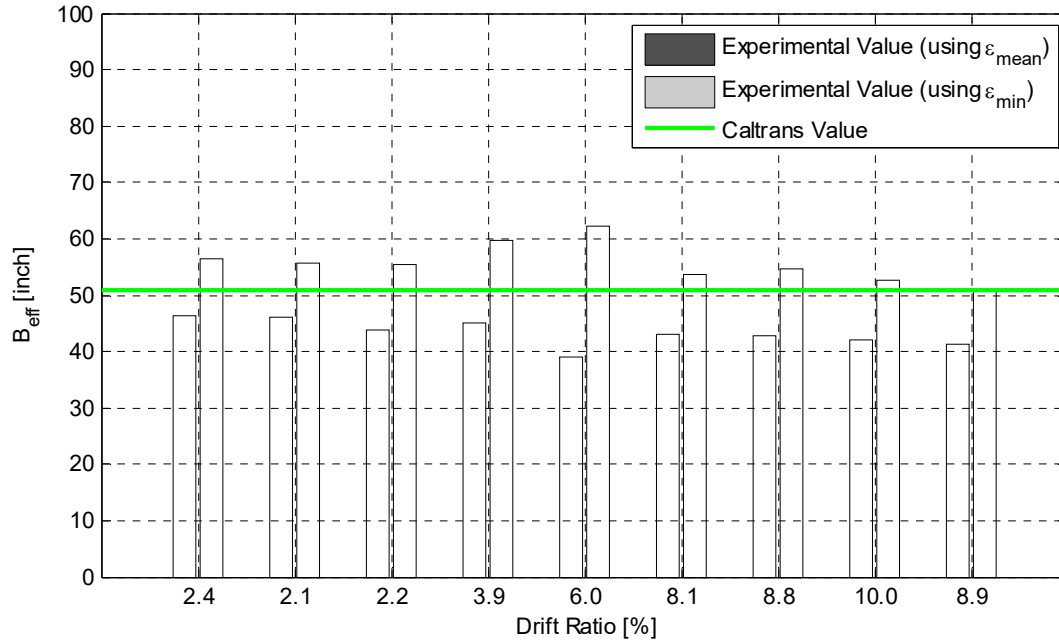
Figure 3.82   Summary of the estimated bent cap effective flange width at Section D from all HS test runs at nine negative loading peaks.
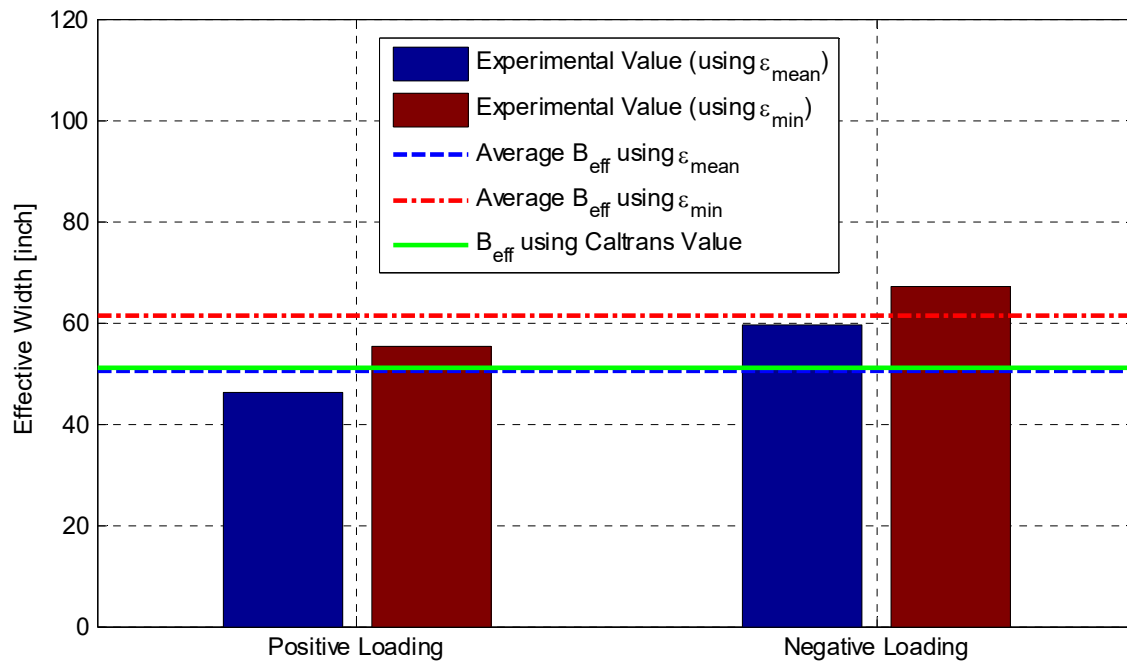
Figure 3.83   Mean effective width from HS test runs from positive and negative loading (bar chart) and overall average effective width from all HS test runs (dashed lines) at Section D as compared to Caltrans SDC effective width value.

3.6.3 Concrete Surface Strain Distribution

The strain distribution from the instrumented reinforcing steel bars in the bent cap beam tension side and its adjacent deck slab transverse reinforcement was found to be more accurate than the measurements in the compression side and those from the embedded and surface concrete gages see Part 1 for a history of the embedded concrete gages in the compression soffit slab side. Here, a sample of the surface concrete strain gages is shown for completeness. Figure 3.84 shows the strain history obtained from six different surface concrete gages, which were located close to Section B and distributed at the east and west sides of the column. The surface concrete gages captured the overall trend of the effective width despite the noisy measurement. This is implied in Figure 3.84 at level W-1 (closest to column and bent cap) versus W-2 and W-3 levels (which were farther from the column and cap beam).
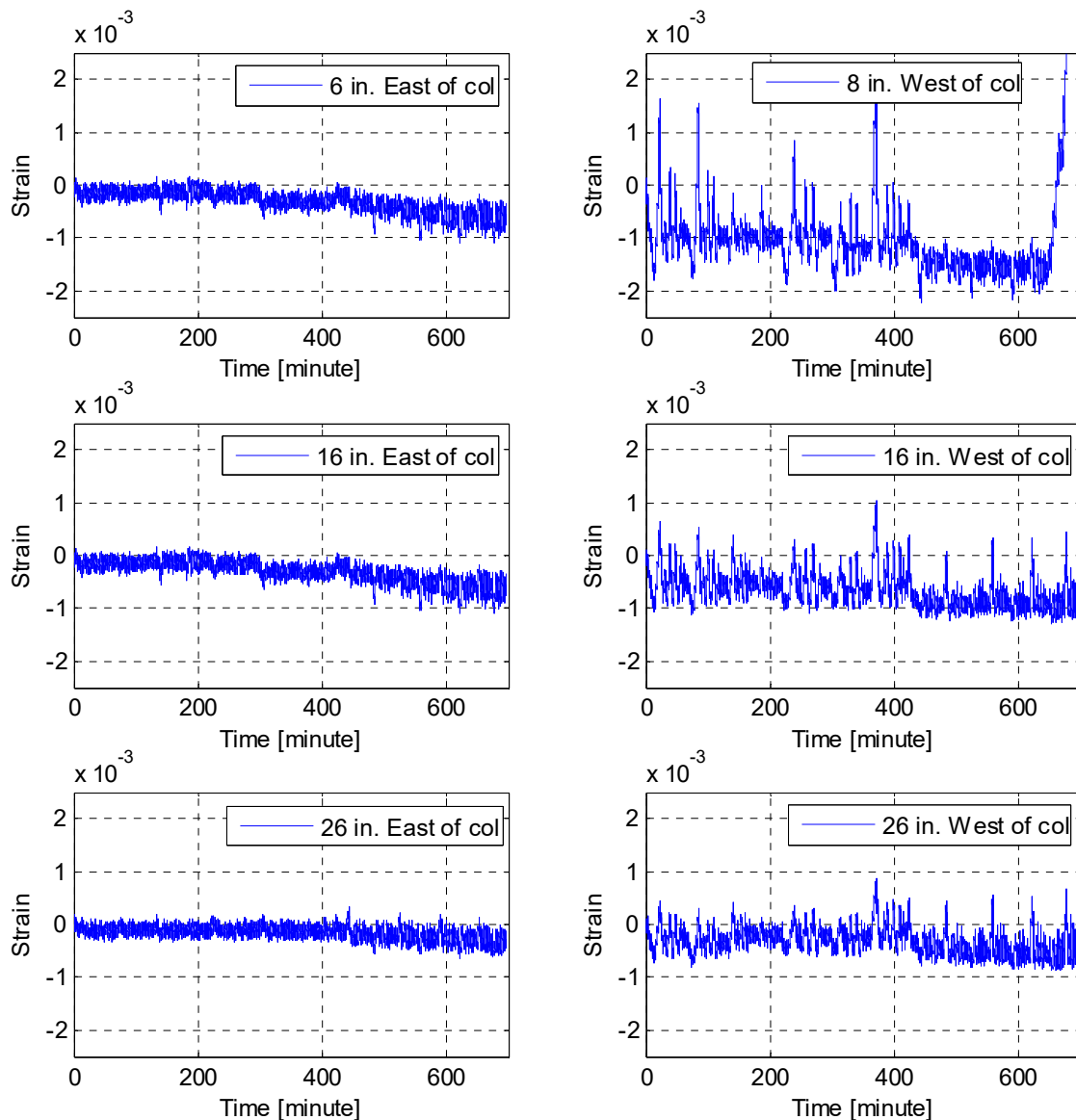
Figure 3.84   **Strain history of six concrete surface gages at Section B for all HS test runs.**

3.7   EFFECTIVENESS OF THE RETROFITTING TECHNIQUE

Based on the experimental results obtained in both Part 1 and 2, the demands increased because of the undertaken retrofit. However, a formal comparison between the overall response of the as-built Specimen No. 1 and the retrofitted Specimen No. 2 was not carried out. Thus, this section briefly compares the global force-displacement, the column and bent cap beam moment-curvature, and the overall average value of the revisited effective flange width from the as-built Specimen No. 1 cyclic tests and the retrofitted Specimen No. 2 HS tests. This comparison aims at investigating the effectiveness of the retrofit and the CFRP jacket in amplifying the column capacity; see Figure 3.85 and Figure 3.86 that compare the global force-displacement and the column moment-curvature relationships in the transverse direction, respectively. Figure 3.87 compares the bent cap beam moment-curvature at Section B for Specimen No. 1 and Specimen No. 2 tests.

Note that the force capacity of the whole sub-assembly and the moment capacity of the column increased by almost 25% in Specimen No. 2 compared to Specimen No. 1 because of the enhanced column confinement due to the CFRP jacket; however, the moment in the cap beam at Section B of Specimen No. 1 was capped at approximately 4500 kip-in in the cyclic test because the column reached its flexural capacity and no further demands were transferred to the cap beam. In the HS tests of Specimen No. 2, the demands on the cap beam increased significantly due to the amplified moment from the column and the 15% gravity load used in these runs relative to the 10% in the cyclic tests of Specimen No. 1. The moment in the cap beam was capped again but at about 6500 kip-in. because either the column or the cap beam had reached capacity. Visual evidence of the cap beam concrete crushing in compression suggests that it was the cap beam that reached its capacity. The observed damage at the end of Specimen No. 1 and Specimen No. 2 tests is shown side-by-side in Figure 3.88. Therefore, it is concluded that the CFRP jacket and retrofit effectively increased the column and the overall system capacity. Worth emphasizing is that the associated increase in the cap beam demands might not be favorable if its capacity is underestimated during the design phase because the failure can migrate to the bent cap.
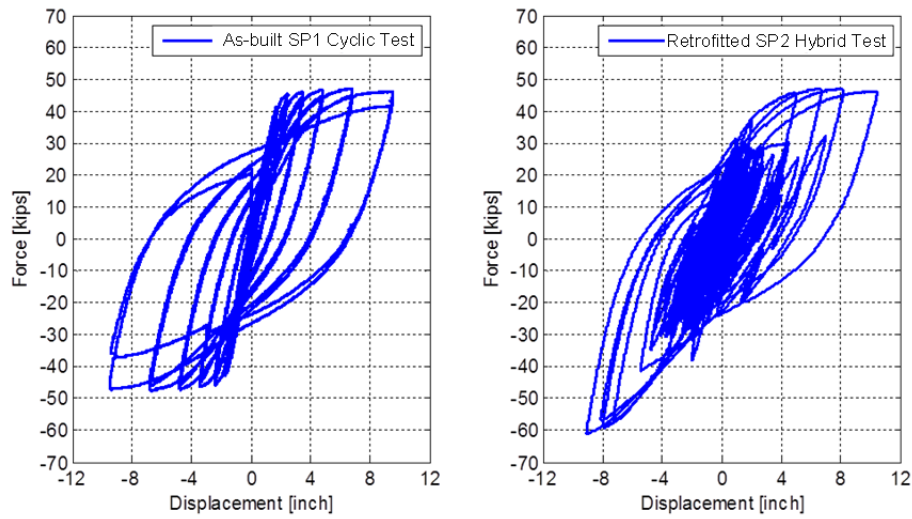
Figure 3.85   Comparison of the global force-displacement relationship in the transverse direction from the as-built Specimen No. 1 cyclic tests and the retrofitted Specimen No. 2 HS tests.
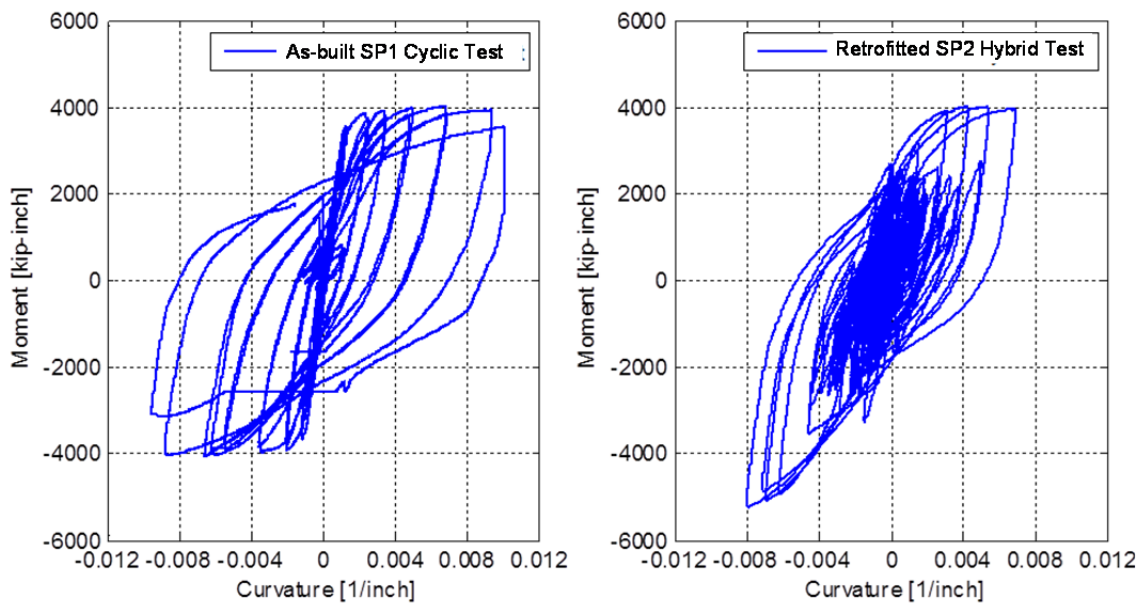
Figure 3.86   Comparison of the column moment-curvature relationship in the transverse direction from the as-built Specimen No. 1 cyclic tests and the retrofitted Specimen No. 2 HS tests.
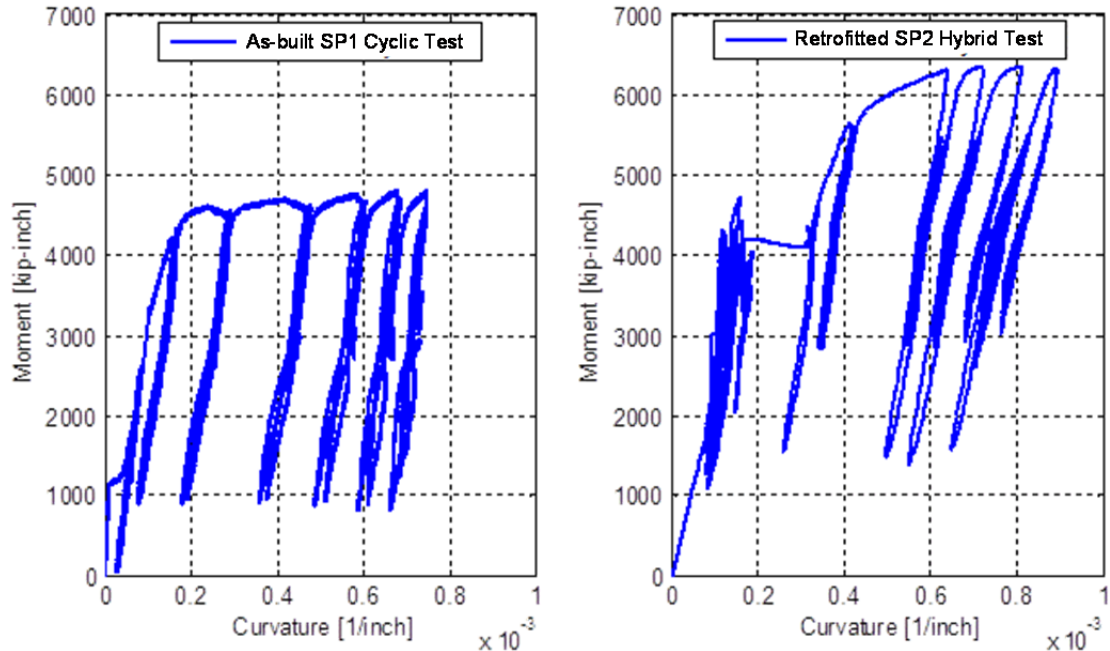
Figure 3.87   Comparison of the bent cap moment-curvature relationship at Section B from the as-built Specimen No. 1 cyclic tests and the retrofitted Specimen No. 2 HS tests.

For completeness, the effective slab width determined experimentally from both the as-built Specimen No. 1 cyclic tests and the retrofitted Specimen No. 2 HS tests is compared. As previously discussed, the area under the strain distribution was computed and transformed to an equivalent strain block with an effective width where two strain values were used; namely, the minimum and the mean strain among the used six gages at a given cross section in the cap beam reinforcement. A summary of the mean effective flange width B_{eff}, which includes the cap beam width from Specimen No. 1 cyclic tests and Specimen No. 2 HS tests along with the overall average value from all tests, is shown in Figure 3.89 and compared to the Caltrans SDC [2013] value. Note that the estimated B_{eff} values from the experiments were significantly higher and slightly higher than the Caltrans SDC value when the minimum and the mean cap beam strain was used, respectively. In addition, the effective width determined from the cyclic tests was relatively higher than that from the HS tests. When related to the slab thickness (t_s), the mean effective slab contribution (some of the slab potion to both sides of the cap beam width) from the tests ranged from approximately $13t_s$ to $19t_s$, compared to the $12t_s$ code value, as shown in Figure 3.89. Accordingly, a recommended value of $18t_s$ is proposed to better reflect the box-girder slab contribution to the width of the integral bent cap beam. Sectional analysis and design implications based on the revisited effective slab width value are presented in detail in Chapter 4, along with post-test analysis.
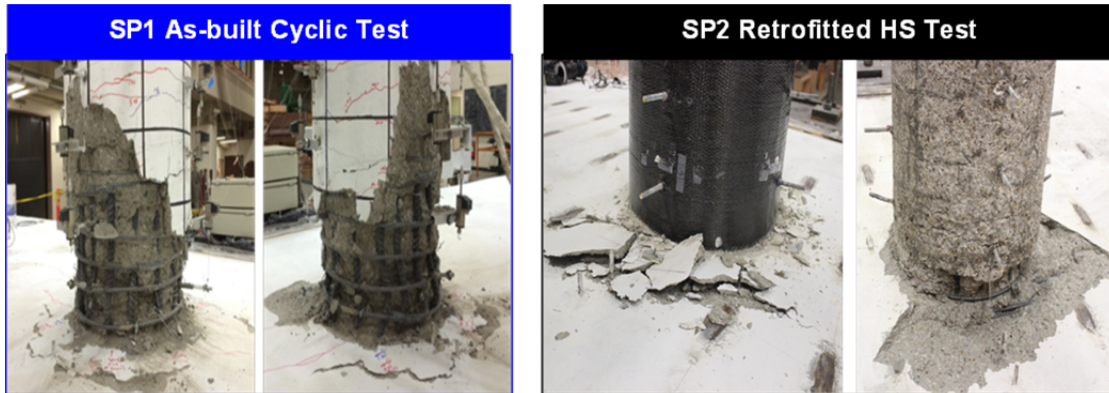
Figure 3.88 Column plastic hinge damage after Specimen No. 1 cyclic tests and cap beam concrete crushing and column flexural cracks (observed after CFRP jacket removal) after Specimen No. 2 HS tests.
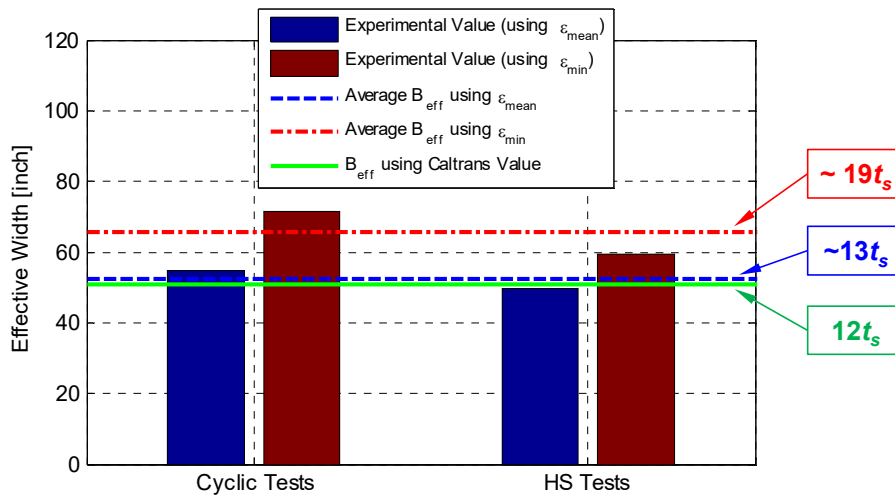
Figure 3.89 Average values for the effective flange width to be added to the cap beam width from the as-built Specimen No. 1 cyclic tests and the retrofitted Specimen No. 2 HS tests and overall mean value from all tests when the cap beam minimum and mean strain values were used.

4   Post-Test Analysis

Finite-element post-test analyses and conventional sectional analyses were conducted to further investigate the bent cap capacity with focus on design optimization. The FE model was first calibrated against Specimen No. 1 cyclic test results. Next, FE analysis was used to determine the cap beam capacity from two hypothetical designs having less reinforcement than what the original design required. The sectional analysis determined the nominal cap beam capacity using two values for the slab effective width with or without including the slab tensile reinforcement within that effective width. Next, the sectional analysis tool was used to investigate the design implications at the full prototype bridge level. To study the design implications of the revisited effective slab width value and the significance of including the slab transverse reinforcement, the Caltrans Academy Bridge was utilized to check the design of the integral bent cap beam that corresponds to three different column designs. This chapter presents (1) the DIANA test specimen model calibration; (2) hypothetical cap beam design FE analysis investigation; (3) test specimen cap beam sectional analysis; and (4) the design implications at the full-scale prototype bridge level.

4.1   DIANA MODEL CALIBRATION

The detailed 3D DIANA [2014] brick-element model of the test specimen previously used in the pre-test analysis was calibrated against the as-built Specimen No. 1 cyclic tests. Parameters were varied to understand the effect of each of these parameters on the specimen model response to determine the best set of parameters for the most accurate match with the experimental test results. First, the effect of the components of the analysis input cyclic load pattern; the transverse direction only versus the bi-directional loading schemes used in the experiments, was explored. Next, the effect of the gravity load was investigated. The effect of each of the concrete total strain-based crack model input parameters was briefly investigated as well. For better calibration, a different set of material model parameters for the column and the box-girder was used to recognize the actual difference in the concrete lifts used in the construction.

All the analyses conducted throughout this stage of the model calibration were nonlinear quasi-static analysis under prescribed cyclic loading patterns that mimicked the experiments of the as-built Specimen No. 1. Two cases for the prescribed displacement input were used in the analysis and adopted from Specimen No. 1 cyclic loading patterns. The first is a bi-directional loading pattern that applied the prescribed displacement input at the column head in the transverse and the longitudinal directions separately, i.e., in a cross orbit where loading is applied in one direction at a time. A shorter input signal was used as well, which applied only the

transverse component of the cyclic loading pattern. The bi-directional and transverse direction only cyclic loading pattern used for the different DIANA post-test analyses are shown in Figure 4.1 and Figure 4.2, respectively.

The analysis results from two different cases conducted under the bi-directional and transverse direction only cyclic load input are compared and presented next. Note that because at least 16 analysis cases—see Section 4.2 —were performed, the transverse direction only input was the one used to study the effect of the material model parameters. A more complex bi-directional input would have been computationally expensive with limited benefit to this particular parametric study.
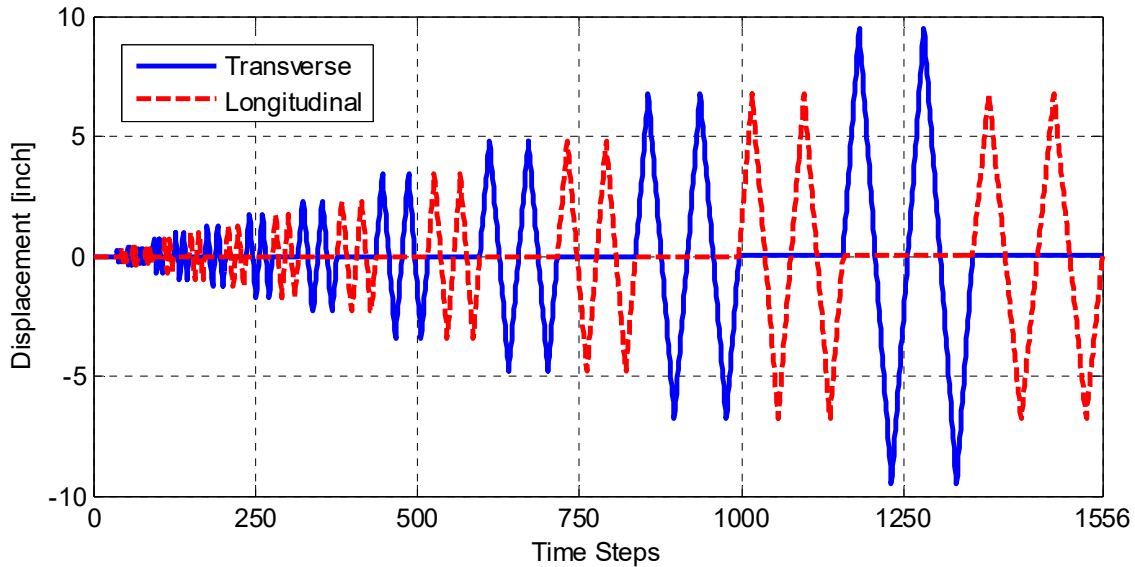
Figure 4.1   **Bi-directional cyclic loading pattern adopted from Specimen No. 1 experiments and used for part of the DIANA post-test analysis.**
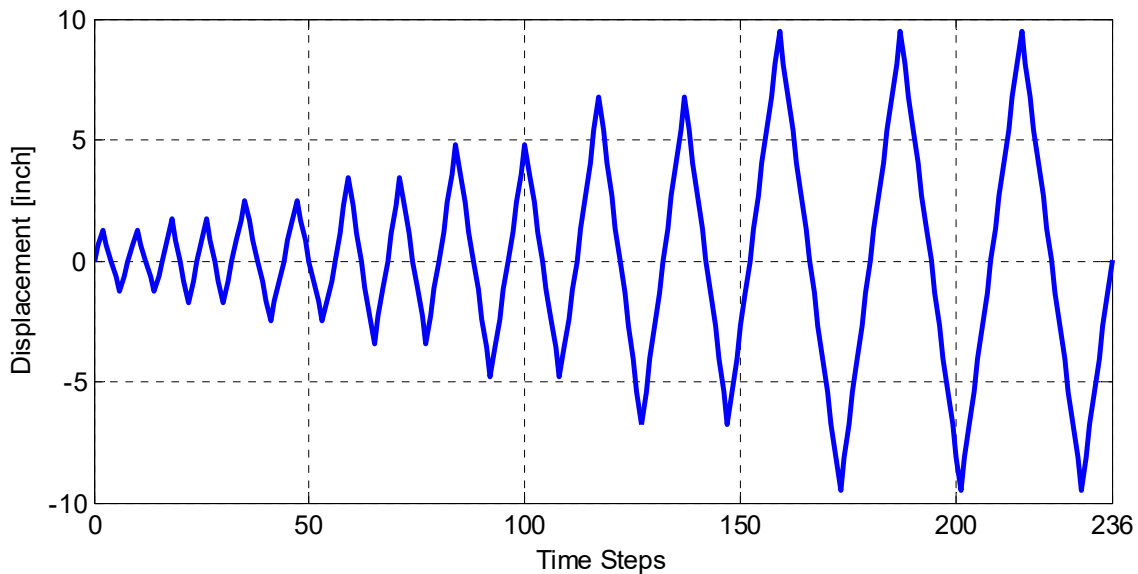
Figure 4.2   **Transverse direction only cyclic loading pattern adopted from Specimen No. 1 experiments and used for part of the DIANA post-test analysis.**

4.1.1 Transverse versus Bi-Directional Input

In order to conduct larger number of parametric studies, a shorter input signal was adopted only in the transverse direction for computational efficiency. Thus, it was desired to check first how much the overall response may differ if the loading and consequent damage in the longitudinal direction is not considered. The bi-directional and transverse direction only input displacement patterns were applied to a preliminary model, which used one set of material model parameters for the FE model. This set was adopted from the mean material properties determined from the material tests. A constant gravity load that is equivalent to 10% of the column axial capacity was applied first in both cases. The obtained force-displacement relationships from the two cases are compared in Figure 4.3, where it is noted that the hysteresis behavior is different. In addition, larger force values were observed when the transverse direction only input was used. This is attributed to the effect of the inelastic behavior of the box-girder, which introduced some damage when loading and included application of cycles in the longitudinal direction in addition to the transverse direction. When only a transverse input was used, all the damage occurred in the column in the vertical plane, which includes the longitudinal axis of the bent cap beam leading to higher transverse force capacity. It can be concluded that incorporating the longitudinal component of loading is necessary for accurate model calibration. However, using the transverse direction only signal can be used as a simplified approach to explore the sensitivity of the overall response to the material input parameters as discussed in Section 4.1.3.

(a)   (b)
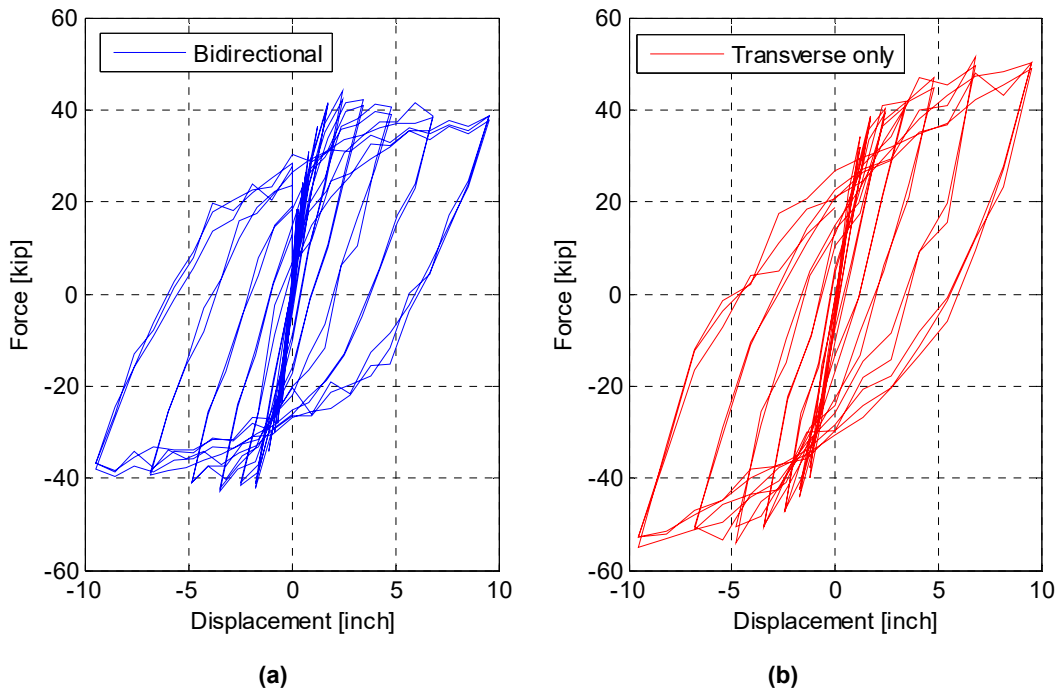
Figure 4.3   Force-displacement relationship in the transverse direction when an (a) bi-directional or (b) transverse direction only cyclic loading pattern was used.

4.1.2 Effect of Gravity

The total vertical reaction at the two roller supports at the ends of the bent cap beam in the DIANA model was compared to the applied total gravity load, because vertical reactions were key in estimating the cap beam moment capacity for further analyses. The DIANA analysis determined that the ratio of the total reaction from the vertical roller supports to the applied gravity load was found to be about 80%. However, the experimentally measured value for the total reaction from the calibrated struts to the applied gravity load was in the vicinity of 70% for both Specimen No. 1 cyclic tests and Specimen No. 2 HS tests, implying that the FE solution distributed the gravity load based on a stiffer bent cap beam, which is attributed to the full vertical restraints at its ends. Modeling the end conditions of the bent cap beam using vertical springs was considered, but or simplicity, instead of using springs, the gravity load was adjusted in the FE analysis such that the bending moments that developed in the bent cap beam matched the values observed from the experiments.

A value of 8% gravity load produced comparable bending moments in the bent cap beam to those obtained under the 10% gravity load from the experiments. Note that applying the gravity before any lateral loading did not incorporate any inelastic behavior in the model; thus, the nonlinear material model parameters did not need to be calibrated for this part of the analysis. However, it was beneficial to check whether the slightly relieved axial load in the analysis would affect column behavior. Accordingly, a nonlinear analysis using the bi-directional cyclic load input was conducted with the 10% gravity and without any gravity load, with the goal of exploring system behavior in the extreme case without any gravity load. Figure 4.4 and Figure 4.5 show the force-displacement relationship comparisons with and without including the gravity load in both the transverse and longitudinal directions, respectively. The figures show that the overall response and force capacity was comparable in both cases. The main difference was the response in the last group of cycles, where a drop in the capacity occurs because of more damage in the bent cap as a result of the additional moment from the gravity load. Applying the 8% gravity load showed a similar response under the last group of cycles to the case of the 10% gravity, as seen in the final calibrated model results presented below. Thus, it was concluded that reducing the gravity load to 8% for the post-test analysis to better match the bent cap beam moment demands should not affect the overall behavior and is a reasonable approximation.
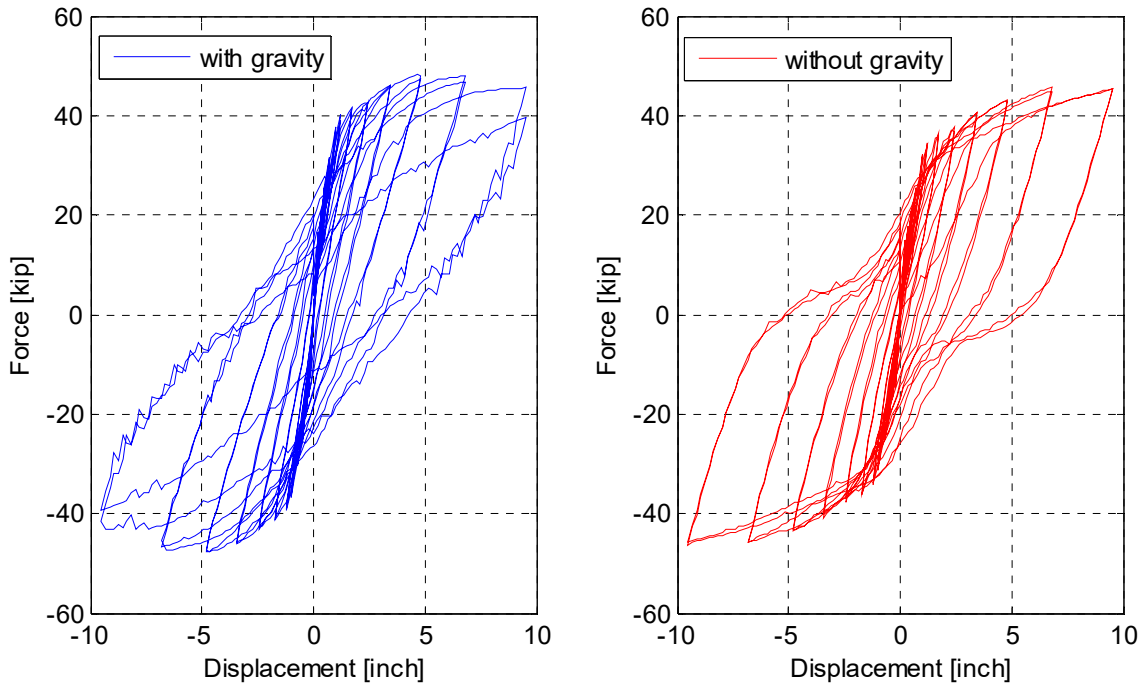
Figure 4.4   Force-displacement relationship in the transverse direction with and without the constant gravity load.
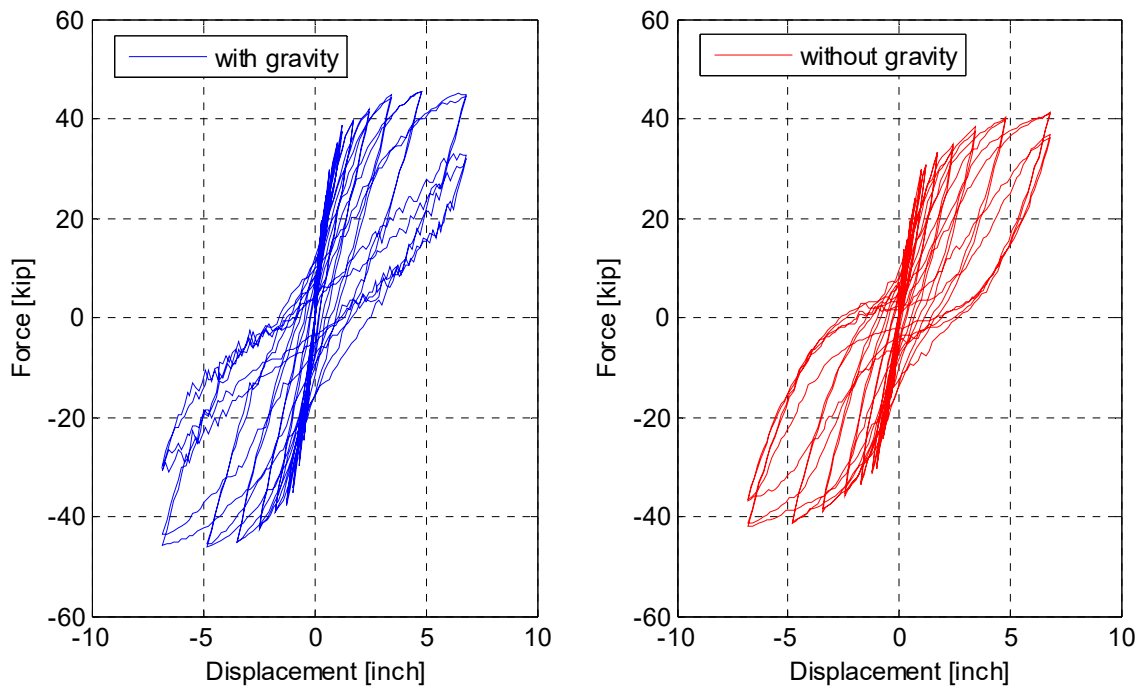
Figure 4.5   Force-displacement relationship in the longitudinal direction with and without the constant gravity load.

4.1.3 Effect of Model Parameters

To facilitate deciding on the best set of material parameters, each of the concrete total crack strain model parameters: Young's modulus (E_c), compressive strength (f_c), tensile strength (f_t), fracture energy (G_f), stress increase due to confinement, and reduction due to lateral cracking was varied one at a time using input from the material tests. The mean values from the material tests for all three concrete lifts were used for the total strain crack model parameters. Additionally, each parameter was varied one a time using the mean value, 50% less than the mean value, and 50% higher than the mean value. This variation used this range of a 50% difference to investigate the relative effect of changing such material parameters on the overall response of the specimen model rather than for calibration purposes. The transverse direction only cyclic loading pattern was used for a computationally inexpensive study.

The force-displacement relationship due to the transverse direction only cyclic loading was compared when each of the previously mentioned parameters was varied. Figure 4.6 shows the effect on the global response due to varying the concrete Young's modulus (E_c) within 50% less or higher than the mean value. Similarly, the overall force-displacement response due to the compressive strength (f_c), tensile strength (f_t), and fracture energy (G_f) variation is shown in Figure 4.7 to Figure 4.9, respectively. Additionally, the total crack strain model in DIANA offers some other modifications to the constitutive model to account for other phenomena, such as compressive strength increase due to confinement and the Vecchio and Collins [1993] relationship for lateral crack reduction. The effect of these two modifications was investigated as well. Figure 4.10 and Figure 4.11, respectively, show the force-displacement relationships when the confinement and crack reduction modifications were either incorporated or not; one parameter at a time.
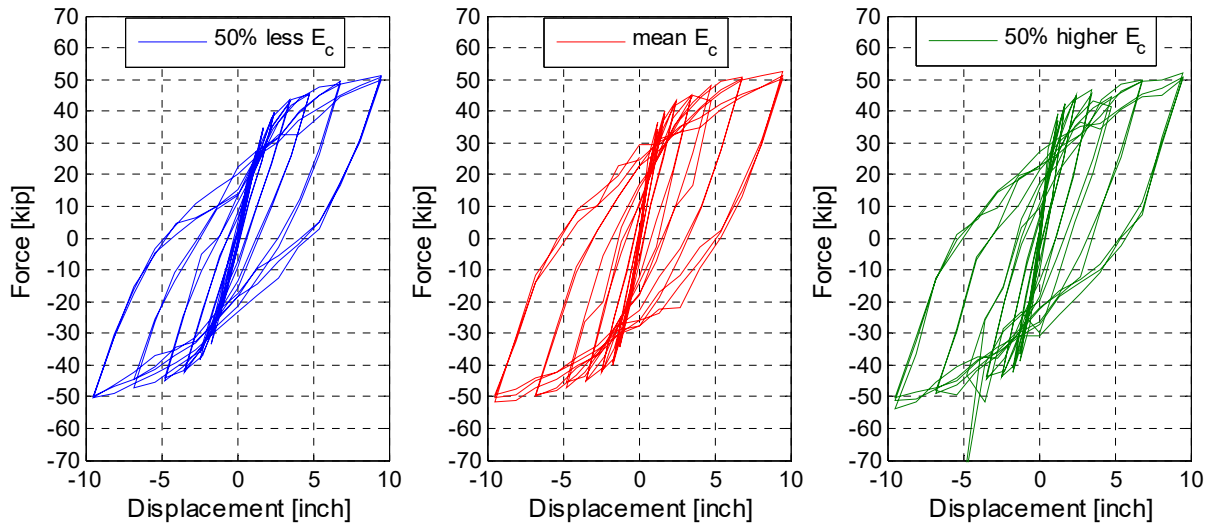
Figure 4.6   **Force-displacement relationships for different Young's modulus (E_c) values.**
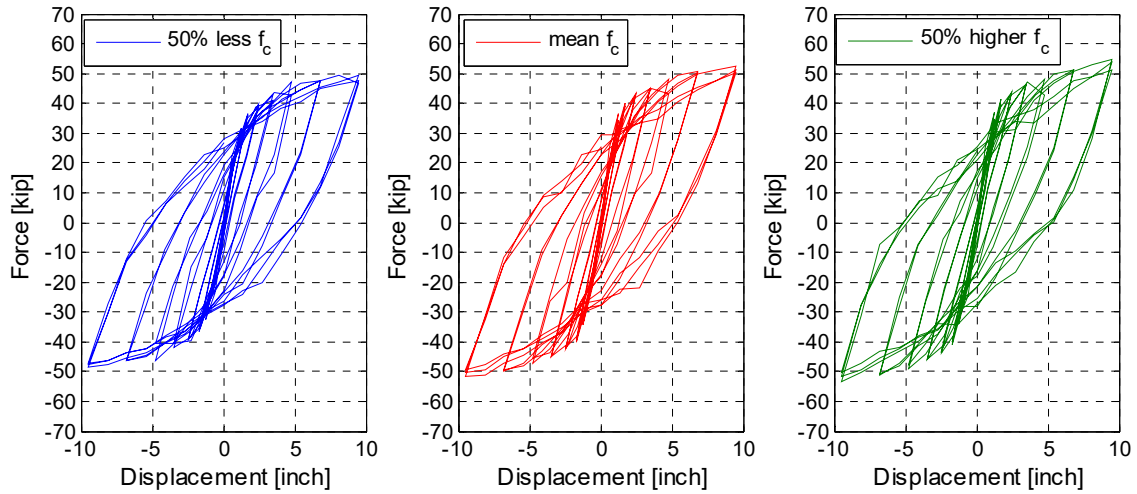
Figure 4.7   Force-displacement relationships for different compressive strength (f_c) values.
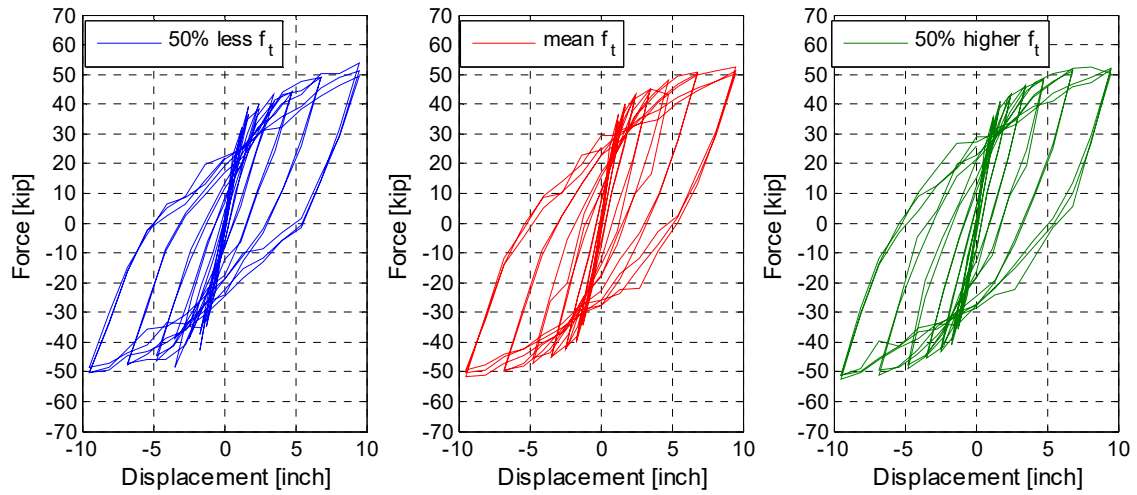
Figure 4.8   Force-displacement relationships for different tensile strength (f_t) values.
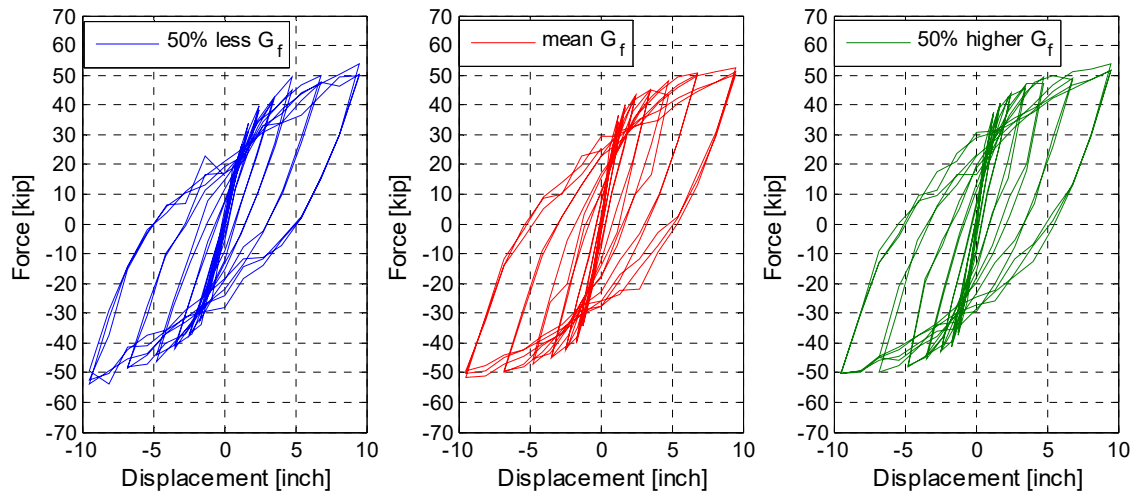
Figure 4.9   Force-displacement relationships for different fracture energy (G_f) values
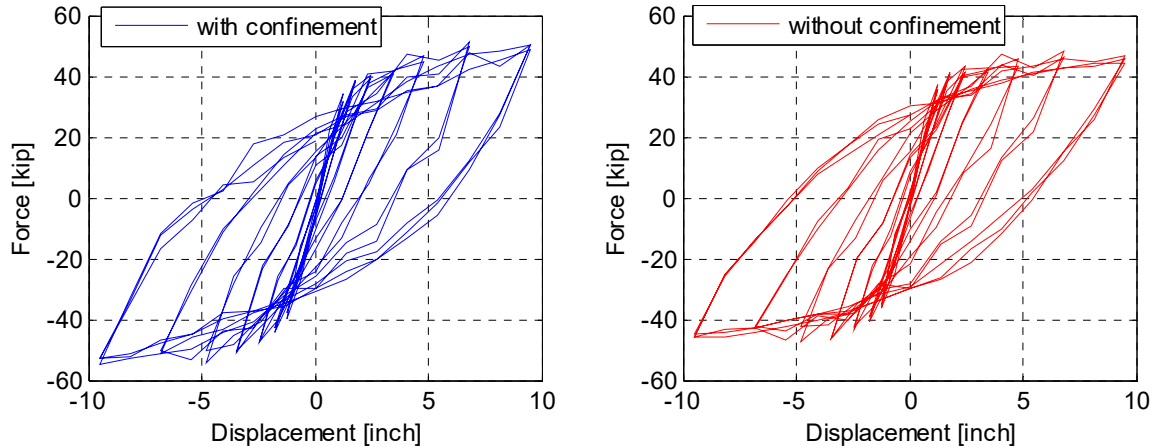
Figure 4.10　**Force-displacement relationships when the stress increase due to the confinement option is either incorporated or not in the model.**
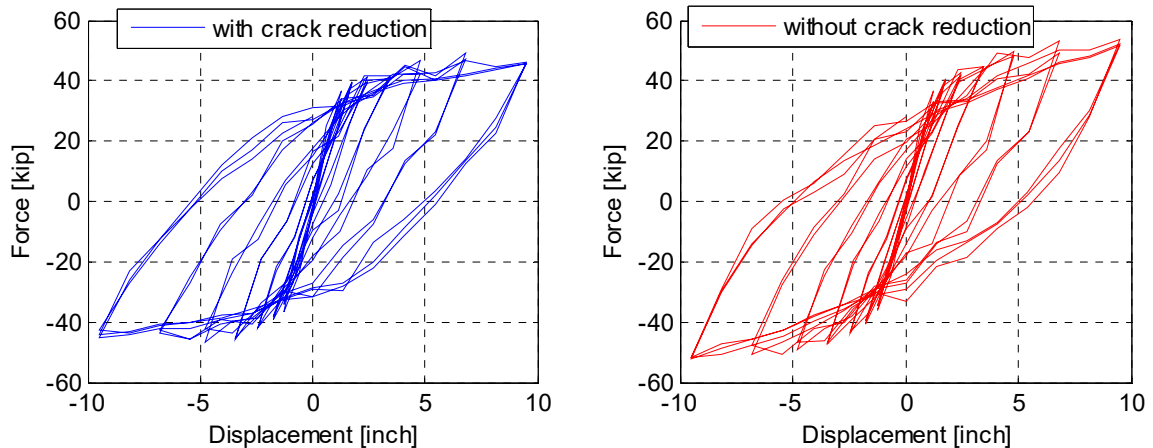
Figure 4.11　**Force-displacement relationships when the reduction due to lateral cracking (as defined by Vecchio and Collins [1993]) is either incorporated or not in the model.**

In general, it can be observed from Figure 4.6 through Figure 4.11 that none of the material model parameters significantly changed the response, the force capacity, or the mode of failure. The parameter that showed a relatively sizable change in the force capacity when it was not incorporated is the Vecchio and Collins [1993] crack reduction, and to a lesser extent the confinement option. Thus, it was concluded that the crack reduction modification always needs to be incorporated for a better capacity capping behavior to best match the experimental results. Interestingly contradicting what was expected, it was shown that using only one set of material properties for the entire model, i.e., for the column, cap beam, and box-girder, did not reflect the natural difference in the concrete properties from the different lifts as varying the compressive strength, for instance, did not affect the response significantly. Therefore, using two different sets of material parameters; one for the column and the other for the box-girder and cap beam were decided for the next phase of exploring the different ways of calibrating the model. The discussion from three different models that used different combinations of sets of material parameters is presented next.

4.1.4 Elastic Column versus Elastic Superstructure

An investigation of whether varying the set of material input parameters for the column from the superstructure affects the response was conducted. This was mainly done to recognize the natural difference in the concrete lifts used during to the different stages of construction. The first lift included only the specimen seat beams and the deck slab, while the second lift included the rest of the box-girder and bent cap beam. Thus, a set of material properties from the second lift was a better candidate for the superstructure concrete model. Finally, the third lift was only for the column; accordingly, the material input for the column constitutive model should be based on the third lift material test results.

To study the effect of the variation in the column material model from the superstructure one, three different DIANA models were utilized. The first model used the mean values from the second concrete lift material tests for defining the superstructure model parameters, whereas the third lift tests were used for the column material input. The second and third models represented the two extreme cases: (1) the column or the superstructure is entirely linear elastic and (2) damage and inelasticity are limited to the counterpart of the elastic one. Thus, the second model used an elastic concrete model for the superstructure, and the column concrete model properties were based on the third concrete lift material tests. The third model used the second concrete lift material tests to define the superstructure material input, while an elastic model was used for the column. The three different models are designated as models A, B, and C, respectively.

The force-displacement relationships in both the transverse and longitudinal directions for the three models are compared in Figure 4.12 and Figure 4.13, respectively. The elastic superstructure case, model B, is shown in the left side of the figures, whereas the case of the elastic column, model C, is shown in the right side of the figures. The full inelastic model with different material properties for column and superstructure, model A, is shown in the middle part of the figures. Clearly, model A represents a transition between the other two extreme cases in terms of the mode of failure and overall system response. A much wider hysteresis and energy dissipation occurred when all the damage was concentrated in the inelastic column of model B. In contrast, a narrower hysteresis, less energy dissipation mechanism, and severe pinching around the zero force value during the unloading were observed when the damage was only concentrated in the superstructure of model C. The response of the full inelastic model with two different sets of material properties was somewhere in-between the two extreme cases of models B and C. This observation was valid for the behavior in both the transverse and longitudinal directions

Two main conclusions can be drawn: (1) the column mode of failure is much more ductile than the superstructure mode of failure, which agrees with the seismic capacity design approach where the superstructure is capacity protected to remain essentially elastic; and (2) the observed experimental response showed a ductile behavior that is, in a generic sense, closer to model B behavior than model C. Therefore, an informed calibration procedure would to push the column properties to the lower bound of the material test values, whereas the superstructure material model is better to adopt the upper bound that approaches the elastic behavior. The two sets of material parameters were adjusted accordingly, and the results were found to be reasonably comparable to the experimental results.
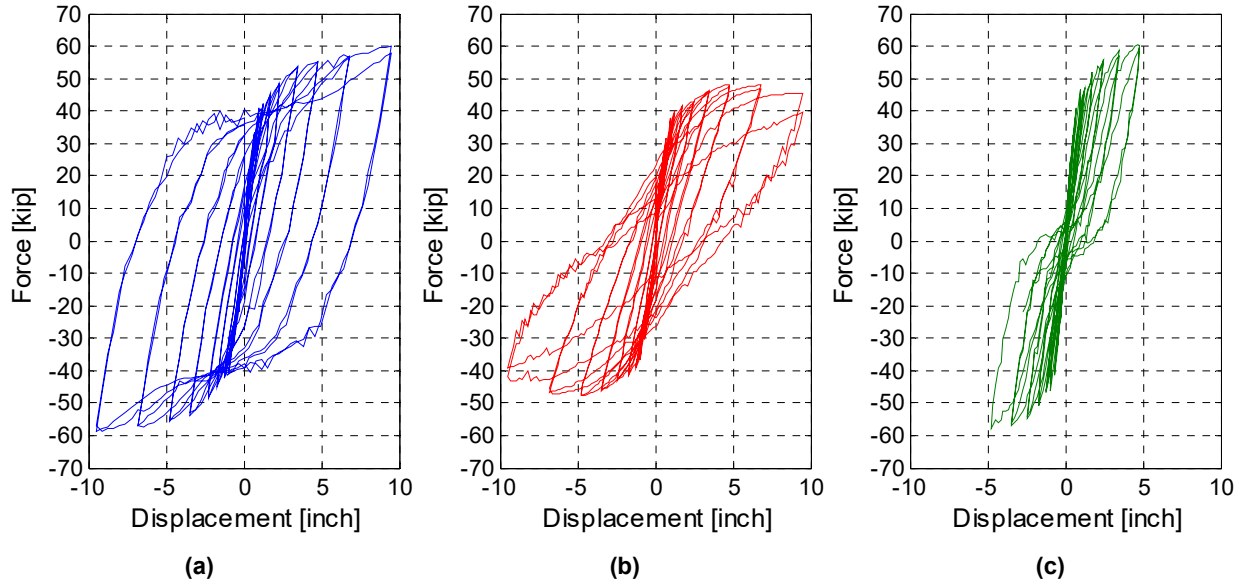
Figure 4.12 Force-displacement relationships in the transverse direction for (b) the fully inelastic model A; (a) the elastic superstructure model B; and (c) the elastic column model C (right).
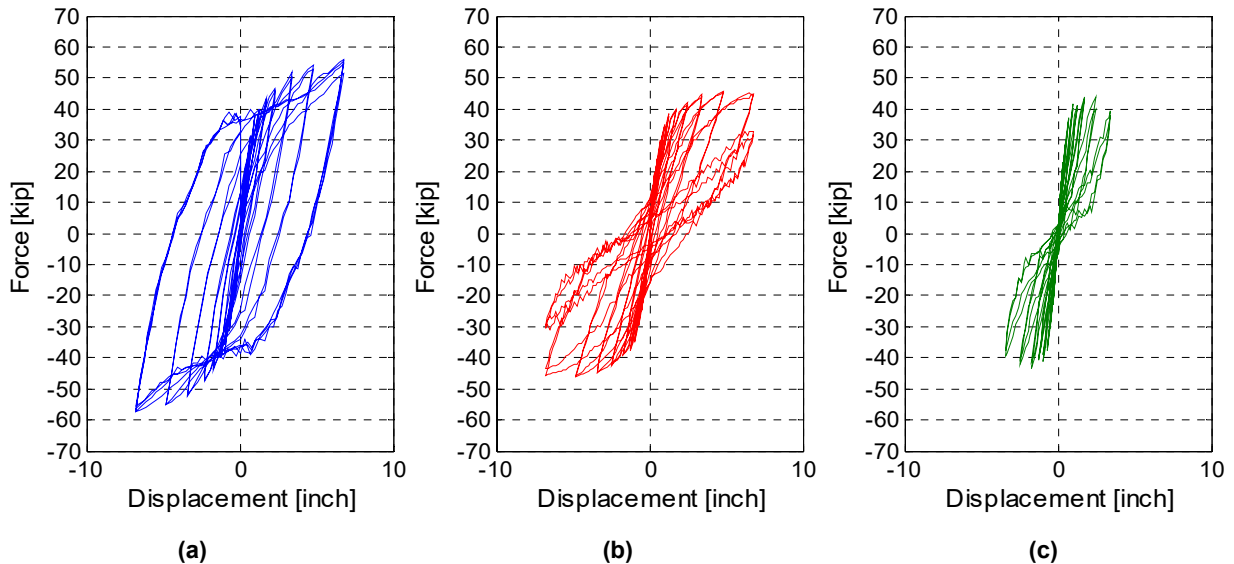
Figure 4.13 Force-displacement relationships in the longitudinal direction for (b) the fully inelastic model A; (a) the elastic superstructure model B; and (c) the elastic column model C.

4.1.5 Final Calibrated Model

The final calibrated model that reasonably matched the experimental results was based on using two different sets of parameters as previously mentioned: one for the column and the other for the bent cap beam and box-girder. This was intended to reflect the different concrete properties of the lifts used to construct the column and superstructure. Accordingly, the input for the column concrete was based on the lower bound values of the third concrete lift material tests. The superstructure, i.e., the bent cap beam and the box-girder, material input was based on the

upper bound of the second concrete lift material test results. Selected results for the global and local behavior from the final calibrated model and relevant comparisons with the experiment results are presented below.

4.1.5.1 Global Behavior

The force-displacement relationships obtained from the final calibrated model in both the transverse and longitudinal directions are shown in Figure 4.14 and Figure 4.15, respectively. The response from the calibrated model is compared to the corresponding experimental response from Specimen No. 1 cyclic loading tests in the same figures. Additionally, the bent cap beam moment history, recorded at Section B, from the calibrated model analysis and the experiments were compared and shown in Figure 4.16. Note that the calibrated FE model reasonably captured the force capacity in both the transverse and longitudinal directions, and the maximum cap beam moment observed during the test with less than 5% difference. The calibrated model provides confidence for further research in investigating cap beam capacity and other design implications.
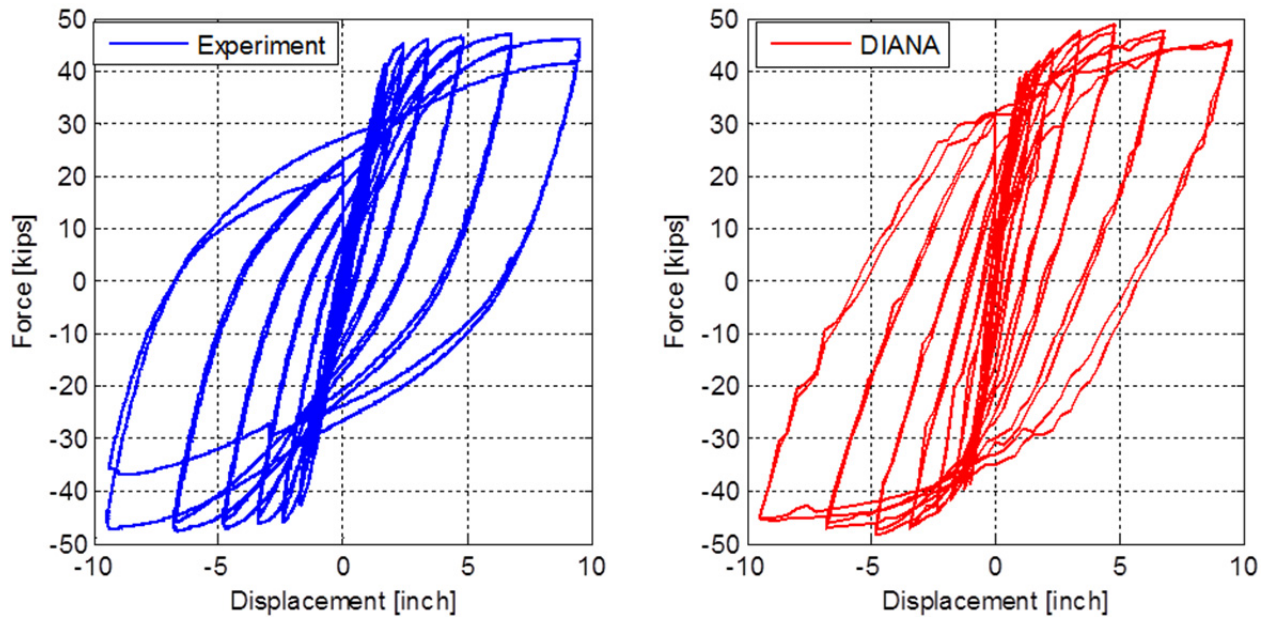
Figure 4.14   Force-displacement relationship in the transverse direction from Specimen No. 1 cyclic tests and the final calibrated DIANA FE model.
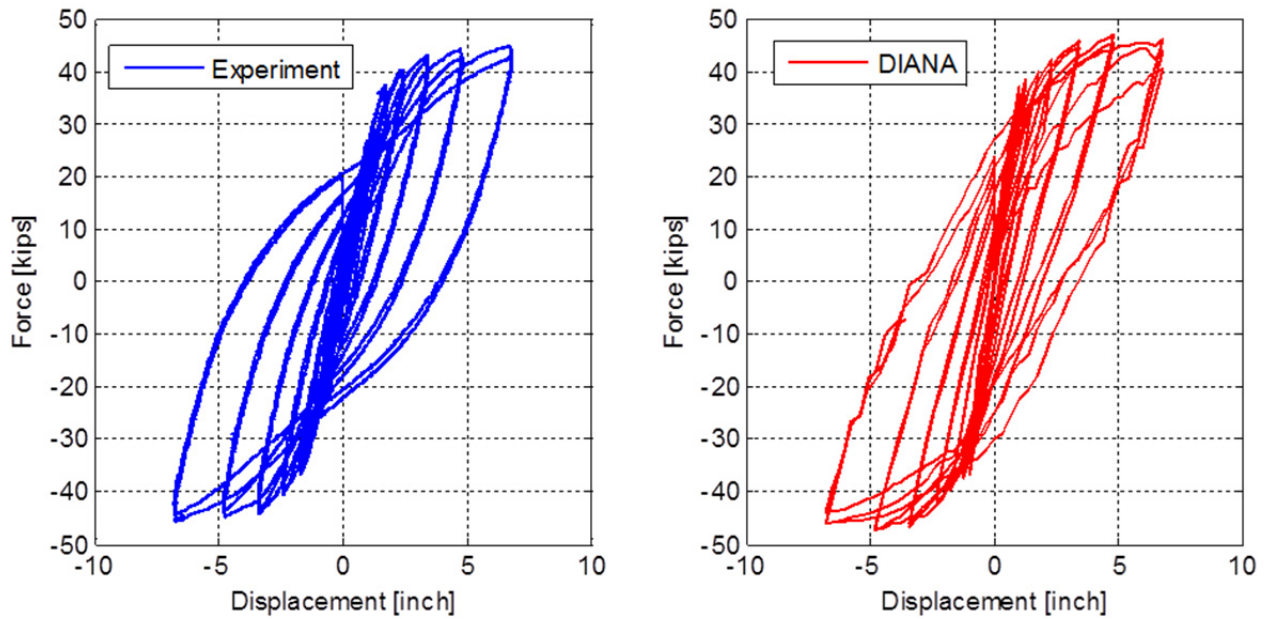
Figure 4.15 Force-displacement relationship in the longitudinal direction from Specimen No. 1 cyclic tests and the final calibrated DIANA FE model.
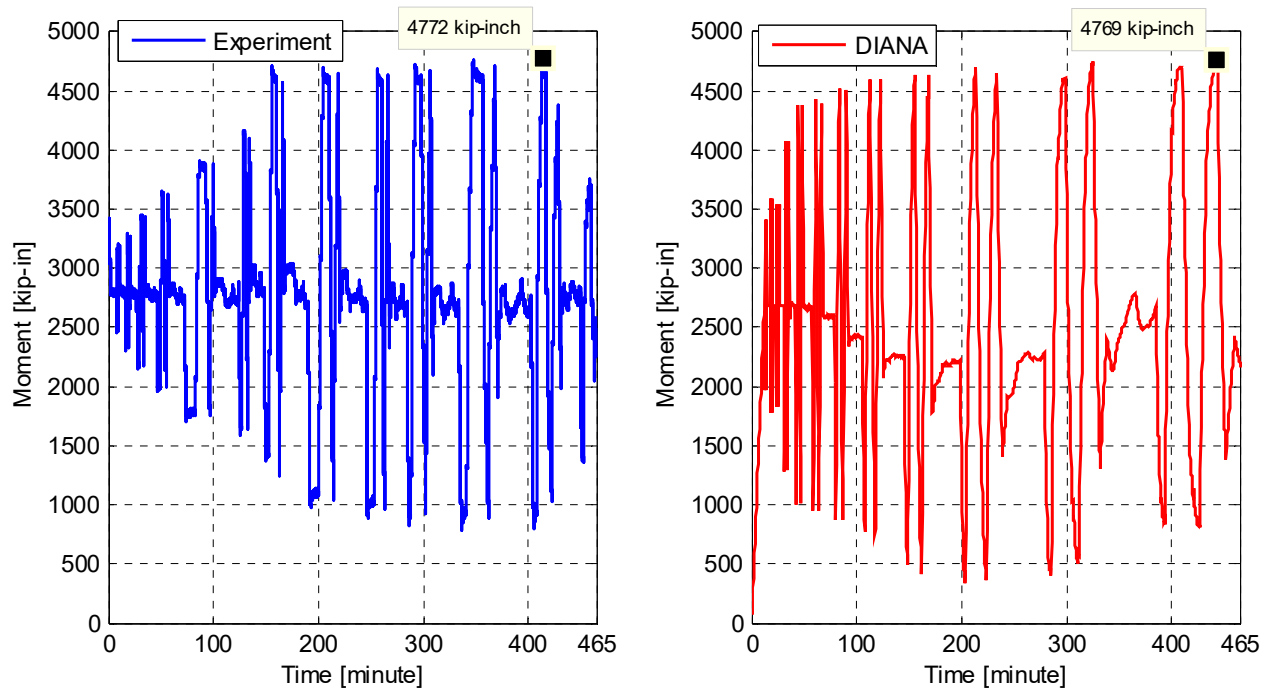
Figure 4.16 Bent cap beam moment history at Section B from Specimen No. 1 cyclic test and the final calibrated DIANA FE model.

4.1.5.2 Local Behavior

To complement the global behavior discussion, the calibrated model was used to investigate several local behavior response quantities as well. Figure 4.17 shows a view from FX+, the DIANA pre- and post-processor, for the crack pattern in the vicinity of the column and bent cap beam as the bi-directional loading progressed. The embedded reinforcement strains were recorded from the analysis; a sample of the strain history due to all the loading cycles at Sections B and D of one of the bent cap embedded reinforcing bars is shown in Figure 4.18. The same strain history from the FE model at Section B is compared to that from the experiments in Figure 4.19. Although the strain values are somewhat different, the model captured the strain evolution as loading progressed in a reasonable manner.

The strain values from the DIANA analysis, as is the case of other local response quantities, are very sensitive to the nonlinear FE solution. Thus, no main conclusions can be drawn based on the FE local behavior; only major observations or trends are noted. Accordingly, the strain distribution was obtained from the analysis and was reordered at the peaks of the different loading cycles to check how accurately the model captures local behavior. The strain distribution at four small loading levels corresponding to drift ratios of 0.4%, 0.8%, 1.4%, and 2.7% and equivalent to ductility levels 0.28μ, 0.56μ, 1.0μ, and 1.96μ, respectively, is shown in Figure 4.20 and Figure 4.21 for Sections B and D, respectively. In addition, Figure 4.22 and Figure 4.23 show the strain distribution for larger loading levels at drift ratios of 3.9%, 5.3%, 7.6%, and 10.5% at Sections B and D, respectively. Note that while the bent cap beam and the box-girder remained elastic at the lower load levels, a uniform bell-shaped strain distribution occurs. At the higher load levels, a nonlinear non-uniform distribution was observed, which was still reasonable enough when compared to one of the strain distributions obtained experimentally. The local strain distribution was obtained for completeness and to explore the capabilities and accuracy of the analysis rather than using it for arriving at any conclusion regarding the effective flange width. However, the results show great potential for further enhancements of the model to capture the local behavior even more accurately.
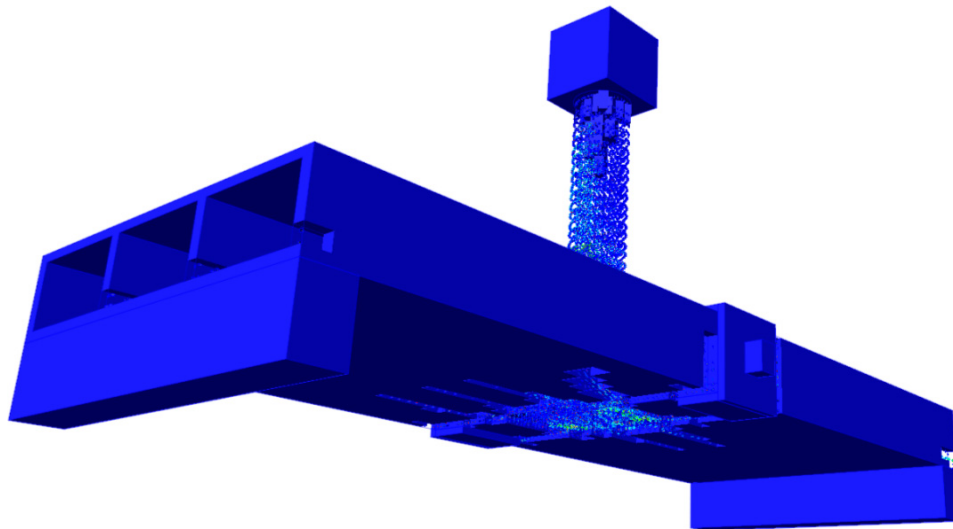
Figure 4.17   Overview of the crack pattern in the vicinity of the column and bent cap beam as observed from the DIANA calibrated model after the bi-directional cyclic load was applied.
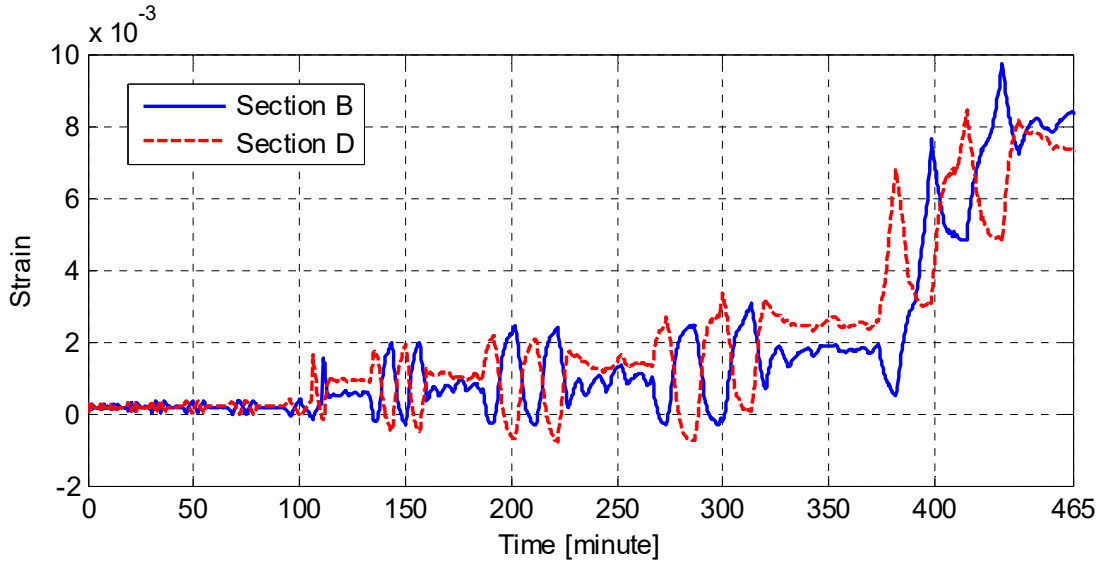
Figure 4.18   Strain history at one of the bent cap reinforcing bars at Sections B and D obtained from the calibrated FE model for all the loading cycles.
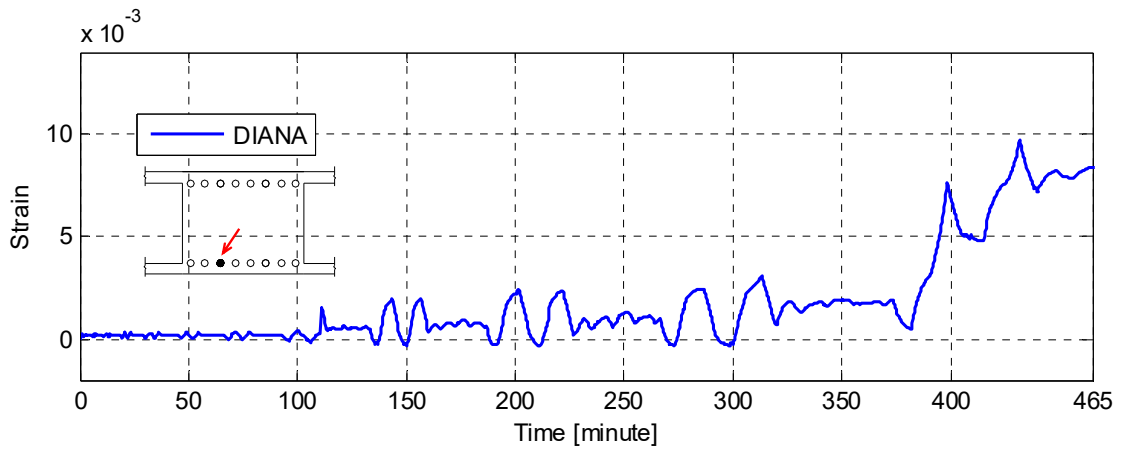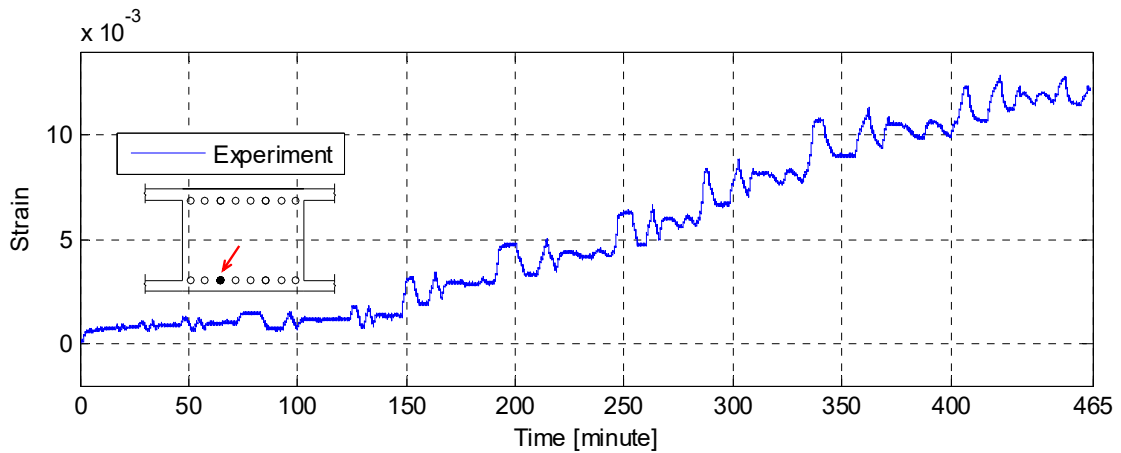
Figure 4.19   Comparison of the strain history at one of the bent cap reinforcing bars in the tension side at Section B from Specimen No. 1 cyclic tests and the calibrated FE model.

120
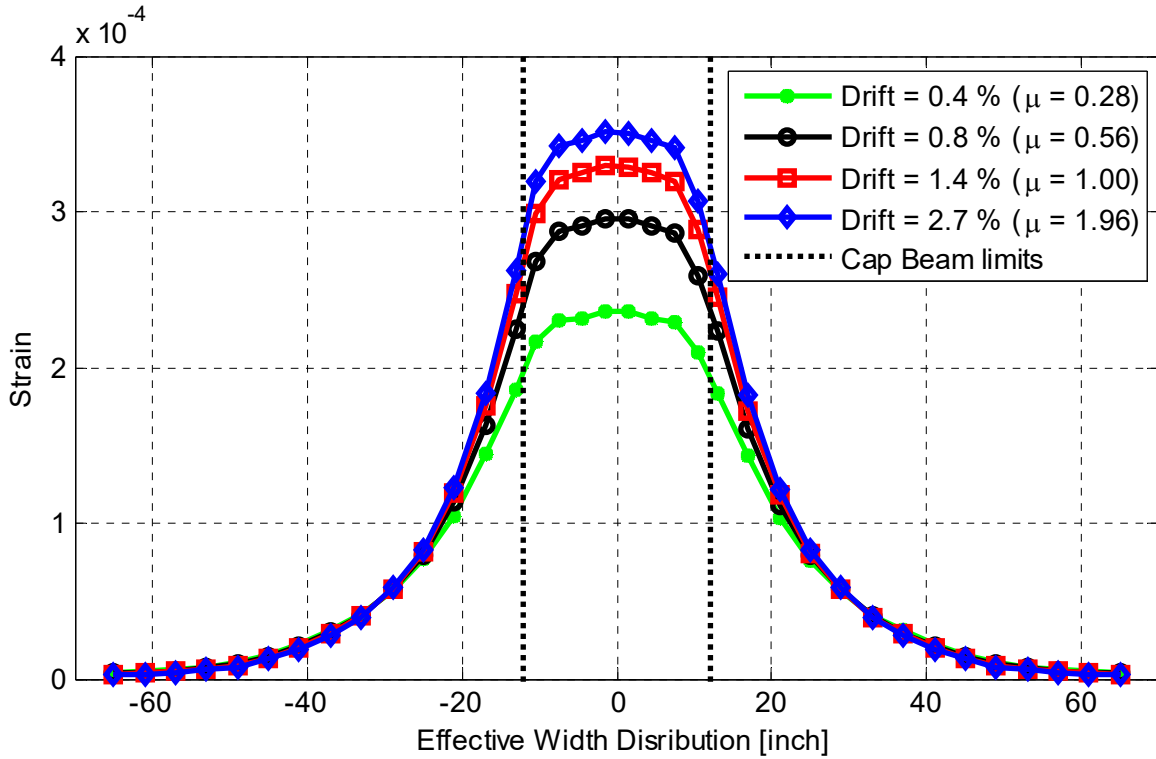
Figure 4.20 Strain distribution at Section B for four different small loading levels as obtained from the calibrated FE model.
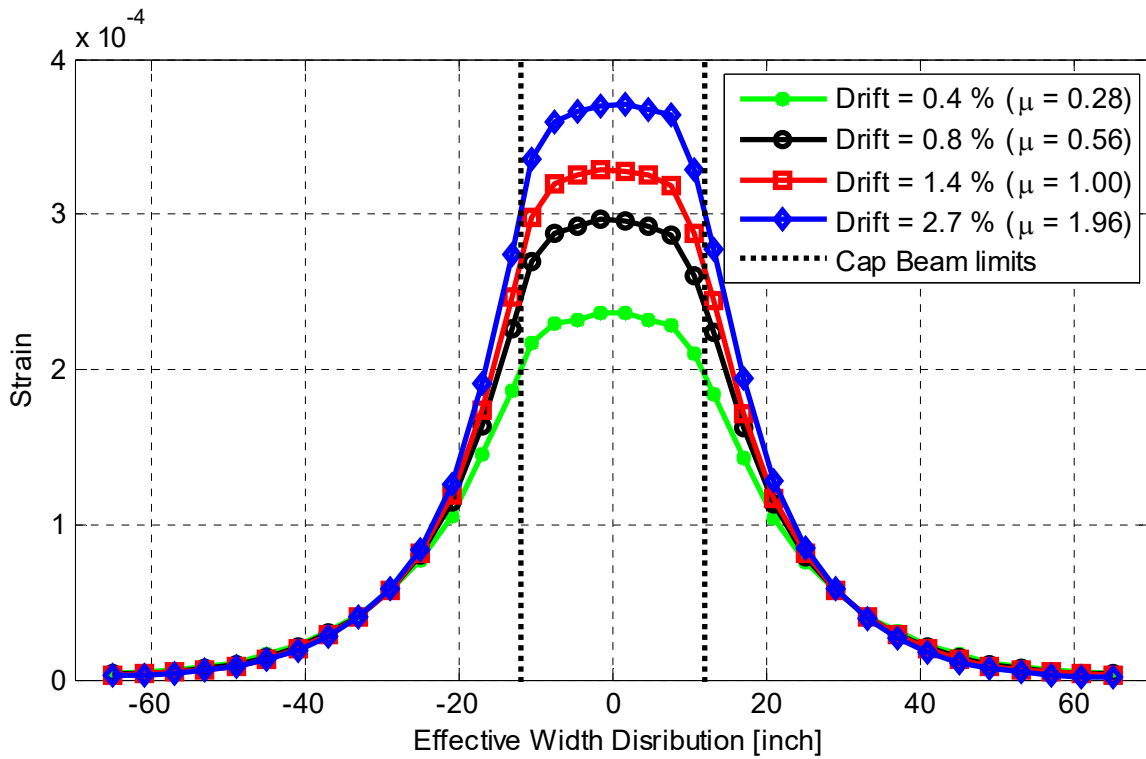
Figure 4.21 Strain distribution at Section D for four different small loading levels as obtained from the calibrated FE model.
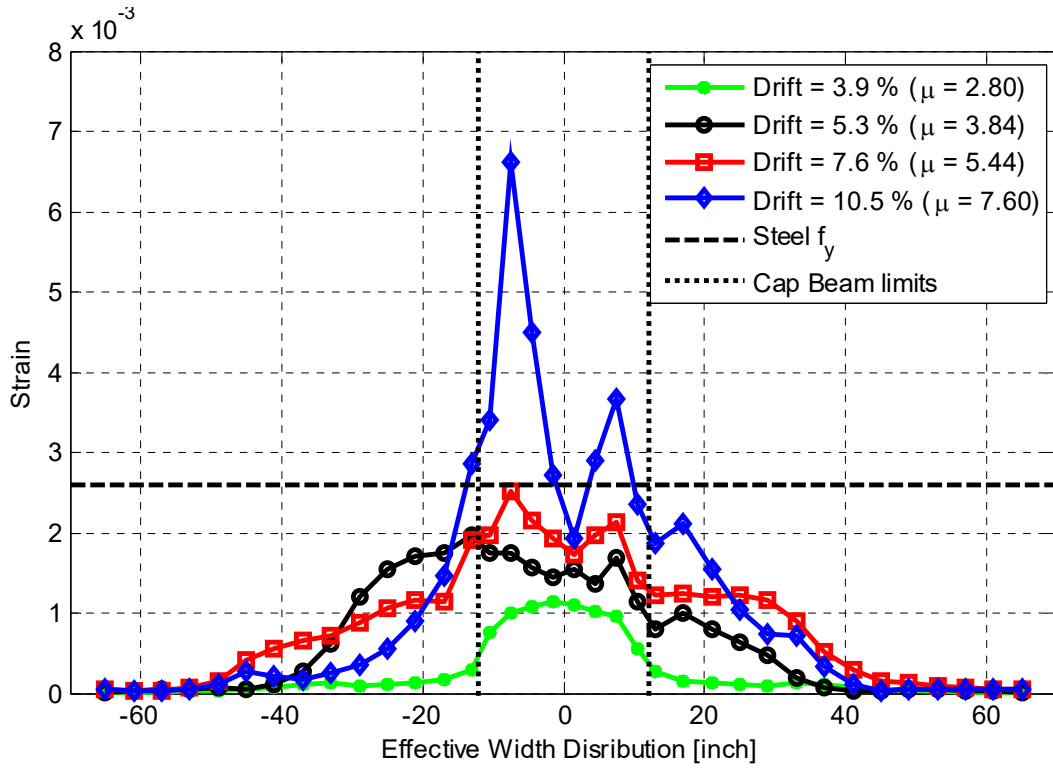
Figure 4.22   Strain distribution at Section B for four different large loading levels as obtained from the calibrated FE model.
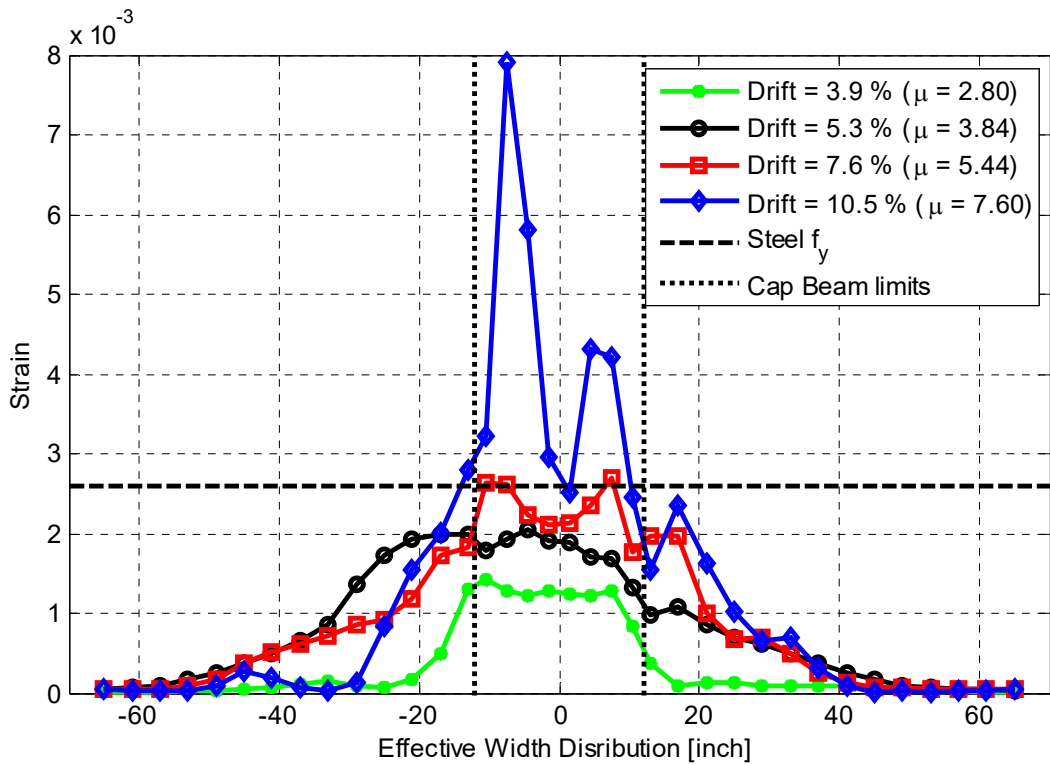
Figure 4.23   Strain distribution at Section D for four different large loading levels as obtained from the calibrated FE model.

4.2   FINITE ELEMENT ANALYSIS FOR DIFFERENT BENT CAP DESIGNS

The calibrated sets of material input parameters in the DIANA FE 3D model for the test specimen were used to investigate the bent cap capacity in case of the original specimen design and two other hypothetical designs. The main objective of this part of the study is to complement the experimental program through determining the bent cap beam capacity and the contribution of the box-girder to the overall system capacity by comparing different cases of the bent cap designs. In this section, less reinforcement in the bent cap was used to form two hypothetical cases of under reinforced bent cap beams to investigate whether the contribution from the box-girder to the system capacity is affected by the bent cap contribution or design. For this reason, the test specimen bent cap original 8 #5 top and bottom reinforcement were replaced with 8 #4 top and bottom reinforcement for the first hypothetical design, and 8 #3 top and bottom reinforcement for the second hypothetical design. For simplicity, the three designs are designated as original design (8 #5), design 1 (8 #4), and design 2 (8 #3).

The objective of this analysis is to determine the bent cap beam capacity rather than actual system response, given that the exact system response has been already identified from both experimentally and through FE analysis. Here, we investigate limiting the mode of failure to concentrate the damage only in the bent cap beam. Accordingly, the calibrated set of material parameters for the superstructure, i.e., the bent cap and the box-girder, was used along with an elastic concrete model for the column, amplifying the demand on the bent cap beam until the capacity is reached. Three different types of analysis were used to determine the bent cap beam capacity. These are nonlinear quasi-static analysis using the bi-directional cyclic loading pattern, vertical pushover analysis, and lateral pushover analysis. Additionally, the full inelastic calibrated model was used to compare the system response from the three designs regardless of whether the cap beam reaches its capacity or not.

4.2.1 Inelastic Model: Cyclic Loading

The final calibrated inelastic DIANA FE model for the test specimen that used two sets of material parameters for the column and the superstructure was further utilized to investigate the overall response when the bent cap beam reinforcement is changed. The three different bent cap designs previously-mentioned were adopted in the inelastic FE model, which was analyzed for three cases under constant gravity load and bi-directional cyclic loading. The obtained force-displacement relationships in the transverse and longitudinal directions from the three designs are compared in Figure 4.24 and Figure 4.25, respectively. The bent cap beam moment history at Section B is compared for the different cases as well in Figure 4.26.

The overall response illustrated in the force-displacement relationships denotes that the system capacity was essentially unchanged irrespective of the bent cap reinforcement as the model of mode of failure and the system capacity was governed by the column rather than the bent cap or box-girder. As observed in Specimen No. 1 cyclic tests, this confirms the observation that the bent cap beam remained essentially elastic as required by the adopted Caltrans and AASHTO capacity design provisions. The moment history shown in Figure 4.26 indicates that similar demand, dictated by the moment capacity, was transferred to the bent cap beam in the three reinforcement designs. These results show that in a successful capacity design approach, only the minimum amount of reinforcing steel is needed in the bent cap beam as long as it is guaranteed that only the column attracts all the damage in case of extreme events. In other

words, if the bent cap capacity is accurately estimated, unnecessary additional bent cap reinforcement can be avoided in the capacity check, and the bent cap design can be optimized accordingly. More details are discussed in the design implications section.
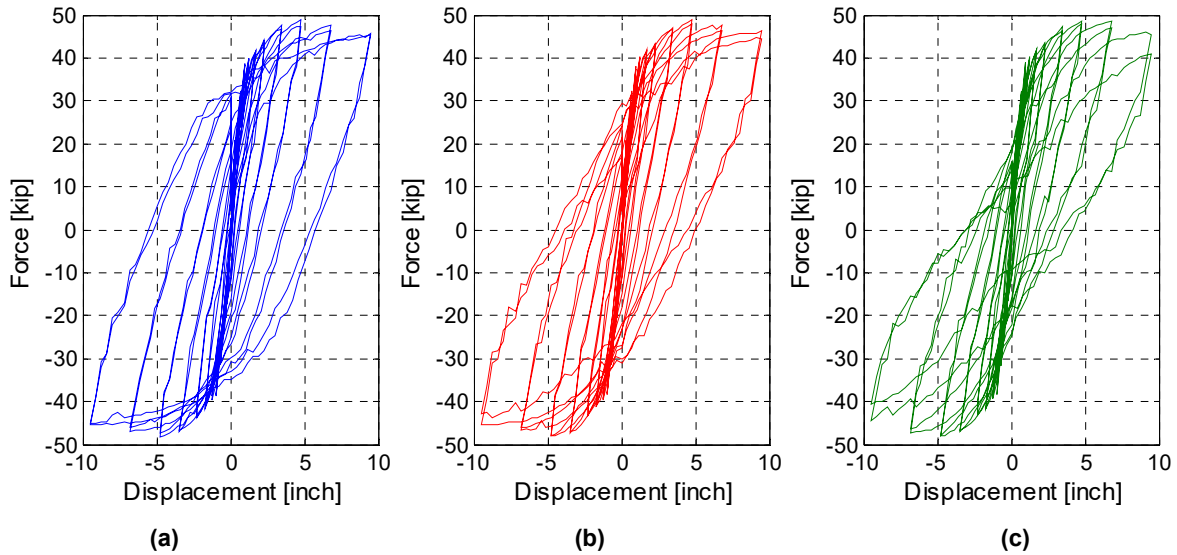
Figure 4.24　Force-displacement relationships in the transverse direction from the calibrated inelastic FE model for three bent cap cases: (a) 8 #5 top and bottom of original design; (b) 8 #4 top and bottom design 1; and (c) 8 #3 top and bottom design 2.
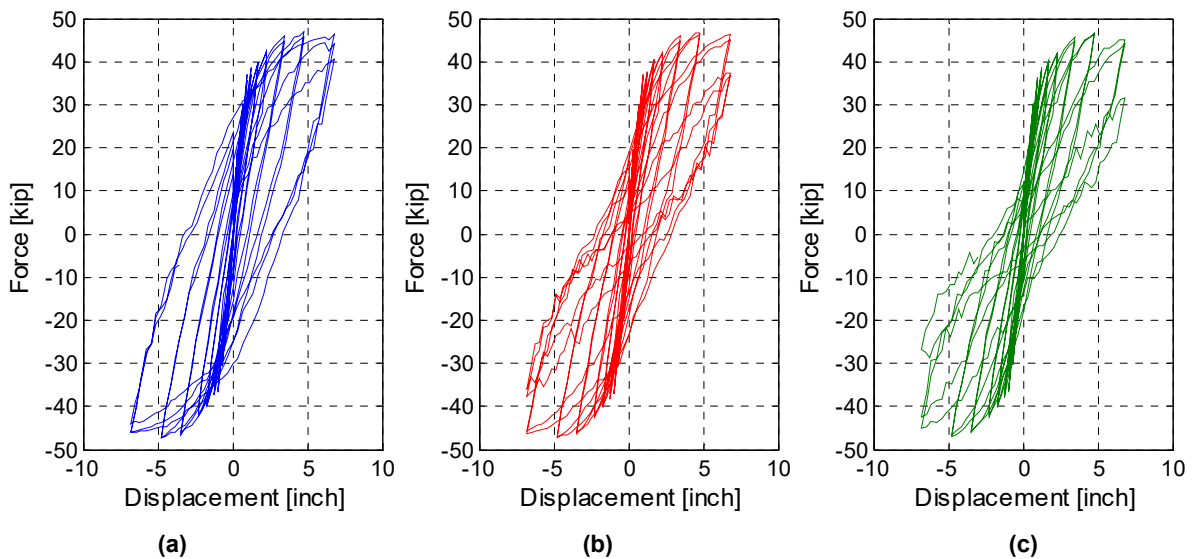
Figure 4.25　Force-displacement relationships in the longitudinal direction from the calibrated inelastic FE model for three bent cap cases: (a) 8 #5 top and bottom original design; (b) 8 #4 top and bottom design 1; and (c) 8 #3 top and bottom design 2.
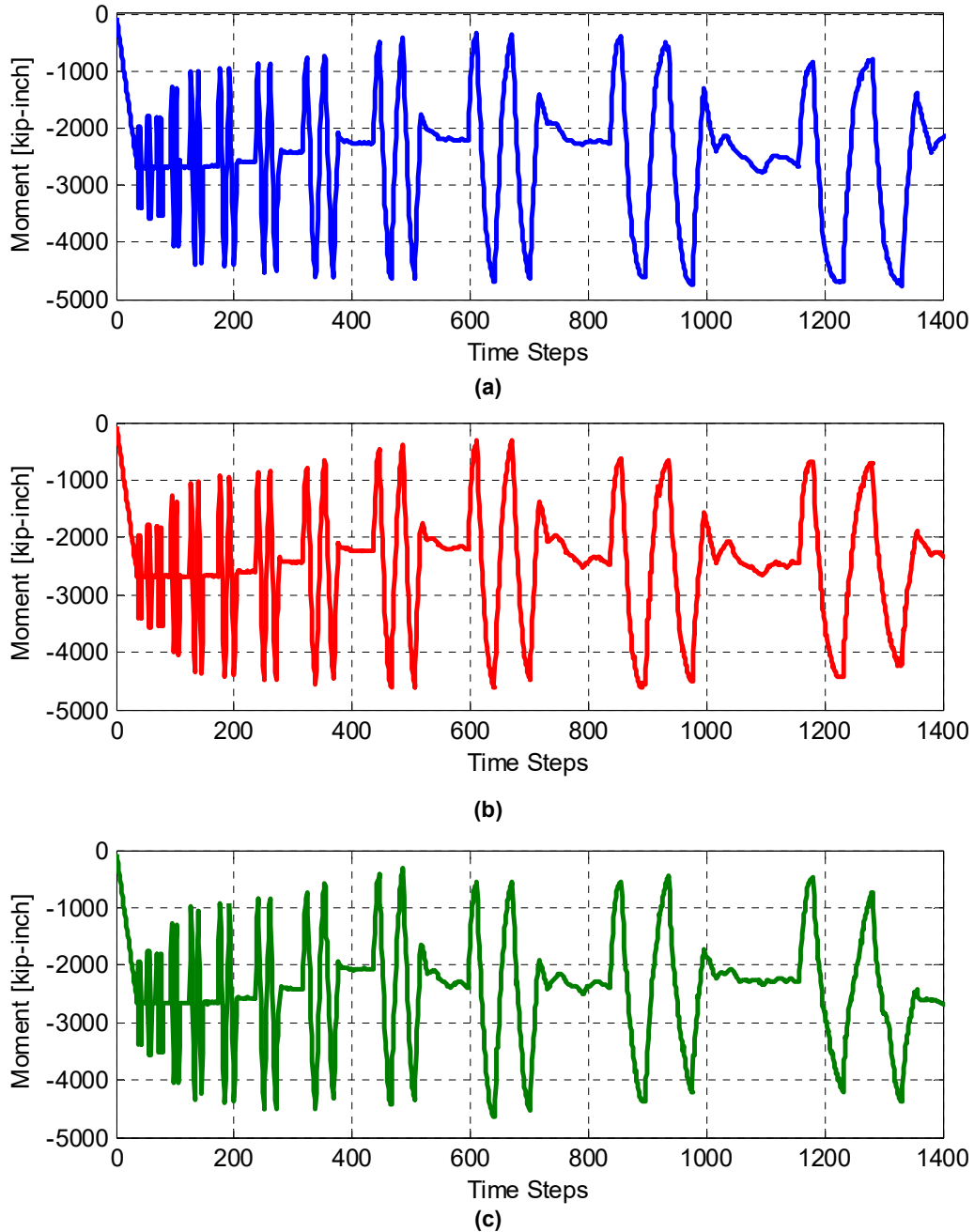
Figure 4.26 **Bent cap beam moment history at Section B from the calibrated inelastic FE model for three cases: (a) 8 #5 top and bottom original design; (b) 8 #4 top and bottom design 1; and (c) 8 #3 top and bottom design 2.**

4.2.2 Elastic Column Model: Cyclic Loading

A completely different perspective of the bent cap beam capacity design check is tackled through the elastic column FE model. The inelastic behavior was limited to the bent cap beam and the box-girder; the column concrete remained elastic to force the damage into the superstructure to analytically determine the bent cap beam and overall system capacity. This hypothetical case is not allowed by the design codes cited within. A similar case might be realized by an overdesign

of a column retrofit to the extent it migrates all the damage to the bent cap beam. Thus, providing an accurate way of estimating the bent cap beam capacity is very beneficial for the seismic capacity design check and for designing informed retrofit strategies.

Here, the final calibrated FE model was modified such that the column used an elastic concrete material model, but the reinforcing bars were still modeled using Von Mises plasticity along with the Voce hardening previously discussed in Chapter 4, Part 1. A bi-directional cyclic loading under constant gravity was applied for the three cases of bent cap reinforcement. Figure 4.27 and Figure 4.28 compare the force-displacement relationships for those bent cap designs from the elastic column model in the transverse and longitudinal directions, respectively; Figure 4.29 shows the bent cap moment history at Section B for the different cases.
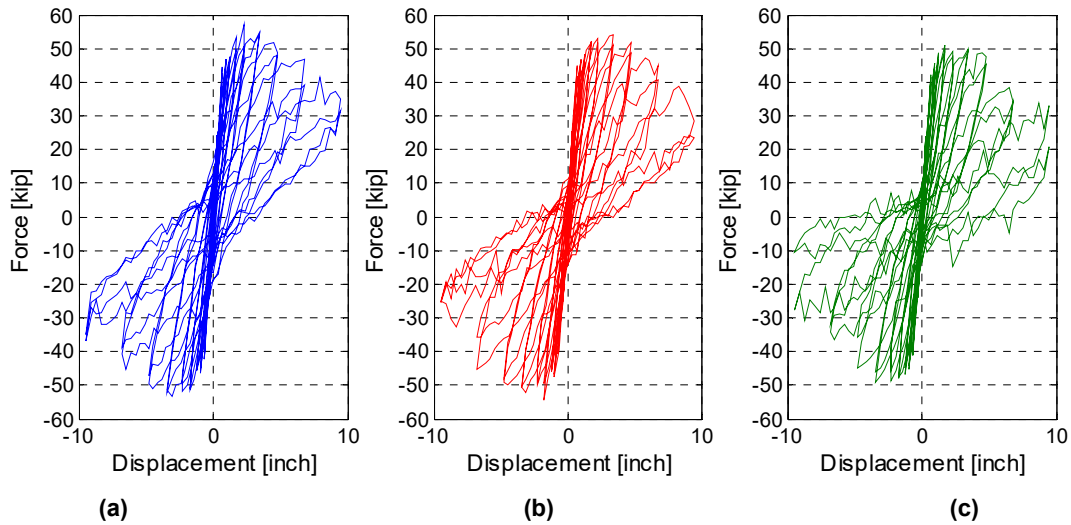
Figure 4.27 **Force-displacement relationships in the transverse direction from the elastic column FE model for three bent cap cases: (a) 8 #5, (b) 8 #4, and (c) 8 #3.**
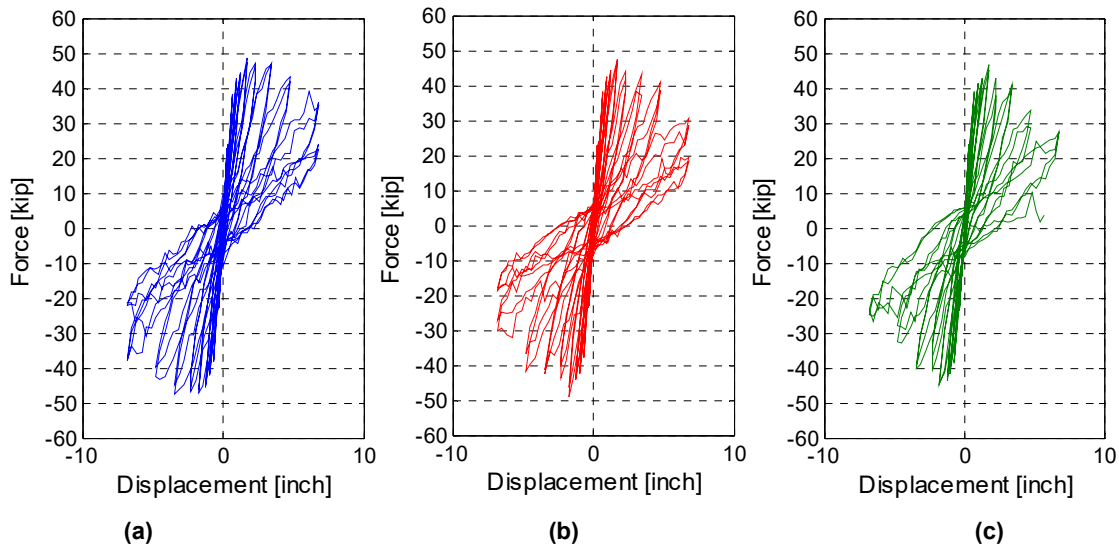
Figure 4.28 **Force-displacement relationships in the longitudinal direction from the elastic column FE model for three bent cap cases: (a) 8 #5, (b) 8 #4, and (c) 8 #3.**

126
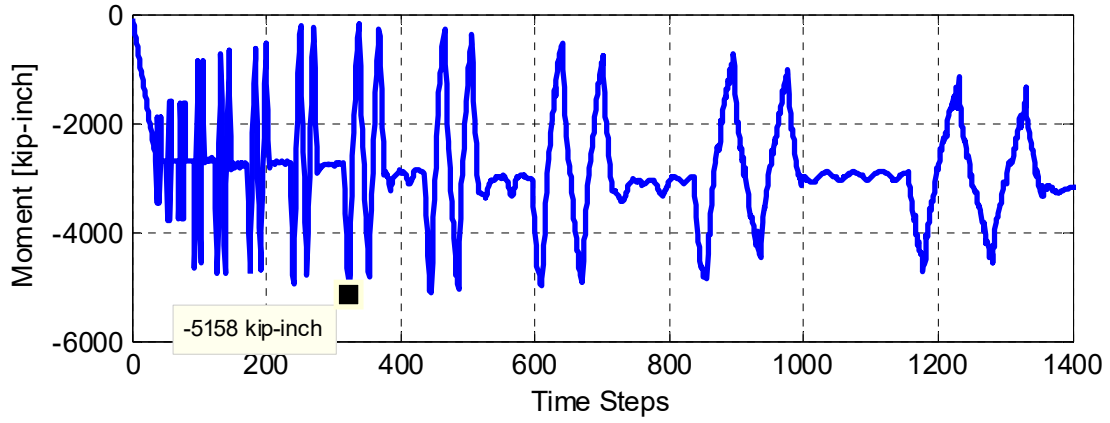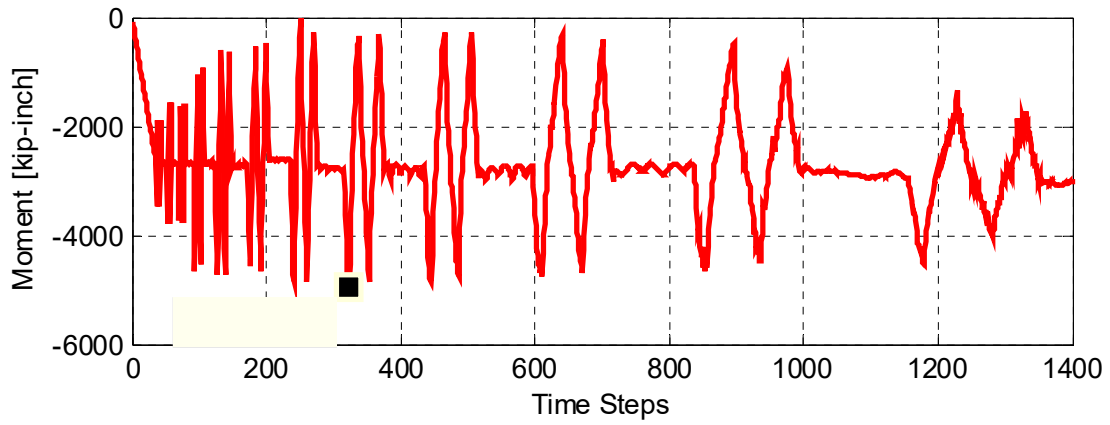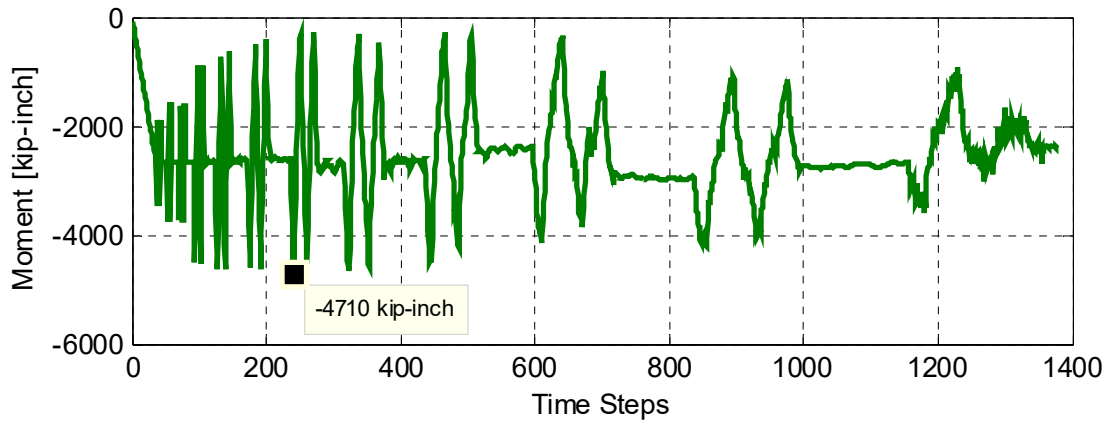
Figure 4.29   **Bent cap beam moment history at Section B from the elastic column FE model for three cases: (a) 8 #5 top and bottom original design; (b) 8 #4 top and bottom design 1; and (c) 8 #3 top and bottom design 2.**

127

The figures show that the overall system capacity was slightly increased when the mode of failure is governed by the bent cap capacity rather than the column. The hysteresis behavior is also different from the ductile column hysteresis as discussed previously. As expected, the bent cap capacity and the overall system capacity in turn was shown to vary as the cap beam design changed. However, the surprising observation is that such variation in the capacity is considered minor with respect to the major change in the bent cap reinforcement. The cap beam moment capacity, identified in Figure 4.29, was found to be 5158 kip-in., 4953 kip-in., and 4710 kip-in. for the case of 8 #5, 8 #4, and 8 #3 top and bottom bent cap reinforcement, respectively. These numbers indicate a maximum drop of 8.7% in the capacity versus an expected drop of almost 63% in capacity if the standard Caltrans provisions are adopted for capacity estimation while excluding slab reinforcement. The significance of these numbers are discussed in Section 4.4. However, the main conclusion that can be drawn from this part of the FE analysis is that there is significant redundancy and force redistribution in the box-girder as the damage and failure of the bent cap progresses. Vertical and lateral pushover analyses were conducted as well to verify if the same conclusion still holds irrespective of the loading type.

4.2.3 Vertical Pushover Elastic Column

An elastic concrete model for the column and the calibrated set of material properties for the superstructure inelastic constitutive total strain crack model was used with the three different bent cap designs to carry out a vertical pushover analysis to determine the capacity of the bent cap beam and the whole bridge sub-assemblage. The vertical pushover in the given test specimen configuration acted on both of the bent cap beam and the longitudinal box-girder. The vertical pushover curve for the three bent cap designs in addition to the developed bending moment at the bent cap at Section B are shown in Figure 4.30 and Figure 4.31, respectively. The vertical force capacity of the whole system was determined in the three bent cap design cases. Only a slight difference in the capacity, which was reached as soon as the inelastic damage started, was observed at the beginning. However, as the pushover analysis continued, the damage spread and the less reinforcement in the bent cap, the more loss of capacity was observed. The moments in the cap beam in the three cases reached comparable peak value, which was again within 10% difference before severe damage started.
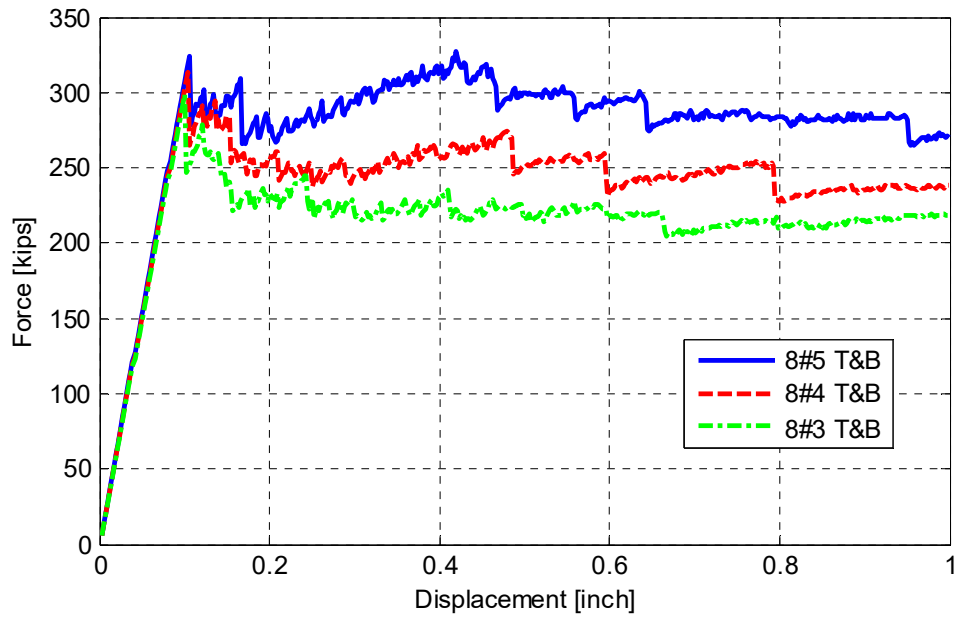
Figure 4.30 Vertical pushover force-displacement curve from the elastic column FE model for three bent cap cases: 8 #5, 8 #4, and 8 #3 top and bottom (T&B) reinforcement.
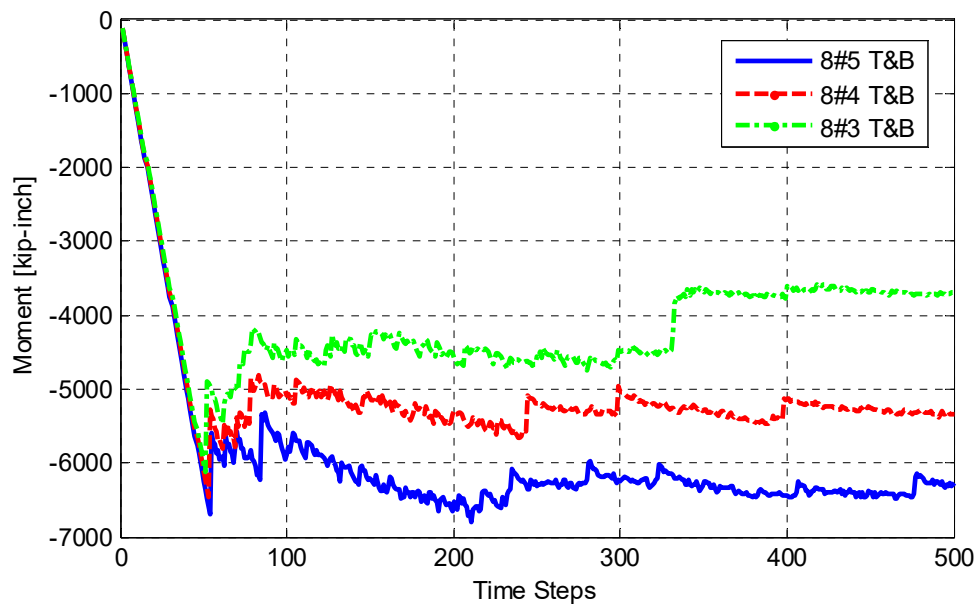
Figure 4.31 Bent cap beam moment history at Section B due to vertical pushover for three bent cap cases: 8 #5, 8 #4, and 8 #3 top and bottom (T&B) reinforcement.

The main conclusion from the vertical pushover analysis is the higher moment and system overall capacity that was observed relative to the cyclic loading case. For example, for the case of the original design of 8 #5 top and bottom reinforcement in the bent cap beam, a moment capacity of 5158 kip-in. was obtained from the cyclic loading versus a 6794 kip-in. from the vertical pushover. This can be explained in light of the resulting moment distribution along the bent cap due to the different cases of loading; see Figure 5.52 in Chapter 5 in Part I. In case of vertical pushover, the mode of failure is symmetric two plastic hinges in the two Sections B and D simultaneously. However, the mode of failure due to lateral loading depends on the loading direction; hence, only one plastic hinge at either Section B or D is developed. The realistic moment distribution that considers the actual column and cap beam cross sections suggests that the critical section where the plastic hinge develops is a larger cross section, which involves partial contribution from the column when two plastic hinges are formed under vertical concentrated load. Therefore, a higher moment capacity was obtained from the vertical pushover. Note that the experimental value for the beam capacity from Specimen No. 2 HS tests was reached as a result of the amplified moment demands from the column along with a 15% gravity load (240 kips). Although the high concentrated gravity load was not enough to fail the bent cap, it suggests that the bent cap beam capacity and the box-girder contribution are significantly influenced by the gravity load.

4.2.4 Lateral Pushover Elastic Column

A lateral pushover analysis in the transverse direction only under constant gravity load was conducted for the three different bent cap designs using the same model utilized previously for the vertical pushover and cyclic loading. Figure 4.32 and Figure 4.33 show the lateral transverse pushover curves and the corresponding bent cap bending moments at Section B, respectively. This analysis case emphasizes the fact that although the column is elastic and the capacity is dictated by the bent cap beam, close values for the moment capacity were obtained for the different bent cap designs. Once again this implies that there is a large force redistribution and redundancy because of the box-girder contribution.
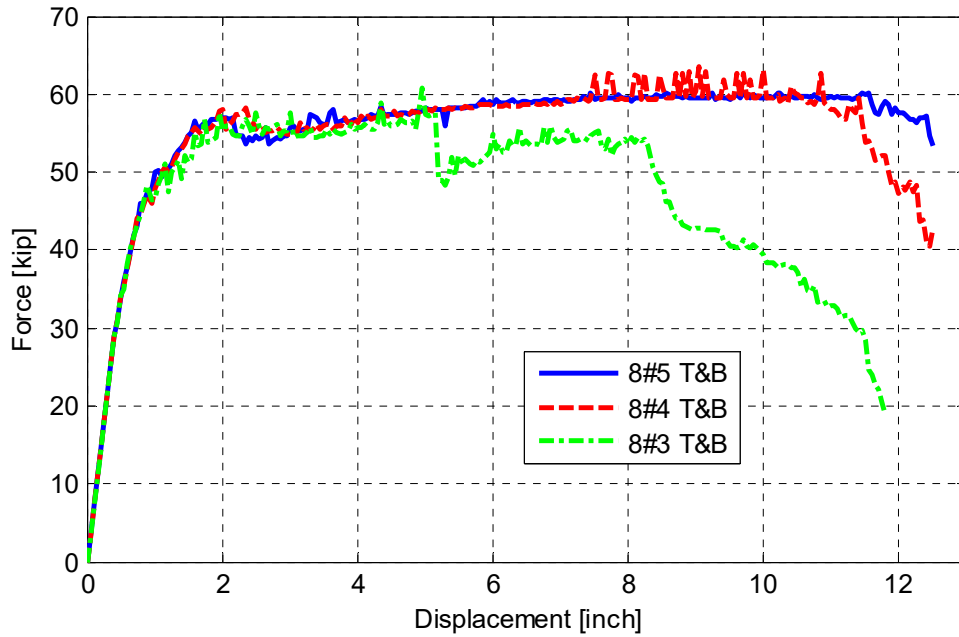
Figure 4.32   Lateral pushover force-displacement curve from the elastic column FE model for three bent cap cases: 8 #5, 8 #4, and 8 #3 top and bottom (T&B) reinforcement.
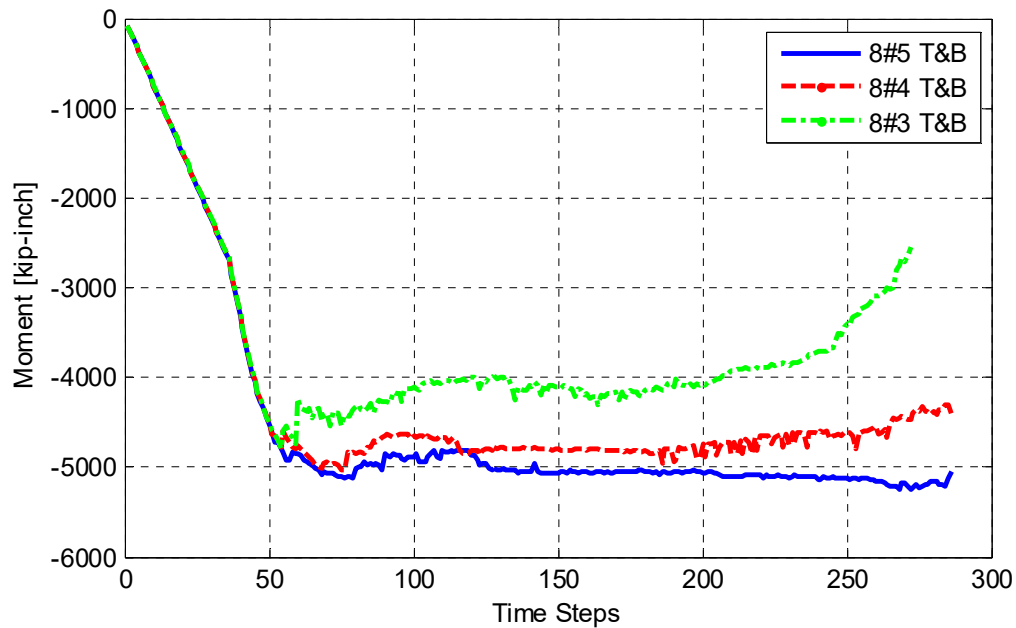
Figure 4.33   Bent cap beam moment history at Section B due to lateral pushover for three bent cap cases: 8 #5, 8 #4, and 8 #3 top and bottom (T&B) reinforcement.

4.2.5 Summary of Bent Cap Capacity

The previous subsections aimed at providing the overall system force-displacement relationships along with the developed moment in the bent cap beam. Next, the cap beam moment capacity from the three designs for the different cases that involved elastic column along with the maximum observed moment from the fully nonlinear calibrated model are summarized and presented in Table 4.1. A better comparison of the different values for the bent cap capacities from different cases of loading can be achieved in light of the analytical estimation of the bent cap capacity using conventional sectional analysis. The next section focuses on such sectional analysis of the bent cap beam different designs.

To recap the values listed in Table 4.1. (1) the moment values from the as-built Specimen No. 1 were capped due to reaching column capacity, whereas the capped bent cap beam moments in the retrofitted Specimen No. 2 were claimed to be the "true" bent cap capacity based on the observed damage; and (2) The capacity obtained from the FE analyses shows that the vertical pushover closely matched the experimental upper bound, which relates to the higher gravity load level (15%) used in the HS tests. According to the table, reducing the reinforcement from 8 #5 to 8 #4, i.e., 35% less reinforcement, was found to reduce the observed capacity by about 5% only for all cases of loading. Meanwhile, the reinforcement reduction from 8 #5 to 8 #3, i.e., 65% reduction, was accompanied by a reduction of only 10% in the observed capacity for the different loading cases. This indicates again that the box-girder contributes significantly to the overall system capacity, implying that large portion of the force and moment demand is redistributed to the box-girder even after extensive yielding or damage of the cap beam.

Table 4.1   Bent cap moment [kip-in] obtained from all cases of FE post-test analysis.

Cap beam Rft. (top & bottom)	Post-test FE analysis				Experiments	
	Elastic Column			Calibrated model	Specimen No. 1 cyclic tests	Specimen No. 2 HS tests
	vertical pushover	lateral pushover	lateral cyclic			
8 #5	6794	5248	5158	4721	4770	6535
8 #4	6452	5031	4953	4720	-	-
8 #3	6120	4793	4710	4645	-	-

4.3   SECTIONAL ANALYSIS

In earthquake engineering research and practice, sectional analysis is instrumental, particularly for capacity design or check of flexural members. A conventional sectional analysis for a beam in flexure aims at obtaining the moment-curvature relationship for the beam section to help identify key response metrics, such as the yielding and the ultimate moment capacity. In bridge design, a moment-curvature analysis or sectional analysis is required for bent columns and cap beams for performing various design checks. The current Caltrans SDC [2013] and AASHTO guide specifications for LRFD seismic bridge design [2011] provisions require calculating the integral bent cap beam capacity as part of the capacity check. This should be performed using the code-defined expected material properties and considering an effective slab width of 12 times the slab thickness (t_s) for box-girder slab contribution without including any slab reinforcement.

The validity of using $12t_s$ for slab contribution without including the slab reinforcement has been challenged through this study. The experimental results suggest that $18t_s$ would better represent the equivalent strain block that reflects the slab contribution. An additional point: the experimental and FE post-test analysis results reflect that the Caltrans and AASHTO provisions underestimate the bent cap beam capacity. To investigate the accuracy of the effective slab width and the cap beam capacity, slab contributions of $12t_s$ and $18t_s$ with (w/) and without (w/o) slab tension reinforcement were used to determine the test specimen bent cap beam capacity. Figure 4.34 shows the integral bent cap beam cross section used in the sectional analysis in three different cases of $12t_s$ w/ and w/o slab reinforcement and case of $18t_s$ w/ slab reinforcement. Note that the sectional analysis should consider the expected material properties as defined by the Caltrans SDC. However, the actual determined material properties from the material tests—see Chapter 3 of Part 1—have been used for better comparison with the experimentally determined capacity from Specimen No. 2 HS tests.

$b_{beam} + 12t_s$ flange width (without slab reinforcement)

$b_{beam} + 12t_s$ flange width (with slab reinforcement)

$b_{beam} + 18t_s$ flange width (with slab reinforcement)
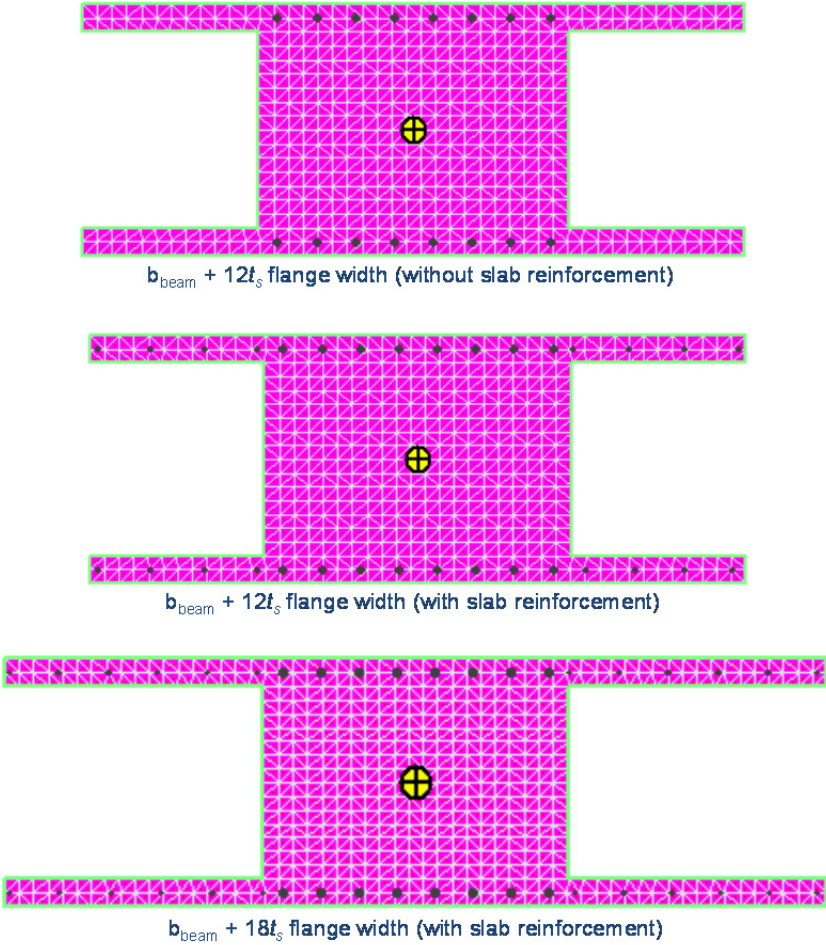
Figure 4.34   Schematic representation of three different cross-sections used to analyze the test specimen bent cap beam section.

The computational program XTRACT [Chadwell and Imbsen 2002] was used for all the sectional analysis conducted in this study. Figure 4.35 shows a typical analysis results report along with the moment-curvature relationship (actual and idealized) for the case of the original bent cap design using the Caltrans provisions: a $12t_s$ slab contribution without slab reinforcement. Note that the ultimate moment reported in the analysis is meant to be the moment value at the ultimate curvature reached. For the purpose of this study, the absolute ultimate moment was recorded for comparison's sake even if it was obtained before the ultimate curvature was reached.

The moment-curvature relationship obtained for the three cross sections defined in Figure 4.34 are shown in Figure 4.36. The figure shows that including the slab reinforcement within the defined effective slab width increases the capacity estimate significantly. To validate this observation at different reinforcement levels, the two hypothetical bent cap beam designs described earlier were used to estimate their capacities using sectional analysis. Table 4.2 summarizes all the results of different designs and cases of slab contribution as obtained from the sectional analysis. The values from the experimental tests are included in this table for comparison's sake. Note that the slab reinforcements in both compression and tension sides of the bent cap beam section were included for simplicity in those cases that considered the slab reinforcement in the interest of preserving symmetry. In general, the effect of the compression steel, whether from the cap beam itself or the adjacent slab reinforcement within the effective width, is minor on the capacity estimates. Thus, the notion of "slab reinforcement" in this discussion always implies the tension side reinforcement even when it is not mentioned explicitly.

Analysis Results:

Failing Material:	Steel1
Failure Strain:	.1000 Tension
Curvature at Initial Load:	0 1/in
Curvature at First Yield:	-.1424E-3 1/in
Ultimate Curvature:	-5.689E-3 1/in
Moment at First Yield:	-3008 kip-in
Ultimate Moment:	-4339 kip-in
Centroid Strain at Yield:	1.012E-3 Ten
Centroid Strain at Ultimate:	48.79E-3 Ten
N.A. at First Yield:	-7.108 in
N.A. at Ultimate:	-8.576 in
Energy per Length:	22.57 kips
Effective Yield Curvature:	.1765E-3 1/in
Effective Yield Moment:	3730 kip-in
Over Strength Factor:	-1.163
EI Effective:	2.11E+7 kip-in^2
Yield EI Effective:	110.6E+3 kip-in^2
Bilinear Harding Slope:	.5233 %
Curvature Ductility:	32.23

Moments about the X-Axis - kip-in

Curvatures about the X-Axis - 1/in

Moment Curvature Relation
Moment Curvature Bilinearization
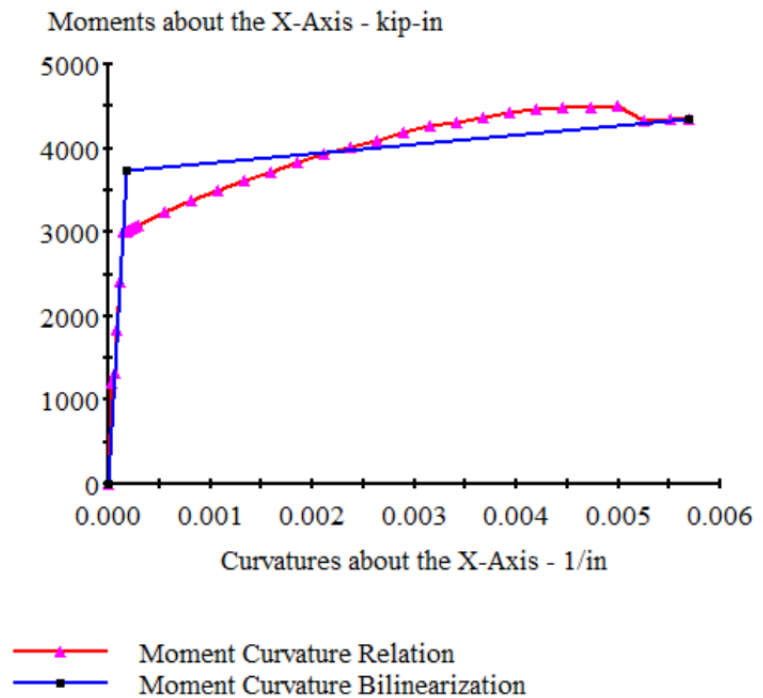
Figure 4.35   Typical moment-curvature analysis report obtained from XTRAXT for the test specimen bent cap using Caltrans provisions.
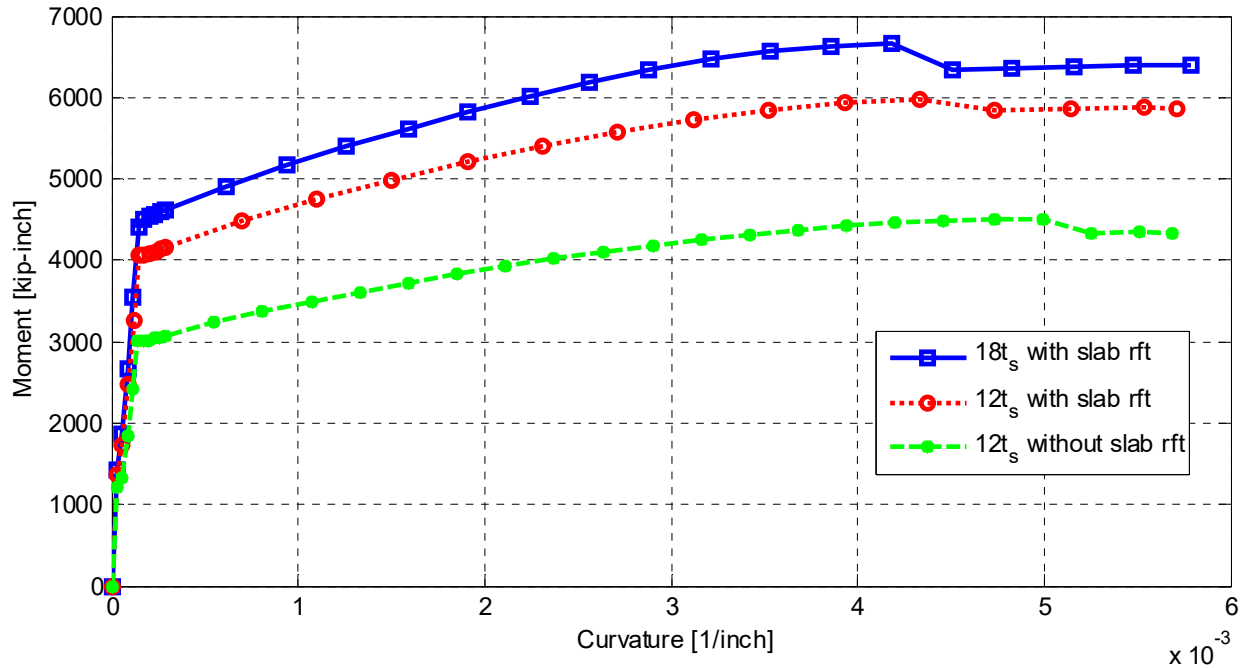
Figure 4.36 Moment-curvature relationships for postulated three different test specimen bent cap beam cross-sections as obtained from XTRACT sectional analysis results.

Table 4.2 Summary of the bent cap moment capacity [kip-in] obtained from the sectional analysis.

Cap beam top rft.	Cap beam bottom rft.	$12t_s$		$18t_s$		Experiments	
		w/o slab rft.	w/ slab rft.	w/o slab rft.	w/ slab rft.	Specimen No. 1 Cyclic Tests	Specimen No. 2 HS Tests
8 #5	8 #5	4504	5977	4566	6855	4770	6535
8 #4	8 #4	2945	4508	2965	5332	-	-
8 #3	8 #3	1667	3305	1676	4132	-	-

As implied in the data in Table 4.1, the observed reduction in the moment capacity from the FE analyses where the beam reinforcement was reduced is much less than that for the nominal flanged-section capacities from the section analyses; see Table 4.2. For example, reducing the bent cap reinforcement from 8#5 to 8#3 led to approximately 9% reduction in the capacity from the FE analysis, whereas a 63% and 45% reduction was observed from the sectional analysis when a $12t_s$ slab contribution was used with and without slab reinforcement, respectively, compared to the case of $18t_s$ slab contribution with slab reinforcement. This better illustrates the previous conclusions gleaned from the FE analyses that the box-girder contributes considerably to the system capacity and significant redundancy and force and moment demand redistributions take place as the cap beam yielding or damage progresses.

The sectional analysis results suggests that neglecting the slab reinforcement underestimates the capacity, however, Considering $18t_s$ for the effective width led to the best

match with the experimentally determined upper bound for the cap beam moment from the HS tests. Note that the capacity reduction when using cap beam of 8 #3 instead of 8 #5 in this case becomes 40% compared to the 63% and 45% mentioned above. A practical design problem is tackled next to investigate the design implications of considering the recommended $18t_s$ effective slab width along with including the slab reinforcement at a full-scale bridge level.

4.4   DESIGN IMPLICATIONS

The main objective of this study was to accurately quantify the box-girder slab contribution to the behavior of the integral bent cap beams in RC box-girder bridges: that is, to better estimate the cap beam strength and stiffness for seismic design and capacity checks purposes. The stiffness calculations of the bent cap rely primarily on the effective slab width under consideration for the flanged I-section of the integral bent cap. The effective moment of inertia of the integral cap beam and the corresponding initial stiffness estimate for the uncracked section should not vary significantly if a $12t_s$ or $18t_s$ effective slab width is used. On the contrary, the strength calculations and capacity estimates were found to vary significantly based on two parameters: (1) the effective slab width and (2) the tension slab reinforcement inclusion within that effective slab width. Based on the study reported herein, such conclusions were based on experimental and analytical evidence but only at the reduced-scale level of the tested column-supper structure sub-assembly. Thus, it would be beneficial to extrapolate those conclusions to the full bridge scale to identify the design implications and potential design optimization of the integral bent cap beams.

The bent cap design of the original Caltrans Academy Bridge was revisited based on three different scenarios of the bent column design. For each scenario, the cap beam design, or more precisely the capacity check, was based on three cases. The first case used the provisions of the current Caltrans SDC [2013] and AASHTO guide specifications for LRFD seismic design of bridges [2011], i.e., using an effective slab width of $12t_s$ without including the tension slab reinforcement. The second and third cases for the full scale bent cap design and capacity check are to include the tension slab reinforcement with $12t_s$ and $18t_s$ effective slab width, respectively. For all cases, the Caltrans SDC expected material properties for a 5000 psi characteristic concrete strength and Grade 60 reinforcing steel are used to resemble actual design conditions. The relevant design criteria and the different bent column design scenarios are presented in the first subsection. The bent cap beam capacity estimates in the three configurations described above is discussed in the second subsection. In conclusion, the capacity check is performed and discussed in the third subsection.

4.4.1 Design Criteria

The typical bridge design process begins by laying out the bridge spans to determine the bridge type and preliminary dimensions of different cross sections. The next step is to estimate the different loading actions primarily based on vertical gravity loads, i.e., dead loads and live traffic loads. Linear elastic analyses are then carried out to determine the different demands. The final step is to perform LRFD design for the sections. Based on the bridge type, location, boundary, and soil conditions, among other parameters, different design approaches might be undertaken to perform lateral design and checks. For the typical case considered in this study, which is a RC box-girder bridge in California, performance-based approaches are typically used for seismic

design and checks. In particular, for the case of the integral bent cap beam that is readily dimensioned and designed using LFRD, a capacity design check is required to guarantee that the bent cap beam remains essentially elastic during extreme seismic events. A weak-column–strong-beam approach is used, which ties the cap beam capacity check directly to the bent column; see Chapter 3 of Part 1 for more details about the bridge seismic design philosophy. In addition, the Academy Bridge design document [2006] provides supplementary details that are specific to the prototype used through this study.
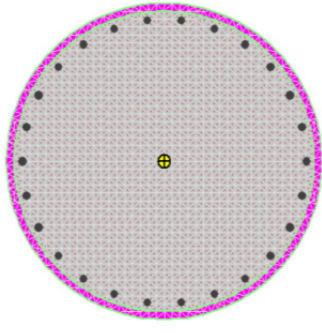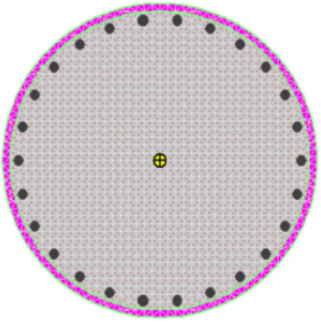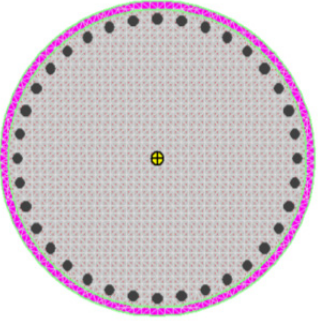
Three scenarios for the Academy Bridge column design are considered and the bent cap beam design is checked accordingly. All the necessary data has been adopted from the Academy Bridge design document [2006] and the relevant design information is briefly presented here for completeness. The typical method for designing the bent columns is to assume a longitudinal reinforcement ratio within the 1% to the 4% code limits and then perform all necessary design checks. The original Academy Bridge design involved a 6-ft diameter column with a 1.44% reinforcement ratio, which satisfied all the design requirements and checks [2006]. To recognize possible scenarios that would require higher column reinforcement ratios, two additional designs with ~2.6% and ~3.5% column reinforcement ratios were used in this study. Sectional analyses were performed for all three column design scenarios, and the column capacity was estimated based on the expected Caltrans material properties. A summary of the original column design and the two additional scenarios and relevant sectional analysis results are presented in Table 4.3.

Once the column design is completed and sectional analyses are used to compute the section capacity, the column overstrength is then estimated to use for the bent cap beam capacity check. The column overstrength is given as 1.2 times the ultimate plastic moment obtained from the sectional analysis. To calculate the moment demands in the bent cap beam based on the column overstrength moment, a nonlinear planer transverse pushover analysis is typically performed. The results from the 2D nonlinear model used for the bent frame as given by the Academy Bridge design document [2006] were used to estimate the bent cap beam moment demands. A schematic illustration of the model used for the transverse pushover analysis is shown in Figure 4.37. The estimated positive and negative bent cap beam moment demands are summarized in Table 4.3.

To perform the bent cap beam capacity check, the current Caltrans and AASHTO provisions require calculating the bent cap beam capacity based on a flanged section that includes a $12t_s$ effective slab width. The readily available design for the bent cap from the vertical load LRFD design is 24 #11 bottom reinforcement and 22 #11 top reinforcement, as given by the design document [2006]. As discussed earlier, the transverse slab reinforcement was required to calculate the bent cap capacity in the other two configurations. The design document [2006] did not include any information on the transverse slab reinforcement since it is not involved in any seismic design checks. Therefore, the standard Caltrans design procedure for choosing the transverse slab reinforcement was adopted to determine the slab reinforcement. The current practice for deciding on RC box-girder soffit and deck slabs dimensions and reinforcement is using the design charts and tables provided by the Caltrans Memo to Designers 10-20 [2008]. An excerpt for the relevant table required for determining the deck slab transverse reinforcement is shown in Figure 4.39, with the applicable data for the Academy Bridge identified. A similar procedure was followed to determine the soffit slab reinforcement. The final Academy Bridge bent cap cross section and slab reinforcement for the case of the $12t_s$

configuration is shown in Figure 4.38. Based on this data, the bent cap capacity was determined for the three selected configurations as discussed in the next.

Table 4.3   **Summary of the three column scenarios for Caltrans Academy Bridge [2006].**

Column Cross Section

Diameter	6 ft	6 ft	6 ft
Long. Rft.	26 #14	26 #18	36 #18
Rft. Ratio	1.44%	2.56%	3.53%
Hoops	#8 @ 5 in.	#8 @ 5 in.	#8 @ 5 in.
Ultimate moment M_p (kip-ft)	14,510	21,140	26,200
Overstrength moment M_o (kip-ft)	17,410	25,370	31,440
Cap beam M_{+ve} demand (kip-ft)	14,970	21,820	27,040
Cap beam M_{-ve} demand (kip-ft)	15,670	22,830	28,300
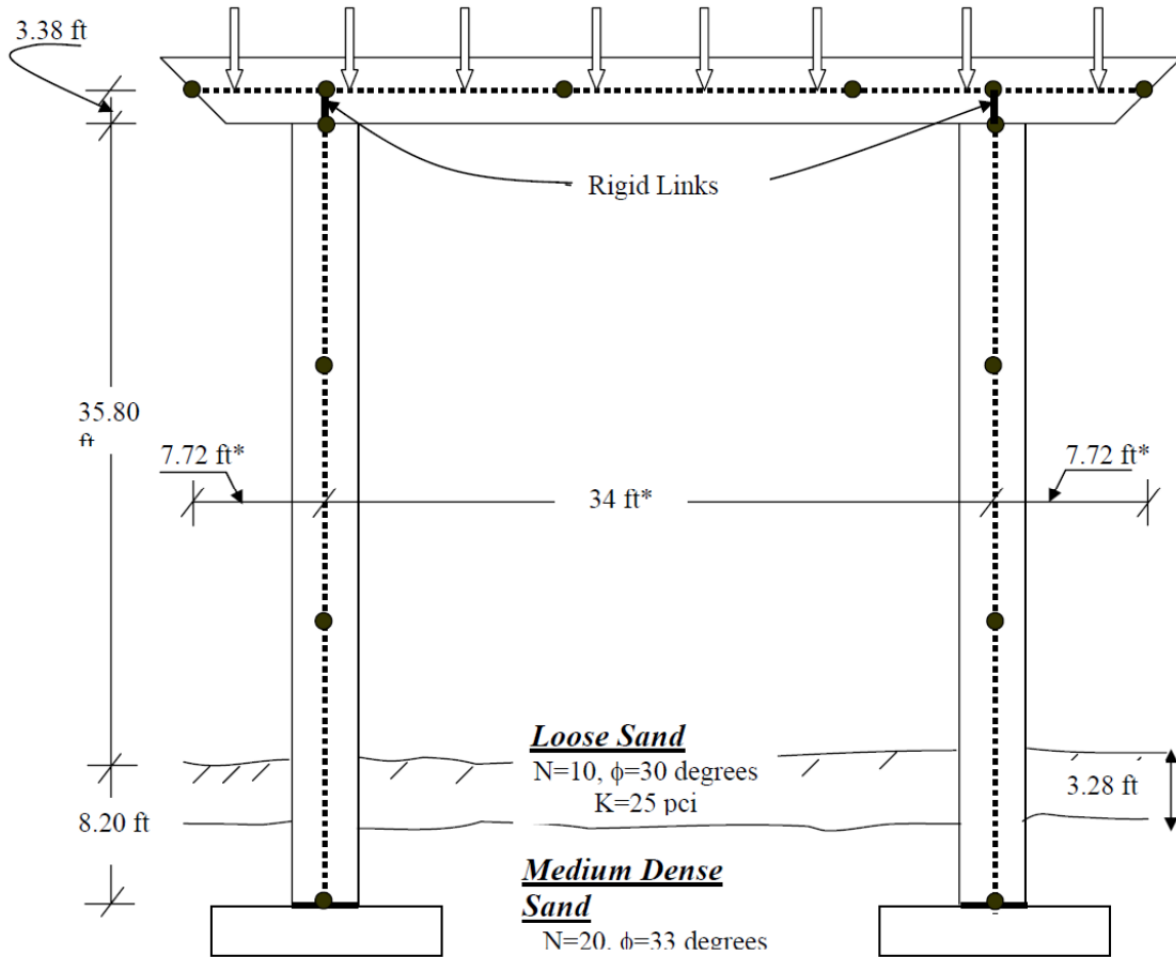
Figure 4.37 Transverse pushover analysis model for bent cap beam demand estimation for the capacity check (Academy Bridge LRFD design document [2006]).
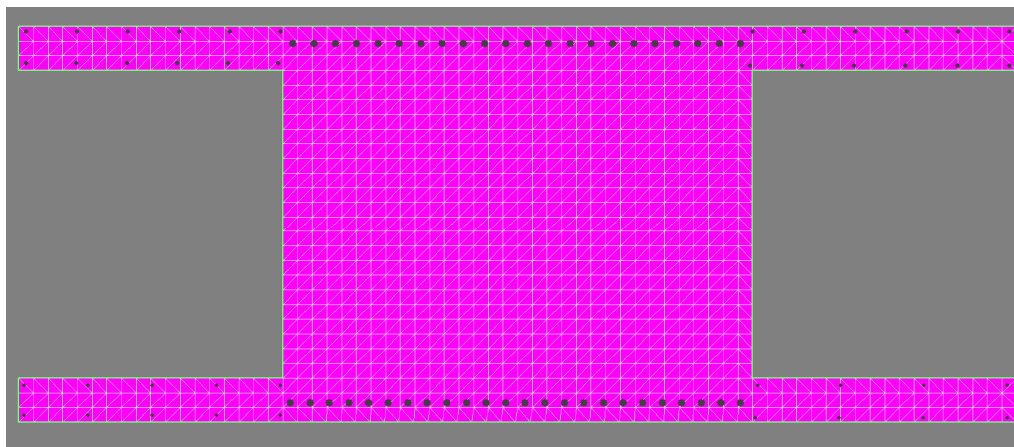
Figure 4.38 Typical bent cap cross section of the full-scale Academy Bridge prototype for the case of $12t_s$ considered as the effective slab contribution and slab transverse reinforcement included in cap beam sectional analysis.

Table 10-20.1(b) Deck Slab Thickness and Reinforcement Schedule

CIP PRESTRESSED BOX, PRECAST-I, & STEEL GIRDERS w/ flange width>=24"						
"S"	"t"	Dimension	Transverse Bars		"D" Bars	"G" Bars
Girder CL to CL Spacing	Top Slab Thickness	"F"	Size	Spacing [1]	#5 Bars	#4 Bars
4'- 0"	7"	5"	#5	12"	3	2
4'- 3"	7"	5"	#5	12"	3	2
4'- 6"	7"	6"	#5	12"	3	2
4'- 9"	7"	6"	#5	12"	3	2
5'- 0"	7"	6"	#5	12"	3	2
5'- 3"	7"	7"	#5	12"	3	2
5'- 6"	7"	7"	#5	12"	4	2
5'- 9"	7"	7"	#5	12"	4	3
6'- 0"	7"	8"	#5	12"	4	3
6'- 3"	7"	8"	#5	12"	4	3
6'- 6"	7 1/8"	9"	#5	12"	4	3
6'- 9"	7 1/8"	9"	#5	11"	5	3
7'- 0"	7 1/4"	9"	#5	11"	5	3
7'- 3"	7 3/8"	10"	#5	11"	5	3
7'- 6"	7 1/2"	10"	#5	11"	5	3
7'- 9"	7 1/2"	11"	#5	11"	5	3
8'- 0"	7 5/8"	11"	#5	11"	6	3
8'- 3"	7 3/4"	11"	#5	11"	6	3
8'- 6"	7 3/4"	1'- 0"	#5	11"	6	3
8'- 9"	7 7/8"	1'- 0"	#5	11"	6	4
9'- 0"	8"	1'- 1"	#5	11"	6	4
9'- 3"	8 1/8"	1'- 1"	#5	11"	7	4
9'- 6"	8 1/8"	1'- 1"	#5	11"	7	4
9'- 9"	8 1/4"	1'- 2"	#5	10"	8	4
10'- 0"	8 3/8"	1'- 2"	#5	10"	8	4
10'- 3"	8 3/8"	1'- 2"	#5	10"	8	4
10'- 6"	8 1/2"	1'- 3"	#5	10"	8	4
10'- 9"	8 5/8"	1'- 3"	#5	10"	8	4
11'- 0"	8 5/8"	1'- 4"	#6	11"	11	4
11'- 3"	8 3/4"	1'- 4"	#6	11"	11	4
11'- 6"	8 7/8"	1'- 4"	#6	11"	11	4
11'- 9"	8 7/8"	1'- 5"	#6	11"	12	5
12'- 0"	9"	1'- 5"	#6	11"	12	5
12'- 3"	9 1/8"	1'- 6"	#6	11"	12	5
12'- 6"	9 1/8"	1'- 6"	#6	11"	12	5
12'- 9"	9 1/4"	1'- 6"	#6	11"	12	5

Figure 4.39   Deck slab dimensioning and reinforcement design aid chart as excerpted from the Caltrans Memo to Designers 10-20 [2008].

4.4.2 Bent Cap Capacity

The necessary data to determine the bent cap capacity was properly acquired as discussed before. Three configurations or cross-sections were considered to investigate how the bent capacity can be accurately estimated and how the design can be optimized. The first configuration is using the provisions of Caltrans SDC, or similarly the AASHTO seismic LRFD specifications, i.e., using an effective slab width of $12t_s$ without including the tension slab reinforcement. The second and third configurations are considering the tension slab reinforcement within $12t_s$ and $18t_s$ effective

slab width, respectively. It should be noted that the double-column bent configuration of the Academy Bridge dictates positive and negative moment demands in the cap beam due to lateral loading. However, neither the top (22 #11) and bottom (24 #11) bent cap beam reinforcement nor the soffit (#5 @ 15 in.) and deck (#6 @ 11 in.) slab reinforcement are symmetric. Therefore, different capacities for positive and negative moments exist.

The conventional sectional analysis procedure using XTRAXT [Chadwell and Imbsen 2002] was adopted to determine the positive and negative bent cap beam capacities in the three different configurations. Figure 4.40 and Figure 4.41 show the moment-curvature relationships for different bent cap beam cross sections (configurations) due to positive and negative moments, respectively. The positive and negative moment notion is defined here to avoid confusion. The negative moment is the moment that causes sagging in the cap beam and requires top reinforcement where tension develops; the positive moment causes hogging in the cap beam and requires bottom reinforcement. Accordingly, the deck (top) slab reinforcement is the tension slab reinforcement for negative moment capacity, whereas the soffit (bottom) slab reinforcement is the tension reinforcement in case of positive moment capacity. Therefore, the positive moment capacity is slightly higher than the negative moment capacity when only the bent cap reinforcement is used in the capacity estimation (22 #11 for top versus 24 #11 for bottom), which can be observed in Figure 4.40 and Figure 4.41. However, the negative capacity exceeds the positive capacity when the slab reinforcement is included, as observed in the same figures. The moment capacities determined from the section analyses were compared to the demands obtained from the transverse pushover analysis for the three column design scenarios to perform a capacity check, as discussed next.
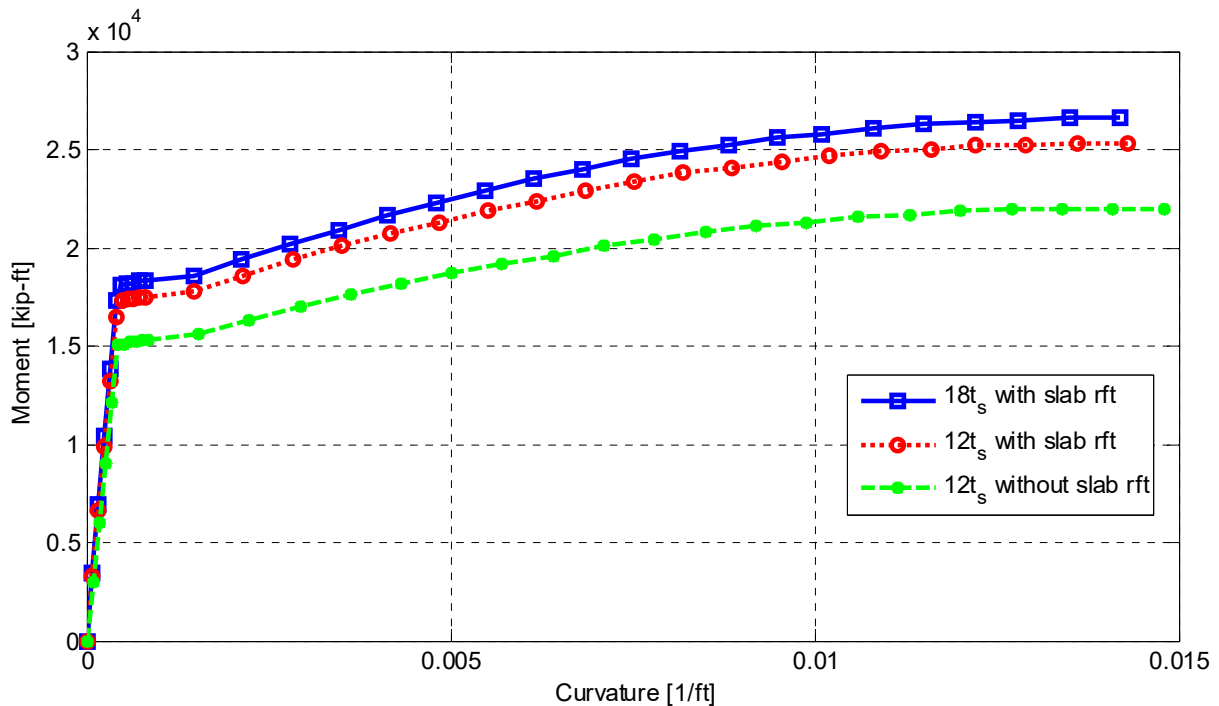
Figure 4.40   **Moment-curvature relationships for positive moment demands for the full-scale Academy Bridge three different bent cap beam cross sections as obtained from XTRACT sectional analysis results.**
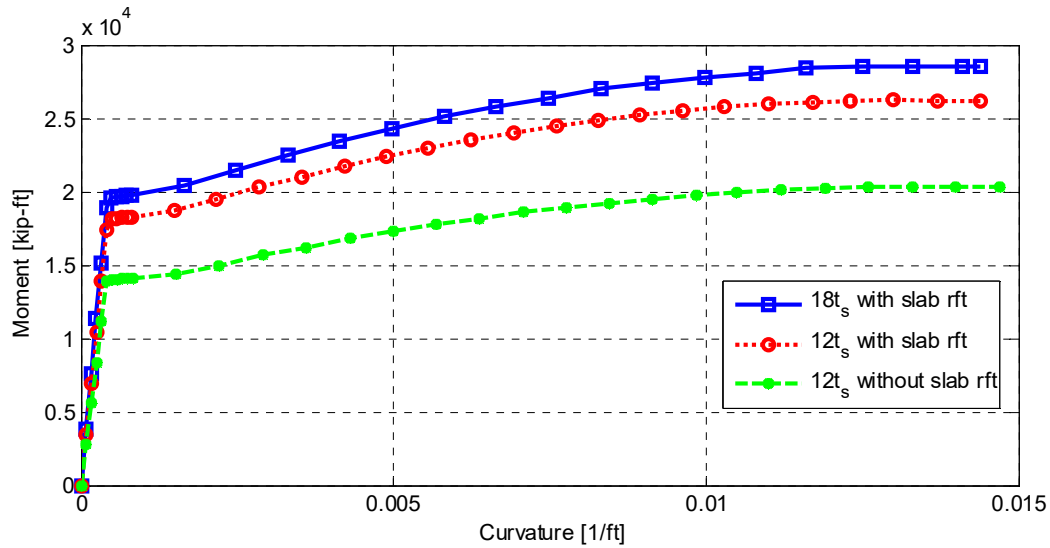
Figure 4.41 Moment-curvature relationships for negative moment demands for the full-scale Academy Bridge three different bent cap beam cross sections as obtained from XTRACT sectional analysis results.

4.4.3 Caltrans SDC Capacity Check

The seismic capacity check is required to avoid unfavorable mode of failure and guarantee that the superstructure—the bent cap beam in this case—remains essentially elastic during extreme seismic events when the ductile bent columns reach their flexural capacities. The check is performed by comparing the demand, which is estimated from the pushover analysis based on columns overstrength moments rather than ultimate plastic moments, versus the capacity estimated for the given bent cap beam design. In this study, three different scenarios for the column design were studied, whereas three different configurations for the capacity estimation were utilized. This resulted in a total of 18 combinations for the capacity check; nine for cases of positive demands and nine for cases of negative demands. The summary of the positive and negative demands in the three scenarios (column design cases) and the estimated capacities for the three different configurations along with the capacity check is shown in Table 4.4 and Table 4.5, respectively.

The tables highlight that there are cases where the seismic capacity check was not satisfied, requiring a revised bent cap beam design. Accordingly, the bent cap beam reinforcement was increased until the obtained beam capacity satisfied the capacity check. The final revised design for the cases that required additional reinforcement along with the ratio of the needed increase in the reinforcement are summarized in Table 4.6 and Table 4.7 for cases of positive and negative demands, respectively. Additionally, Table 4.8 summarizes the overall increase in the reinforcement relative to the original design when positive and negative moment designs are combined. Based on these tables, neglecting the slab reinforcement does not require revised design only for the 1.5% column design scenario, but also requires much higher reinforcement to satisfy the capacity checks for higher demands from 2.5% and 3.5% column design scenarios. Moreover, including the slab reinforcement, especially within the recommended $18t_s$ effective slab width from this study, requires the least design alteration and leads to the most optimized bent cap beam design.

Table 4.4   Bent cap seismic capacity check for positive moment demands due to three design cases.

Case	Column Design	Moment Demand [kip-ft]	$12t_s$ no slab rft.		$12t_s$ with slab rft.		$18t_s$ with slab rft.	
			Capacity	Satisfy Capacity Check?	Capacity	Satisfy Capacity Check?	Capacity	Satisfy Capacity Check?
1	1.44%	14,970	21,990	YES	25,260	YES	26,590	YES
2	2.58%	21,820	21,990	YES	25,260	YES	26,590	YES
3	3.50%	27,040	21,990	NO	25,260	NO	26,590	NO

Table 4.5   Bent cap seismic capacity check for negative moment demands due to three design cases.

Case	Column Design	Moment Demand [kip-ft]	$12t_s$ no slab rft.		$12t_s$ with slab rft.		$18t_s$ with slab rft.	
			Capacity	Satisfy Capacity Check?	Capacity	Satisfy Capacity Check?	Capacity	Satisfy Capacity Check?
1	1.44%	15,670	20,270	YES	26,170	YES	28,460	YES
2	2.58%	22,830	20,270	NO	26,170	YES	28,460	YES
3	3.50%	28,300	20,270	NO	26,170	NO	28,460	YES

Table 4.6   Revised bent cap design and capacity check for positive moment demands resulting from the three different column design cases.

	Case	1	2	3
	Column Design	1.44%	2.58%	3.50%
	Moment Demand [kip-ft]	14,970	21,820	27,040
$12t_s$ no slab rft.	Original Design	24 #11	24 #11	24 #11
	Original Capacity	21,990	21,990	21,990
	New Design	no change	no change	32#11
	New Capacity	no change	no change	28,790
	Increase in Rft. [%]	0	0	33.3
$12t_s$ with slab rft.	Original Design	24 #11	24 #11	24 #11
	Original Capacity	25,260	25,260	25,260
	New Design	no change	no change	26 #11
	New Capacity	no change	no change	27,100
	Increase in Rft. [%]	0	0	8.3
$18t_s$ with slab rft.	Original Design	24 #11	24 #11	24 #11
	Original Capacity	26,590	26,590	26,590
	New Design	no change	no change	26 #11
	New Capacity	no change	no change	28,680
	Increase in Rft. [%]	0	0	8.3

Table 4.7 Revised bent cap design and capacity check for negative moment demands resulting from the three different column design cases.

Case		1	2	3
Column Design		1.44%	2.58%	3.50%
Moment Demand [kip-ft]		15,670	22,830	28,300
12t_s no slab rft.	Original Design	22 #11	22 #11	22 #11
	Original Capacity	20,270	20,270	20,270
	New Design	no change	24 #11	32 #11
	New Capacity	no change	22,050	28,790
	Increase in Rft. [%]	**0**	**9.1**	**45.5**
12t_s with slab rft.	Original Design	22 #11	22 #11	22 #11
	Original Capacity	26,170	26,170	26,170
	New Design	no change	no change	26 #11
	New Capacity	no change	no change	29,740
	Increase in Rft. [%]	**0**	**0**	**8.3**
18t_s with slab rft.	Original Design	22 #11	22 #11	22 #11
	Original Capacity	28,460	28,460	28,460
	New Design	no change	no change	no change
	New Capacity	no change	no change	no change
	Increase in Rft. [%]	**0**	**0**	**0**

Table 4.8 Summary of additional bent cap reinforcement required to satisfy the seismic capacity check for three different column design cases.

Case		1	2	3
Column Design (long. rft. ratio) [%]		1.44	2.58	3.50
12t_s no slab rft.	Increase in Bottom rft. [%]	0.00	9.10	33.30
	Increase in Top rft. [%]	0.00	0.00	45.50
	Total Increase in rft. [%]	**0.00**	**4.55**	**39.40**
12t_s with slab rft.	Increase in Bottom rft. [%]	0.00	0.00	8.30
	Increase in Top rft. [%]	0.00	0.00	8.30
	Total Increase in rft. [%]	**0.00**	**0.00**	**8.30**
18t_s with slab rft.	Increase in Bottom rft. [%]	0.00	0.00	8.30
	Increase in Top rft. [%]	0.00	0.00	0.00
	Total Increase in rft. [%]	**0.00**	**0.00**	**4.15**

144

5 Full-Bridge Parametric Study

The computational framework conducted in this study consisted of a pre-test analysis phase, which was discussed in Part I of this report, and a post-test analysis phase, which is discussed in this report. The first stage of the post-test analysis considered the calibration of the detailed DIANA FE model of the tested specimen and a parametric study at the specimen (sub-assemblage) level as discussed before in the companion report. The second stage extended the parametric study to the prototype bridge level to investigate the effect of the bridge geometry on the bent cap effective width and strain distribution. Nine linear elastic FE models were generated and adopted from the unskewed two-column bent Caltrans Academy Bridge to consider different girders spacing and different soffit and deck slabs thicknesses. The details of the geometric parameters considered in this study, the strain distribution in the bent cap at different sections under combined gravity and lateral load, and the estimated effective slab width for the different bridges are presented and discussed in this chapter.

5.1 GEOMETRIC PARAMETERS

Several geometric parameters are associated with box-girder bridges such as the superstructure depth, the box-girders spacing, the slab thicknesses, etc. Typically, the geometric design of the bridges is governed by the traffic loads, which determine the number of lanes, and the feasible structural system, which is governed by the bents spacing and bridge spans. A bridge span will control the superstructure depth, which in turn affects the box-girder geometry. However, there is some flexibility in deciding on the girders spacing and the corresponding slab thicknesses. Thus, the objective of this parametric study at the prototype bridge level is to investigate whether varying the box-girder geometry affects the integral bent cap effective width and slab contribution. In particular, two of the box-girder geometric parameters were considered in this study; the girders spacing and the soffit and deck slab thicknesses.

In practice, there are guidelines for choosing the girders spacing in reinforced and prestressed concrete superstructures. For the Caltrans Academy Bridge, the box girders spacing is recommended to be within 1.5 to 2.0 times the superstructure depth (6.75 ft in this case), i.e., centerline to centerline spacing of girders within 10.125 to 13.5 ft is recommended. Three values for the spacing were chosen for the first parameter of this study to obtain a practical design and numbers of girders. These are 9-, 11-, and 14-ft clear spacing between the box-girder webs; there are design aids and tables that help the bridge engineers in practice choose the box-girder soffit and deck slabs thicknesses and reinforcement based on the girders spacing. According to the chosen spacing values, three sets of soffit and deck slabs thicknesses were chosen. These are 8

1/2, 9 1/8, 10 1/8 in. for the deck slab along with 6 3/4, 8 1/4, 10 1/8 in. for the soffit slab, respectively. Accordingly, nine combinations of the chosen box-girder web spacing and slabs thicknesses were available as illustrated and summarized in Figure 5.1.Table 5.1 also summarizes the nine bridge cases, where each three cases having similar slab thicknesses but different web spacing are grouped together. A geometric parameter that relates the variation in the slab thicknesses and girders web spacing is proposed and shown in Table 5.1as well. This parameter is the aspect ratio of the clear box-girder cell width-to-depth, i.e., the ratio between the clear spacing between the webs and the clear depth between the soffit and deck slabs. This aspect ratio was considered in this study in investigating the effective width variation as discussed later in Section 5.4.

The parametric study considered linear elastic detailed FE models to determine the strain distribution in the bent cap beam and adjacent soffit and deck slabs in both compression and tension under combined vertical and lateral loading. Only linear elastic material model was used for concrete. This is because the objective of this parametric study was to investigate whether the box-girder geometry affects the bent cap effective width or slab contribution rather than exploring the bent cap capacity, as in case of the experimental program or the parametric study at the specimen level discussed earlier. The detailed DIANA FE model for one of the nine bridges considered in the parametric study is shown in Figure 5.2, and the two sections where the strain distribution is determined are identified. Each of the nine different bridges considered here was analyzed under the gravity dead loads combined with lateral forces applied transversely at the two bents planes. The lateral force value was chosen to produce maximum bending moments in the bent cap that is less than the yielding moment to represent realistic conditions within the linear elastic range. Embedded reinforcement was used in the bent cap and both soffit and deck slabs transverse direction for accurate representation of the bent stiffness in the transverse direction is shown in Figure 5.2. The embedded reinforcement bars were also used in the post-processing to acquire the strain data to obtain the strain distribution at the two sections identified in Figure 5.2. Note that the concrete elastic material properties were adopted from the calibrated specimen FE model. These are the Poisson's ratio and the Young's modulus. A discussion of the strain distribution and the equivalent strain block is presented next in the following sections.

Table 5.1   Summary of different geometry of the bridges used in the parametric study.

Bridge Group	Group 1			Group 2			Group 3		
Bridge ID	1	4	7	2	5	8	3	6	9
Soffit slab thickness (in)	6.75	6.75	6.75	8.25	8.25	8.25	10.13	10.13	10.13
Deck slab thickness (in.)	8.50	8.50	8.50	9.13	9.13	9.13	10.13	10.13	10.13
Box-gider clear spacing, b (in)	168	132	108	168	132	108	168	132	108
Box-girder net depth, d (in)	65.75	65.75	65.75	63.63	63.63	63.63	60.75	60.75	60.75
Box-girder cell aspect ratio (b/d)	2.56	2.01	1.64	2.64	2.07	1.70	2.77	2.17	1.78

Bridge 1   Bridge 2   Bridge 3

Bridge 4   Bridge 5   Bridge 6

Bridge 7   Bridge 8   Bridge 9
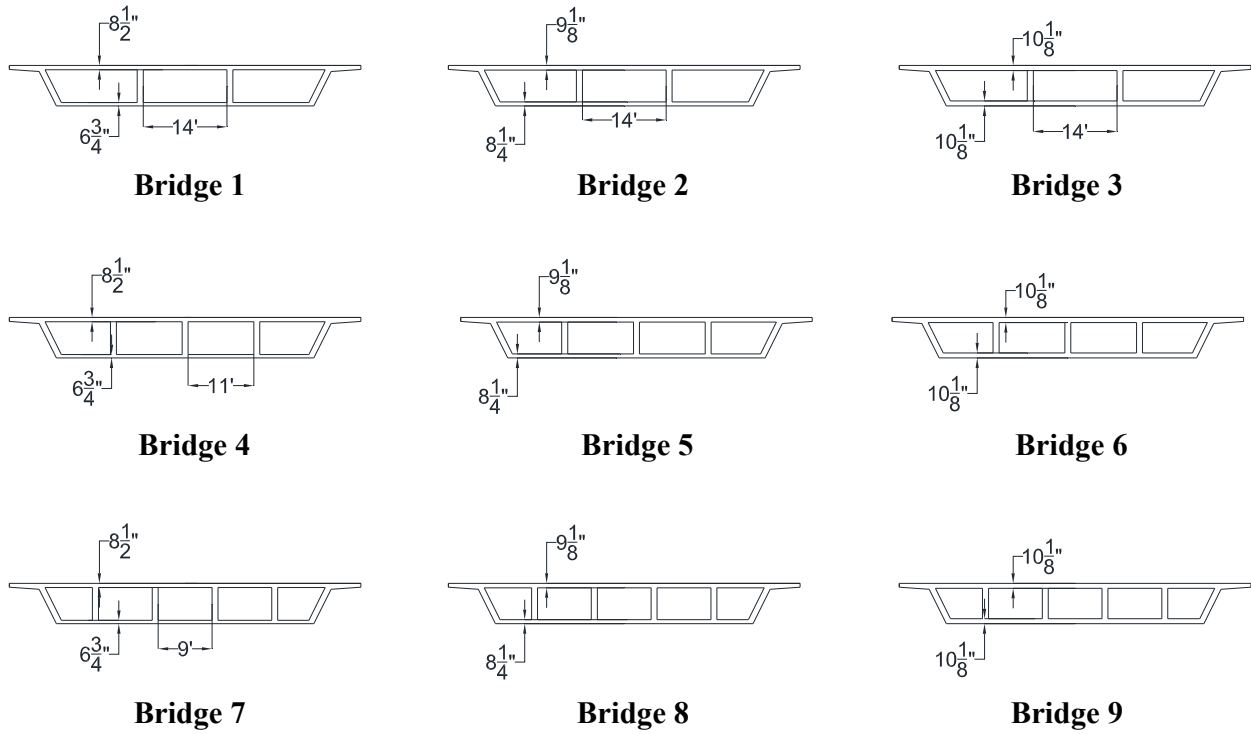
Figure 5.1   **Cross sections of the different prototype bridges adopted from the Academy Bridge to investigate the effect of the box-girder soffit and deck slab thicknesses and girder web spacing.**
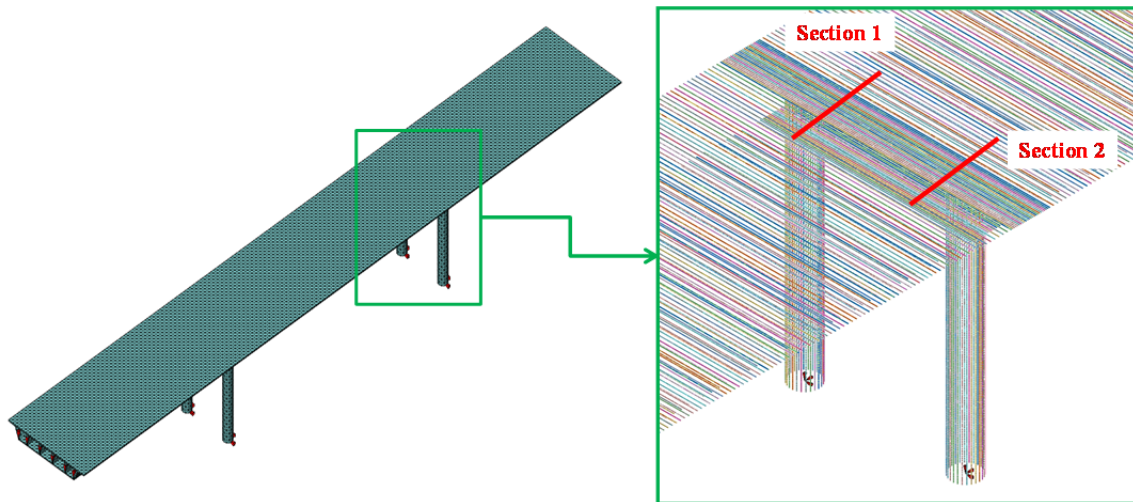
Figure 5.2   **Finite element DIANA model of Bridge 1 (from Figure 5.1): concrete solid element mesh (left) and embedded reinforcement with identified bent cap critical bending moment sections.**

5.2   STRAIN DISTRIBUTION

One of the main response quantities that have been extensively investigated throughout this study is the strain distribution in the bent cap beam and its adjacent slabs. The importance of the strain distribution is associated with the equivalent effective slab width of integral bent caps and the box-girder slabs contribution to the bent cap stiffness and capacity, which is the main focus of the experimental and computational programs of this study. The strain distribution obtained from the detailed DIANA FE bridge models is presented in this section. The equivalent strain block obtained from strain distributions is shown also here in this section and discussed in more details below.

5.2.1 Bridge 1 Strain Distribution

The strain distributions obtained from bridge 1 in the parametric study are discussed first to show how and where these distributions were obtained. A summary of all the strain distributions is shown next in the following subsection. The strain distribution was used to determine the equivalent strain block to determine the effective slab width of the bent cap using a similar framework as the experimental program. The reader is referred to Part 1 of this report for details of the procedure adopted to obtain the equivalent strain block. Note that two strain values were previously used to define the equivalent strain block, namely, the mean and the minimum strain values within the bent cap reinforcement. However, for the sake of this bridge parametric study, only the mean strain value inside the bent cap was used to define the equivalent strain block. That is because the strain observed within the bent cap was more uniform than what was observed during the experiments due to the lack of the concentrated gravity load that was dictated by the test set-up.

The distributions were all obtained under combined vertical and lateral transverse load applied in the direction defined in Figure 5.3. The figure also shows an elevation view of the strain distribution along the bent cap profile (aligned with the bridge transverse direction). The figure demonstrates the bending moments distribution that cause tension in the soffit slab and compression in the deck slab at Section 1 (left-hand side of the figure), while causing tension in the deck slab side and compression in the soffit at Section 2 (right-hand side of the figure). Hence, four locations were used to obtain the strain distributions and their equivalent strain blocks herein. The four locations are either referred to by the sections, i.e., top side at Section 1 for instance, or referred to by the strain and slab type, i.e., tensile strain in the soffit slab for instance. Moreover, Figure 5.4 and Figure 5.5 show a side view of the tensile and compression strain distribution, respectively, along the bent cap cross section and the adjacent soffit and deck slabs.

Strain values were obtained at every other reinforcement bar in the bent cap and the adjacent slabs to post-process the results and calculate the effective slab width from the equivalent strain block. Each time the strain was obtained at one of the four locations previously discussed, the equivalent strain block was calculated, as shown in Figure 5.6 through Figure 5.9 for the case of bridge 1 as an example. Figure 5.6 and Figure 5.7 show the distribution at Section 1 at the tension and compression sides, respectively. Similarly, Figure 5.8 and Figure 5.9 show the distribution at Section 2 at the tension and compression sides, respectively. Note that the strain is higher in the soffit slab side than the deck slab side at both Sections 1 and 2.
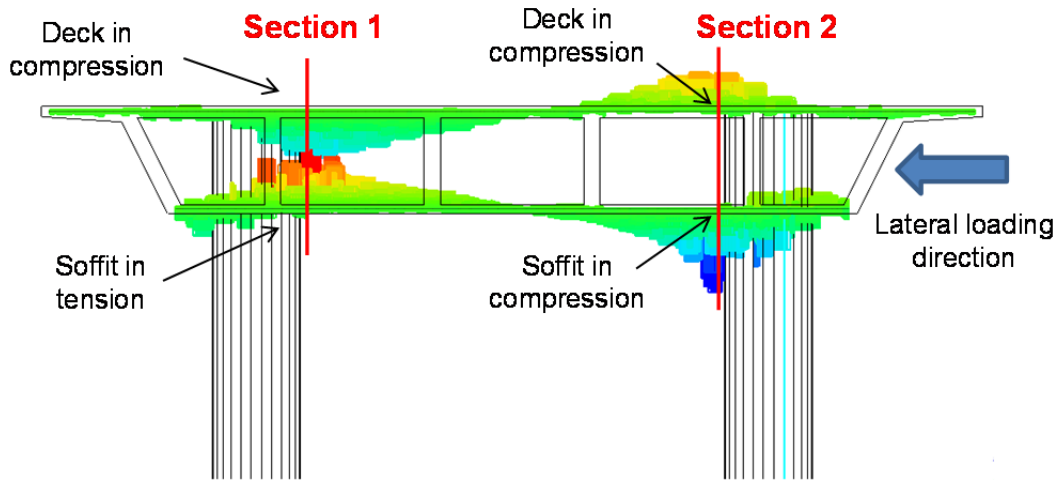
Figure 5.3   **Elevation view of the strain distribution along the bent cap and locations of maximum tensile and compression strain identified at Sections 1 and 2.**
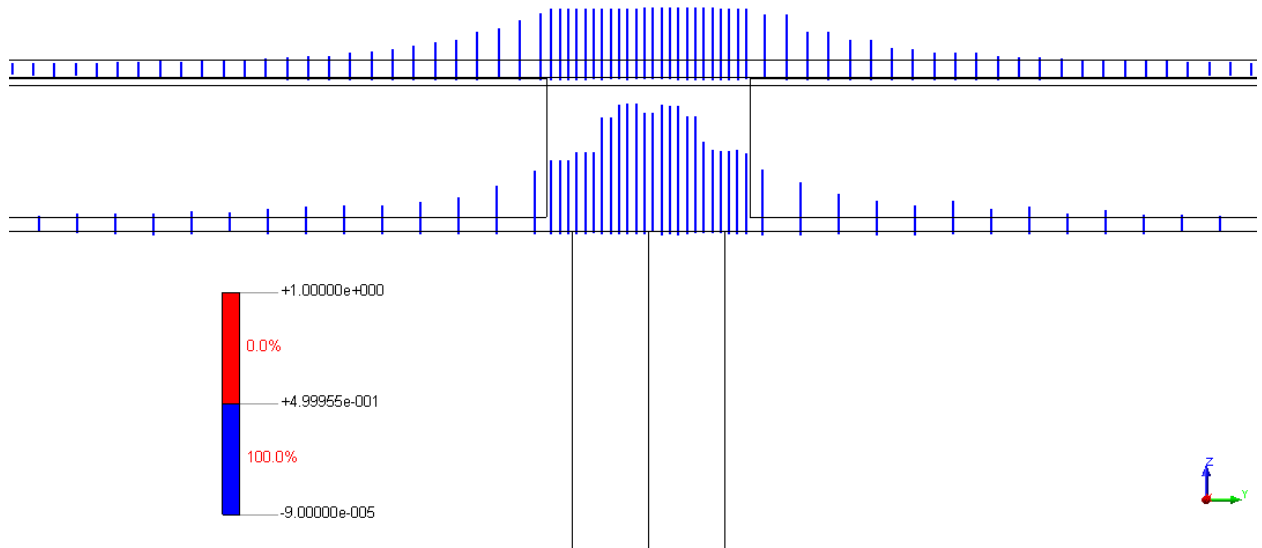
Figure 5.4   **Side view of the tensile strain distribution in the bent cap beam and the adjacent slab transverse reinforcement under combined vertical and lateral loading for bridge 1 (identified in Figure 5.1 and Figure 5.2).**
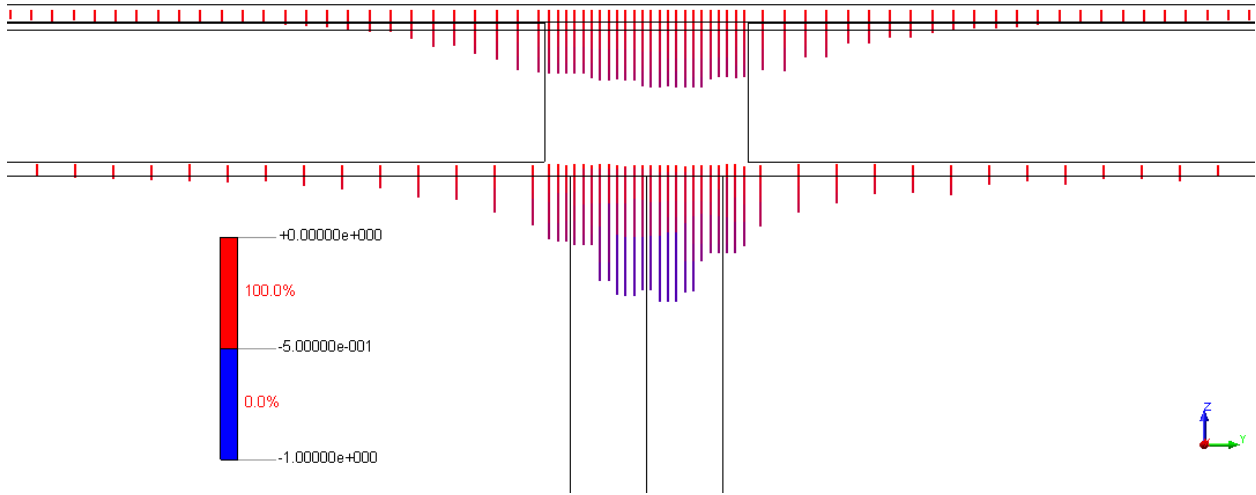
Figure 5.5   Side view of the compression strain distribution in the bent cap beam and the adjacent slab transverse reinforcement under combined vertical and lateral loading for bridge 1 (identified in Figure 5.1 and Figure 5.2).
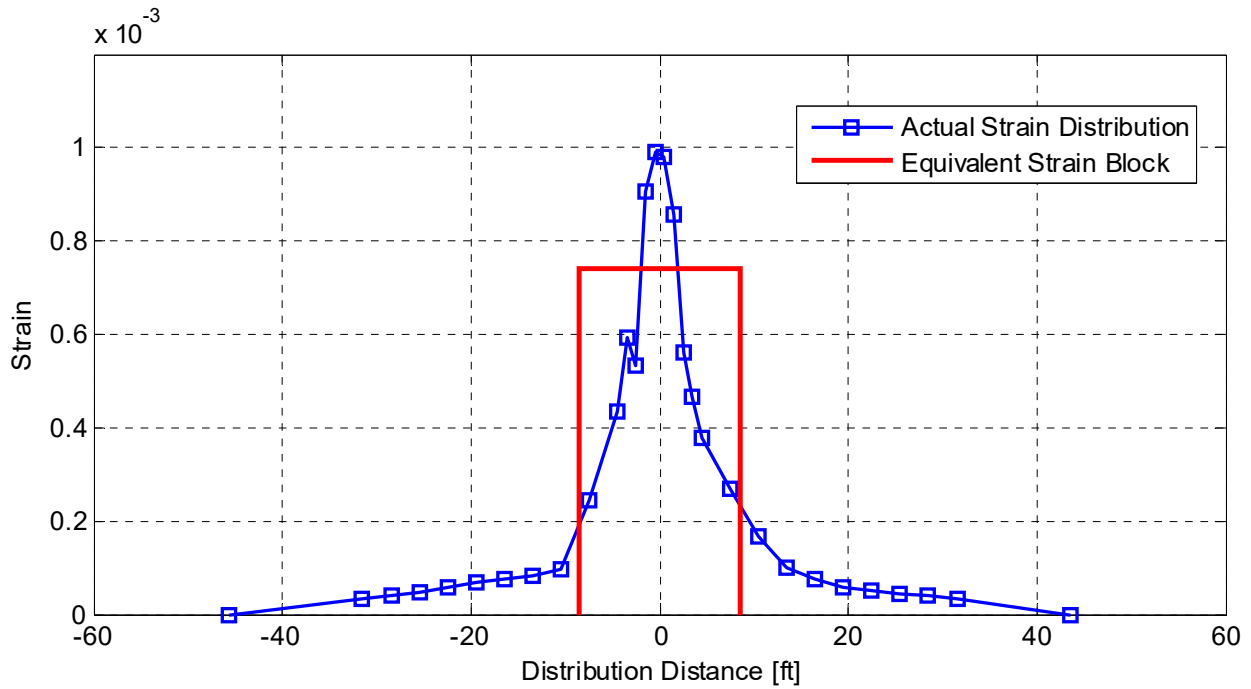
Figure 5.6   Tensile strain distribution in the bent cap and soffit slab transverse reinforcement at Section 1 (identified in Figure 5.2) under combined gravity and lateral transverse load as obtained from DIANA FE linear elastic model.
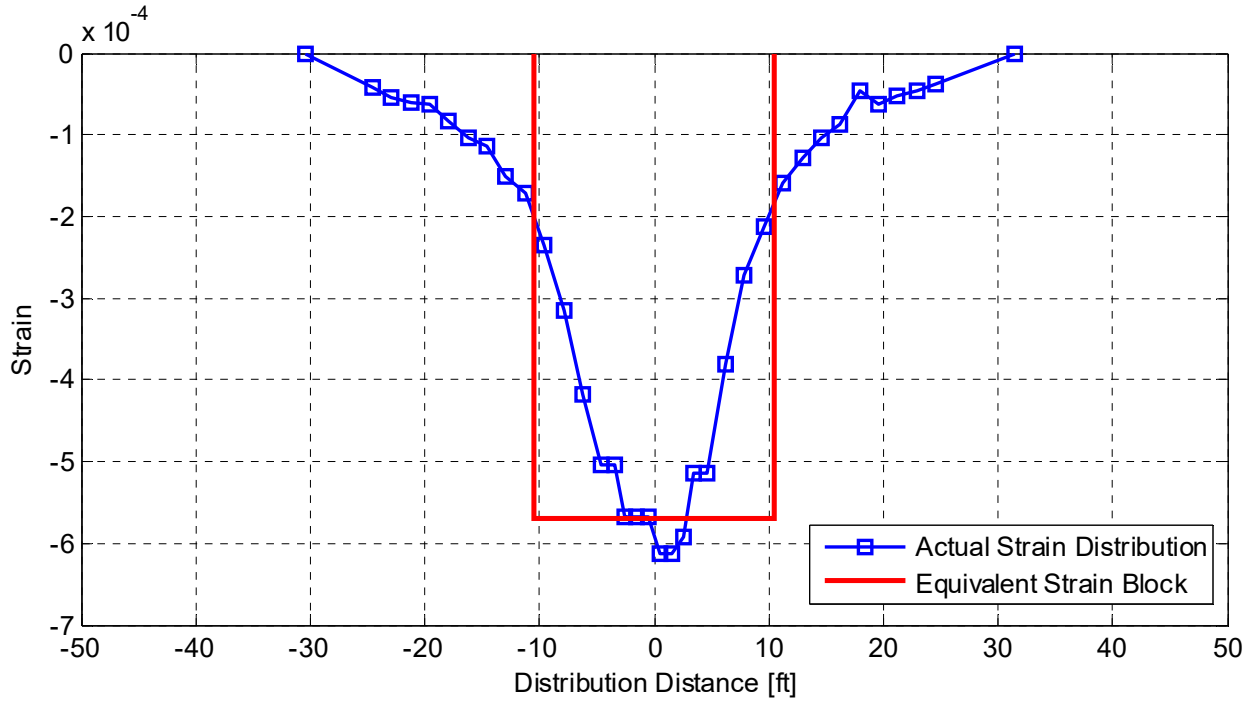
Figure 5.7 Compression strain distribution in the bent cap and deck slab transverse reinforcement at Section 1 (identified in Figure 5.2) under combined gravity and lateral transverse load as obtained from DIANA FE linear elastic model.
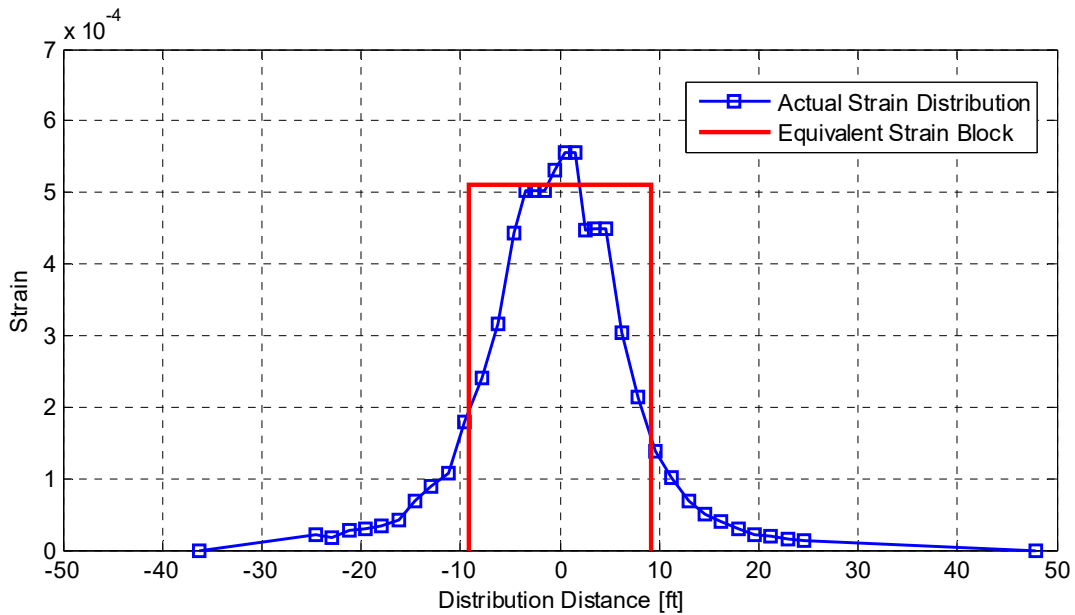
Figure 5.8 Tensile strain distribution in the bent cap and deck slab transverse reinforcement at Section 2 (identified in Figure 5.2) under combined gravity and lateral transverse load as obtained from DIANA FE linear elastic model.
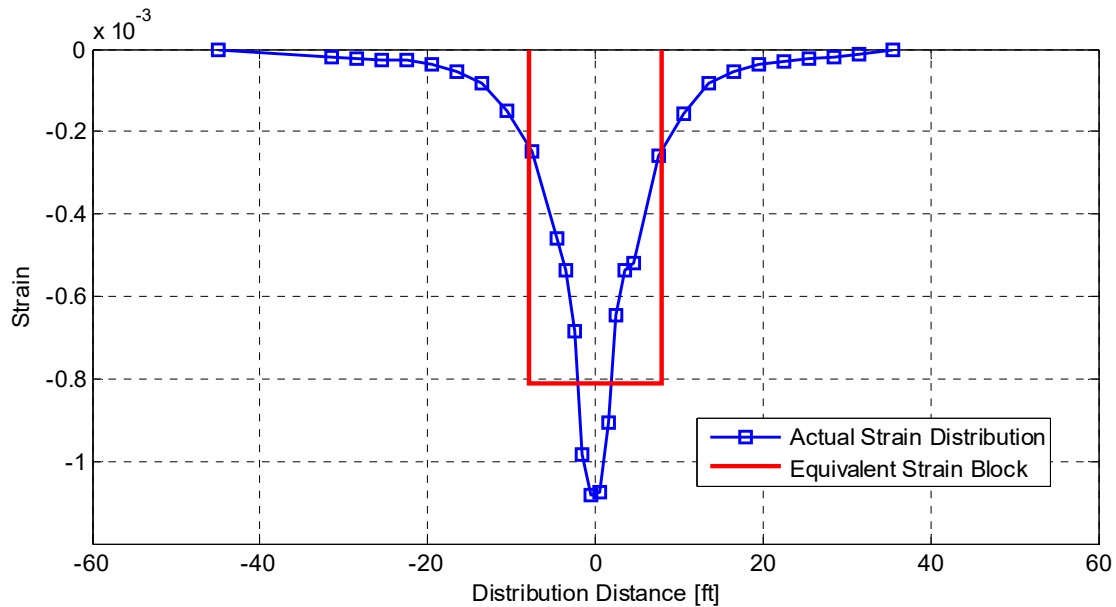
Figure 5.9   **Compression strain distribution in the bent cap and deck slab transverse reinforcement at Section 1 (identified in Figure 5.2) under combined gravity and lateral transverse load as obtained from DIANA FE linear elastic model.**

5.2.2 All Bridges Strain Distribution

Similar to the results shown for bridge 1 in the previous subsection, a summary of all the results for all nine bridges are presented in Figure 5.10 through Figure 5.13 and compared for each of the four locations here. Each figure shows a 3×3 matrix, where each row compares the bridges that have similar girders spacing and each column compares the bridges with similar set of soffit and deck slab thicknesses. The convention adopted here groups each three bridges with similar soffit and deck slab thicknesses together to obtain three groups as follows: group 1 comprises bridges 1, 4, and 7, group 2 comprises bridges 2, 5, and 8, and group 3 comprises bridges 3, 6, and 9, which was also identified earlier in Table 5.1. Figure 5.10 and Figure 5.11 show the tensile strain distribution and its corresponding equivalent strain block using the bent cap mean strain values for the deck and soffit slab sides, respectively. Similarly, Figure 5.12 and Figure 5.13 show the compression strain distribution and its corresponding equivalent strain block for the deck and soffit slab sides, respectively.
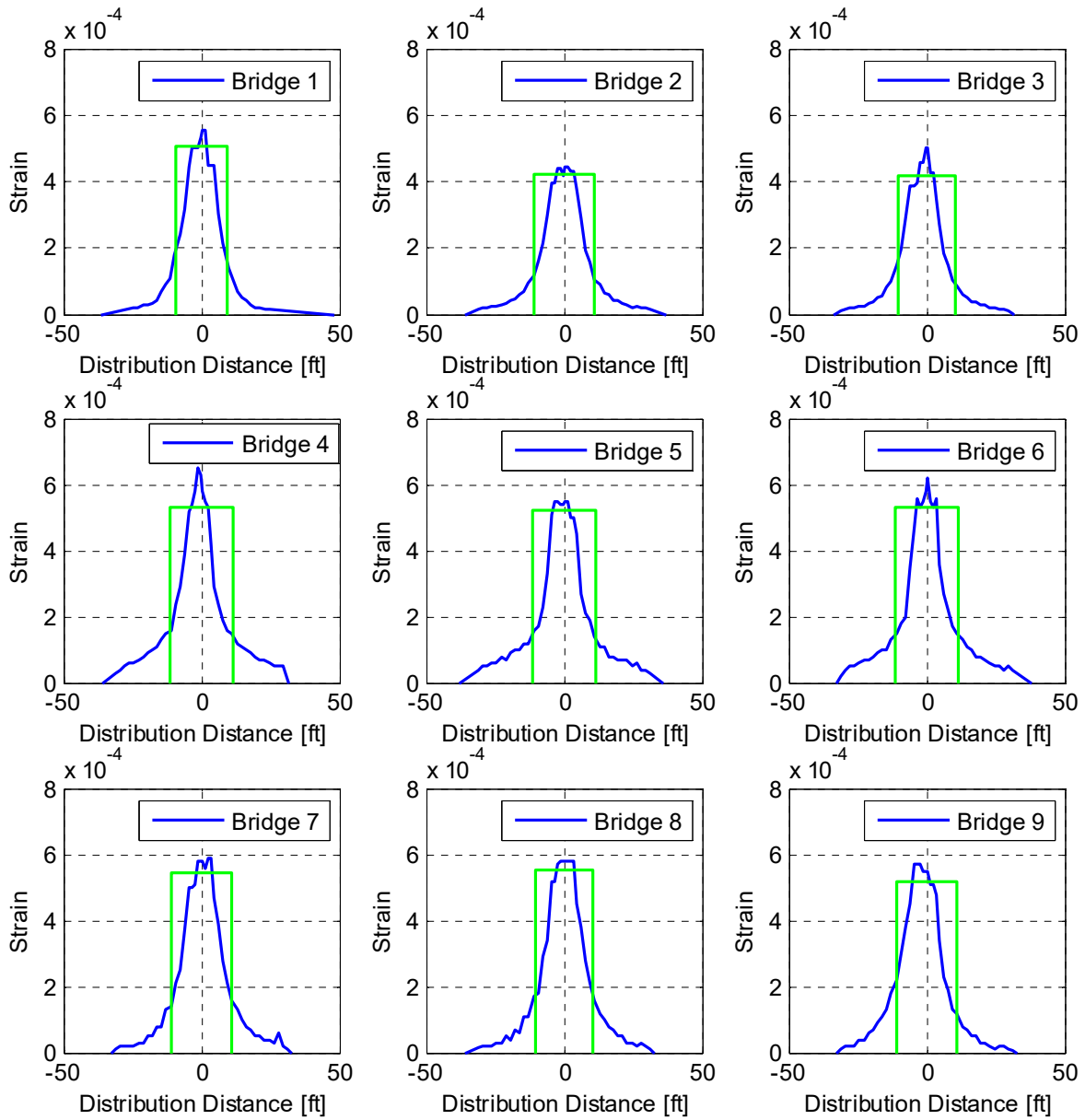
Figure 5.10 Summary of the strain distribution and the corresponding equivalent strain block in tension at the deck slab side at Section 1 for all bridges considered in the parametric study.

153
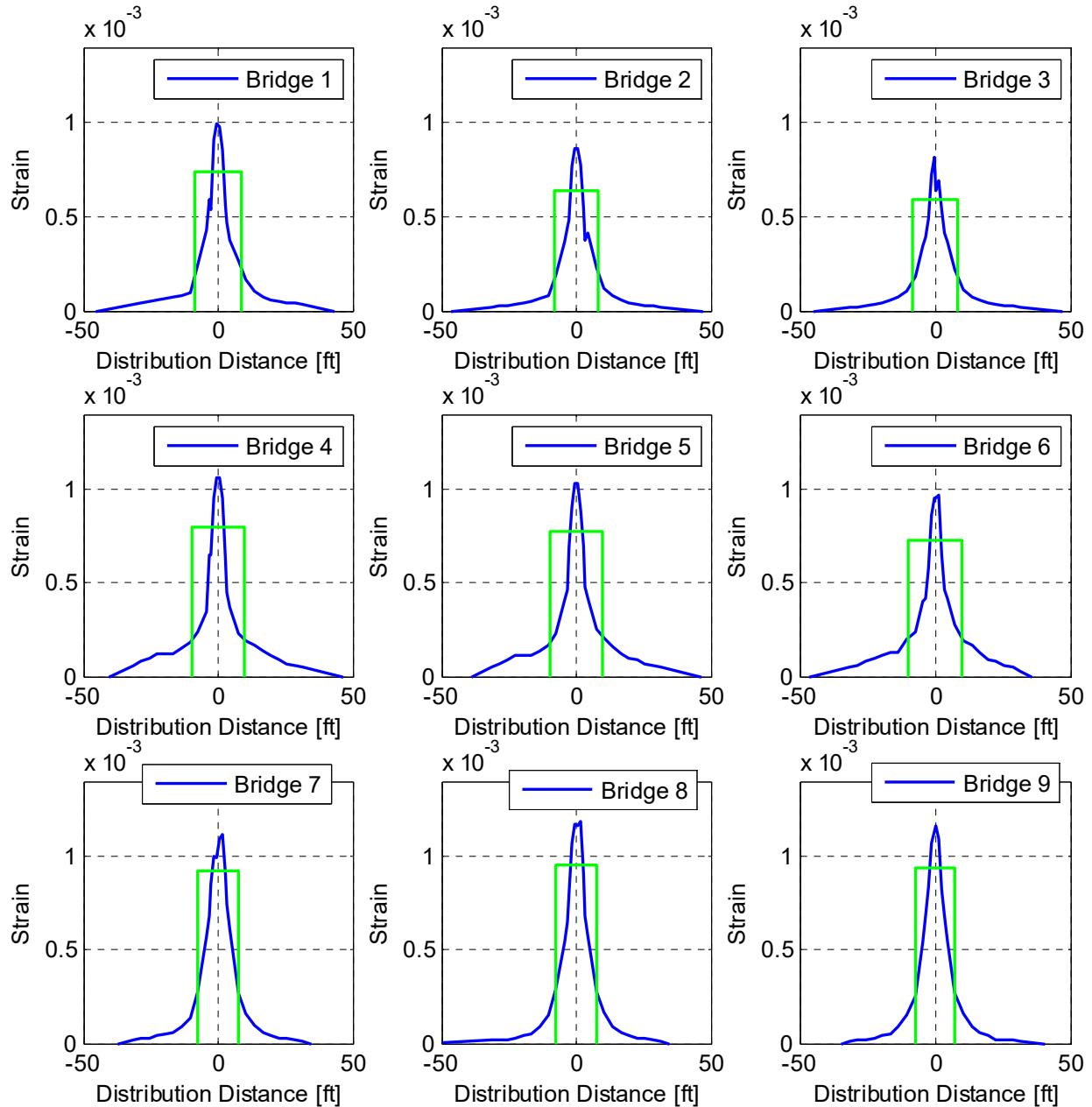
Figure 5.11   **Summary of the strain distribution and the corresponding equivalent strain block in tension at the soffit slab side at Section 2 for all bridges considered in the parametric study.**

Several observations can be made from the figures. First, the strain is consistently larger in the soffit slab side than the deck slab side whether in tension or compression. Given the uncracked nature of the concrete sections dictated by the elastic material model used in this study, the bent cap's neutral axis shifted towards the deck slab side. Note that this observation could have been attributed only to the larger deck slab thickness compared to the soffit slab. However, for group 3 (bridges 3, 6, and 9), both soffit and deck slab have same thickness (10.125 in.) and the same observation of larger strain values in the soffit side still holds. Hence, one explanation, that is associated with the compression and tension forces equilibrium, is that

the contribution from the deck slab is larger than that from the soffit slab to account for the lower strain values. This observation is confirmed from the effective slab width calculations as discussed in the next section. Another observation from the figures is that the strain distribution is flatter inside the bent cap at the deck slab side. This can be attributed to the proximity of the soffit slab maximum strain location to the bent column where the bent cap cross-section depth suddenly increases. This results in more localized strains at the soffit slab side than at the deck side, which can be another reason for the observed higher soffit side strains.
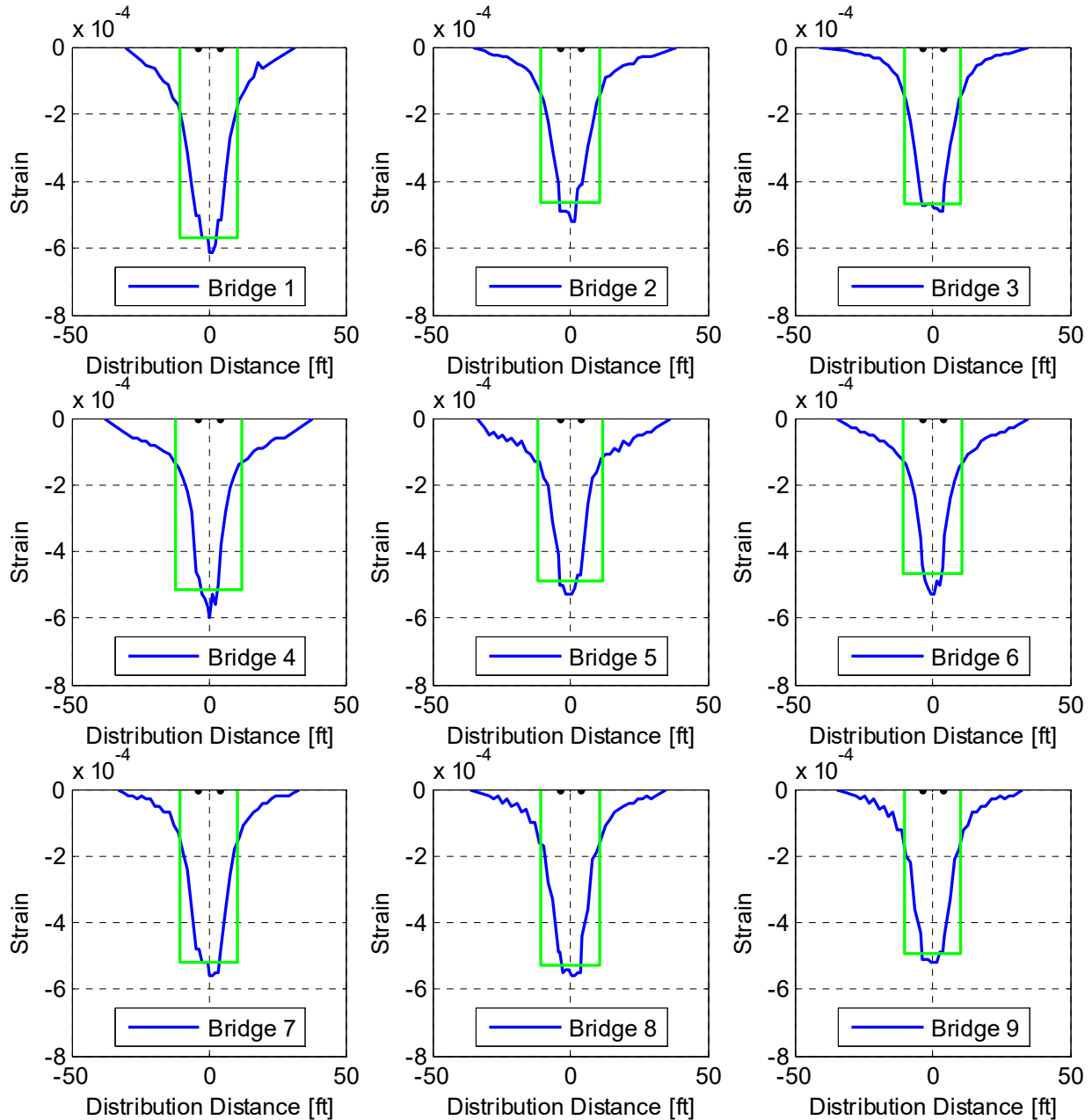
Figure 5.12   **Summary of the strain distribution and the corresponding equivalent strain block in compression at the deck slab side at Section 2 for all bridges considered in the parametric study.**
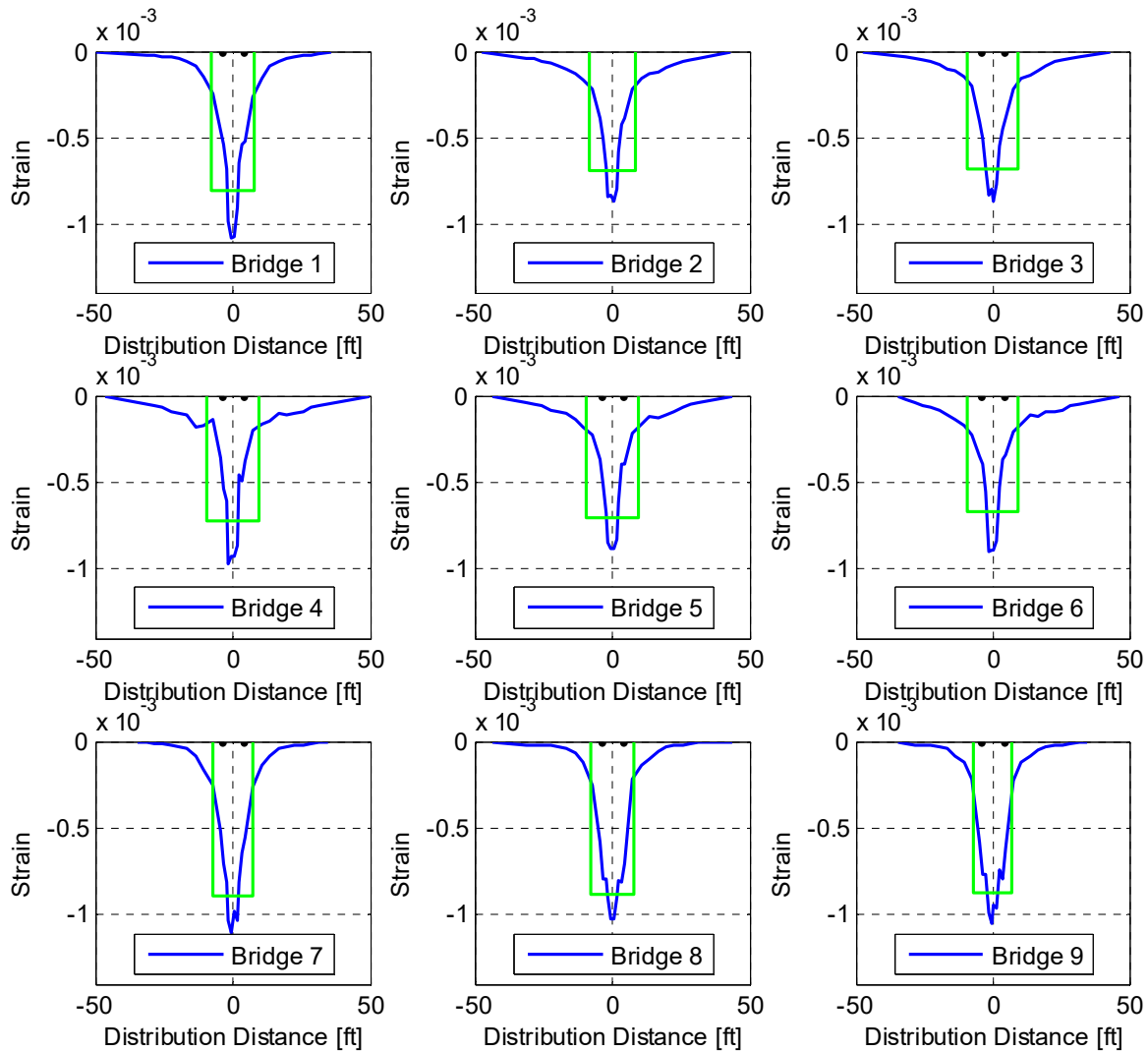
Figure 5.13 Summary of the strain distribution and the corresponding equivalent strain block in compression at the soffit slab side at Section 1 for all bridges considered in the parametric study

5.3 EFFECTIVE SLAB WIDTH

The procedure for estimating the bent cap effective slab width as explained in detail in the companion report is adopted here. The total effective width calculated from the equivalent strain block and the slab contribution expressed in terms of the slab thickness are presented for each of the nine bridges involved in the parametric study and compared against the Caltrans SDC [2011] and AASHTO [2013] values.

5.3.1 Total Effective Width (B_{eff})

The total effective slab width, designated as B_{eff} throughout this study, consists of the bent cap width and the slab contribution from each of the two sides of the bent cap. The B_{eff} is calculated directly from the equivalent strain block width that is based on the mean value of the strain

inside the bent cap. Figure 5.14 and Figure 5.15 summarize the bent cap effective slab width at the deck slab side in tension and compression, respectively. Similarly, Figure 5.16 and Figure 5.17 show the effective slab width at the soffit slab side in tension and compression, respectively. Each of these figures compares each of the bridge groups against the Caltrans SDC [2011] value estimated as the bent cap width plus 12 times the slab thickness. Each group is compared against the same value because a given group represents the bridges with similar slab thickness but different girder spacing. Thus, comparing different bridges among the same group demonstrates the effect of the girder spacing, while comparing bridges with same spacing from different groups demonstrates the effect of the slab thickness.
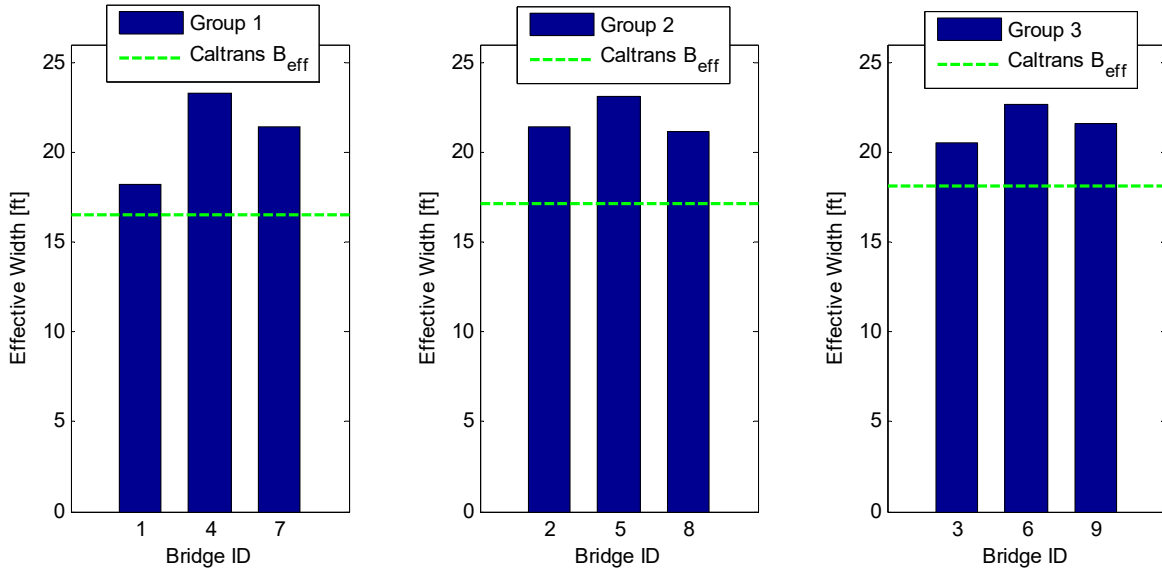
Figure 5.14 Integral bent cap effective width (*B*$_{eff}$) in tension at the deck slab side for all bridges along with the Caltrans value for each group.
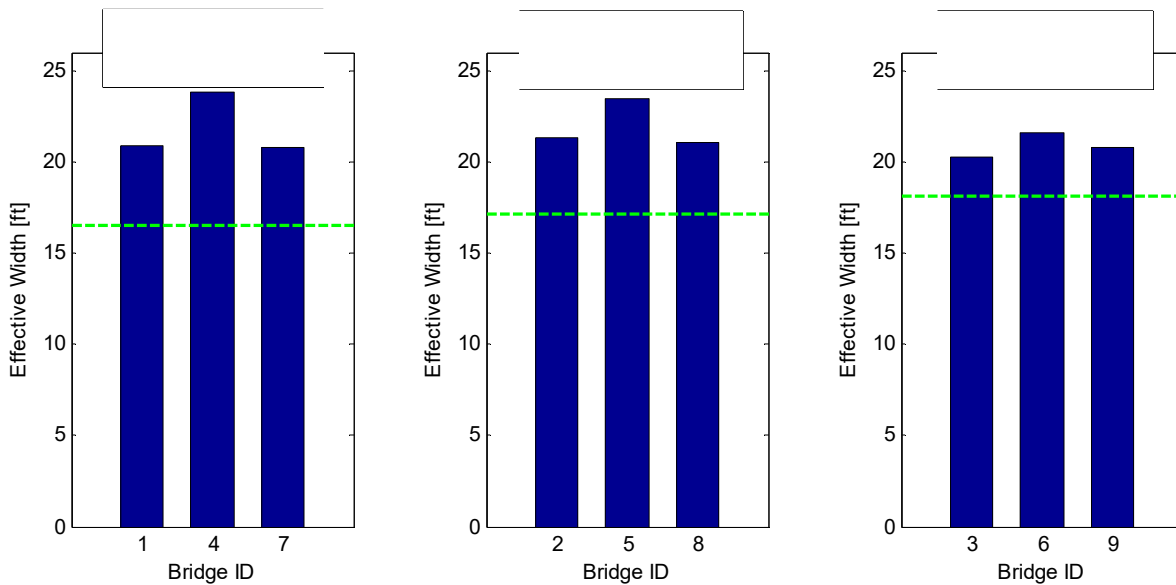
Figure 5.15 Integral bent cap effective width (*B*$_{eff}$) in compression at the deck slab side for all bridges along with the Caltrans value for each group.
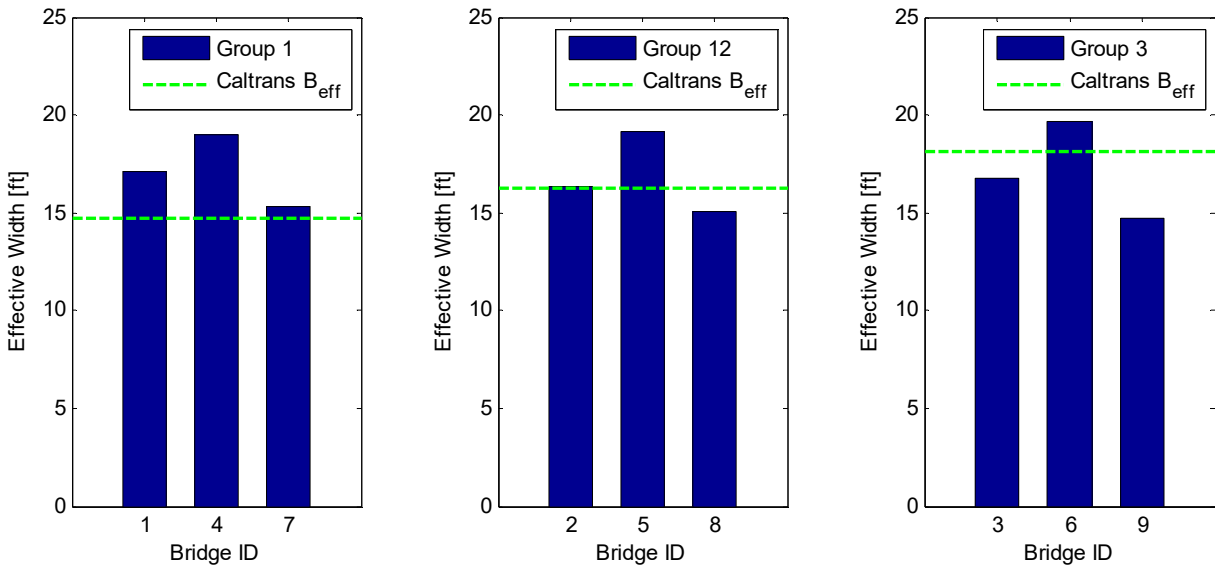
Figure 5.16   Integral bent cap effective width (B_{eff}) in tension at the soffit slab side for all bridges along with the Caltrans value for each group.
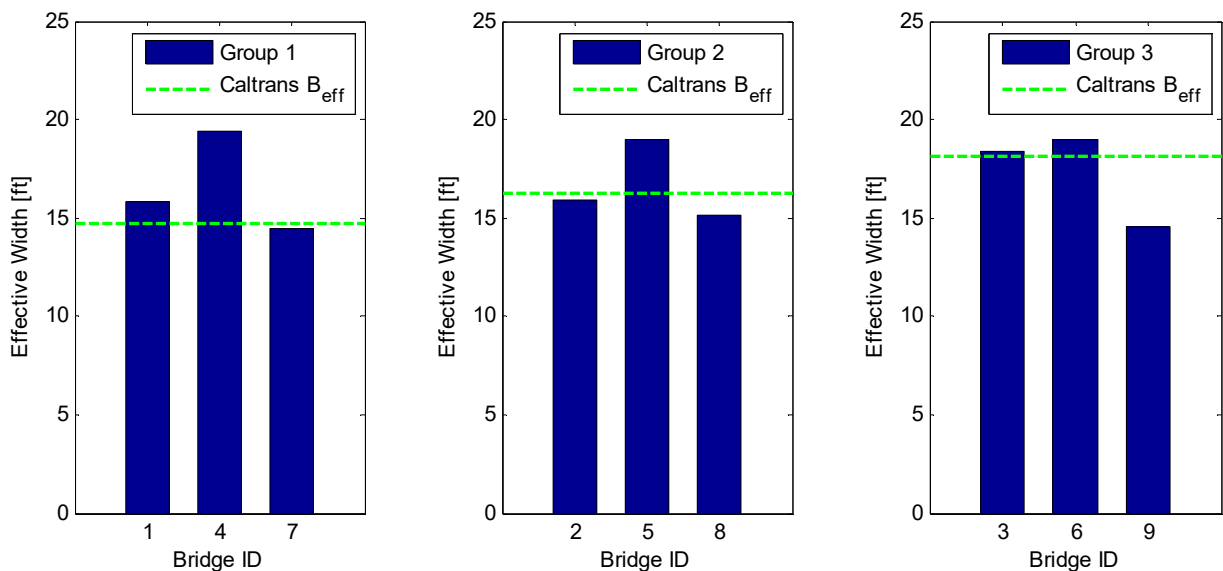
Figure 5.17   Integral bent cap effective width (B_{eff}) in compression at the soffit slab side for all bridges along with the Caltrans value for each group.

The same information given by the above figures is summarized in a tabular form in Table 5.2. From the figures and the table, it can be observed that a larger effective width is estimated at the deck side. This confirms the observation made from the strain values and distributions discussed in the previous section. The code-based value for the effective slab width is rendered very conservative with respect to the estimated values from the FE parametric study at the deck slab side, and only conservative at some of the cases at the soffit slab side. Note that there is not an obvious trend for the effect of either the box-girder web spacing or slab thicknesses on the bent cap effective width. However, the figures demonstrate that those cases

where the web spacing is 11 ft showed the largest effective width, i.e., largest slab contribution. This can be attributed to the distribution of the box-girder webs where a web that exists directly at the column-bent cap interface where the maximum bending moments are expected leads to the largest slab contribution and effective slab width. This was the case in bridges 4, 5, and 6 where the spacing was 11 ft regardless of the slab thickness. Moreover, note the slab thickness does not significantly change the effective slab width. For a different representation of the results, discussed next how the slab contributions are related to the slab thickness, i.e., expressed in terms of t_s.

Table 5.2   **Summary of the total effective width (B_{eff}) estimated at both compression and tension sides of both sections for all bridges used in the parametric study.**

Bridge Group		Group 1			Group 2			Group 3			Mean Value
Bridge ID		**1**	**4**	**7**	**2**	**5**	**8**	**3**	**6**	**9**	
Total Effective Width, B_{eff} (ft)	Section 1 - top *(Deck in Compression)*	20.87	23.81	20.77	21.31	23.42	21.09	20.29	21.62	20.78	21.55
	Section 1 - bottom *(Soffit in Tension)*	17.13	18.95	15.34	16.32	19.17	15.07	16.75	19.65	14.74	17.01
	Section 2 - top *(Deck in Tension)*	18.22	23.26	21.39	21.37	23.13	21.17	20.56	22.67	21.57	21.48
	Section 2 - bottom *(Soffit in Compression)*	15.82	19.41	14.50	15.90	19.01	15.16	18.36	18.97	14.59	16.86

5.3.2   Slab Contribution in terms of Slab thickness (t_s)

For a more consistent comparison against the code-based $12t_s$ value given by the Caltrans SDC [2011] and the AASHTO seismic guidelines [2013], the slab contribution is calculated in terms of the slab thickness for each of the nine bridges at the four observed strain locations. Figure 5.18 and Figure 5.19 show the slab contribution at the deck side in tension and compression, respectively. Figure 5.20 and Figure 5.21 show the slab contribution at the soffit slab side also in tension and compression, respectively. Table 5.3 summarizes the slab contribution values for all cases.
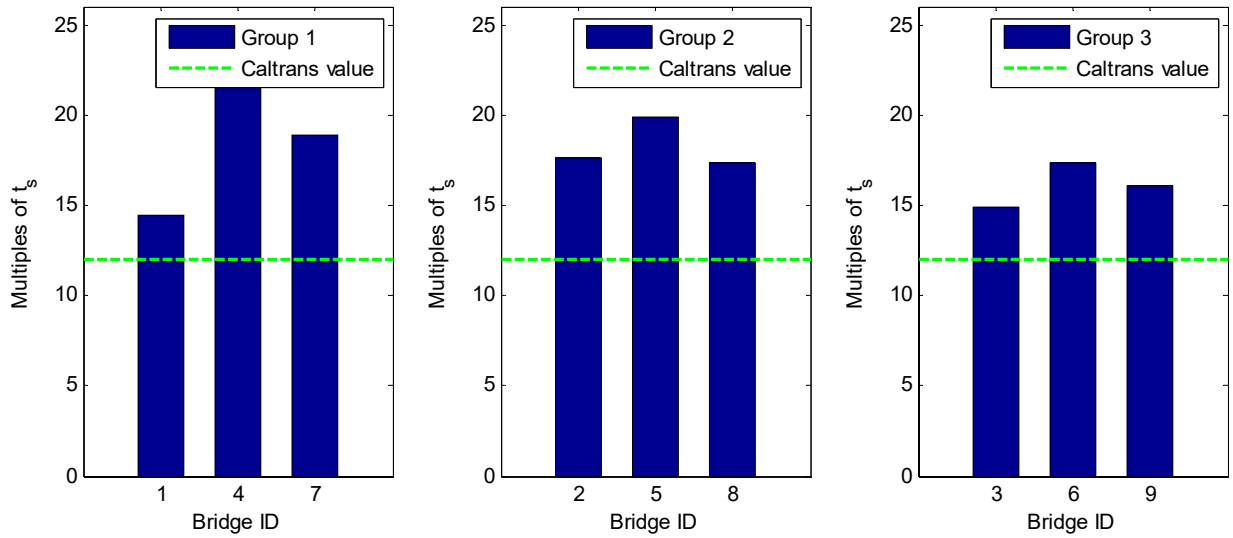
Figure 5.18   The effective slab portion as related to the slab thickness (t_s) for the bent cap in tension at the deck slab side for all bridges along with the 12t_s Caltrans value.
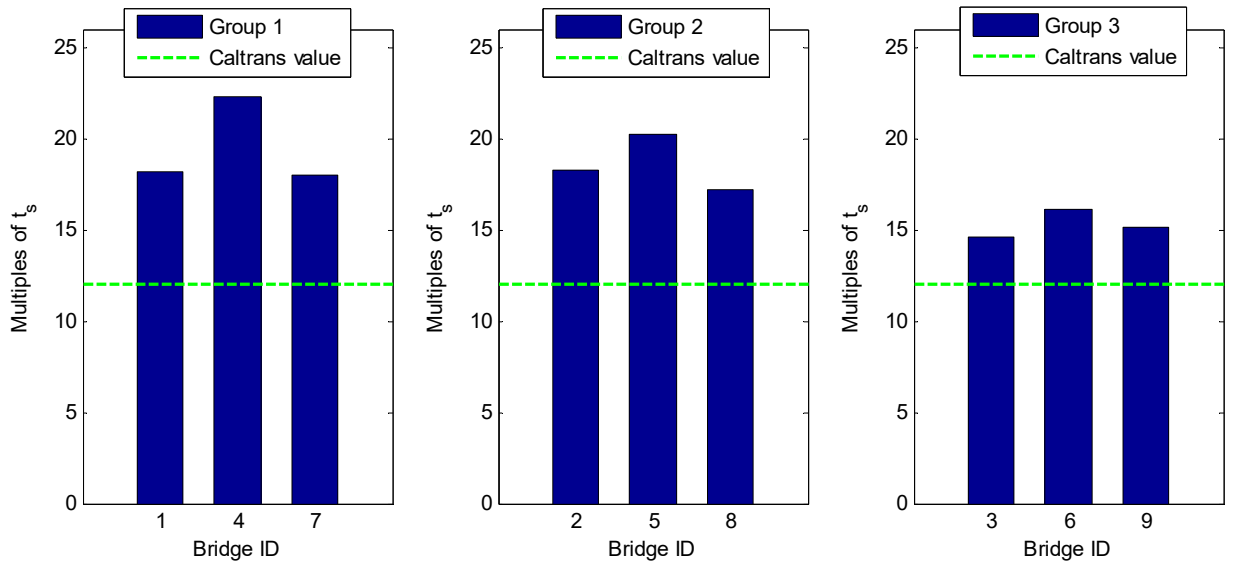
Figure 5.19   The effective slab portion as related to the slab thickness (t_s) for the bent cap in compression at the deck slab side for all bridges along with the 12t_s Caltrans value.

From the figures and the table, similar observations can be made from the total effective slab width. The deck side contribution is larger than the soffit side. Overall, the code value is conservative, as suggested by the mean values calculated for all nine bridges at each of the four observed strain locations. Overall average values of 17.71t_s and 17.56t_s were obtained for the deck slab contribution in tension and compression, respectively. Similarly, average values of 13.28t_s and 12.97t_s were obtained for the soffit slab contribution in tension and compression, respectively. These values closely agree with the experimental values estimated from both

Specimen No. 1 cyclic tests and Specimen No. 2 HS tests that were discussed in the companion report and Chapter 3 of this report, respectively. The figures also suggest that bridges 4, 5, and 6 where the clear box-girder web spacing is 11 ft demonstrated the largest slab contribution. To combine the effect of both box-girder web spacing and slab thicknesses, the aspect ratio of the clear box-girder cell width-to-depth ratio is used to investigate the effective slab width as discussed in the next.
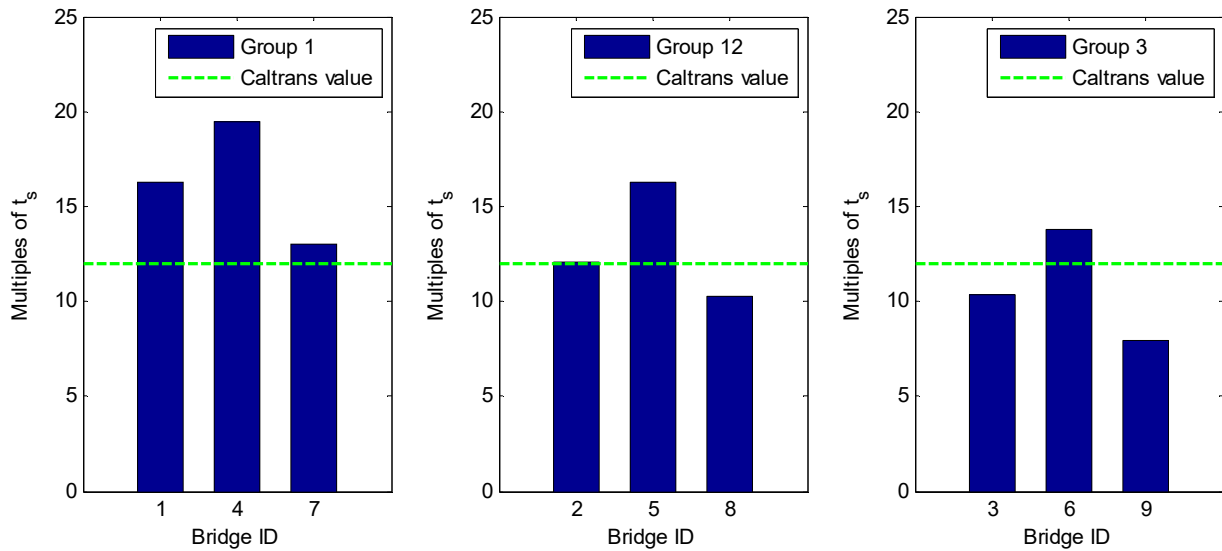
Figure 5.20 The effective slab portion as related to the slab thickness (t_s) for the bent cap in tension at the soffit slab side for all bridges along with the 12t_s Caltrans value.
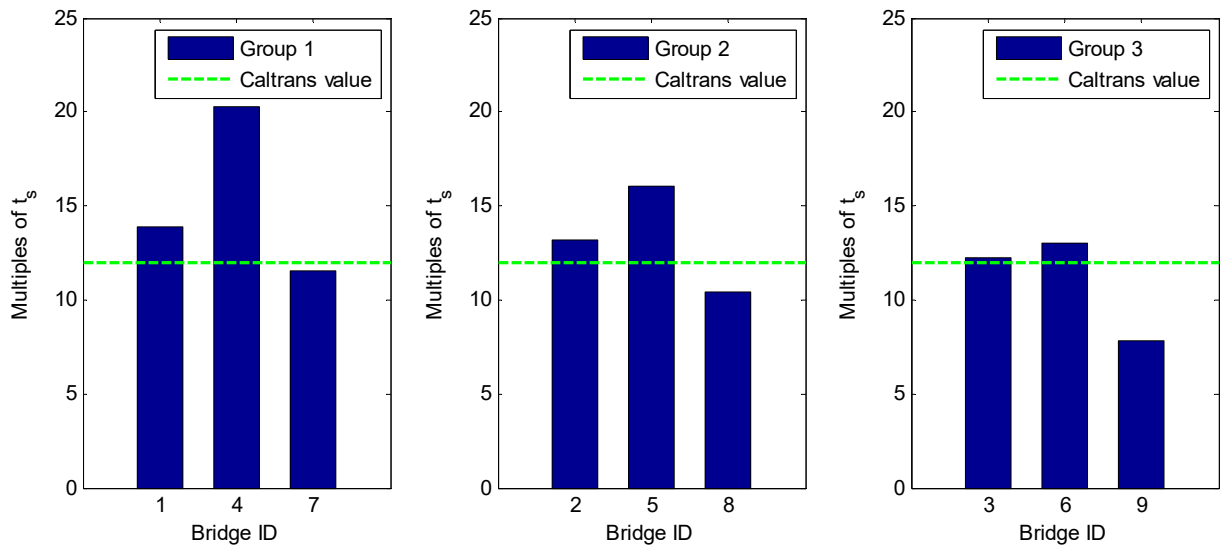
Figure 5.21 The effective slab portion as related to the slab thickness (t_s) for the bent cap in compression at the soffit slab side for all bridges along with the 12t_s Caltrans value.

Table 5.3   Summary of the effective slab width portion estimated as multiples of t_s at both compression and tension sides of both sections for all bridges used in the parametric study.

Bridge Group		Group 1			Group 2			Group 3			Mean Value
Bridge ID		**1**	**4**	**7**	**2**	**5**	**8**	**3**	**6**	**9**	
Effective Slab Width (multiples of t_s)	Section 1 - top (Deck in Compression)	18.17	22.32	18.03	17.50	20.28	17.21	14.57	16.14	15.15	17.71
	Section 1 - bottom (Soffit in Tension)	16.23	19.47	13.05	12.10	16.25	10.28	10.37	13.81	7.99	13.28
	Section 2 - top (Deck in Tension)	14.43	21.54	18.90	17.58	19.90	17.32	14.89	17.39	16.08	17.56
	Section 2 - bottom (Soffit in Compression)	13.90	20.28	11.56	11.49	16.01	10.41	12.28	13.00	7.81	12.97

5.4   EFFECT OF BOX-GIRDER GEOMETRY

The main objective of the full bridge parametric study is to investigate the effect of the box-girder geometry (web spacing and slab thicknesses) on the bent cap effective slab width and slab contribution. The second objective is to calculate the effective slab width at the prototype bridge level in different cases under combined vertical and lateral loads to compare it against the given code value. Although Sections 5.2 and 5.3 provided insight with regard to the second objective, they did not provide a conclusive insight about the effect of the box-girder geometry. Thus, a parameter that reflects the box-girder geometry was considered in relation to the observed effective slab width. Ideally, it is desirable to optimize the box-girder geometry to obtain the largest slabs contribution to the bent cap beam for enhanced strength and stiffness. Thus, the effective width variation with respect to the box-girder net cell aspect ratio is investigated for box-girder geometry optimization. Figure 5.22 and Figure 5.23 show the soffit and deck slabs in tension and compression, respectively. Note that given the slab thicknesses and web spacing combinations of the nine bridges, nine different values were obtained for the box-girder cell aspect ratio that varied from almost 1.6 to 2.8 (refer to Table 5.1 for the exact values for each of the nine bridges). From the figures, it can be shown that the largest slab contribution, and in turn effective slab width, was observed at cell aspect ratios in the range of 2 to 2.15. This range for the cell aspect is recommended to take into consideration when the box-girder geometry is laid out. The larger contribution from the deck slab is also demonstrated in Figure 5.22 and Figure 5.23, where the effective slab width is consistently higher at the deck side whether in tension or compression.
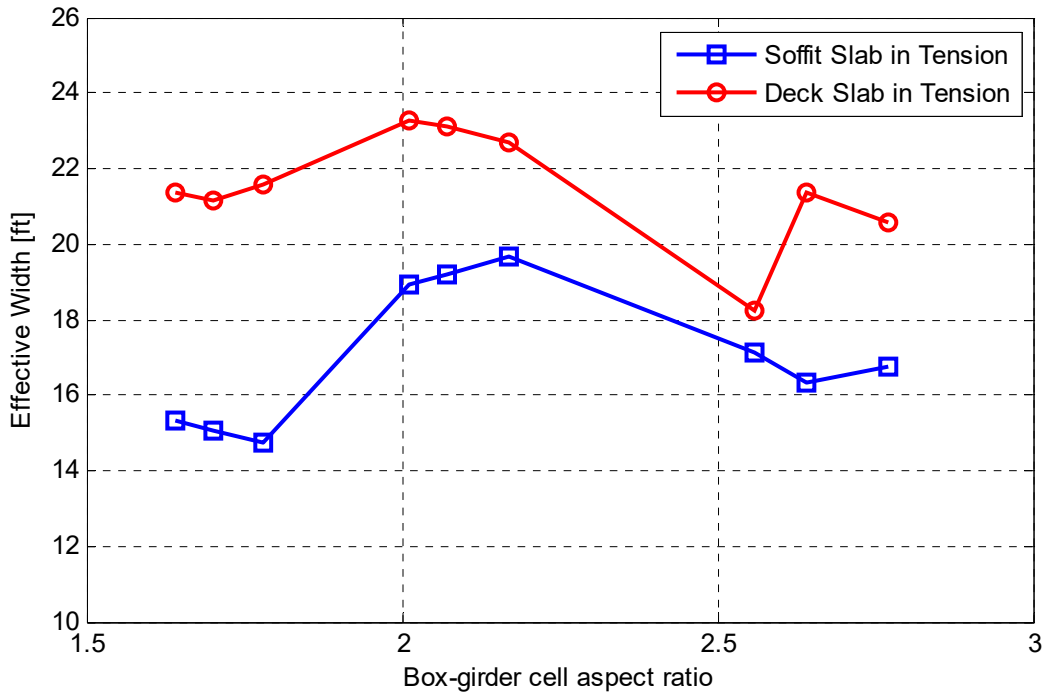
Figure 5.22 Variation of bent cap effective width in tension at each of the soffit slab (Section 1 in Figure 5.2) and the deck slab (Section 2 in Figure 5.2) with respect to the box-girder cells aspect ratio.
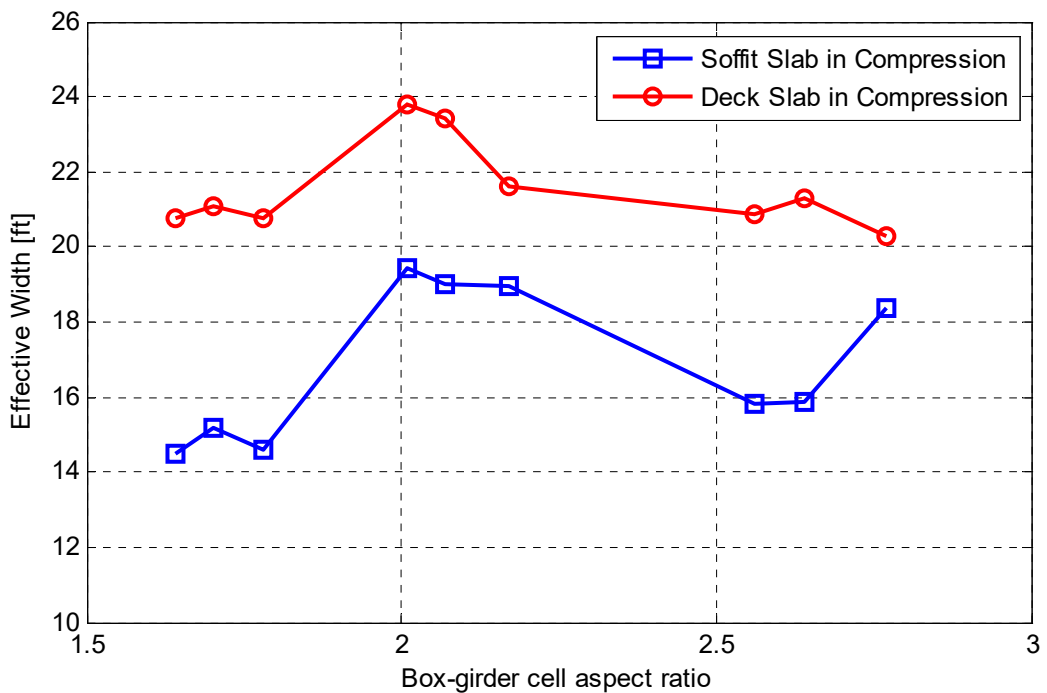
Figure 5.23 Variation of bent cap effective width in compression at each of the soffit slab (Section 2 in Figure 5.2) and the deck slab (Section 1 in Figure 5.2) with respect to the box-girder cells aspect ratio.

6 Conclusions and Future Research

A summary of the experimental and computational frameworks developed, the main conclusions, and recommendations for future work based on the full study is presented here. This chapter provides the summary and the conclusions from both parts of the report (Parts I and II) for the convenience of the reader and for completeness.

6.1 SUMMARY

The study reported in the two parts of the report comprised computational and experimental frameworks to investigate the structural behavior and seismic response of bent cap beams in as-built and retrofitted RC box-girder bridges under the combined effect of vertical and lateral loading. In particular, the contribution of the box-girder slabs to the stiffness and strength of the integral bent caps was evaluated for optimized design and enhanced capacity estimation. Four main objectives of this study are highlighted: (a) revisiting the effective slab width for integral bent caps in RC box-girder bridges; (b) an investigation the effectiveness of CFRP column retrofit in enhancing column capacity in light of the consequent amplified demands on bent cap and the resulting subassembly performance; (c) the development and successful performance of multi-DOF Hybrid Simulation (HS) tests using a new practical approach for HS communication; and (d) calibration of a detailed FE model for investigating the influence of box-girder contribution for several hypothetical cases of higher levels of bent cap damage when the bent cap beam reinforcement is reduced.

The computational part of the study consisted of two phases: pre-test and post-test analysis. The experimental program involved testing two ¼-scale column-bent cap beam–box-girder sub-assemblies using quasi-static and HS testing methods. The test specimens were adopted from a prototype that was slightly modified from the Caltrans Academy Bridge and were designed in light of the most recent AASHTO and Caltrans SDC provisions. An overview of the different parts of the study is summarized in the following paragraphs.

The first phase of the computational framework, i.e., the pre-test analysis phase, utilized 1D, 2D, and 3D FE models, which were developed and used to carry out different types of analyses that varied from linear elastic static analysis to nonlinear time-history analysis. Different models were developed for both of the full prototype bridge and the test specimen using OpenSees, SAP2000, and DIANA FE packages. The pre-test analysis successfully verified the expected subassembly behavior, provided the input for the final gravity load levels and

lateral loading protocol, delivered the expected loads and straining actions for test set-up design, and provided necessary information for instrumentation distribution.

The pre-test analysis was then followed by the experimental program that comprised the core of the study. The first stage of the experimental program involved quasi-static cyclic loading tests of the first specimen (Specimen No. 1) in as-built and repaired conditions. Bi-directional cyclic loading tests in both transverse and longitudinal directions were conducted under constant gravity load. A rapid repair scheme was adopted for the tested specimen using a three-layer CFRP column jacket. The partial repair aimed at providing at least minimal capacity for the specimen to be reused for the HS development and trial runs. However, a quasi-static cyclic test similar to the one applied to the as-built specimen was carried out for the repaired specimen for comparison purposes and to verify the essentially elastic status of the bent cap beam.

The second stage of the experimental program used the HS testing technique for providing realistic dynamic response input to the test specimens as the lateral loading. A new practical approach that utilized readily available laboratory data acquisition systems as a middleware for feasible HS communication was achieved. The proper communication among the HS components and the verification of the HS system were first performed using test runs conducted on standalone hydraulic actuators, i.e., they were not attached to any physical specimens. Next, the same Specimen No. 1 that was tested as-built, was repaired, retested in quasi-static cyclic tests, and was utilized one last time to carry out actual HS trial tests. All the HS trials were successful, which verified the robustness of the developed HS system. The column of Specimen No. 2 was retrofitted using CFRP jacketing before any testing to increase the demands on the bent cap beam. The retrofitted Specimen No. 2 was then tested using multi-degree of freedom HS under constant gravity load and using unidirectional and bi-directional near-fault ground motions in several intensity levels and polarity.

The post-test analysis was the final stage of the study. The results from the as-built first specimen cyclic tests were used to calibrate the most detailed 3D FE model, which was previously developed as part of the pre-test analysis stage. The calibrated model was used to explore the effect of reducing the bent cap reinforcement on the overall system behavior and to investigate how the box-girder contributes at higher levels of bent cap damage. The design implications of the main outcome from all of the different analyses and experiments concluded this study. A short illustrative design example was carried out to investigate the implications of the revisited effective slab width and bent cap capacity estimation on the optimization of the bent cap design for a full-scale bridge. The computational framework was concluded with another parametric study at the full bridge level to investigate the effect of the box-girder geometry, namely, the webs spacing and slab thicknesses on the slab contributions and the bent cap effective width to optimize the box-girder geometry for the most efficient slabs contribution to the bent cap structural behavior.

6.2   CONCLUSIONS

Several conclusions were drawn from this study as follows:

- The preliminary prototype bridge triaxial time history analysis showed that the inclusion of the vertical excitation component can lead to unfavorable damage or failure in the bent cap beams. A large number of near-fault ground motions were used to run time history analysis on the modified Academy Bridge prototype with and without the vertical excitation component. Six out of 88 considered ground motions led to excessive curvature values, i.e., plastic hinge damage at different locations of the bent cap beam only when the vertical excitation was included. These six ground motions were concluded to cause highest demands in the bent cap independently from the column capacity due to the vertical excitations. This observation violates the fundamental design principle of strong beam–weak column capacity design concept required by the Caltrans SDC and AASHTO seismic design guidelines, and calls for further investigation.

- The most detailed and accurate 3D DIANA model for the test specimen successfully predicted the subassembly behavior and mode of failure. A lateral force capacity was determined from the DIANA nonlinear pushover analysis to be almost 45 kips, which is only within 5% difference from the 47.5 kips experimentally determined capacity. Different modes of failures were observed from the 3D DIANA model under different gravity load levels combined with lateral pushover. At the 10% gravity load level, which was used in the large-level cyclic loading tests, the predicted mode of failure from the analysis matched the experimentally observed failure mode of column plastic hinging. The detailed DIANA model was further calibrated and used in post-test analysis.

- The observed as-built Specimen No. 1 behavior satisfied all the Caltrans SDC design objectives. The mode of failure was a fully developed plastic hinge in the sub-assembly column whereas the bent cap beam and superstructure remained essentially elastic. The performance of the bridge system exceeded the minimum required performance levels set by Caltrans SDC. The bridge sub-assembly, and particularly its ductile column, successfully achieved a 7.6 ductility level, which corresponds to a 10.5% drift ratio in the transverse direction; a 5.4 ductility level that corresponds to 7.5% drift ratio was achieved in the longitudinal direction. The buckled column rebars started to rupture at the 5.4 ductility level loading in the longitudinal direction, leading to capacity loss. The 5.4 ductility level was still superior to the minimum displacement ductility of 4.0 required by Caltrans SDC.

- The bridge sub-assembly tests showed slightly different stiffness in the transverse and the longitudinal directions. This is attributed to the slightly more flexible column–box-girder connection relative to the column-bent cap connection. The slightly higher transverse stiffness observation was more pronounced in the as-built Specimen No. 1 tests compared to the retrofitted Specimen No. 2 tests because the stiffness in the longitudinal direction is sensitive to the soffit and deck slab thicknesses, which governs the box-girder overall stiffness. Therefore, due to construction imperfections, the stiffness can vary, as observed in the two specimens. In addition, Specimen No. 1 stiffness degradation in both transverse and longitudinal directions was monitored and related to the different ductility levels and drift ratios. Only Specimen No. 1 was considered in that regard as it experienced the desired column mode of failure as required by code provisions. At 7.56 ductility level, the transverse

stiffness was about 13% of its initial value, while a longitudinal stiffness of almost 10% of the initial value was observed at 5.40 ductility level, i.e., the specimen lost close to 90% of its initial stiffness at the final damaged state.

- The rapid CFRP repair technique successfully achieved its objective of partially restoring Specimen No. 1 test sub-assembly capacity and significantly increased the stiffness in both transverse and longitudinal directions. To quantify the repair effectiveness, a maximum increase of 25% in the capacity was obtained due to the repair relative to the residual capacity after all column rebars buckled and six of them ruptured. Moreover, an increase of more than 300% was achieved in the stiffness from the final damaged state because of the repair. Note that regardless of the significant increase in the stiffness, the original initial stiffness and strength were not fully achieved. It is also noted that the injection of the cracks prior to the application of the CFRP was the main contributor to this increase of the stiffness and not the CFRP jacket itself.

- The retrofit CFRP technique was effective in increasing Specimen No. 2 column capacity due to the enhanced confinement. It was observed that the force capacity of the whole sub-assembly and the moment capacity of the column increased by almost 25% in Specimen No. 2 compared to Specimen No. 1 The jacket confinement prevented any concrete spalling or bar buckling or rupture, which is important for post-earthquake bridge resiliency as it minimizes the down time for any column repairs. From a research perspective, the retrofit scheme also achieved its intended objective of increasing the demands on the bent cap beam and delaying or preventing the column failure, which allowed for investigation of bent cap beam mechanism in order to better estimate the bent cap capacity. Consequently, the amplified moment demands from the higher gravity level and retrofitted column led Specimen No. 2 bent cap moment to cap at about 6500 kip-in. versus a maximum value of approximately 4500 kip-in. in Specimen No. 1 cyclic tests.

- The bent cap beam experienced yielding in the as-built Specimen No. 1 tests but remained essentially elastic. The essentially elastic state was confirmed by visual evidence that no extensive cracking took place at the tension side nor concrete crushing occurred in the compression side. In addition, the bent cap beam behaved linearly elastic when the sub-assembly was repaired and retested. A more accurate value for the yield moment of the bent cap beam was determined accordingly. The yield moment rendered the recommended Caltrans SDC and AASHTO bent cap beam flanged section conservative in terms of the effective slab width contribution.

- The onset of the bent cap beam damage and its moment capacity were captured through the retrofitted Specimen No. 2 HS tests. The overall system force capacity and the bent cap beam moment were both capped and reached a steady state regardless of the amplified HS test scales. Visual damage of Specimen No. 2, i.e., concrete crushing in the bent cap compression side and only uniform flexural crack pattern in the column underneath the CFRP jacket, suggested that the capacity reached was dictated by the bent cap capacity. The moment cap value of almost 6500 kip-in. was justified to be a reasonable experimental estimate of the bent cap beam capacity. Sectional analysis based on the Caltrans SDC provisions and actual material properties specified that the bent cap beam capacity is only around 5000 kip-in. Consequently, both the Caltrans and AASHTO, provisions were found to underestimate the bent cap capacity as was shown for the yield moment obtained from Specimen No. 1 as well.

- A simple procedure was devised to experimentally determine the bent cap beam effective slab width using the equivalent strain block concept from Specimen No. 1 cyclic tests and Specimen No. 2 HS tests. Two strain values from the different reinforcing steel bars in the bent cap were used for the equivalent strain block. These were the minimum and mean of six instrumented bars at a given cross section. Consequently, the effective slab width was evaluated for all Specimen No. 1 and Specimen No. 2 test runs and for different sections, mainly in the tension side. The results from the compression side were not conclusive because the strain measurements were sensitive to the concentrated gravity load. The results for the effective slab width, obtained from the tension side, rendered the $12t_s$ Caltrans SDC and AASHTO code value for effective slab width unnecessarily conservative. The overall mean value for the effective width as determined from all the as-built Specimen No. 1 cyclic loading tests was $13.7t_s$ and $21.2t_s$ when the cap beam mean and minimum strain values were used, respectively. Smaller estimates for the effective slab width were obtained from Specimen No. 2 HS tests. These were $11.5t_s$ and $15.8t_s$ when the cap beam mean and minimum strain values were used, respectively. Thus, the original $12t_s$ code value was supplemented by a proposed revised value of $18t_s$ for investigating the bent cap beam capacity estimation and design implications. The basis for choosing the $18t_s$ value for the effective slab width is that it reasonably resembled the mean of the $21.2t_s$ and $15.8t_s$ upper bounds from the experiments, whereas the original $12t_s$ resembled the mean of the $13.7t_s$ and $11.5t_s$ lower bounds.

- A practical HS system that utilizes readily available laboratory data acquisition systems along with inexpensive TCP/IP-Ethernet connections to establish the communication between the physical and computational substructures was successfully developed, verified, and utilized in Specimen No. 2 HS tests. The main development included augmenting the PI data acquisition with a new interface to communicate with OpenFresco from the computational side and the DSP card from the experimental side. The new interface utilized an inexpensive Ethernet connection to replace expensive shared memory communication cards, such as SCRAMNet, for communicating with the computational side. Moreover, a DSP algorithm complemented the new interface to control the laboratory hardware and receive the physical substructure feedback. A new test set-up component in OpenFresco was successfully developed as well to perform geometric transformations between the global DOFs in the computational model and the actuators' local DOFs for command displacements and force feedback measurements. The HS test trials using only the hydraulic actuators and the repaired Specimen No. 1 successfully validated the new communication interface and new OpenFresco geometric transformation experimental set-up object. Accordingly, the validation tests provided confidence on the robustness of the HS system to be used for Specimen No. 2 tests.

- The detailed DIANA 3D FE model for the test specimen was calibrated against the as-built Specimen No. 1 cyclic test results. The calibrated model successfully captured the global behavior of the sub-assemblage and the bending moments that developed in the bent cap beam within a 5% difference. The sensitivity of the global behavior observed from the FE analysis was investigated under different model and constitutive material input parameters as part of the FE model calibration. It was concluded that using two different sets of material model parameters for the column and the superstructure that reflected the natural material properties in the different concrete lifts used in construction led to the best match with the

experimental results. Thus, it is recommended for better analysis practices to use different material properties for the bridge bent component, if needed, to reflect actual conditions, especially for capacity checks and nonlinear analysis.

- The FE analysis using the calibrated set of material parameters determined the cap beam capacity from the original test specimen design in addition to two hypothetical designs with less reinforcement than what the original design required. The capacity obtained from the vertical pushover closely matched the experimental upper bound, which was related in part to the higher gravity load level (15%) used in the HS tests where the cap beam reached its capacity. Moreover, the results from the hypothetically reduced-reinforcement bent cap designs revealed that only a slight reduction, which is not proportional to the reinforcement reduction, was observed in the system and the cap beam capacity. This indicates that the box-girder contributes significantly to the overall system capacity and implies that a large portion of the force and moment demand is redistributed to the box-girder after the cap beam experiences extensive yielding or damage.

- The underestimated yield moment and ultimate moment capacity from the code-based sectional analysis relative to the experimentally observed value was claimed to be a consequence of (1) excluding the tension-side slab reinforcement, and (2) conservatively using only a $12t_s$ effective slab width. Therefore, different configurations for the integral bent cap required for capacity estimation that involved including or excluding the tension-side slab reinforcement within $12t_s$ or $18t_s$, were studied for different bent cap designs through sectional analysis. It was concluded that excluding the slab reinforcement underestimates significantly the bent cap beam capacity. Moreover, the best match with the experimentally observed value for the cap beam capacity from Specimen No. 2 HS tests was achieved from sectional analysis that considered flanged section with slab reinforcement and $18t_s$ effective slab contribution. Consequently, it is recommended to include the transverse deck and soffit slab tension reinforcement within a revised $18t_s$ effective slab width in the bent cap yield and capacity moment estimation.

- The design implications of the above recommendation of including the slab reinforcement within $18t_s$ effective slab width for capacity estimation of bent caps were explored for the full bridge level. The design of the full-scale bent cap of the Caltrans Academy Bridge was checked in three different column design scenarios that corresponded to approximately 1.5%, 2.5%, and 3.5% longitudinal column reinforcement. A seismic capacity check was performed in light of Caltrans SDC provisions using different moment demands from the three scenarios and considering different bent cap beam configurations of a $12t_s$ and $18t_s$ effective slab width with and without slab reinforcement. It was concluded that neglecting the slab reinforcement did not require a revised design only for the 1.5% column design scenario; however, a much higher reinforcement was required to satisfy the capacity checks for higher demands from 2.5% and 3.5% column design scenarios. Meanwhile, including the slab reinforcement within the revised $18t_s$ effective slab width proposed by this study required the least design alteration and led to the most optimized bent cap beam design.

- The design implications previously shown are valid in all the cases where higher column demands require revising the bent cap design to satisfy the seismic capacity check. An important application of the recommended bent cap capacity estimation procedure is pronounced in undertaking older bridges retrofitting for resiliency. A typical retrofit scheme

that aims at strengthening the column, as studied within, amplifies the moment demands on the cap beam, i.e., the consequences of the 3.5% column design showed in the design implications can be reproduced using a less reinforced column that is efficiently retrofitted. Ignoring a check of the bent cap capacity against the new retrofitted column capacity could lead to an undesirable mode of failure that has migrated to the bent cap because of the amplified demands, especially in cases of overdesigned retrofit. Accurate estimation of bent cap capacity is necessary in this case to guarantee that it remains essentially elastic in case of extreme events. In addition, a different retrofit design might be needed if the accurately-estimated bent cap capacity falls short behind the retrofitted column overstrength moment. Therefore, it can be stated that the accuracy of the bent cap capacity estimation can lead to optimized reinforcement in case of new bridge designs and informed retrofit decisions in case of older existing bridges.

- From the full-bridge parametric study, the strain values were higher in the soffit slab transverse reinforcement; in turn, the effective width at the deck slab side was consistently larger than the soffit slab side. In addition, the $12t_s$ code-based value for the effective slab width was rendered conservative from the FE models for the full bridge. As observed in from the bridge parametric study, there is not an obvious trend or significant effect of either the box-girder web spacing or slab thicknesses on the bent cap effective width. However, a larger slab contribution to the bent cap behavior can be achieved if the box-girder webs are aligned such that a web meets the bent cap at the maximum bending moment locations. Moreover, maintaining an aspect ratio around 2.0 for the box-girder cells width-to-depth ratio results in the largest contribution from both deck and soffit slabs whether they are in tension or compression.

- The main conclusions and design implications based on this study and implications in terms of design guidelines and possible code amendments are as follows:

  o The $12t_s$ code value for effective slab width is unnecessarily conservative. A revised value of $18t_s$ is recommended for accurate account of box-girder soffit and deck slab contributions to the integral bent cap stiffness and strength;

  o Transverse deck and soffit slab tension reinforcement within an effective slab width, which is similar to the revised $18t_s$, should be included in the bent cap capacity estimation;

  o The box-girder slab contribution should be carefully and accurately considered in the seismic design capacity check to avoid unnecessary use of bent cap reinforcement beyond what is required to satisfy the LRFD design for gravity loads;

  o Accurate bent cap capacity estimate should be an integral part of the repair and retrofit designs for resilient infrastructure to avoid undesirable failure modes, leading to prolonged downtime and uneconomical post-event repair in case of extreme events. This is particularly critical for older bridges that were not designed using the strong-beam–weak-column capacity approach, i.e., the cap beam capacity is not necessarily higher than the column capacity. In such cases, an overdesigned column repair or retrofit might migrate the damage to the superstructure, requiring retrofit of the bent cap or superstructure. Thus, the capacity design check is recommended for repair and retrofit decisions of older bridges as well as an existing condition assessment.

6.3 FUTURE WORK

Several research topics that are appropriate for future investigations can be extended from this the study. The following are relevant possible topics:

- An analytical investigation of the different parameters that could affect the bent cap beam behavior and the box-girder slab contribution at the full bridge level should be conducted. The set of the calibrated nonlinear material model parameters can be further used in a full bridge model. Global bridge geometrical parameters, such as the bridge spans, superstructure depth, thicknesses of the soffit and deck slab, etc., can be varied to investigate how these parameters affect the bent cap effective width and design. The current standards typically relate the effective slab width of the bent cap to the soffit and deck slab thicknesses. However, if other bridge geometric parameters are found to influence the effective slab width, then relating the effective width to such parameters via simple expressions should be beneficial.

- Comprehensive study of the effect of the vertical excitation, especially in near fault regions, on the superstructure, bent caps, and outriggers of bridges should be pursued. One part of the preliminary pre-test analysis conducted in this study rendered the bent cap beam vulnerable to excessive plastic damage due to vertical excitations. This was observed from the full prototype bridge OpenSees nonlinear dynamic analysis that used triaxial earthquake excitations, i.e., an analysis that included the vertical excitation component. A 3D full bridge model should be considered for investigating any possible unfavorable modes of failure or damage due to the lack of proper account for the vertical excitations in bridge design. The 3D modeling is recommended because the vertical forces resulting from vertical excitations are sensitive to the mass distribution of the superstructure. Thus, approximate lumped mass at selected nodes of the bridge superstructure and bent cap model are not the most accurate method for tackling the issue of vertical excitations.

- An investigation of the behavior of bent caps in different bridge types beyond the RC box-girder bridges should be considered. Composite steel and RC bridge superstructures that still connect to a RC bent cap beam is another popular type of bridge the bent cap behavior warrants a proper investigation. The contribution from the RC box-girder slabs is natural in integral bent caps because of the monolithic connections. However, composite girders have stiffening and strengthening effects as well, raising the issue of revisiting this effect for proper bent cap capacity estimation for seismic capacity design checks.

- An investigation of the behavior of bent caps in different bridge geometries and configurations is needed. In particular, skew bridges with various skew angles might affect the overall box-girder soffit and deck slab contributions and, more critically, the bent cap beam capacity. Thus, a comprehensive study that relates the bent cap beam behavior, effective slab width, and capacity estimation to the skewness of the bridge would be useful. Currently, the Caltrans SDC and AASHTO recommend a similar $12t_s$ value for the effective width in a direction orthogonal to the bent cap axis. This value might be strongly dependent on the skew angle and requires further investigation.

- An investigation of the contribution of the slab to bridge girders in the longitudinal direction should be conducted. Several studies have already studied the effective slab width and the slab contribution in composite bridge girders. The RC and PC box-girders need to be further

investigated for a more accurate estimate of the slab contribution and the box-girder capacity, which is required for the bridge seismic capacity check in the longitudinal direction. Moreover, exploring the effect of post-tensioning on the effective slab width and including the prestressing and non-prestressing steel in the capacity estimation of the overall box-girder and the individual girders would be also useful.

REFERENCES

AASHTO (2007). *LRFD Bridge Design Specification*, American Association of State Highway and Transportation Officials, Washington, D.C.

AASHTO (2011) *AASHTO Guide Specifications for LRFD Seismic Bridge Design*, 2nd ed., American Association of State Highway and Transportation Officials. Washington, D.C.

Bayer V., Dorka U.E., Füllekrugc U., Gschwilmd J. (2005). On real-time pseudo-dynamic sub-structure testing: algorithm, numerical and experimental results, *Aerospace Sci. Tech*., 9(3): 223–232.

Bursi O.S., Shing P.S.B. (1996). Evaluation of some implicit time-stepping algorithms for pseudodynamic tests, *Earthq. Eng. Struct. Dyn.,* 25: 333–355.

Caltrans (2006). *LRFD Design Example B November 3, 2006 – Version 1.1*, AASHTO, California Department of Transportation, Sacramento, CA.

Caltrans (2008). *Deck and Soffit Slabs, Memo to Designers 10–20*, California Department of Transportation, Sacramento, CA.

Caltrans (2013). *Seismic Design Criteria Version 1.7*, California Department of Transportation, Sacramento, CA.

Chadwell C.B., Imbsen R.A. (2002). *XTRACT-Cross-Section Analysis Software for Structural and Earthquake Engineering*, TRC, Rancho Cordova, CA, *http://www. imbsen. com/xtract. Htm*, (Aug. 30, 2011).

Chang S.-Y., Tsai K.-C., Chen K.-C. (1998). Improved time integration for pseudodynamic tests, *Earthq. Eng. Struct. Dyn*., 27(7): 711–730.

Chang Y.-Y. (2008). *Multi-Site Network Hybrid Testing of a Multi-Span Bridge System*, PhD.\ Dissertation, Department of Civil Engineering, Carleton University, Ottawa, Canada.

Computers and Structures Inc., (2012) *SAP2000 V14: Integrated Finite Element Analysis and Design of Structures Basic Analysis Reference Manual*, Berkeley, CA.

Darby A.P., Blakeborough A., Williams M.S. (1999). Real-time substructure test using hydraulic actuator, ASCE, *J. Eng. Mech.*, 125(10): 1133–1139.

Darby A.P., Blakeborough A., Williams M.S. (2001). Improved control algorithm for real-time substructure testing, *Earthq. Eng. Struct. Dyn.,* 30(3): 431–448.

Dermitzakis S.N., Mahin S.A. (1985). Development of substructuring techniques for on-line computer controlled seismic performance testing, *Report No. UBC/EERC-85/04*, Earthquake Engineering Research Center, University of California, Berkeley, CA.

Elkhoraibi T., Mosalam K.M. (2007). Generalized hybrid simulation framework for structural systems subjected to seismic loading, *PEER Report No. 2007/101*, Pacific Earthquake Engineering Research Center, University of California, Berkeley, CA.

Frankie T., Abdelnaby A., Silva P., Sanders D., Elnashai A., Spencer B., Kuchma D., Chang C.-M. (2013). Hybrid simulation of curved four-span bridge, ASCE, *Proceedings Structures Congress*, pp. 721–732.

Günay S., Mosalam K.M. (2014). Seismic performance evaluation of high voltage disconnect switches using real-time hybrid simulation: Part II: parametric study, *Earthq. Eng. Struct. Dyn*., 43(8): 1223–1237.

Horiuchi T., Inoue M., Konno T., Namita Y. (1999). Real-time hybrid experimental system with actuator delay compensation and its application to a piping system with energy absorber, *Earthq. Eng. Struct. Dyn.,* 28(10): 1121–1141.

Kim S.J., Elnashai A.S. (2008) Seismic assessment of RC structures considering vertical ground motion, *Report 08-03*, Mid-America Earthquake Center, Urbana-Champaign, IL.

Kumar P., Mosalam K.M., Abbasi S., Abbasi N., Kargahi M. (2014) Reinforced concrete bridge columns repaired with fiber reinforced polymer jackets, *Proceedings ASCE Structures Congress*, pp. 429–440, Boston, MA.

Magonette G. (2001). Development and application of large-scale continuous pseudo-dynamic testing techniques, *Philosophical Trans. Royal Soc.: Math. Phys. Eng. Sci.,* 359: 1771–1799.

Mahin S.A., Shing P.S.B. (1985). Pseudodynamic method for seismic testing, ASCE, *J. Struct. Eng.,* (7): 1482–1503.

Mahin S.A., Williams M.E. (1980). *Computer Controlled Seismic Performance Testing. Dynamic Response of Structures: Experimentation, Observation, Prediction and Control*, New York, NY.

Mahin, S. A., Shing, P. S. B., Thewalt, C. R., Hanson, R. D. (1989). Pseudodynamic test method—current status and future directions, ASCE, *J. Struct. Eng*., 115(8): 2113–2128..

McKenna F., Fenves G.L., Scott M.H., Jeremic B. (2000). *Open System for Earthquake Engineering Simulation (OpenSees)*, Pacific Earthquake Engineering Research Center, University of California, Berkeley, CA

Mosalam K.M., Moustafa M.A., Günay S., Triki I., Takhirov S. (2012). *Seismic Performance of Substation Insulator Posts for Vertical-Break Disconnect Switches*, California Energy Commission. Publication No. CEC-500-2012-XXX.

Mosalam K.M., Günay S. (2014). Seismic performance evaluation of high voltage disconnect switches using real-time hybrid simulation: Part I: system development and validation, *Earthq. Eng. Struct. Dyn*., 43(8): 1205–1222.

Mosqueda G. (2003). *Continuous Hybrid Simulation with Geographically Distributed Substructures*, PhD Dissertation, Department of Civil and Environmental Engineering, University of California, Berkeley, CA, 232 pgs.

Mosqueda G., Stojadinovic B., Hanley J., Sivaselvan M., Reinhorn A.M. (2008). Hybrid seismic response simulation on a geographically distributed bridge model, ASCE, *J. Struct. Eng*., 134(4): 535–543.

Nakashima M., Ishii. K., Kamagata S., Tsutsumi H., Ando K. (1988). feasibility of pseudo dynamic test using substructuring techniques, *Proceedings, Ninth World Conference on Earthquake Engineering*, Tokyo, Japan.

Nakashima M., Kaminosono T., Ishida I., Ando K. (1990). Integration techniques for substructure pseudo dynamic test, Proceedings, *Fourth U.S. National Conference on Earthquake Engineering*, Earthquake Engineering Research Institute, Palm Springs, CA.

Nakashima M., Kato M., Takaoka E. (1992). Development of real-time pseudo-dynamic testing, *Earthq. Eng. Struct. Dyn*., 21(1): 79–92.

Nakashima M., Masaoka N. (1999). Real-time on-line test for MDOF systems, *Earthq. Eng. Struct. Dyn*., 28(4): 393–420.

Newmark N.M. (1959). A method of computation for structural dynamics, ASCE, *J. Eng. Mech*., 85 (EM3): 67–94.

Orebaugh A., Ramirez, G., Beale, J. (2006). *Wireshark & Ethereal network protocol analyzer toolkit*. Syngress.

Schellenberg A.H., Mahin S.A., Fenves G.L. (2009). Advanced implementation of hybrid simulation, *PEER Report No. 2009/104*, Pacific Earthquake Engineering Research Center, University of California, Berkeley, CA.

Shing P.B., Vannan M.T., Cater E. (1991). Implicit time integration for pseudodynamic tests, *Earthq. Eng. Struct. Dyn.,* 20(6): 551–576.

Shing P.B., Mahin S.A. (1983). Experimental error propagation in pseudodynamic testing, UCB/EERC-83/12, Earthquake Engineering Research Center, University of California, Berkeley, CA, 168 pgs.

Stoten D., Magonette G. (2001). *Developments in the Automatic Control of Experimental Facilities*, Laboratorio Nacional de Engenharia Civil, 2001.

Takanashi K., Udagawa K., Seki M., Okada T., Tanaka H. (1975). Non-linear earthquake response analysis of structures by a computer-actuator on-line system (details of the system), *Trans. Arch. Institute Japan*, 229: 77–83.

Terzic V., Stojadinovic B. (2010). Post-earthquake traffic capacity of modern bridges in California, *PEER Report No. 2010/103*, Pacific Earthquake Engineering Research Center, University of California, Berkeley, CA.

Thewalt C.R., Mahin S.A. (1987). Hybrid solution technique for generalized pseudodynamic testing, *Report No. EERC-87/09*, Earthquake Engineering Research Center, University of California, Berkeley, CA.

Thewalt C.R., Roman M. (1994). Performance parameters for pseudodynamic tests, ASCE, *J. Struct. Eng.,* 120(9): 2768–2781.

TNO Diana (2014). User's Manual - Release 9.5, Delft, Netherlands.

Vecchio F.J., Collins M.P. (1993). Compression response of cracked reinforced concrete, ASCE, *J. Struct. Eng.,* 119(12): 3590–3610.

Wang K.J., Tsai K.C., Wang S.J., Cheng W.C., Yang Y.S. (2007). ISEE: Internet-based simulation for earthquake engineering: Part II: The application protocol approach, *Earthq. Eng. Struct. Dyn*., 36(15): 2307–2323.

Xin-Jiang, C., Shi-Zhu T. (2009). Seismic hybrid simulation of multi-span bridge, in *ICCTP*, pp. 1–6.

Yamazaki Y., Nakashima M., Kaminosono T. (1989). Reliability of pseudodynamic test in earthquake response simulation, ASCE, *J. Struct. Eng.,* 115(8): 2098–2112.

Yang Y.S., Hsieh S.H., Tsai K.C., Wang S.J., Wang K.J., Cheng W C., Hsu C.W. (2007). ISEE: internet-based simulation for earthquake engineering. Part I: Database approach, *Earthq. Eng. Struct. Dyn*., 36(15): 2291–2306.

PEER REPORTS

PEER reports are available as a free PDF download from http://peer.berkeley.edu/publications/peer_reports_complete.html. Printed hard copies of PEER reports can be ordered directly from our printer by following the instructions at http://peer.berkeley.edu/publications/peer_reports.html. For other related questions about the PEER Report Series, contact the Pacific Earthquake Engineering Research Center, 325 Davis Hall mail code 1792, Berkeley, CA 94720. Tel.: (510) 642-3437; Fax: (510) 665-1655; Email: peer_editor@berkeley.edu

PEER 2015/10   *Structural Behavior of Column-Bent Cap Beam-Box Girder Systems in Reinforced Concrete Bridges Subjected to Gravity and Seismic Loads. Part II: Hybrid Simulation and Post-Test Analysis.* Mohamed A. Moustafa and Khalid M. Mosalam. November 2015.

PEER 2015/09   *Structural Behavior of Column-Bent Cap Beam-Box Girder Systems in Reinforced Concrete Bridges Subjected to Gravity and Seismic Loads. Part I: Pre-Test Analysis and Quasi-Static Experiments.* Mohamed A. Moustafa and Khalid M. Mosalam. September 2015.

PEER 2015/08   *NGA-East: Adjustments to Median Ground-Motion Models for Center and Eastern North America.* August 2015.

PEER 2015/07   *NGA-East: Ground-Motion Standard-Deviation Models for Central and Eastern North America.* Linda Al Atik. June 2015.

PEER 2015/06   *Adjusting Ground-Motion Intensity Measures to a Reference Site for which V_{S30} = 3000 m/sec.* David M. Boore. May 2015.

PEER 2015/05   *Hybrid Simulation of Seismic Isolation Systems Applied to an APR-1400 Nuclear Power Plant.* Andreas H. Schellenberg, Alireza Sarebanha, Matthew J. Schoettler, Gilberto Mosqueda, Gianmario Benzoni, and Stephen A. Mahin. April 2015.

PEER 2015/04   *NGA-East: Median Ground-Motion Models for the Central and Eastern North America Region.* April 2015.

PEER 2015/03   *Single Series Solution for the Rectangular Fiber-Reinforced Elastomeric Isolator Compression Modulus.* James M. Kelly and Niel C. Van Engelen. March 2015.

PEER 2015/02   *A Full-Scale, Single-Column Bridge Bent Tested by Shake-Table Excitation.* Matthew J. Schoettler, José I. Restrepo, Gabriele Guerrini, David E. Duck, and Francesco Carrea. March 2015.

PEER 2015/01   *Concrete Column Blind Prediction Contest 2010: Outcomes and Observations.* Vesna Terzic, Matthew J. Schoettler, José I. Restrepo, and Stephen A Mahin. March 2015.

PEER 2014/20   *Stochastic Modeling and Simulation of Near-Fault Ground Motions for Performance-Based Earthquake Engineering.* Mayssa Dabaghi and Armen Der Kiureghian. December 2014.

PEER 2014/19   *Seismic Response of a Hybrid Fiber-Reinforced Concrete Bridge Column Detailed for Accelerated Bridge Construction.* Wilson Nguyen, William Trono, Marios Panagiotou, and Claudia P. Ostertag. December 2014.

PEER 2014/18   *Three-Dimensional Beam-Truss Model for Reinforced Concrete Walls and Slabs Subjected to Cyclic Static or Dynamic Loading.* Yuan Lu, Marios Panagiotou, and Ioannis Koutromanos. December 2014.

PEER 2014/17   *PEER NGA-East Database.* Christine A. Goulet, Tadahiro Kishida, Timothy D. Ancheta, Chris H. Cramer, Robert B. Darragh, Walter J. Silva, Youssef M.A. Hashash, Joseph Harmon, Jonathan P. Stewart, Katie E. Wooddell, and Robert R. Youngs. October 2014.

PEER 2014/16   *Guidelines for Performing Hazard-Consistent One-Dimensional Ground Response Analysis for Ground Motion Prediction.* Jonathan P. Stewart, Kioumars Afshari, and Youssef M.A. Hashash. October 2014.

PEER 2014/15   *NGA-East Regionalization Report: Comparison of Four Crustal Regions within Central and Eastern North America using Waveform Modeling and 5%-Damped Pseudo-Spectral Acceleration Response.* Jennifer Dreiling, Marius P. Isken, Walter D. Mooney, Martin C. Chapman, and Richard W. Godbee. October 2014.

PEER 2014/14   *Scaling Relations between Seismic Moment and Rupture Area of Earthquakes in Stable Continental Regions.* Paul Somerville. August 2014.

PEER 2014/13   *PEER Preliminary Notes and Observations on the August 24, 2014, South Napa Earthquake.* Grace S. Kang (Editor), Stephen A. Mahin (Editors). September 2014.

PEER 2014/12   *Reference-Rock Site Conditions for Central and Eastern North America: Part II – Attenuation (Kappa) Definition.* Kenneth W. Campbell, Youssef M.A. Hashash, Byungmin Kim, Albert R. Kottke, Ellen M. Rathje, Walter J. Silva, and Jonathan P. Stewart. August 2014.

PEER 2014/11 *Reference-Rock Site Conditions for Central and Eastern North America: Part I - Velocity Definition*. Youssef M.A. Hashash, Albert R. Kottke, Jonathan P. Stewart, Kenneth W. Campbell, Byungmin Kim, Ellen M. Rathje, Walter J. Silva, Sissy Nikolaou, and Cheryl Moss. August 2014.

PEER 2014/10 *Evaluation of Collapse and Non-Collapse of Parallel Bridges Affected by Liquefaction and Lateral Spreading*. Benjamin Turner, Scott J. Brandenberg, and Jonathan P. Stewart. August 2014.

PEER 2014/09 *PEER Arizona Strong-Motion Database and GMPEs Evaluation*. Tadahiro Kishida, Robert E. Kayen, Olga-Joan Ktenidou, Walter J. Silva, Robert B. Darragh, and Jennie Watson-Lamprey. June 2014.

PEER 2014/08 *Unbonded Pretensioned Bridge Columns with Rocking Detail*. Jeffrey A. Schaefer, Bryan Kennedy, Marc O. Eberhard, John F. Stanton. June 2014.

PEER 2014/07 *Northridge 20 Symposium Summary Report: Impacts, Outcomes, and Next Steps*. May 2014.

PEER 2014/06 *Report of the Tenth Planning Meeting of NEES/E-Defense Collaborative Research on Earthquake Engineering*. December 2013.

PEER 2014/05 *Seismic Velocity Site Characterization of Thirty-One Chilean Seismometer Stations by Spectral Analysis of Surface Wave Dispersion.* Robert Kayen, Brad D. Carkin, Skye Corbet, Camilo Pinilla, Allan Ng, Edward Gorbis, and Christine Truong. April 2014.

PEER 2014/04 *Effect of Vertical Acceleration on Shear Strength of Reinforced Concrete Columns.* Hyerin Lee and Khalid M. Mosalam. April 2014.

PEER 2014/03 *Retest of Thirty-Year-Old Neoprene Isolation Bearings.* James M. Kelly and Niel C. Van Engelen. March 2014.

PEER 2014/02 *Theoretical Development of Hybrid Simulation Applied to Plate Structures.* Ahmed A. Bakhaty, Khalid M. Mosalam, and Sanjay Govindjee. January 2014.

PEER 2014/01 *Performance-Based Seismic Assessment of Skewed Bridges.* Peyman Kaviani, Farzin Zareian, and Ertugrul Taciroglu. January 2014.

PEER 2013/26 *Urban Earthquake Engineering. Proceedings of the U.S.-Iran Seismic Workshop.* December 2013.

PEER 2013/25 *Earthquake Engineering for Resilient Communities: 2013 PEER Internship Program Research Report Collection.* Heidi Tremayne (Editor), Stephen A. Mahin (Editor), Jorge Archbold Monterossa, Matt Brosman, Shelly Dean, Katherine deLaveaga, Curtis Fong, Donovan Holder, Rakeeb Khan, Elizabeth Jachens, David Lam, Daniela Martinez Lopez, Mara Minner, Geffen Oren, Julia Pavicic, Melissa Quinonez, Lorena Rodriguez, Sean Salazar, Kelli Slaven, Vivian Steyert, Jenny Taing, and Salvador Tena. December 2013.

PEER 2013/24 *NGA-West2 Ground Motion Prediction Equations for Vertical Ground Motions.* September 2013.

PEER 2013/23 *Coordinated Planning and Preparedness for Fire Following Major Earthquakes.* Charles Scawthorn. November 2013.

PEER 2013/22 *GEM-PEER Task 3 Project: Selection of a Global Set of Ground Motion Prediction Equations.* Jonathan P. Stewart, John Douglas, Mohammad B. Javanbarg, Carola Di Alessandro, Yousef Bozorgnia, Norman A. Abrahamson, David M. Boore, Kenneth W. Campbell, Elise Delavaud, Mustafa Erdik and Peter J. Stafford. December 2013.

PEER 2013/21 *Seismic Design and Performance of Bridges with Columns on Rocking Foundations.* Grigorios Antonellis and Marios Panagiotou. September 2013.

PEER 2013/20 *Experimental and Analytical Studies on the Seismic Behavior of Conventional and Hybrid Braced Frames.* Jiun-Wei Lai and Stephen A. Mahin. September 2013.

PEER 2013/19 *Toward Resilient Communities: A Performance-Based Engineering Framework for Design and Evaluation of the Built Environment.* Michael William Mieler, Bozidar Stojadinovic, Robert J. Budnitz, Stephen A. Mahin and Mary C. Comerio. September 2013.

PEER 2013/18 *Identification of Site Parameters that Improve Predictions of Site Amplification.* Ellen M. Rathje and Sara Navidi. July 2013.

PEER 2013/17 *Response Spectrum Analysis of Concrete Gravity Dams Including Dam-Water-Foundation Interaction.* Arnkjell Løkke and Anil K. Chopra. July 2013.

PEER 2013/16 *Effect of hoop reinforcement spacing on the cyclic response of large reinforced concrete special moment frame beams.* Marios Panagiotou, Tea Visnjic, Grigorios Antonellis, Panagiotis Galanis, and Jack P. Moehle. June 2013.

PEER 2013/15 *A Probabilistic Framework to Include the Effects of Near-Fault Directivity in Seismic Hazard Assessment.* Shrey Kumar Shahi, Jack W. Baker. October 2013.

PEER 2013/14 *Hanging-Wall Scaling using Finite-Fault Simulations.* Jennifer L. Donahue and Norman A. Abrahamson. September 2013.

PEER 2013/13 *Semi-Empirical Nonlinear Site Amplification and its Application in NEHRP Site Factors.* Jonathan P. Stewart and Emel Seyhan. November 2013.

PEER 2013/12 *Nonlinear Horizontal Site Response for the NGA-West2 Project.* Ronnie Kamai, Norman A. Abramson, Walter J. Silva. May 2013.

PEER 2013/11 *Epistemic Uncertainty for NGA-West2 Models.* Linda Al Atik and Robert R. Youngs. May 2013.

PEER 2013/10 *NGA-West 2 Models for Ground-Motion Directionality.* Shrey K. Shahi and Jack W. Baker. May 2013.

PEER 2013/09 *Final Report of the NGA-West2 Directivity Working Group.* Paul Spudich, Jeffrey R. Bayless, Jack W. Baker, Brian S.J. Chiou, Badie Rowshandel, Shrey Shahi, and Paul Somerville. May 2013.

PEER 2013/08 *NGA-West2 Model for Estimating Average Horizontal Values of Pseudo-Absolute Spectral Accelerations Generated by Crustal Earthquakes.* I. M. Idriss. May 2013.

PEER 2013/07 *Update of the Chiou and Youngs NGA Ground Motion Model for Average Horizontal Component of Peak Ground Motion and Response Spectra.* Brian Chiou and Robert Youngs. May 2013.

PEER 2013/06 *NGA-West2 Campbell-Bozorgnia Ground Motion Model for the Horizontal Components of PGA, PGV, and 5%-Damped Elastic Pseudo-Acceleration Response Spectra for Periods Ranging from 0.01 to 10 sec.* Kenneth W. Campbell and Yousef Bozorgnia. May 2013.

PEER 2013/05 *NGA-West 2 Equations for Predicting Response Spectral Accelerations for Shallow Crustal Earthquakes.* David M. Boore, Jonathan P. Stewart, Emel Seyhan, Gail M. Atkinson. May 2013.

PEER 2013/04 *Update of the AS08 Ground-Motion Prediction Equations Based on the NGA-West2 Data Set.* Norman Abrahamson, Walter Silva, and Ronnie Kamai. May 2013.

PEER 2013/03 *PEER NGA-West2 Database.* Timothy D. Ancheta, Robert B. Darragh, Jonathan P. Stewart, Emel Seyhan, Walter J. Silva, Brian S.J. Chiou, Katie E. Wooddell, Robert W. Graves, Albert R. Kottke, David M. Boore, Tadahiro Kishida, and Jennifer L. Donahue. May 2013.

PEER 2013/02 *Hybrid Simulation of the Seismic Response of Squat Reinforced Concrete Shear Walls.* Catherine A. Whyte and Bozidar Stojadinovic. May 2013.

PEER 2013/01 *Housing Recovery in Chile: A Qualitative Mid-program Review.* Mary C. Comerio. February 2013.

PEER 2012/08 *Guidelines for Estimation of Shear Wave Velocity.* Bernard R. Wair, Jason T. DeJong, and Thomas Shantz. December 2012.

PEER 2012/07 *Earthquake Engineering for Resilient Communities: 2012 PEER Internship Program Research Report Collection.* Heidi Tremayne (Editor), Stephen A. Mahin (Editor), Collin Anderson, Dustin Cook, Michael Erceg, Carlos Esparza, Jose Jimenez, Dorian Krausz, Andrew Lo, Stephanie Lopez, Nicole McCurdy, Paul Shipman, Alexander Strum, Eduardo Vega. December 2012.

PEER 2012/06 *Fragilities for Precarious Rocks at Yucca Mountain.* Matthew D. Purvance, Rasool Anooshehpoor, and James N. Brune. December 2012.

PEER 2012/05 *Development of Simplified Analysis Procedure for Piles in Laterally Spreading Layered Soils.* Christopher R. McGann, Pedro Arduino, and Peter Mackenzie–Helnwein. December 2012.

PEER 2012/04 *Unbonded Pre-Tensioned Columns for Bridges in Seismic Regions.* Phillip M. Davis, Todd M. Janes, Marc O. Eberhard, and John F. Stanton. December 2012.

PEER 2012/03 *Experimental and Analytical Studies on Reinforced Concrete Buildings with Seismically Vulnerable Beam-Column Joints.* Sangjoon Park and Khalid M. Mosalam. October 2012.

PEER 2012/02 *Seismic Performance of Reinforced Concrete Bridges Allowed to Uplift during Multi-Directional Excitation.* Andres Oscar Espinoza and Stephen A. Mahin. July 2012.

PEER 2012/01 *Spectral Damping Scaling Factors for Shallow Crustal Earthquakes in Active Tectonic Regions.* Sanaz Rezaeian, Yousef Bozorgnia, I. M. Idriss, Kenneth Campbell, Norman Abrahamson, and Walter Silva. July 2012.

PEER 2011/10 *Earthquake Engineering for Resilient Communities: 2011 PEER Internship Program Research Report Collection.* Eds. Heidi Faison and Stephen A. Mahin. December 2011.

PEER 2011/09 *Calibration of Semi-Stochastic Procedure for Simulating High-Frequency Ground Motions.* Jonathan P. Stewart, Emel Seyhan, and Robert W. Graves. December 2011.

PEER 2011/08 *Water Supply in regard to Fire Following Earthquake.* Charles Scawthorn. November 2011.

PEER 2011/07 *Seismic Risk Management in Urban Areas. Proceedings of a U.S.-Iran-Turkey Seismic Workshop.* September 2011.

PEER 2011/06   *The Use of Base Isolation Systems to Achieve Complex Seismic Performance Objectives.* Troy A. Morgan and Stephen A. Mahin. July 2011.

PEER 2011/05   *Case Studies of the Seismic Performance of Tall Buildings Designed by Alternative Means.* Task 12 Report for the Tall Buildings Initiative. Jack Moehle, Yousef Bozorgnia, Nirmal Jayaram, Pierson Jones, Mohsen Rahnama, Nilesh Shome, Zeynep Tuna, John Wallace, Tony Yang, and Farzin Zareian. July 2011.

PEER 2011/04   *Recommended Design Practice for Pile Foundations in Laterally Spreading Ground.* Scott A. Ashford, Ross W. Boulanger, and Scott J. Brandenberg. June 2011.

PEER 2011/03   *New Ground Motion Selection Procedures and Selected Motions for the PEER Transportation Research Program.* Jack W. Baker, Ting Lin, Shrey K. Shahi, and Nirmal Jayaram. March 2011.

PEER 2011/02   *A Bayesian Network Methodology for Infrastructure Seismic Risk Assessment and Decision Support.* Michelle T. Bensi, Armen Der Kiureghian, and Daniel Straub. March 2011.

PEER 2011/01   *Demand Fragility Surfaces for Bridges in Liquefied and Laterally Spreading Ground.* Scott J. Brandenberg, Jian Zhang, Pirooz Kashighandi, Yili Huo, and Minxing Zhao. March 2011.

PEER 2010/05   *Guidelines for Performance-Based Seismic Design of Tall Buildings.* Developed by the Tall Buildings Initiative. November 2010.

PEER 2010/04   *Application Guide for the Design of Flexible and Rigid Bus Connections between Substation Equipment Subjected to Earthquakes.* Jean-Bernard Dastous and Armen Der Kiureghian. September 2010.

PEER 2010/03   *Shear Wave Velocity as a Statistical Function of Standard Penetration Test Resistance and Vertical Effective Stress at Caltrans Bridge Sites.* Scott J. Brandenberg, Naresh Bellana, and Thomas Shantz. June 2010.

PEER 2010/02   *Stochastic Modeling and Simulation of Ground Motions for Performance-Based Earthquake Engineering.* Sanaz Rezaeian and Armen Der Kiureghian. June 2010.

PEER 2010/01   *Structural Response and Cost Characterization of Bridge Construction Using Seismic Performance Enhancement Strategies.* Ady Aviram, Božidar Stojadinović, Gustavo J. Parra-Montesinos, and Kevin R. Mackie. March 2010.

PEER 2009/03   *The Integration of Experimental and Simulation Data in the Study of Reinforced Concrete Bridge Systems Including Soil-Foundation-Structure Interaction.* Matthew Dryden and Gregory L. Fenves. November 2009.

PEER 2009/02   *Improving Earthquake Mitigation through Innovations and Applications in Seismic Science, Engineering, Communication, and Response. Proceedings of a U.S.-Iran Seismic Workshop.* October 2009.

PEER 2009/01   *Evaluation of Ground Motion Selection and Modification Methods: Predicting Median Interstory Drift Response of Buildings.* Curt B. Haselton, Ed. June 2009.

PEER 2008/10   *Technical Manual for Strata.* Albert R. Kottke and Ellen M. Rathje. February 2009.

PEER 2008/09   *NGA Model for Average Horizontal Component of Peak Ground Motion and Response Spectra.* Brian S.-J. Chiou and Robert R. Youngs. November 2008.

PEER 2008/08   *Toward Earthquake-Resistant Design of Concentrically Braced Steel Structures.* Patxi Uriz and Stephen A. Mahin. November 2008.

PEER 2008/07   *Using OpenSees for Performance-Based Evaluation of Bridges on Liquefiable Soils.* Stephen L. Kramer, Pedro Arduino, and HyungSuk Shin. November 2008.

PEER 2008/06   *Shaking Table Tests and Numerical Investigation of Self-Centering Reinforced Concrete Bridge Columns.* Hyung IL Jeong, Junichi Sakai, and Stephen A. Mahin. September 2008.

PEER 2008/05   *Performance-Based Earthquake Engineering Design Evaluation Procedure for Bridge Foundations Undergoing Liquefaction-Induced Lateral Ground Displacement.* Christian A. Ledezma and Jonathan D. Bray. August 2008.

PEER 2008/04   *Benchmarking of Nonlinear Geotechnical Ground Response Analysis Procedures.* Jonathan P. Stewart, Annie On-Lei Kwok, Yousseff M. A. Hashash, Neven Matasovic, Robert Pyke, Zhiliang Wang, and Zhaohui Yang. August 2008.

PEER 2008/03   *Guidelines for Nonlinear Analysis of Bridge Structures in California.* Ady Aviram, Kevin R. Mackie, and Božidar Stojadinović. August 2008.

PEER 2008/02   *Treatment of Uncertainties in Seismic-Risk Analysis of Transportation Systems.* Evangelos Stergiou and Anne S. Kiremidjian. July 2008.

PEER 2008/01   *Seismic Performance Objectives for Tall Buildings.* William T. Holmes, Charles Kircher, William Petak, and Nabih Youssef. August 2008.

PEER 2007/12   *An Assessment to Benchmark the Seismic Performance of a Code-Conforming Reinforced Concrete Moment-Frame Building.* Curt Haselton, Christine A. Goulet, Judith Mitrani-Reiser, James L. Beck, Gregory G. Deierlein, Keith A. Porter, Jonathan P. Stewart, and Ertugrul Taciroglu. August 2008.

PEER 2007/11   *Bar Buckling in Reinforced Concrete Bridge Columns.* Wayne A. Brown, Dawn E. Lehman, and John F. Stanton. February 2008.

PEER 2007/10   *Computational Modeling of Progressive Collapse in Reinforced Concrete Frame Structures.* Mohamed M. Talaat and Khalid M. Mosalam. May 2008.

PEER 2007/09   *Integrated Probabilistic Performance-Based Evaluation of Benchmark Reinforced Concrete Bridges.* Kevin R. Mackie, John-Michael Wong, and Božidar Stojadinović. January 2008.

PEER 2007/08   *Assessing Seismic Collapse Safety of Modern Reinforced Concrete Moment-Frame Buildings.* Curt B. Haselton and Gregory G. Deierlein. February 2008.

PEER 2007/07   *Performance Modeling Strategies for Modern Reinforced Concrete Bridge Columns.* Michael P. Berry and Marc O. Eberhard. April 2008.

PEER 2007/06   *Development of Improved Procedures for Seismic Design of Buried and Partially Buried Structures.* Linda Al Atik and Nicholas Sitar. June 2007.

PEER 2007/05   *Uncertainty and Correlation in Seismic Risk Assessment of Transportation Systems.* Renee G. Lee and Anne S. Kiremidjian. July 2007.

PEER 2007/04   *Numerical Models for Analysis and Performance-Based Design of Shallow Foundations Subjected to Seismic Loading.* Sivapalan Gajan, Tara C. Hutchinson, Bruce L. Kutter, Prishati Raychowdhury, José A. Ugalde, and Jonathan P. Stewart. May 2008.

PEER 2007/03   *Beam-Column Element Model Calibrated for Predicting Flexural Response Leading to Global Collapse of RC Frame Buildings.* Curt B. Haselton, Abbie B. Liel, Sarah Taylor Lange, and Gregory G. Deierlein. May 2008.

PEER 2007/02   *Campbell-Bozorgnia NGA Ground Motion Relations for the Geometric Mean Horizontal Component of Peak and Spectral Ground Motion Parameters.* Kenneth W. Campbell and Yousef Bozorgnia. May 2007.

PEER 2007/01   *Boore-Atkinson NGA Ground Motion Relations for the Geometric Mean Horizontal Component of Peak and Spectral Ground Motion Parameters.* David M. Boore and Gail M. Atkinson. May. May 2007.

PEER 2006/12   *Societal Implications of Performance-Based Earthquake Engineering.* Peter J. May. May 2007.

PEER 2006/11   *Probabilistic Seismic Demand Analysis Using Advanced Ground Motion Intensity Measures, Attenuation Relationships, and Near-Fault Effects.* Polsak Tothong and C. Allin Cornell. March 2007.

PEER 2006/10   *Application of the PEER PBEE Methodology to the I-880 Viaduct.* Sashi Kunnath. February 2007.

PEER 2006/09   *Quantifying Economic Losses from Travel Forgone Following a Large Metropolitan Earthquake.* James Moore, Sungbin Cho, Yue Yue Fan, and Stuart Werner. November 2006.

PEER 2006/08   *Vector-Valued Ground Motion Intensity Measures for Probabilistic Seismic Demand Analysis*. Jack W. Baker and C. Allin Cornell. October 2006.

PEER 2006/07   *Analytical Modeling of Reinforced Concrete Walls for Predicting Flexural and Coupled–Shear-Flexural Responses*. Kutay Orakcal, Leonardo M. Massone, and John W. Wallace. October 2006.

PEER 2006/06   *Nonlinear Analysis of a Soil-Drilled Pier System under Static and Dynamic Axial Loading.* Gang Wang and Nicholas Sitar. November 2006.

PEER 2006/05   *Advanced Seismic Assessment Guidelines.* Paolo Bazzurro, C. Allin Cornell, Charles Menun, Maziar Motahari, and Nicolas Luco. September 2006.

PEER 2006/04   *Probabilistic Seismic Evaluation of Reinforced Concrete Structural Components and Systems.* Tae Hyung Lee and Khalid M. Mosalam. August 2006.

PEER 2006/03   *Performance of Lifelines Subjected to Lateral Spreading.* Scott A. Ashford and Teerawut Juirnarongrit. July 2006.

PEER 2006/02   *Pacific Earthquake Engineering Research Center Highway Demonstration Project.* Anne Kiremidjian, James Moore, Yue Yue Fan, Nesrin Basoz, Ozgur Yazali, and Meredith Williams. April 2006.

PEER 2006/01   *Bracing Berkeley. A Guide to Seismic Safety on the UC Berkeley Campus.* Mary C. Comerio, Stephen Tobriner, and Ariane Fehrenkamp. January 2006.

PEER 2005/16   *Seismic Response and Reliability of Electrical Substation Equipment and Systems.* Junho Song, Armen Der Kiureghian, and Jerome L. Sackman. April 2006.

PEER 2005/15   *CPT-Based Probabilistic Assessment of Seismic Soil Liquefaction Initiation.* R. E. S. Moss, R. B. Seed, R. E. Kayen, J. P. Stewart, and A. Der Kiureghian. April 2006.

PEER 2005/14   *Workshop on Modeling of Nonlinear Cyclic Load-Deformation Behavior of Shallow Foundations.* Bruce L. Kutter, Geoffrey Martin, Tara Hutchinson, Chad Harden, Sivapalan Gajan, and Justin Phalen. March 2006.

PEER 2005/13 *Stochastic Characterization and Decision Bases under Time-Dependent Aftershock Risk in Performance-Based Earthquake Engineering.* Gee Liek Yeo and C. Allin Cornell. July 2005.

PEER 2005/12 *PEER Testbed Study on a Laboratory Building: Exercising Seismic Performance Assessment.* Mary C. Comerio, editor. November 2005.

PEER 2005/11 *Van Nuys Hotel Building Testbed Report: Exercising Seismic Performance Assessment.* Helmut Krawinkler, editor. October 2005.

PEER 2005/10 *First NEES/E-Defense Workshop on Collapse Simulation of Reinforced Concrete Building Structures.* September 2005.

PEER 2005/09 *Test Applications of Advanced Seismic Assessment Guidelines.* Joe Maffei, Karl Telleen, Danya Mohr, William Holmes, and Yuki Nakayama. August 2006.

PEER 2005/08 *Damage Accumulation in Lightly Confined Reinforced Concrete Bridge Columns.* R. Tyler Ranf, Jared M. Nelson, Zach Price, Marc O. Eberhard, and John F. Stanton. April 2006.

PEER 2005/07 *Experimental and Analytical Studies on the Seismic Response of Freestanding and Anchored Laboratory Equipment.* Dimitrios Konstantinidis and Nicos Makris. January 2005.

PEER 2005/06 *Global Collapse of Frame Structures under Seismic Excitations*. Luis F. Ibarra and Helmut Krawinkler. September 2005.

PEER 2005//05 *Performance Characterization of Bench- and Shelf-Mounted Equipment.* Samit Ray Chaudhuri and Tara C. Hutchinson. May 2006.

PEER 2005/04 *Numerical Modeling of the Nonlinear Cyclic Response of Shallow Foundations.* Chad Harden, Tara Hutchinson, Geoffrey R. Martin, and Bruce L. Kutter. August 2005.

PEER 2005/03 *A Taxonomy of Building Components for Performance-Based Earthquake Engineering.* Keith A. Porter. September 2005.

PEER 2005/02 *Fragility Basis for California Highway Overpass Bridge Seismic Decision Making*. Kevin R. Mackie and Božidar Stojadinović. June 2005.

PEER 2005/01 *Empirical Characterization of Site Conditions on Strong Ground Motion.* Jonathan P. Stewart, Yoojoong Choi, and Robert W. Graves. June 2005.

PEER 2004/09 *Electrical Substation Equipment Interaction: Experimental Rigid Conductor Studies.* Christopher Stearns and André Filiatrault. February 2005.

PEER 2004/08 *Seismic Qualification and Fragility Testing of Line Break 550-kV Disconnect Switches.* Shakhzod M. Takhirov, Gregory L. Fenves, and Eric Fujisaki. January 2005.

PEER 2004/07 *Ground Motions for Earthquake Simulator Qualification of Electrical Substation Equipment*. Shakhzod M. Takhirov, Gregory L. Fenves, Eric Fujisaki, and Don Clyde. January 2005.

PEER 2004/06 *Performance-Based Regulation and Regulatory Regimes.* Peter J. May and Chris Koski. September 2004.

PEER 2004/05 *Performance-Based Seismic Design Concepts and Implementation: Proceedings of an International Workshop.* Peter Fajfar and Helmut Krawinkler, editors. September 2004.

PEER 2004/04 *Seismic Performance of an Instrumented Tilt-up Wall Building.* James C. Anderson and Vitelmo V. Bertero. July 2004.

PEER 2004/03 *Evaluation and Application of Concrete Tilt-up Assessment Methodologies.* Timothy Graf and James O. Malley. October 2004.

PEER 2004/02 *Analytical Investigations of New Methods for Reducing Residual Displacements of Reinforced Concrete Bridge Columns.* Junichi Sakai and Stephen A. Mahin. August 2004.

PEER 2004/01 *Seismic Performance of Masonry Buildings and Design Implications.* Kerri Anne Taeko Tokoro, James C. Anderson, and Vitelmo V. Bertero. February 2004.

PEER 2003/18 *Performance Models for Flexural Damage in Reinforced Concrete Columns.* Michael Berry and Marc Eberhard. August 2003.

PEER 2003/17 *Predicting Earthquake Damage in Older Reinforced Concrete Beam-Column Joints.* Catherine Pagni and Laura Lowes. October 2004.

PEER 2003/16 *Seismic Demands for Performance-Based Design of Bridges.* Kevin Mackie and Božidar Stojadinović. August 2003.

PEER 2003/15 *Seismic Demands for Nondeteriorating Frame Structures and Their Dependence on Ground Motions.* Ricardo Antonio Medina and Helmut Krawinkler. May 2004.

PEER 2003/14   *Finite Element Reliability and Sensitivity Methods for Performance-Based Earthquake Engineering.* Terje Haukaas and Armen Der Kiureghian. April 2004.

PEER 2003/13   *Effects of Connection Hysteretic Degradation on the Seismic Behavior of Steel Moment-Resisting Frames.* Janise E. Rodgers and Stephen A. Mahin. March 2004.

PEER 2003/12   *Implementation Manual for the Seismic Protection of Laboratory Contents: Format and Case Studies.* William T. Holmes and Mary C. Comerio. October 2003.

PEER 2003/11   *Fifth U.S.-Japan Workshop on Performance-Based Earthquake Engineering Methodology for Reinforced Concrete Building Structures.* February 2004.

PEER 2003/10   *A Beam-Column Joint Model for Simulating the Earthquake Response of Reinforced Concrete Frames.* Laura N. Lowes, Nilanjan Mitra, and Arash Altoontash. February 2004.

PEER 2003/09   *Sequencing Repairs after an Earthquake: An Economic Approach.* Marco Casari and Simon J. Wilkie. April 2004.

PEER 2003/08   *A Technical Framework for Probability-Based Demand and Capacity Factor Design (DCFD) Seismic Formats.* Fatemeh Jalayer and C. Allin Cornell. November 2003.

PEER 2003/07   *Uncertainty Specification and Propagation for Loss Estimation Using FOSM Methods.* Jack W. Baker and C. Allin Cornell. September 2003.

PEER 2003/06   *Performance of Circular Reinforced Concrete Bridge Columns under Bidirectional Earthquake Loading*. Mahmoud M. Hachem, Stephen A. Mahin, and Jack P. Moehle. February 2003.

PEER 2003/05   *Response Assessment for Building-Specific Loss Estimation.* Eduardo Miranda and Shahram Taghavi. September 2003.

PEER 2003/04   *Experimental Assessment of Columns with Short Lap Splices Subjected to Cyclic Loads*. Murat Melek, John W. Wallace, and Joel Conte. April 2003.

PEER 2003/03   *Probabilistic Response Assessment for Building-Specific Loss Estimation.* Eduardo Miranda and Hesameddin Aslani. September 2003.

PEER 2003/02   *Software Framework for Collaborative Development of Nonlinear Dynamic Analysis Program.* Jun Peng and Kincho H. Law. September 2003.

PEER 2003/01   *Shake Table Tests and Analytical Studies on the Gravity Load Collapse of Reinforced Concrete Frames.* Kenneth John Elwood and Jack P. Moehle. November 2003.

PEER 2002/24   *Performance of Beam to Column Bridge Joints Subjected to a Large Velocity Pulse.* Natalie Gibson, André Filiatrault, and Scott A. Ashford. April 2002.

PEER 2002/23   *Effects of Large Velocity Pulses on Reinforced Concrete Bridge Columns.* Greg L. Orozco and Scott A. Ashford. April 2002.

PEER 2002/22   *Characterization of Large Velocity Pulses for Laboratory Testing.* Kenneth E. Cox and Scott A. Ashford. April 2002.

PEER 2002/21   *Fourth U.S.-Japan Workshop on Performance-Based Earthquake Engineering Methodology for Reinforced Concrete Building Structures*. December 2002.

PEER 2002/20   *Barriers to Adoption and Implementation of PBEE Innovations.* Peter J. May. August 2002.

PEER 2002/19   *Economic-Engineered Integrated Models for Earthquakes: Socioeconomic Impacts.* Peter Gordon, James E. Moore II, and Harry W. Richardson. July 2002.

PEER 2002/18   *Assessment of Reinforced Concrete Building Exterior Joints with Substandard Details.* Chris P. Pantelides, Jon Hansen, Justin Nadauld, and Lawrence D. Reaveley. May 2002.

PEER 2002/17   *Structural Characterization and Seismic Response Analysis of a Highway Overcrossing Equipped with Elastomeric Bearings and Fluid Dampers: A Case Study.* Nicos Makris and Jian Zhang. November 2002.

PEER 2002/16   *Estimation of Uncertainty in Geotechnical Properties for Performance-Based Earthquake Engineering.* Allen L. Jones, Steven L. Kramer, and Pedro Arduino. December 2002.

PEER 2002/15   *Seismic Behavior of Bridge Columns Subjected to Various Loading Patterns*. Asadollah Esmaeily-Gh. and Yan Xiao. December 2002.

PEER 2002/14   *Inelastic Seismic Response of Extended Pile Shaft Supported Bridge Structures.* T.C. Hutchinson, R.W. Boulanger, Y.H. Chai, and I.M. Idriss. December 2002.

PEER 2002/13   *Probabilistic Models and Fragility Estimates for Bridge Components and Systems.* Paolo Gardoni, Armen Der Kiureghian, and Khalid M. Mosalam. June 2002.

PEER 2002/12 *Effects of Fault Dip and Slip Rake on Near-Source Ground Motions: Why Chi-Chi Was a Relatively Mild M7.6 Earthquake.* Brad T. Aagaard, John F. Hall, and Thomas H. Heaton. December 2002.

PEER 2002/11 *Analytical and Experimental Study of Fiber-Reinforced Strip Isolators.* James M. Kelly and Shakhzod M. Takhirov. September 2002.

PEER 2002/10 *Centrifuge Modeling of Settlement and Lateral Spreading with Comparisons to Numerical Analyses.* Sivapalan Gajan and Bruce L. Kutter. January 2003.

PEER 2002/09 *Documentation and Analysis of Field Case Histories of Seismic Compression during the 1994 Northridge, California, Earthquake.* Jonathan P. Stewart, Patrick M. Smith, Daniel H. Whang, and Jonathan D. Bray. October 2002.

PEER 2002/08 *Component Testing, Stability Analysis and Characterization of Buckling-Restrained Unbonded Braces^{TM}.* Cameron Black, Nicos Makris, and Ian Aiken. September 2002.

PEER 2002/07 *Seismic Performance of Pile-Wharf Connections.* Charles W. Roeder, Robert Graff, Jennifer Soderstrom, and Jun Han Yoo. December 2001.

PEER 2002/06 *The Use of Benefit-Cost Analysis for Evaluation of Performance-Based Earthquake Engineering Decisions.* Richard O. Zerbe and Anthony Falit-Baiamonte. September 2001.

PEER 2002/05 *Guidelines, Specifications, and Seismic Performance Characterization of Nonstructural Building Components and Equipment.* André Filiatrault, Constantin Christopoulos, and Christopher Stearns. September 2001.

PEER 2002/04 *Consortium of Organizations for Strong-Motion Observation Systems and the Pacific Earthquake Engineering Research Center Lifelines Program: Invited Workshop on Archiving and Web Dissemination of Geotechnical Data, 4–5 October 2001.* September 2002.

PEER 2002/03 *Investigation of Sensitivity of Building Loss Estimates to Major Uncertain Variables for the Van Nuys Testbed.* Keith A. Porter, James L. Beck, and Rustem V. Shaikhutdinov. August 2002.

PEER 2002/02 *The Third U.S.-Japan Workshop on Performance-Based Earthquake Engineering Methodology for Reinforced Concrete Building Structures.* July 2002.

PEER 2002/01 *Nonstructural Loss Estimation: The UC Berkeley Case Study.* Mary C. Comerio and John C. Stallmeyer. December 2001.

PEER 2001/16 *Statistics of SDF-System Estimate of Roof Displacement for Pushover Analysis of Buildings.* Anil K. Chopra, Rakesh K. Goel, and Chatpan Chintanapakdee. December 2001.

PEER 2001/15 *Damage to Bridges during the 2001 Nisqually Earthquake.* R. Tyler Ranf, Marc O. Eberhard, and Michael P. Berry. November 2001.

PEER 2001/14 *Rocking Response of Equipment Anchored to a Base Foundation.* Nicos Makris and Cameron J. Black. September 2001.

PEER 2001/13 *Modeling Soil Liquefaction Hazards for Performance-Based Earthquake Engineering.* Steven L. Kramer and Ahmed-W. Elgamal. February 2001.

PEER 2001/12 *Development of Geotechnical Capabilities in OpenSees.* Boris Jeremić. September 2001.

PEER 2001/11 *Analytical and Experimental Study of Fiber-Reinforced Elastomeric Isolators.* James M. Kelly and Shakhzod M. Takhirov. September 2001.

PEER 2001/10 *Amplification Factors for Spectral Acceleration in Active Regions.* Jonathan P. Stewart, Andrew H. Liu, Yoojoong Choi, and Mehmet B. Baturay. December 2001.

PEER 2001/09 *Ground Motion Evaluation Procedures for Performance-Based Design.* Jonathan P. Stewart, Shyh-Jeng Chiou, Jonathan D. Bray, Robert W. Graves, Paul G. Somerville, and Norman A. Abrahamson. September 2001.

PEER 2001/08 *Experimental and Computational Evaluation of Reinforced Concrete Bridge Beam-Column Connections for Seismic Performance.* Clay J. Naito, Jack P. Moehle, and Khalid M. Mosalam. November 2001.

PEER 2001/07 *The Rocking Spectrum and the Shortcomings of Design Guidelines.* Nicos Makris and Dimitrios Konstantinidis. August 2001.

PEER 2001/06 *Development of an Electrical Substation Equipment Performance Database for Evaluation of Equipment Fragilities.* Thalia Agnanos. April 1999.

PEER 2001/05 *Stiffness Analysis of Fiber-Reinforced Elastomeric Isolators.* Hsiang-Chuan Tsai and James M. Kelly. May 2001.

PEER 2001/04 *Organizational and Societal Considerations for Performance-Based Earthquake Engineering.* Peter J. May. April 2001.

PEER 2001/03   *A Modal Pushover Analysis Procedure to Estimate Seismic Demands for Buildings: Theory and Preliminary Evaluation.* Anil K. Chopra and Rakesh K. Goel. January 2001.

PEER 2001/02   *Seismic Response Analysis of Highway Overcrossings Including Soil-Structure Interaction.* Jian Zhang and Nicos Makris. March 2001.

PEER 2001/01   *Experimental Study of Large Seismic Steel Beam-to-Column Connections.* Egor P. Popov and Shakhzod M. Takhirov. November 2000.

PEER 2000/10   *The Second U.S.-Japan Workshop on Performance-Based Earthquake Engineering Methodology for Reinforced Concrete Building Structures.* March 2000.

PEER 2000/09   *Structural Engineering Reconnaissance of the August 17, 1999 Earthquake: Kocaeli (Izmit), Turkey.* Halil Sezen, Kenneth J. Elwood, Andrew S. Whittaker, Khalid Mosalam, John J. Wallace, and John F. Stanton. December 2000.

PEER 2000/08   *Behavior of Reinforced Concrete Bridge Columns Having Varying Aspect Ratios and Varying Lengths of Confinement.* Anthony J. Calderone, Dawn E. Lehman, and Jack P. Moehle. January 2001.

PEER 2000/07   *Cover-Plate and Flange-Plate Reinforced Steel Moment-Resisting Connections.* Taejin Kim, Andrew S. Whittaker, Amir S. Gilani, Vitelmo V. Bertero, and Shakhzod M. Takhirov. September 2000.

PEER 2000/06   *Seismic Evaluation and Analysis of 230-kV Disconnect Switches.* Amir S. J. Gilani, Andrew S. Whittaker, Gregory L. Fenves, Chun-Hao Chen, Henry Ho, and Eric Fujisaki. July 2000.

PEER 2000/05   *Performance-Based Evaluation of Exterior Reinforced Concrete Building Joints for Seismic Excitation.* Chandra Clyde, Chris P. Pantelides, and Lawrence D. Reaveley. July 2000.

PEER 2000/04   *An Evaluation of Seismic Energy Demand: An Attenuation Approach.* Chung-Che Chou and Chia-Ming Uang. July 1999.

PEER 2000/03   *Framing Earthquake Retrofitting Decisions: The Case of Hillside Homes in Los Angeles.* Detlof von Winterfeldt, Nels Roselund, and Alicia Kitsuse. March 2000.

PEER 2000/02   *U.S.-Japan Workshop on the Effects of Near-Field Earthquake Shaking.* Andrew Whittaker, ed. July 2000.

PEER 2000/01   *Further Studies on Seismic Interaction in Interconnected Electrical Substation Equipment.* Armen Der Kiureghian, Kee-Jeung Hong, and Jerome L. Sackman. November 1999.

PEER 1999/14   *Seismic Evaluation and Retrofit of 230-kV Porcelain Transformer Bushings*. Amir S. Gilani, Andrew S. Whittaker, Gregory L. Fenves, and Eric Fujisaki. December 1999.

PEER 1999/13   *Building Vulnerability Studies: Modeling and Evaluation of Tilt-up and Steel Reinforced Concrete Buildings.* John W. Wallace, Jonathan P. Stewart, and Andrew S. Whittaker, editors. December 1999.

PEER 1999/12   *Rehabilitation of Nonductile RC Frame Building Using Encasement Plates and Energy-Dissipating Devices.* Mehrdad Sasani, Vitelmo V. Bertero, James C. Anderson. December 1999.

PEER 1999/11   *Performance Evaluation Database for Concrete Bridge Components and Systems under Simulated Seismic Loads.* Yael D. Hose and Frieder Seible. November 1999.

PEER 1999/10   *U.S.-Japan Workshop on Performance-Based Earthquake Engineering Methodology for Reinforced Concrete Building Structures.* December 1999.

PEER 1999/09   *Performance Improvement of Long Period Building Structures Subjected to Severe Pulse-Type Ground Motions*. James C. Anderson, Vitelmo V. Bertero, and Raul Bertero. October 1999.

PEER 1999/08   *Envelopes for Seismic Response Vectors.* Charles Menun and Armen Der Kiureghian. July 1999.

PEER 1999/07   *Documentation of Strengths and Weaknesses of Current Computer Analysis Methods for Seismic Performance of Reinforced Concrete Members.* William F. Cofer. November 1999.

PEER 1999/06   *Rocking Response and Overturning of Anchored Equipment under Seismic Excitations.* Nicos Makris and Jian Zhang. November 1999.

PEER 1999/05   *Seismic Evaluation of 550 kV Porcelain Transformer Bushings.* Amir S. Gilani, Andrew S. Whittaker, Gregory L. Fenves, and Eric Fujisaki. October 1999.

PEER 1999/04   *Adoption and Enforcement of Earthquake Risk-Reduction Measures.* Peter J. May, Raymond J. Burby, T. Jens Feeley, and Robert Wood.

PEER 1999/03   *Task 3 Characterization of Site Response General Site Categories*. Adrian Rodriguez-Marek, Jonathan D. Bray, and Norman Abrahamson. February 1999.

PEER 1999/02   *Capacity-Demand-Diagram Methods for Estimating Seismic Deformation of Inelastic Structures: SDF Systems*. Anil K. Chopra and Rakesh Goel. April 1999.

PEER 1999/01   *Interaction in Interconnected Electrical Substation Equipment Subjected to Earthquake Ground Motions.* Armen Der Kiureghian, Jerome L. Sackman, and Kee-Jeung Hong. February 1999.

PEER 1998/08   *Behavior and Failure Analysis of a Multiple-Frame Highway Bridge in the 1994 Northridge Earthquake.* Gregory L. Fenves and Michael Ellery. December 1998.

PEER 1998/07   *Empirical Evaluation of Inertial Soil-Structure Interaction Effects.* Jonathan P. Stewart, Raymond B. Seed, and Gregory L. Fenves. November 1998.

PEER 1998/06   *Effect of Damping Mechanisms on the Response of Seismic Isolated Structures.* Nicos Makris and Shih-Po Chang. November 1998.

PEER 1998/05   *Rocking Response and Overturning of Equipment under Horizontal Pulse-Type Motions.* Nicos Makris and Yiannis Roussos. October 1998.

PEER 1998/04   *Pacific Earthquake Engineering Research Invitational Workshop Proceedings, May 14–15, 1998: Defining the Links between Planning, Policy Analysis, Economics and Earthquake Engineering.* Mary Comerio and Peter Gordon. September 1998.

PEER 1998/03   *Repair/Upgrade Procedures for Welded Beam to Column Connections.* James C. Anderson and Xiaojing Duan. May 1998.

PEER 1998/02   *Seismic Evaluation of 196 kV Porcelain Transformer Bushings.* Amir S. Gilani, Juan W. Chavez, Gregory L. Fenves, and Andrew S. Whittaker. May 1998.

PEER 1998/01   *Seismic Performance of Well-Confined Concrete Bridge Columns.* Dawn E. Lehman and Jack P. Moehle. December 2000.

ONLINE PEER REPORTS

The following PEER reports are available by Internet only at http://peer.berkeley.edu/publications/peer_reports_complete.html.
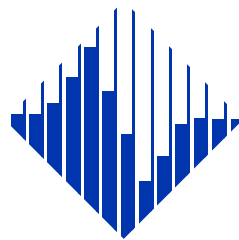
PEER 2012/103 *Performance-Based Seismic Demand Assessment of Concentrically Braced Steel Frame Buildings.* Chui-Hsin Chen and Stephen A. Mahin. December 2012.

PEER 2012/102 *Procedure to Restart an Interrupted Hybrid Simulation: Addendum to PEER Report 2010/103.* Vesna Terzic and Bozidar Stojadinovic. October 2012.

PEER 2012/101 *Mechanics of Fiber Reinforced Bearings.* James M. Kelly and Andrea Calabrese. February 2012.

PEER 2011/107 *Nonlinear Site Response and Seismic Compression at Vertical Array Strongly Shaken by 2007 Niigata-ken Chuetsu-oki Earthquake.* Eric Yee, Jonathan P. Stewart, and Kohji Tokimatsu. December 2011.

PEER 2011/106 *Self Compacting Hybrid Fiber Reinforced Concrete Composites for Bridge Columns.* Pardeep Kumar, Gabriel Jen, William Trono, Marios Panagiotou, and Claudia Ostertag. September 2011.

PEER 2011/105 *Stochastic Dynamic Analysis of Bridges Subjected to Spacially Varying Ground Motions.* Katerina Konakli and Armen Der Kiureghian. August 2011.

PEER 2011/104 *Design and Instrumentation of the 2010 E-Defense Four-Story Reinforced Concrete and Post-Tensioned Concrete Buildings.* Takuya Nagae, Kenichi Tahara, Taizo Matsumori, Hitoshi Shiohara, Toshimi Kabeyasawa, Susumu Kono, Minehiro Nishiyama (Japanese Research Team) and John Wallace, Wassim Ghannoum, Jack Moehle, Richard Sause, Wesley Keller, Zeynep Tuna (U.S. Research Team). June 2011.

PEER 2011/103 *In-Situ Monitoring of the Force Output of Fluid Dampers: Experimental Investigation.* Dimitrios Konstantinidis, James M. Kelly, and Nicos Makris. April 2011.

PEER 2011/102 *Ground-motion prediction equations 1964 - 2010.* John Douglas. April 2011.

PEER 2011/101 *Report of the Eighth Planning Meeting of NEES/E-Defense Collaborative Research on Earthquake Engineering.* Convened by the Hyogo Earthquake Engineering Research Center (NIED), NEES Consortium, Inc. February 2011.

PEER 2010/111 *Modeling and Acceptance Criteria for Seismic Design and Analysis of Tall Buildings.* Task 7 Report for the Tall Buildings Initiative - Published jointly by the Applied Technology Council. October 2010.

PEER 2010/110 *Seismic Performance Assessment and Probabilistic Repair Cost Analysis of Precast Concrete Cladding Systems for Multistory Buildings.* Jeffrey P. Hunt and Božidar Stojadinovic. November 2010.

PEER 2010/109 *Report of the Seventh Joint Planning Meeting of NEES/E-Defense Collaboration on Earthquake Engineering. Held at the E-Defense, Miki, and Shin-Kobe, Japan, September 18–19, 2009.* August 2010.

PEER 2010/108 *Probabilistic Tsunami Hazard in California.* Hong Kie Thio, Paul Somerville, and Jascha Polet, preparers. October 2010.

PEER 2010/107 *Performance and Reliability of Exposed Column Base Plate Connections for Steel Moment-Resisting Frames.* Ady Aviram, Božidar Stojadinovic, and Armen Der Kiureghian. August 2010.

PEER 2010/106 *Verification of Probabilistic Seismic Hazard Analysis Computer Programs.* Patricia Thomas, Ivan Wong, and Norman Abrahamson. May 2010.

PEER 2010/105 *Structural Engineering Reconnaissance of the April 6, 2009, Abruzzo, Italy, Earthquake, and Lessons Learned.* M. Selim Günay and Khalid M. Mosalam. April 2010.

PEER 2010/104 *Simulating the Inelastic Seismic Behavior of Steel Braced Frames, Including the Effects of Low-Cycle Fatigue.* Yuli Huang and Stephen A. Mahin. April 2010.

PEER 2010/103 *Post-Earthquake Traffic Capacity of Modern Bridges in California.* Vesna Terzic and Božidar Stojadinović. March 2010.

PEER 2010/102 *Analysis of Cumulative Absolute Velocity (CAV) and JMA Instrumental Seismic Intensity (I_{JMA}) Using the PEER–NGA Strong Motion Database.* Kenneth W. Campbell and Yousef Bozorgnia. February 2010.

PEER 2010/101 *Rocking Response of Bridges on Shallow Foundations.* Jose A. Ugalde, Bruce L. Kutter, and Boris Jeremic. April 2010.

PEER 2009/109 *Simulation and Performance-Based Earthquake Engineering Assessment of Self-Centering Post-Tensioned Concrete Bridge Systems.* Won K. Lee and Sarah L. Billington. December 2009.

PEER 2009/108 *PEER Lifelines Geotechnical Virtual Data Center.* J. Carl Stepp, Daniel J. Ponti, Loren L. Turner, Jennifer N. Swift, Sean Devlin, Yang Zhu, Jean Benoit, and John Bobbitt. September 2009.

PEER 2009/107 *Experimental and Computational Evaluation of Current and Innovative In-Span Hinge Details in Reinforced Concrete Box-Girder Bridges: Part 2: Post-Test Analysis and Design Recommendations.* Matias A. Hube and Khalid M. Mosalam. December 2009.

PEER 2009/106 *Shear Strength Models of Exterior Beam-Column Joints without Transverse Reinforcement.* Sangjoon Park and Khalid M. Mosalam. November 2009.

PEER 2009/105 *Reduced Uncertainty of Ground Motion Prediction Equations through Bayesian Variance Analysis.* Robb Eric S. Moss. November 2009.

PEER 2009/104 *Advanced Implementation of Hybrid Simulation.* Andreas H. Schellenberg, Stephen A. Mahin, Gregory L. Fenves. November 2009.

PEER 2009/103 *Performance Evaluation of Innovative Steel Braced Frames.* T. Y. Yang, Jack P. Moehle, and Božidar Stojadinovic. August 2009.

PEER 2009/102 *Reinvestigation of Liquefaction and Nonliquefaction Case Histories from the 1976 Tangshan Earthquake.* Robb Eric Moss, Robert E. Kayen, Liyuan Tong, Songyu Liu, Guojun Cai, and Jiaer Wu. August 2009.

PEER 2009/101 *Report of the First Joint Planning Meeting for the Second Phase of NEES/E-Defense Collaborative Research on Earthquake Engineering.* Stephen A. Mahin et al. July 2009.

PEER 2008/104 *Experimental and Analytical Study of the Seismic Performance of Retaining Structures.* Linda Al Atik and Nicholas Sitar. January 2009.

PEER 2008/103 *Experimental and Computational Evaluation of Current and Innovative In-Span Hinge Details in Reinforced Concrete Box-Girder Bridges. Part 1: Experimental Findings and Pre-Test Analysis.* Matias A. Hube and Khalid M. Mosalam. January 2009.

PEER 2008/102 *Modeling of Unreinforced Masonry Infill Walls Considering In-Plane and Out-of-Plane Interaction.* Stephen Kadysiewski and Khalid M. Mosalam. January 2009.

PEER 2008/101 *Seismic Performance Objectives for Tall Buildings.* William T. Holmes, Charles Kircher, William Petak, and Nabih Youssef. August 2008.

PEER 2007/101 *Generalized Hybrid Simulation Framework for Structural Systems Subjected to Seismic Loading.* Tarek Elkhoraibi and Khalid M. Mosalam. July 2007.

PEER 2007/100 *Seismic Evaluation of Reinforced Concrete Buildings Including Effects of Masonry Infill Walls.* Alidad Hashemi and Khalid M. Mosalam. July 2007.

PEER Core Institutions:
University of California, Berkeley (Lead Institution)
California Institute of Technology
Oregon State University
Stanford University
University of California, Davis
University of California, Irvine
University of California, Los Angeles
University of California, San Diego
University of Southern California
University of Washington

PEER reports can be ordered at http://peer.berkeley.edu/publications/peer_reports.html or by contacting

Pacific Earthquake Engineering Research Center
University of California, Berkeley
325 Davis Hall, mail code 1792
Berkeley, CA 94720-1792
Tel: 510-642-3437
Fax: 510-642-1655
Email: peer_editor@berkeley.edu

ISSN 1547-0587X